

Nuclear Structure with Unitarily Transformed Two-Body plus Phenomenological Three-Body Interactions

Vom Fachbereich Physik
der Technischen Universität Darmstadt

zur Erlangung des Grades
eines Doktors der Naturwissenschaften
(Dr. rer. nat.)

genehmigte

Dissertation

von

Dipl.-Phys. Anneke Günther
aus Eckernförde

Darmstadt 2011
D17

Referent: Prof. Dr. Robert Roth
Korreferent: Prof. Dr. Jochen Wambach

Tag der Einreichung: 14.12.2010
Tag der Prüfung: 02.02.2011

Summary

The importance of three-nucleon forces for a variety of nuclear structure phenomena is apparent in various investigations. This thesis provides a first step towards the inclusion of realistic three-nucleon forces by studying simple phenomenological three-body interactions.

The Unitary Correlation Operator Method (UCOM) and the Similarity Renormalization Group (SRG) provide two different approaches to derive soft phase-shift equivalent nucleon-nucleon (NN) interactions via unitary transformations. Although their motivations are quite different the NN interactions obtained with the two methods exhibit some similarities.

The application of the UCOM- or SRG-transformed Argonne V18 potential in the Hartree-Fock (HF) approximation and including the second-order energy corrections emerging from many-body perturbation theory (MBPT) reveals that the systematics of experimental ground-state energies can be reproduced by some of the interactions considering a series of closed-shell nuclei across the whole nuclear chart. However, charge radii are systematically underestimated, especially for intermediate and heavy nuclei. This discrepancy to experimental data is expected to result from neglected three-nucleon interactions.

As first ansatz for a three-nucleon force, we consider a finite-range three-body interaction of Gaussian shape. Its influence on ground-state energies and charge radii is discussed in detail on the basis of HF plus MBPT calculations and shows a significant improvement in the description of experimental data.

As the handling of the Gaussian three-body interaction is time-extensive, we show that it can be replaced by a regularized three-body contact interaction exhibiting a very similar behavior. An extensive study characterizes its properties in detail and confirms the improvements with respect to nuclear properties. To take into account information of an exact numerical solution of the nuclear eigenvalue problem, the No-Core Shell Model is applied to calculate the ${}^4\text{He}$ ground-state energy.

As they are of direct interest for nuclear astrophysics collective excitation modes, namely giant resonances, are investigated in the framework of the Random Phase Approximation. Including the full three-body interaction would be very time-demanding. Therefore, a density-dependent two-body interaction is used instead. This simple interaction leads to a significant improvement in the description of the isovector dipole and isoscalar quadrupole resonances while the isoscalar monopole resonances remain in good agreement with experimental data compared to the results obtained with pure unitarily transformed two-body interactions.

Zusammenfassung

Eine Vielzahl von Kernstrukturuntersuchungen belegt, dass Dreinukleonenkräfte einen wesentlichen Einfluß auf verschiedene Observablen haben. Als ersten Schritt hin zur Verwendung von realistischen Dreinukleonenkräften werden in dieser Arbeit einfache phänomenologische Dreiteilchenwechselwirkungen untersucht.

Sowohl die Methode der Unitären Korrelatoren (UCOM) als auch die Ähnlichkeits-Renormierungsgruppe (SRG) verwenden unitäre Transformationen, um weiche streuphasenäquivalente Nukleon-Nukleon (NN) Wechselwirkungen abzuleiten. Obwohl die beiden Methoden von unterschiedlichen Ansätzen ausgehen, weisen die aus dem realistischen Argonne V18 Potential gewonnenen NN Wechselwirkungen eine Reihe von Gemeinsamkeiten auf.

Auf der Grundlage der Hartree-Fock (HF) Methode und der Vielteilchenstörungstheorie (MBPT) zweiter Ordnung kann die Systematik der Grundzustandsenergien einer Reihe von Kernen mit abgeschlossenen Schalen mit Hilfe einiger der unitär transformierten NN Wechselwirkungen über die gesamte Nuklidkarte hinweg reproduziert werden. Die Ladungsradien werden dagegen systematisch zu klein vorhergesagt, insbesondere für mittelschwere und schwere Kerne. Es wird erwartet, dass diese Abweichungen auf vernachlässigte Dreiteilchenwechselwirkungen zurückzuführen sind.

Als erster Ansatz wird der Einfluß einer gaußförmigen Dreiteilchenwechselwirkung im Rahmen von HF und MBPT untersucht, was zu einer deutlich besseren Beschreibung der experimentellen Daten führt.

Da Rechnungen mit der gaußförmigen Dreiteilchenwechselwirkung sehr zeitaufwändig sind, wird sie durch eine regularisierte Dreiteilchenkontaktwechselwirkung ersetzt, die vergleichbare Ergebnisse liefert. Die Eigenschaften dieser Wechselwirkung werden untersucht und die verbesserte Beschreibung von Grundzustandsobservablen bestätigt. Um einen Referenzpunkt aus einer exakten numerischen Lösung des nuklearen Eigenwertproblems zu erhalten, wird die ^4He Grundzustandsenergie im Rahmen des No-Core Schalenmodells berechnet.

Abschließend werden kollektive Anregungen, die besonders für Anwendungen in der nuklearen Astrophysik interessant sind, im Rahmen der Random Phase Approximation studiert. Da die Verwendung der Dreiteilchenkontaktwechselwirkung in dieser Methode zu zeitaufwändig wäre, wird sie durch eine dichteabhängige Zweiteilchenwechselwirkung ersetzt. Verglichen mit den Ergebnissen von reinen unitär transformierten Zweiteilchenwechselwirkungen führt die Einbeziehung der phänomenologischen Wechselwirkung zu einer deutlichen Verbesserung bei der Beschreibung der isovektoriellen Dipol- und der isoskalaren Quadrupolriesenresonanzen, während die isoskalaren Monopolriesenresonanzen gleichbleibend gut reproduziert werden.

Contents

1	<i>Introduction</i>	1
2	<i>Unitarily Transformed Interactions</i>	7
2.1	Realistic Nucleon-Nucleon Potentials	7
2.2	Unitary Correlation Operator Method	9
2.2.1	Correlation Operators	10
2.2.2	Correlated Wave Functions	12
2.2.3	Cluster Expansion	15
2.2.4	Correlated Interaction	16
2.2.5	Correlated Two-Body Matrix Elements	19
2.2.6	Optimal Correlation Functions	23
2.3	Similarity Renormalization Group	27
2.3.1	SRG Flow Equation	27
2.3.2	Evolution of Two-Body Matrix Elements	28
2.3.3	Evolved Wave Functions and Matrix Elements	30
2.3.4	Connections between UCOM and SRG	32
2.3.5	SRG-Generated UCOM Correlation Functions	34
3	<i>Many-Body Calculations</i>	41
3.1	The Hartree-Fock Method	41
3.2	Ground-State Energies and Charge Radii	44
3.3	Single-Particle Spectra	52
3.4	Low-Order Many-Body Perturbation Theory	55
3.5	Second-Order Energy Corrections	59
4	<i>Gaussian Three-Body Interaction</i>	65
4.1	Calculation of Matrix Elements	65
4.1.1	Cartesian Matrix Elements	66
4.1.2	Coordinate Transformation	68

4.2	Ground-State Energies and Charge Radii	71
4.3	Perturbative Energy Corrections	77
5	<i>Three-Body Contact Interaction</i>	81
5.1	Calculation of Matrix Elements	81
5.2	Ground-State Energies and Charge Radii	87
5.3	Single-Particle Spectra	91
5.4	Perturbative Energy Corrections	94
6	<i>Few-Body Calculations</i>	103
6.1	The No-Core Shell Model	103
6.2	^4He Ground-State Energy	104
7	<i>Collective Excitations</i>	107
7.1	Random Phase Approximation	107
7.2	Multipole Transitions	109
7.3	Sum Rules	110
7.4	Giant Resonances	114
7.4.1	Isoscalar Giant Monopole Resonance	115
7.4.2	Isovector Giant Dipole Resonance	122
7.4.3	Isoscalar Giant Quadrupole Resonance	126
7.4.4	Comparison of Giant Resonances	130
8	<i>Conclusions</i>	133
A	<i>Derivation of the Hartree-Fock Equations</i>	139
A.1	The Variational Principle	139
A.2	The Hartree-Fock Method	140
B	<i>Basic Concepts of Perturbation Theory</i>	147
C	<i>Basic Concepts of the Random Phase Approximation</i>	149
D	<i>Normal Ordering</i>	153
E	<i>Figures</i>	155
E.1	Hartree-Fock Results for the Contact Interaction	155

E.2	Perturbative Energy Corrections for the Contact Interaction	158
E.3	Collective Excitations	160
<i>F</i>	<i>Notation</i>	<i>165</i>

Chapter 1

Introduction

The existence of a diversity of chemical elements is the most fundamental precondition for the existence of our planet earth. During the cooling of the universe after the big bang no elements heavier than lithium were formed. Only some of the chemical elements up to iron are produced by fusion in the inner cores of stars. For the production of all other elements hotter and denser environments are required, which appear in different astrophysical scenarios such as red giants, novae, and supernovae. Nuclear astrophysics aims at the modeling of nucleosynthesis via various processes like the rapid neutron capture process (*r*-process) that proceeds in supernovae. On the basis of the *r*-process the existence of most neutron-rich nuclei up to the neutron dripline can be understood. In contrast, the slow neutron capture process (*s*-process) stays close to the valley of stability, while the rapid proton capture process (*rp*-process) covers the proton-rich part of the nuclear chart. These nucleosynthesis processes are sketched in Figure 1.1, where the nuclear chart consisting of the stable elements, the known unstable isotopes, and the nuclei that are expected to exist but are (still) unknown is shown. To allow for reliable statements about the various nucleosynthesis processes a detailed fundamental knowledge of atomic nuclei, stable as well as unstable and exotic ones, is indispensable.

The properties of stable nuclei have been investigated in numerous experiments, e.g. at various accelerator facilities, since a long time. In recent years experimental techniques for the study of unstable and exotic nuclei have been developed. Nonetheless, a reliable theoretical framework is inevitable, on the one hand to explain experimental observations and to offer guidelines for the development of further experiments and on the other hand to provide reliable predictions for exotic nuclei that cannot (yet)

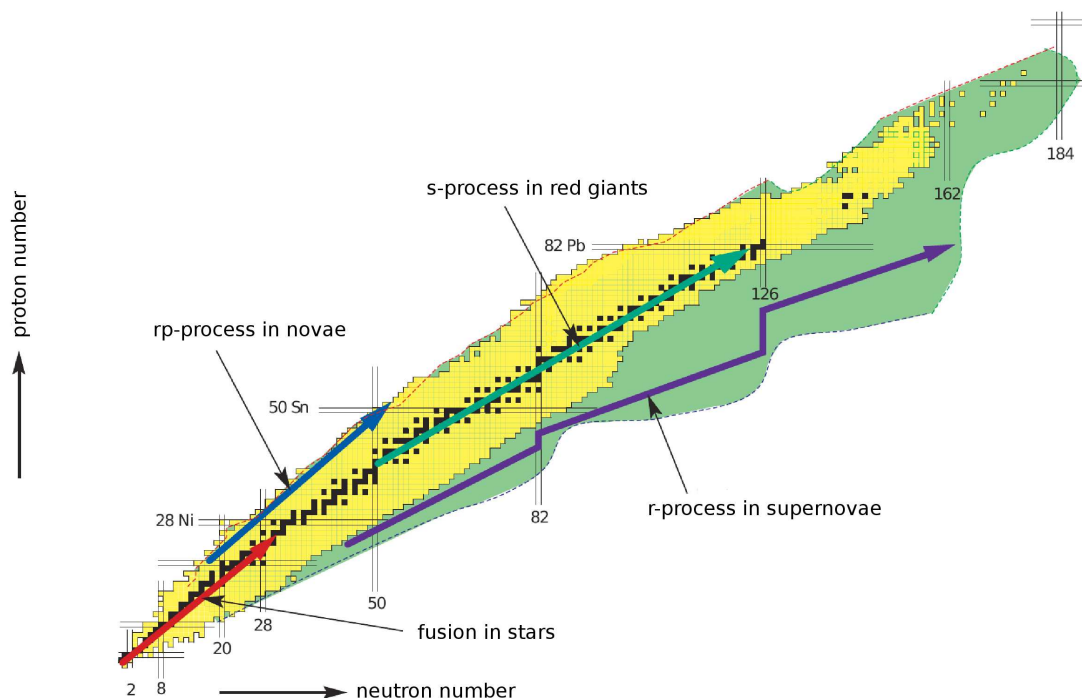


Figure 1.1: Nuclear chart consisting of stable isotopes (black), known unstable isotopes (yellow), and unknown isotopes (green) where some of the possible nucleosynthesis processes are indicated [1].

be studied experimentally. The theoretical framework is developed step by step in constant connection to experimental advance, which is a difficult task as it cannot simply be derived from first principles. First of all, the theory has to reliably reproduce well-known properties of stable and unstable nuclei, e.g. ground-state properties and certain excitations. Built on this well-established foundation one can provide predictions for observables and phenomena that are not experimentally accessible. For example information on very short-lived exotic nuclei that is required for modeling the nucleosynthesis, supernovae, etc., or the possible existence of an island of stability in the region of superheavy elements.

The accurate theoretical description of atomic nuclei is a difficult task for several reasons. On the one hand the interaction between the nucleons is of complex nature and on the other hand the quantum mechanical many-body problem has to be solved, which cannot be done analytically.

Nucleons are no elementary particles but consist of quarks and gluons interacting via the strong interaction, which is described by Quantum Chromodynamics (QCD).

Unfortunately, in the low-energy regime relevant for nuclear physics the QCD cannot be treated perturbatively, which means that the nuclear interaction cannot be easily derived from QCD. The most consistent approach to this problem currently available is provided by chiral effective field theory, where the nucleons and pions are regarded as relevant degrees of freedom and chiral symmetry is taken into account. It is, thus, possible to derive a systematic expansion of an effective nuclear interaction in the framework of chiral perturbation theory. One advantage of this approach is that it offers consistent three-body and higher many-body interactions in addition to the two-nucleon interaction [2]. However, these chiral interactions are not yet well-studied and especially the inclusion of suitable three-body interactions may lead to unforeseen effects [3, 4].

A more established approach to nuclear interactions is given by the so-called realistic potentials, e.g. the Argonne V18 [5], CD-Bonn [6], and Nijmegen [7] potentials, which reproduce experimental two-nucleon observables like scattering phase-shifts with high precision. The Argonne V18 is a combination of the one-pion exchange describing the long-range behavior and phenomenological intermediate and short-range terms.

A closer inspection of the realistic potentials reveals that their momentum space representations contain large off-diagonal matrix elements due to strong short-range correlations induced by the nuclear interaction, i.e. low-momentum states are connected to states with high-lying momenta. The short-range correlations are mainly caused by the hard core, i.e., the strong short-range repulsion in the central part of the interaction, and tensor forces. Consequently, large model spaces are required to obtain converged results in the framework of various many-body methods. For light nuclei, the corresponding computational effort may still be manageable. But at least for the investigation of intermediate and heavy nuclei such large model spaces cannot be handled.

A solution to this problem is offered by different approaches. The Unitary Correlation Operator Method (UCOM) [8–10] was developed to facilitate the convergence of calculations in moderate model spaces by constructing a soft interaction via a unitary transformation. To build the unitary transformation operator short-range central and tensor correlations are considered explicitly. The transformation is designed such that the resulting interaction is phase-shift equivalent to the underlying bare potential. In momentum space the UCOM transformation leads to a suppression of off-diagonal matrix elements and thus to a band-diagonal structure of the Hamiltonian, which in turn improves the convergence behavior significantly.

The transformed interactions obtained with the Similarity Renormalization Group (SRG) [10, 11] exhibit several similarities with the UCOM-transformed interactions,

although the SRG starts from a different motivation. The idea of SRG is to use a renormalization group flow equation in order to pre-diagonalize the Hamilton matrix with respect to a given basis. When choosing the appropriate generator for the transformation the resulting interaction is, like the UCOM-transformed interaction, phase-shift equivalent to the underlying interaction and exhibits a band-diagonal structure with respect to momentum-space matrix elements. Both types of unitary transformations lead to a decoupling of low and high momenta.

The properties of the different unitarily transformed nucleon-nucleon (NN) interactions can be investigated by applying various many-body methods for the study of different observables. A diversity of many-body approaches is available, each with its inherent advantages and limitations. The No-Core Shell Model (NCSM) performs an exact diagonalization of the Hamilton matrix but it is restricted to light nuclei [12]. For the investigation of intermediate and heavy nuclei mean-field approaches like the Hartree-Fock (HF) method are suitable [13]. In the HF approximation the use of the bare Argonne V18 would not even yield bound nuclei. Thus, using a transformed interaction is inevitable. The HF states are not capable of describing any correlations. For that purpose, many-body perturbation theory (MBPT) can be applied on top of the HF results.

Using these methods one can study simultaneously the properties of the NN interactions and their influence on different ground-state observables. For the investigation of excited states, the Random Phase Approximation (RPA) proves to be an appropriate method, which is also based on HF results [14]. This method is especially suited for the investigation of collective excitations such as giant resonances, which are of direct interest for applications in nuclear astrophysics.

By construction, the unitarily transformed interactions contain irreducible contributions to all particle numbers, but they are truncated at the two-body level discarding three-body and higher many-body forces. The investigation of ground-state properties of closed-shell nuclei across the whole nuclear chart reveals systematic deviations from experimental data, e.g. charge radii are underestimated. This is expected to result from neglected genuine and induced three-body forces. In recent years, it became clear that the consideration of three-body forces is inevitable for an accurate description of atomic nuclei. The most consistent way of including three-body forces would be to start from the chiral two- plus three-nucleon interaction and perform the unitary transformations including all terms up to three-body level. As this approach was only investigated very recently [3, 4], we choose a more pragmatic approach by supplementing the unitarily transformed two-nucleon interactions by phenomenological three-body forces.

The aim of this thesis is on the one hand to investigate the impact of simple phenomenological three-body forces on different observables and on the other hand to establish an efficient handling of three-body interactions and to extend the many-body methods such that three-body terms can be included in a computationally feasible manner.

In order to provide a complete and consistent discussion of the influence of phenomenological three-body interactions, we start by considering the pure NN interactions. The Argonne V18 is used as starting point for the construction of soft phase-shift equivalent NN interactions via UCOM and SRG. In Chapter 2, the UCOM and SRG approaches are presented in some detail.

In Chapter 3 we will derive the formalism required for the application of unitarily transformed two-body plus phenomenological three-body interactions in the Hartree-Fock approximation and in many-body perturbation theory. Furthermore, we will investigate ground-state energies and charge radii of closed-shell nuclei across the whole nuclear chart on the basis of pure two-body interactions. These studies reveal that the charge radii are systematically underestimated for intermediate and heavy nuclei. Thus, the necessity of including three-body interactions is demonstrated.

As a first ansatz for a phenomenological three-body interaction we introduce a finite-range three-body interaction of Gaussian shape in Chapter 4. After the calculation of the three-body matrix elements, the impact of the Gaussian three-body interaction on ground-state energies and charge radii is discussed in detail. The three-body interaction is first included in the HF method as we want to determine the free parameters of this interaction such that the experimental charge radii are reproduced across the whole nuclear chart. Unfortunately, the Gaussian three-body interaction requires an enormous computational effort, which inhibits calculations in model spaces large enough to warrant convergence. We can show, however, that the results obtained with the Gaussian three-body interaction are similar to those of a regularized three-body contact interaction.

The matrix elements of the regularized contact interaction are derived in Chapter 5. As for the Gaussian interaction, the parameters of the contact interaction are determined on the basis of HF calculations in order to reproduce the experimental charge radii. Subsequently, the influence of long-range correlations is studied in the framework of many-body perturbation theory. The handling of the three-body contact interaction is efficient such that calculations in large model spaces are feasible.

In Chapter 6 the three-body contact interaction is included in the No-Core Shell Model. After a short discussion of the formalism, the NCSM is used to confirm the choice of the parameters on the basis of an exact calculation of the ${}^4\text{He}$ ground-state

energy.

Finally, we focus on excited states in the framework of the Random Phase Approximation in Chapter 7. The inclusion of the three-body contact interaction in RPA would be computationally too demanding. Therefore, it is replaced by a density-dependent two-body contact interaction, which is approximately equivalent in this case. The RPA is especially suitable for the study of collective excitations, e.g. giant resonances.

The main statements of this work are summarized in Chapter 8 together with a prospect on continuative investigations.

This work is complemented by several appendices. In Appendices A – C the basic concepts of the applied many-body methods are summarized. In Appendix D the normal ordering of a general three-body interaction is derived as a possibility to provide an effective two-body interaction. In Appendix E supplementary figures are collected, that complete the set of figures discussed in Chapters 5 and 7 but reveal no further physical insight. Finally, frequently used symbols and acronyms are listed in Appendix F.

Chapter 2

Unitarily Transformed Interactions

In this chapter we discuss the different transformed nucleon-nucleon (NN) potentials that provide the starting point for the subsequent investigations. We start by summarizing the main aspects of the realistic Argonne V18 potential in Section 2.1, which will be used for all calculations discussed in this thesis. Since the bare Argonne V18 potential is not suitable for performing efficient many-body calculations in finite model spaces, we will introduce two approaches, namely the Unitary Correlation Operator Method (UCOM) in Section 2.2 and the Similarity Renormalization Group (SRG) in Section 2.3, which both provide a possibility to generate a soft interaction suitable for the application in different many-body methods.

2.1 Realistic Nucleon-Nucleon Potentials

Realistic NN potentials are designed to reproduce phase shifts in scattering experiments and other low-energy two-body observables with high precision. Therefore, they prove to be a good starting point for nuclear structure calculations. Among the various realistic nucleon-nucleon potentials we will only consider the Argonne V18 [5], which will be used in the subsequent investigations. The Argonne V18 is a nonrelativistic potential with a local operator structure that has been fit directly to both pp and np data as well as low-energy nn scattering parameters and deuteron properties. The potential consists of an electromagnetic part, a one-pion-exchange part describing the long-range behavior, and an intermediate and short-range phenomenological part:

$$v = v^{\text{EM}} + v^{\pi} + v^R . \quad (2.1)$$

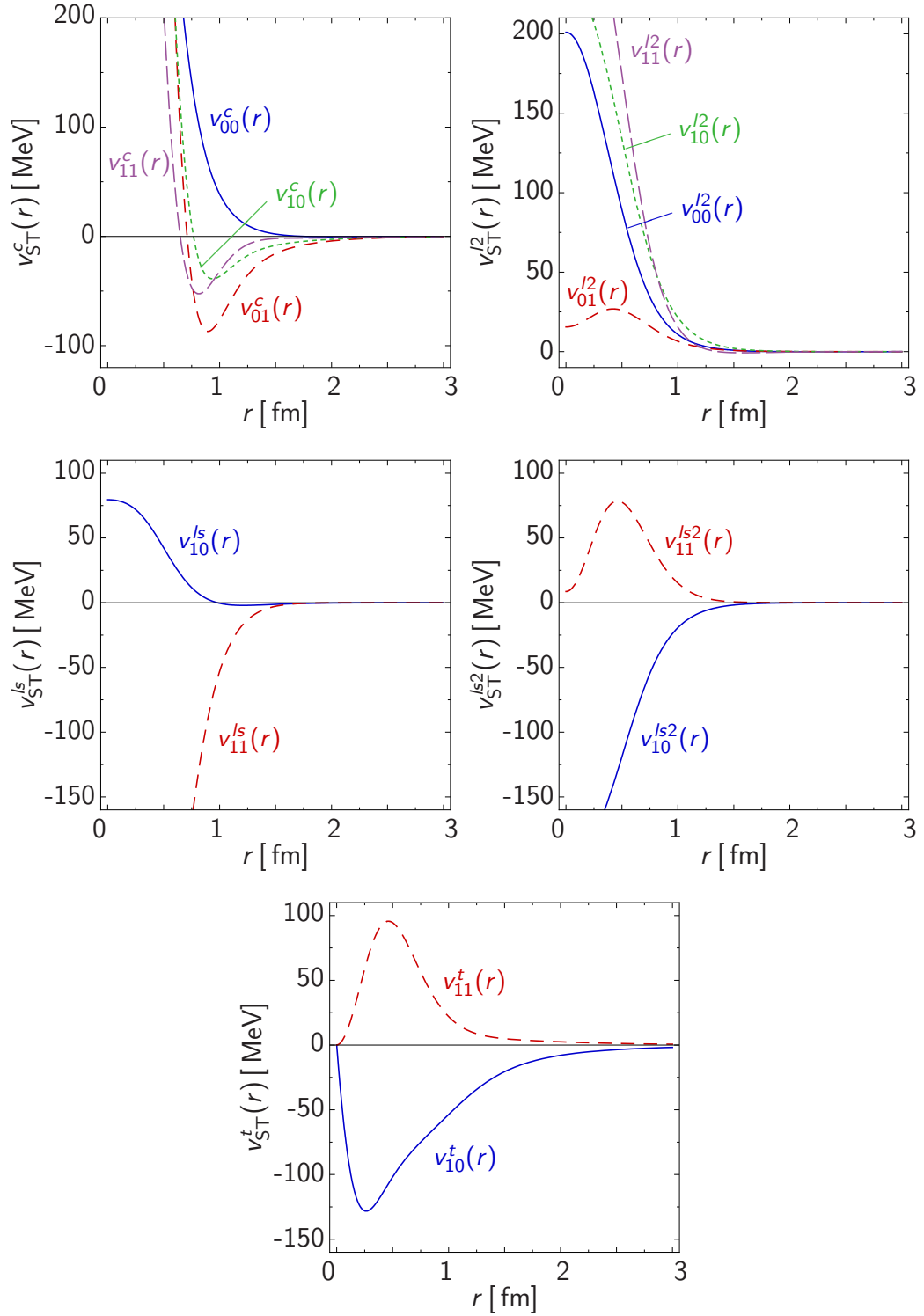


Figure 2.1: Radial dependencies of the Argonne V18 potential for the different contributions in the respective spin-isospin channels.

The phenomenological part is expressed as a sum of central, quadratic angular momentum, tensor, spin-orbit and quadratic spin-orbit terms:

$$v_{ST}^R = v_{ST}^c(r) + v_{ST}^{l2}(r)L^2 + v_{ST}^t(r)S_{12} + v_{ST}^{ls}(r)\mathbf{L} \cdot \mathbf{S} + v_{ST}^{ls2}(r)(\mathbf{L} \cdot \mathbf{S})^2 . \quad (2.2)$$

The radial dependencies $v_{ST}^i(r)$ are parameterized in an appropriate manner and fit to experimental data. For illustration the radial dependencies are displayed in Figure 2.1 for the respective spin-isospin channels, where to the tensor part the contribution emerging from the one-pion exchange has been added.

Alternatively, the strong interaction potential can be projected into an operator format with 18 terms:

$$v_{ij} = \sum_{p=1}^{18} v_p(r_{ij})O_{ij}^p , \quad (2.3)$$

giving the potential its name. Of these 18 operators, 14 are charge-independent while three are charge-dependent and one is charge-asymmetric.

2.2 Unitary Correlation Operator Method

The development of realistic NN potentials reproducing experimental data with high precision, like the Argonne V18, is the basis for an ab initio description of nuclei. Due to the enormous computational effort, these investigations are restricted to light nuclei. For the description of heavier nuclei, while staying as close as possible to an ab initio treatment of the many-body problem, the many-body Hilbert space has to be truncated to a smaller subspace. The combination of realistic NN potentials with simple many-body states, e.g. a superposition of Slater-determinants, reveals a fundamental problem: The strong short-range correlations induced by the nuclear interaction cannot be adequately described by simple many-body states in a small Hilbert space.

These correlations are already revealed in the deuteron solution, which is visualized in Figure 2.2, where the spin-projected two-body density resulting from an exact calculation based on the Argonne V18 potential is shown [9, 15]. The repulsive core of the interaction leads to a suppression of the two-body density at small interparticle distances, while the effect of the tensor force is manifested in the strong dependence on the relative distance and the spin alignments leading to the "doughnut" and "dumbbell" shapes for antiparallel and parallel spins, respectively.

The Unitary Correlation Operator Method (UCOM) [8–10, 15] was developed in order to handle this problem by explicitly dealing with the strong short-range correlations

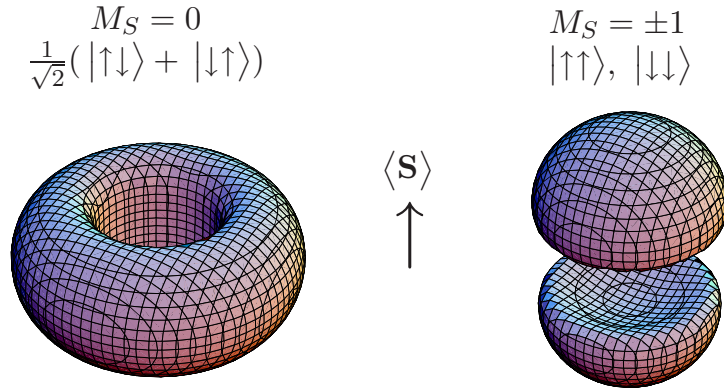


Figure 2.2: Two-body density of the deuteron calculated with the AV18 potential and projected onto the two possibilities of antiparallel spins (left) and parallel spins (right). Shown are the isodensity surfaces for $\varrho_{1M_S}^{(2)} = 0.005 \text{ fm}^{-3}$ (taken from [15]).

induced by the nuclear interaction by means of a unitary transformation. The main features of the Unitary Correlation Operator Method will be discussed in the following subsections.

2.2.1 Correlation Operators

The idea of the UCOM is to imprint the short-range correlations into a simple many-body state $|\Psi\rangle$ that can be a Slater-determinant in the simplest case. This is achieved via a state-independent unitary transformation using the correlation operator C :

$$|\tilde{\Psi}\rangle = C|\Psi\rangle, \quad (2.4)$$

leading to a correlated state $|\tilde{\Psi}\rangle$ that is no longer a Slater determinant due to the complex structure of the short-range correlations [8–10, 15]. Instead of correlating the many-body state one can also perform a unitary transformation of the operators

$$\tilde{O} = C^\dagger O C, \quad (2.5)$$

which are then evaluated in the untransformed model space. These two approaches are equivalent as we can see by considering expectation values or matrix elements:

$$\langle \tilde{\Psi} | O | \tilde{\Psi}' \rangle = \langle \Psi | C^\dagger O C | \Psi' \rangle = \langle \Psi | \tilde{O} | \Psi' \rangle. \quad (2.6)$$

Hence, one can choose the form that is technically more advantageous for the respective application.

As mentioned above, the most dominant short-range correlations are the central and tensor ones. Therefore, it is convenient to decompose the correlation operator C into two operators C_r and C_Ω describing the central and tensor correlations, respectively. Since the correlation operators are unitary they can be expressed as exponentials involving hermitian generators [8, 15]:

$$C = C_\Omega C_r = \exp\left\{-i \sum_{i<j} g_{\Omega,ij}\right\} \exp\left\{-i \sum_{i<j} g_{r,ij}\right\}, \quad (2.7)$$

where we have assumed the generators g_r and g_Ω to be two-body operators since the correlations are induced by a two-body potential. The detailed form of the generators is determined by the structure of the central and tensor correlations.

Central Correlations

The repulsive core of the central part of the NN interaction prohibits that two nucleons in a many-nucleon system approach each other too closely. This leads to a suppression of the two-body density at small interparticle distances (cf. Fig. 2.2). Hence, the central correlator is constructed such that two nucleons are shifted apart if their distance is smaller than the range of the repulsive core and are instead concentrated in the attractive region of the NN potential. This radial shift is generated by the projection of the relative momentum $\mathbf{q} = \frac{1}{2}(\mathbf{p}_1 - \mathbf{p}_2)$ onto the distance vector $\mathbf{r} = \mathbf{x}_1 - \mathbf{x}_2$ of two nucleons:

$$q_r = \frac{1}{2}(\mathbf{q} \cdot \frac{\mathbf{r}}{r} + \frac{\mathbf{r}}{r} \cdot \mathbf{q}). \quad (2.8)$$

The radial dependence of the transformation is encapsulated in the shift function $s_{ST}(r)$ for each spin-isospin channel that depends on the structure of the underlying NN potential. The hermitized form of the central generator can thus be written as [8, 16]

$$g_r = \sum_{S,T} \frac{1}{2} (s_{ST}(r) q_r + q_r s_{ST}(r)) \Pi_{ST}, \quad (2.9)$$

where the operator Π_{ST} projects onto two-body spin S and isospin T .

Tensor Correlations

The correlations induced by the tensor force of the NN interaction entangle the alignment of the spins of a nucleon pair with their relative spatial orientation. For the description of these correlations, we construct the tensor correlation operator such

that it only acts on the orbital part of the relative wave function of two nucleons. Therefore, we define the orbital momentum operator \mathbf{q}_Ω :

$$\mathbf{q}_\Omega = \mathbf{q} - \frac{\mathbf{r}}{r}q_r = \frac{1}{2r^2}(\mathbf{L} \times \mathbf{r} - \mathbf{r} \times \mathbf{L}) \quad (2.10)$$

with the relative orbital angular momentum operator $\mathbf{L} = \mathbf{r} \times \mathbf{q}$, which generates shifts orthogonal to the radial momentum $\frac{r}{r}q_r$. The complex structure of the tensor correlations can be described by the tensor operator $S_{12}(\mathbf{r}, \mathbf{q}_\Omega)$, where the general tensor operator of rank 2 reads

$$S_{12}(\mathbf{a}, \mathbf{b}) = \frac{3}{2}[(\boldsymbol{\sigma}_1 \cdot \mathbf{a})(\boldsymbol{\sigma}_2 \cdot \mathbf{b}) + (\boldsymbol{\sigma}_1 \cdot \mathbf{b})(\boldsymbol{\sigma}_2 \cdot \mathbf{a})] - \frac{1}{2}(\boldsymbol{\sigma}_1 \cdot \boldsymbol{\sigma}_2)(\mathbf{a} \cdot \mathbf{b} + \mathbf{b} \cdot \mathbf{a}) . \quad (2.11)$$

Therefore, this operator is used to construct the generator for the tensor correlator [9, 17]

$$g_\Omega = \sum_T \vartheta_T(r) S_{12}(\mathbf{r}, \mathbf{q}_\Omega) \Pi_{1T} , \quad (2.12)$$

where the function $\vartheta_T(r)$ describes the size and distance dependence of the transverse shift. The tensor operator $S_{12}(\mathbf{r}, \mathbf{q}_\Omega)$ entering in this generator has the same structure as the standard tensor operator $S_{12} = S_{12}(\frac{r}{r}, \frac{r}{r})$ generating the tensor force.

2.2.2 Correlated Wave Functions

To illustrate the effect of the central and tensor correlation operators, we consider their impact on a two-nucleon wave function. We only have to consider the relative wave function since the correlation operators do not affect the center-of-mass motion. The uncorrelated two-body state is written as LS -coupled angular momentum eigenstate $|\phi(LS)JMTM_T\rangle$, where the radial wave function is denoted as $\phi(r)$ in coordinate-space representation. We will omit the quantum numbers M and M_T in the following since they are not affected by the unitary transformation.

In coordinate representation, the action of the central correlation operator $C_r = \exp(-i g_r)$ resembles a norm-conserving coordinate transformation of the radial wave function [10]

$$\begin{aligned} \langle r(L'S)JT | C_r | \phi(LS)JT \rangle &= \frac{R_-(r)}{r} \sqrt{R'_-(r)} \phi(R_-(r)) \delta_{L'L} \\ \langle r(L'S)JT | C_r^\dagger | \phi(LS)JT \rangle &= \frac{R_+(r)}{r} \sqrt{R'_+(r)} \phi(R_+(r)) \delta_{L'L} \end{aligned} \quad (2.13)$$

while the orbital part, spin and isospin remain unchanged. The correlation functions

$R_{\pm}(r)$ are mutually inverse, $R_{\pm}(R_{\mp}(r)) = r$, and are connected to the shift function $s(r)$ by the integral equation

$$\int_r^{R_{\pm}(r)} \frac{d\xi}{s(\xi)} = \pm 1, \quad (2.14)$$

where we have suppressed the (S, T) -dependence for brevity. For slowly varying shift functions, the correlation functions can be approximated by

$$R_{\pm}(r) \approx r \pm s(r). \quad (2.15)$$

This illustrates that two nucleons having the distance r are shifted by the distance $s(r)$.

Contrary to the central correlator, the tensor correlator $C_{\Omega} = \exp(-ig_{\Omega})$ does not affect the radial part of the relative two-body wave function but acts only on the angular part. The tensor operator $S_{12}(\mathbf{r}, \mathbf{q}_{\Omega})$ entering in the generator for the tensor correlator has only off-diagonal matrix elements in the LS -coupled basis:

$$\langle (J \pm 1, 1)JT | S_{12}(\mathbf{r}, \mathbf{q}_{\Omega}) | (J \mp 1, 1)JT \rangle = \pm 3i\sqrt{J(J+1)}. \quad (2.16)$$

Hence, total angular momentum is conserved, and the matrix exponential can be evaluated in a subspace of fixed J , i.e. the matrix elements of the full tensor correlator can be computed. States with $L = J$ remain unaffected by the tensor correlator while states with $L = J \pm 1$ are connected to states with $L = J \mp 1$:

$$\langle r(L'S)JT | C_{\Omega} | \phi(LS)JT \rangle = \begin{cases} \phi(r) & , L' = L = J \\ \cos \theta_J(r) \phi(r) & , L' = L = J \pm 1 \\ \pm \sin \theta_J(r) \phi(r) & , L' = J \pm 1, L = J \mp 1 \end{cases} \quad (2.17)$$

with the abbreviation $\theta_J(r) = 3\sqrt{J(J+1)}\vartheta(r)$.

Applying the central and tensor correlator subsequently leads to the fully correlated wave function

$$\begin{aligned} & \langle r(L'S)JT | C_{\Omega} C_r | \phi(LS)JT \rangle \\ &= \begin{cases} \frac{R_-(r)}{r} \sqrt{R'_-(r)} \phi(R_-(r)) & , L' = L = J \\ \cos \theta_J(r) \frac{R_-(r)}{r} \sqrt{R'_-(r)} \phi(R_-(r)) & , L' = L = J \pm 1 \\ \pm \sin \theta_J(r) \frac{R_-(r)}{r} \sqrt{R'_-(r)} \phi(R_-(r)) & , L' = J \pm 1, L = J \mp 1 \end{cases} \end{aligned} \quad (2.18)$$

in coordinate-space representation.

As an illustration of the important role of the central and tensor correlations, we show in Figure 2.3 how a simple two-nucleon trial wave function is turned into

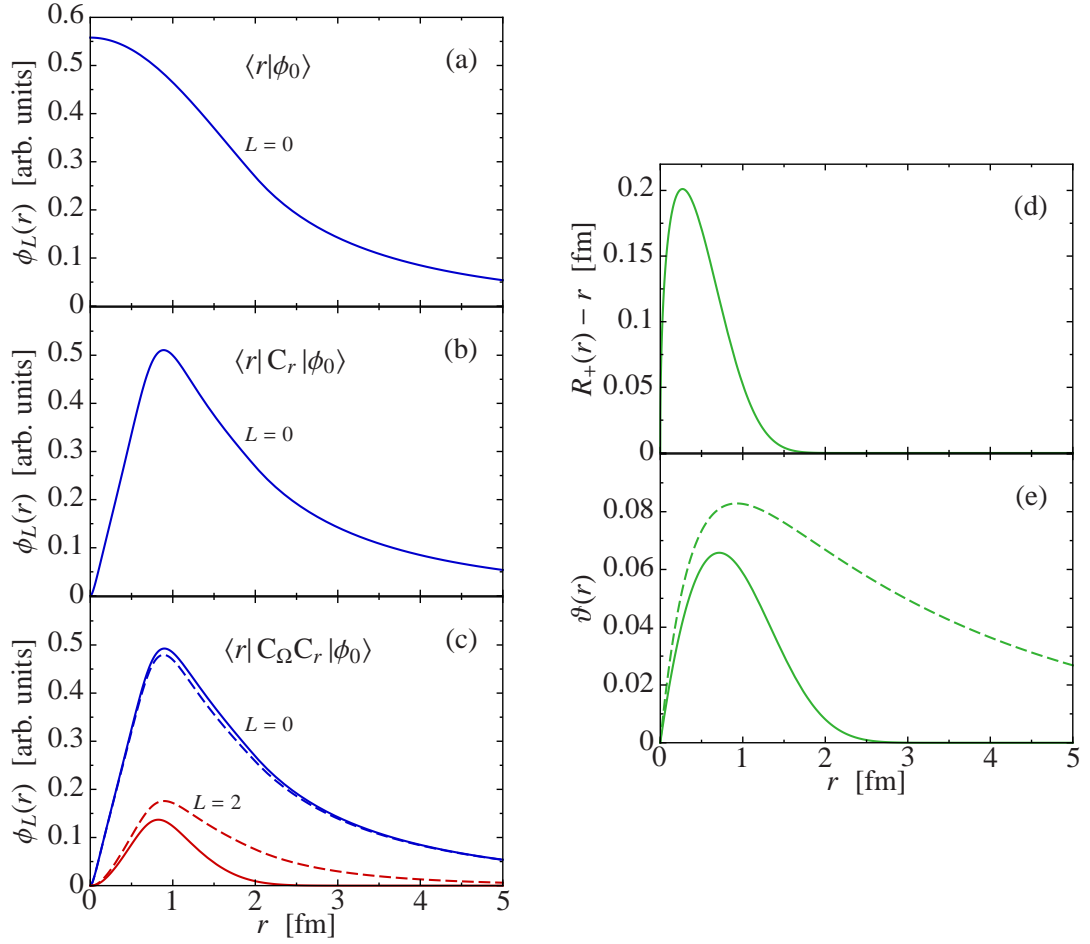


Figure 2.3: Starting from the trial wave function (a), applying the central correlator with correlation function (d) yields wave function (b). Subsequent application of the tensor correlator with correlation function (e) generates wave function (c), see text. (taken from [10]).

an almost realistic deuteron solution. We start from a simple S -wave trial state $|\phi_0(LS)JT\rangle = |\phi_0(01)10\rangle$ depicted in Figure 2.3(a). Applying the central correlator with the correlation function shown in Figure 2.3(d) yields the central correlated wave function $\langle r|C_r|\phi_0(01)10\rangle = \frac{R_-(r)}{r}\sqrt{R'_-(r)}\langle R_-(r)|\phi_0(01)10\rangle$ (Fig. 2.3(b)) containing a correlation hole at small interparticle distances. The subsequent application of the tensor correlator generates a D -wave admixture that depends on the tensor correlation function $\vartheta(r)$ depicted in Figure 2.3(e). The fully correlated wave function [15]

$$\begin{aligned}
 \langle r | C_\Omega C_r | \phi_0(01)10 \rangle &= \cos(3\sqrt{2}\vartheta(r)) \frac{R_-(r)}{r} \sqrt{R'_-(r)} \langle R_-(r) \frac{r}{r} | \phi_0(01)10 \rangle \\
 &+ \sin(3\sqrt{2}\vartheta(r)) \frac{R_-(r)}{r} \sqrt{R'_-(r)} \langle R_-(r) \frac{r}{r} | \phi_0(21)10 \rangle
 \end{aligned} \tag{2.19}$$

is shown in Figure 2.3(c). In order to generate a realistic deuteron wave function the tensor correlation needs to be of long range (dashed curve in Figure 2.3). But the aim of the UCOM is to cover only short-range state-independent correlations. The long-range correlations have to be described by the many-body model space. Thus, we will restrict the range of the tensor correlation function leading to the solid curves in Figure 2.3(c) and (e).

2.2.3 Cluster Expansion

After the illustrative discussion of correlated wave functions, we consider a more formal aspect concerning correlated operators. The generators of the correlation operators are restricted to two-body operators but the correlation operator itself contains irreducible contributions of higher particle numbers because it is the exponential of the generator. Likewise, the similarity transformation of an arbitrary operator O leads to a correlated operator containing irreducible contributions to all particle numbers, which can be expressed via the cluster expansion [9, 15]:

$$\tilde{O} = C^\dagger O C = \sum_{k=1}^A \tilde{O}^{[k]}, \tag{2.20}$$

where $\tilde{O}^{[k]}$ denotes the irreducible k -body part. For a n -body operator all contributions with $k < n$ vanish.

Assuming a generic Hamiltonian

$$H = T + V_{NN} + V_{3N} \tag{2.21}$$

containing the kinetic energy as well as a two- and a three-nucleon interaction, the application of the correlation operator yields

$$\tilde{H} = \tilde{T}^{[1]} + (\tilde{T}^{[2]} + \tilde{V}_{NN}^{[2]}) + (\tilde{T}^{[3]} + \tilde{V}_{NN}^{[3]} + \tilde{V}_{3N}^{[3]}) + \dots \tag{2.22}$$

The significance of the higher-order terms decreases with increasing order. In principle, it is possible to evaluate the higher-order contributions of the cluster expansion.

However, already the calculation of the third order and its inclusion in many-body calculations is very involved. Therefore, we restrict ourselves to the evaluation of the first and second order of the cluster expansion which leads to the two-body approximation of a general operator O

$$\tilde{O}^{C2} = \tilde{O}^{[1]} + \tilde{O}^{[2]} . \quad (2.23)$$

For the Hamiltonian this reads

$$\tilde{H}^{C2} = \tilde{T}^{[1]} + (\tilde{T}^{[2]} + \tilde{V}_{NN}^{[2]}) \equiv T + V_{UCOM} , \quad (2.24)$$

where $\tilde{T}^{[1]} = T$ and the correlated interaction V_{UCOM} is defined as the two-body part of the correlated Hamiltonian containing the correlated kinetic energy and the correlated NN potential. The parameters of the correlation functions will be adjusted such that the term $\tilde{T}^{[3]} + \tilde{V}_{NN}^{[3]} + \tilde{V}_{3N}^{[3]}$ becomes small, i.e. the induced third order of the cluster expansion and genuine three-body forces cancel each other to a large extent. Nonetheless, the application of different many-body methods reveals that three-body forces – induced and genuine – are not negligible [10,13,18,19]. Therefore, we mimic the omitted three-body contributions by introducing phenomenological three-body forces, and investigate their impact on different observables. This approach provides a first step towards the inclusion of realistic three-body forces.

2.2.4 Correlated Interaction

Since the correlation operators are given in an explicit operator form, also the correlated interaction can be written in an operator representation. The unitary transformation is restricted to the two-body approximation, as discussed in Section 2.2.3, therefore it is sufficient to consider the transformation in the two-nucleon system. We assume the following generic operator form for the bare NN potential [18]:

$$V = \sum_p \frac{1}{2} (v_p(r) O_p + O_p v_p(r)) , \quad (2.25)$$

where the charge-independent part of the Argonne V18 can be expressed via the operators

$$O_p = \left\{ 1, (\boldsymbol{\sigma}_1 \cdot \boldsymbol{\sigma}_2), q_r^2, q_r^2 (\boldsymbol{\sigma}_1 \cdot \boldsymbol{\sigma}_2), \mathbf{L}^2, \mathbf{L}^2 (\boldsymbol{\sigma}_1 \cdot \boldsymbol{\sigma}_2), \right. \\ \left. (\mathbf{L} \cdot \mathbf{S}), S_{12} \left(\frac{\mathbf{r}}{r}, \frac{\mathbf{r}}{r} \right), S_{12}(\mathbf{L}, \mathbf{L}) \right\} \otimes \{1, (\boldsymbol{\tau}_1 \cdot \boldsymbol{\tau}_2)\} . \quad (2.26)$$

For simplicity, the charge-dependent terms are not considered here although they are included in the correlated interaction V_{UCOM} .

The kinetic energy in two-body space is split into a center-of-mass contribution t_{cm} , which is not affected by the UCOM transformation and a relative contribution t_{rel} , which is in turn divided into a radial and an angular part:

$$T = t_{\text{cm}} + t_{\text{rel}} = t_{\text{cm}} + t_r + t_{\Omega} = t_{\text{cm}} + \frac{1}{m_N} \left(q_r^2 + \frac{\mathbf{L}^2}{r^2} \right) \quad (2.27)$$

with the nucleon mass m_N .

As the correlated interaction can be written as $V_{\text{UCOM}} = C_r^\dagger C_\Omega^\dagger H C_\Omega C_r - T$, we start with the application of the tensor correlator to the required operators.

Tensor Correlated Hamiltonian

To evaluate the transformation with the tensor correlation operator we can use the Baker-Campbell-Hausdorff expansion [15, 18]

$$C_\Omega^\dagger O C_\Omega = \exp(i g_\Omega) O \exp(-i g_\Omega) = O + i [g_\Omega, O] + \frac{i^2}{2!} [g_\Omega, [g_\Omega, O]] + \dots \quad (2.28)$$

In general, this expansion yields an infinite series. Only for some operators, the similarity transformation can be evaluated exactly.

Firstly, the distance operator r is invariant under the transformation:

$$C_\Omega^\dagger r C_\Omega = r \quad (2.29)$$

since it commutes with the tensor generator g_Ω . For the radial momentum q_r^2 , the expansion terminates after the second order and yields

$$C_\Omega^\dagger q_r^2 C_\Omega = q_r^2 - \{\vartheta'(r) q_r + q_r \vartheta'(r)\} S_{12}(\mathbf{r}, \mathbf{q}_\Omega) + \{\vartheta'(r) S_{12}(\mathbf{r}, \mathbf{q}_\Omega)\}^2 \quad (2.30)$$

with $S_{12}(\mathbf{r}, \mathbf{q}_\Omega)^2 = 9\{\mathbf{S}^2 + 3(\mathbf{L} \cdot \mathbf{S}) + (\mathbf{L} \cdot \mathbf{S})^2\}$. For all other basic operators the Baker-Campbell-Hausdorff expansion does not terminate. In first order, the following commutators have to be calculated:

$$\begin{aligned} [g_\Omega, S_{12} \left(\frac{\mathbf{r}}{r}, \frac{\mathbf{r}}{r} \right)] &= i \vartheta(r) \left\{ -24 \Pi_{S=1} - 18(\mathbf{L} \cdot \mathbf{S}) + 3 S_{12} \left(\frac{\mathbf{r}}{r}, \frac{\mathbf{r}}{r} \right) \right\} \\ [g_\Omega, (\mathbf{L} \cdot \mathbf{S})] &= i \vartheta(r) \{-\bar{S}_{12}(\mathbf{q}_\Omega, \mathbf{q}_\Omega)\} \\ [g_\Omega, \mathbf{L}^2] &= i \vartheta(r) \{2 \bar{S}_{12}(\mathbf{q}_\Omega, \mathbf{q}_\Omega)\} \\ [g_\Omega, S_{12}(\mathbf{L}, \mathbf{L})] &= i \vartheta(r) \{7 \bar{S}_{12}(\mathbf{q}_\Omega, \mathbf{q}_\Omega)\} \end{aligned} \quad (2.31)$$

with the abbreviation

$$\bar{S}_{12}(\mathbf{q}_\Omega, \mathbf{q}_\Omega) = 2r^2 S_{12}(\mathbf{q}_\Omega, \mathbf{q}_\Omega) + S_{12}(\mathbf{L}, \mathbf{L}) - \frac{1}{2} S_{12}\left(\frac{\mathbf{r}}{r}, \frac{\mathbf{r}}{r}\right). \quad (2.32)$$

Through the evaluation of the first-order commutators, the additional tensor operator $\bar{S}_{12}(\mathbf{q}_\Omega, \mathbf{q}_\Omega)$ is generated, which will in turn generate further operators in the next order. In order to yield a closed representation of the tensor correlated operators, one, therefore, has to truncate the number of newly emerging operators. Usually, contributions beyond the third order in angular and orbital angular momentum are neglected.

Central and Tensor Correlated Hamiltonian

Contrary to the tensor correlations, the central correlations can be evaluated analytically for all relevant operators. Starting with the distance operator r , the picture of a coordinate transformation, which we have already introduced in Section 2.2.2, is confirmed [15, 18]:

$$C_r^\dagger r C_r = R_+(r) \quad (2.33)$$

with the correlation function $R_+(r)$. Due to the unitarity of the correlation operators, $C_r^\dagger = C_r^{-1}$, an arbitrary function of r transforms as

$$C_r^\dagger f(r) C_r = f(C_r^\dagger r C_r) = f(R_+(r)). \quad (2.34)$$

This affects especially the radial dependencies of the various contributions of the NN potential. The correlation of the components of the relative momentum operator read

$$C_r^\dagger q_r C_r = \frac{1}{\sqrt{R'_+(r)}} q_r \frac{1}{\sqrt{R'_+(r)}}, \quad C_r^\dagger \mathbf{q}_\Omega C_r = \frac{r}{R_+(r)} \mathbf{q}_\Omega, \quad (2.35)$$

and for the square of the radial momentum one finds

$$C_r^\dagger q_r^2 C_r = \frac{1}{2} \left\{ \frac{1}{R'_+(r)^2} q_r^2 + q_r^2 \frac{1}{R'_+(r)^2} \right\} + \frac{7R''_+(r)^2}{4R'_+(r)^4} - \frac{R'''_+(r)}{2R'_+(r)^3}. \quad (2.36)$$

Thus, the transformation of the square of the radial momentum operator generates an additional local potential.

All other basic operators as well as those generated by the application of the tensor correlator through the Baker-Campbell-Hausdorff expansion are invariant under similarity transformation with the central correlation operator.

Correlated Interaction V_{UCOM}

Collecting the terms for the different central and tensor correlated operators, we can formulate the correlated interaction V_{UCOM} , which can – like the underlying bare NN potential – be written in a closed operator representation [10, 18]:

$$V_{\text{UCOM}} = \sum_p \frac{1}{2} [\tilde{V}_p(r) \tilde{O}_p + \tilde{O}_p \tilde{V}_p(r)] \quad (2.37)$$

containing the operators

$$\begin{aligned} \tilde{O}_p = \left\{ \right. & 1, (\boldsymbol{\sigma}_1 \cdot \boldsymbol{\sigma}_2), q_r^2, q_r^2 (\boldsymbol{\sigma}_1 \cdot \boldsymbol{\sigma}_2), \mathbf{L}^2, \mathbf{L}^2 (\boldsymbol{\sigma}_1 \cdot \boldsymbol{\sigma}_2), (\mathbf{L} \cdot \mathbf{S}), \\ & S_{12} \left(\frac{\mathbf{r}}{r}, \frac{\mathbf{r}}{r} \right), S_{12}(\mathbf{L}, \mathbf{L}), \bar{S}_{12}(\mathbf{q}_\Omega, \mathbf{q}_\Omega), q_r S_{12}(\mathbf{r}, \mathbf{q}_\Omega), \\ & \left. \mathbf{L}^2(\mathbf{L} \cdot \mathbf{S}), \mathbf{L}^2 \bar{S}_{12}(\mathbf{q}_\Omega, \mathbf{q}_\Omega), \dots \right\} \otimes \{1, (\boldsymbol{\tau}_1 \cdot \boldsymbol{\tau}_2)\} . \end{aligned} \quad (2.38)$$

These are not all operators generated by the Baker-Campbell-Hausdorff expansion during the tensor transformation, however, the inclusion of these terms is sufficient for most applications.

The examination of the effect of the similarity transformations using the central and tensor correlation operators shows how the application of the correlators changes the operator structure of the bare potential. The central correlator reduces the short-range repulsion in the local part while creating an additional nonlocal repulsion, and the tensor correlator generates additional central and new nonlocal tensor contributions.

The operator representation of the correlated interaction is of great advantage for the application in many-body methods that are not based on a simple oscillator or plane-wave basis. Furthermore, the UCOM allows for a straightforward investigation of different observables, since one only has to transform all operators of interest in the same way as the Hamiltonian.

Due to the finite range of the correlation functions $s(r)$ and $\vartheta(r)$, the correlation operators act as unit operators at large distances. Hence, asymptotic properties of a two-body wave function are preserved, i.e., the correlated interaction is phase-shift equivalent to the underlying bare NN potential.

2.2.5 Correlated Two-Body Matrix Elements

For the application in different many-body methods two-body matrix elements of the correlated interaction are required. The calculation of matrix elements discussed in the

following is independent of the particular choice of the basis, however, throughout this thesis we will only apply the harmonic oscillator basis. The two-body states are divided into a center-of-mass and a relative state via a Talmi-Moshinsky transformation. Since the unitary transformation does not affect the center-of-mass part, we only have to calculate the relative matrix elements

$$\begin{aligned} \langle n(LS)JMTM_T | V_{\text{UCOM}} | n'(L'S)JMTM_T \rangle = \\ \langle n(LS)JMTM_T | C_r^\dagger C_\Omega^\dagger H_{\text{int}} C_\Omega C_r - T_{\text{int}} | n'(L'S)JMTM_T \rangle, \end{aligned} \quad (2.39)$$

where we assume LS -coupled basis states $|n(LS)JMTM_T\rangle$ with radial quantum number n and use the intrinsic Hamiltonian H_{int} containing the intrinsic kinetic energy T_{int} (cf. Sec. 3.1). The corresponding wave function will be denoted as $\phi_{n,L}(r)$ and the radial wave function as $u_{n,L}(r)$:

$$\langle r(LS)JMTM_T | n(LS)JMTM_T \rangle = \phi_{n,L}(r) = \frac{u_{n,L}(r)}{r}. \quad (2.40)$$

The NN interaction explicitly depends on the isospin projection quantum number M_T through Coulomb and other charge-dependent terms. Nevertheless, we will omit this quantum number as well as the projection M of total angular momentum in the following, since we again only discuss the charge-independent contributions.

The calculation of matrix elements can be performed in different ways. One possible approach is to use the operator representation of the correlated interaction and evaluate the matrix elements directly. However, for the formulation of a closed operator representation it was necessary to truncate the Baker-Campbell-Hausdorff expansion employed for the evaluation of the tensor correlations. When calculating matrix elements, this approximation can be avoided if we apply the tensor correlator to the basis states. The central correlator will still be applied to the operators as this transformation is given by a simple and exact expression. Therefore, we have to rearrange the order of the correlation operators by exploiting the identity

$$\begin{aligned} C_r^\dagger C_\Omega^\dagger H_{\text{int}} C_\Omega C_r &= (C_r^\dagger C_\Omega^\dagger C_r) C_r^\dagger H_{\text{int}} C_r (C_r^\dagger C_\Omega C_r) \\ &= \tilde{C}_\Omega^\dagger C_r^\dagger H_{\text{int}} C_r \tilde{C}_\Omega, \end{aligned} \quad (2.41)$$

where the "centrally correlated" tensor correlator is given by

$$\tilde{C}_\Omega = C_r^\dagger C_\Omega C_r = \exp[-i\vartheta(R_+(r))S_{12}(\mathbf{r}, \mathbf{q}_\Omega)]. \quad (2.42)$$

As already discussed in Section 2.2.2, the tensor correlator acts on LS -coupled two-body wave functions in the following way [10]:

$$\langle r(L'S)JT | \tilde{C}_\Omega | n(LS)JT \rangle = \begin{cases} \phi_{n,L}(r) & , L' = L = J \\ \cos \tilde{\theta}_J(r) \phi_{n,L}(r) & , L' = L = J \pm 1 \\ \pm \sin \tilde{\theta}_J(r) \phi_{n,L}(r) & , L' = J \pm 1, L = J \mp 1 \end{cases} \quad (2.43)$$

with $\tilde{\theta}_J(r) = 3\sqrt{J(J+1)}\vartheta(R_+(r))$. Thus, two-body states with $L = J$ remain unchanged while states with $L = J \pm 1$ are coupled to states with $L = J \mp 1$. Based on these relations, the correlated two-body matrix elements can be evaluated exactly.

We again consider the operator set

$$\begin{aligned} \mathcal{O} = & \left\{ 1, (\boldsymbol{\sigma}_1 \cdot \boldsymbol{\sigma}_2), q_r^2, q_r^2(\boldsymbol{\sigma}_1 \cdot \boldsymbol{\sigma}_2), \mathbf{L}^2, \mathbf{L}^2(\boldsymbol{\sigma}_1 \cdot \boldsymbol{\sigma}_2), \right. \\ & \left. (\mathbf{L} \cdot \mathbf{S}), S_{12}\left(\frac{\mathbf{r}}{r}, \frac{\mathbf{r}}{r}\right), S_{12}(\mathbf{L}, \mathbf{L}) \right\} \otimes \{1, (\boldsymbol{\tau}_1 \cdot \boldsymbol{\tau}_2)\} \end{aligned} \quad (2.44)$$

containing the operators to express the charge-independent part of the Argonne V18. Firstly, we calculate the matrix elements for the local contributions of the form $V(r)\mathcal{O}$ which fulfill the condition $[r, \mathcal{O}] = [q_r, \mathcal{O}] = 0$, i.e. all operators of the set (2.44) except the q_r^2 terms.

On the diagonal matrix elements with $L = L' = J$, the tensor correlator acts like the unit operator, i.e. they are only affected by the central correlator, yielding [10, 18]

$$\begin{aligned} \langle n(JS)JT | C_r^\dagger C_\Omega^\dagger V(r) \mathcal{O} C_\Omega C_r | n'(JS)JT \rangle = \\ \int dr u_{n,J}^*(r) u_{n',J}(r) \tilde{V}(r) \langle (JS)JT | \mathcal{O} | (JS)JT \rangle \end{aligned} \quad (2.45)$$

in coordinate representation. The correlated radial dependence of the potential is simply given by $\tilde{V}(r) = V(R_+(r))$. Applying the tensor correlator to the states, we obtain for the diagonal matrix elements with $L = L' = J \mp 1$

$$\begin{aligned} \langle n(J \mp 1, 1)JT | C_r^\dagger C_\Omega^\dagger V(r) \mathcal{O} C_\Omega C_r | n'(J \mp 1, 1)JT \rangle = \\ \int dr u_{n,J \mp 1}^*(r) u_{n',J \mp 1}(r) \tilde{V}(r) \\ \times \left[\langle (J \mp 1, 1)JT | \mathcal{O} | (J \mp 1, 1)JT \rangle \cos^2 \tilde{\theta}_J(r) \right. \\ + \langle (J \pm 1, 1)JT | \mathcal{O} | (J \pm 1, 1)JT \rangle \sin^2 \tilde{\theta}_J(r) \\ \left. \pm \langle (J \mp 1, 1)JT | \mathcal{O} | (J \pm 1, 1)JT \rangle 2 \cos \tilde{\theta}_J(r) \sin \tilde{\theta}_J(r) \right] \end{aligned} \quad (2.46)$$

with $\tilde{\theta}_J(r) = \theta_J(R_+(r))$. Finally, the off-diagonal matrix elements with $L = J \mp 1$ and $L' = J \pm 1$ are given by

$$\begin{aligned}
 \langle n(J \mp 1, 1)JT | C_r^\dagger C_\Omega^\dagger V(r) O C_\Omega C_r | n'(J \pm 1, 1)JT \rangle = \\
 \int dr u_{n, J \mp 1}^*(r) u_{n', J \pm 1}(r) \tilde{V}(r) \\
 \times \left[\langle (J \mp 1, 1)JT | O | (J \pm 1, 1)JT \rangle \cos^2 \tilde{\theta}_J(r) \right. \\
 - \langle (J \pm 1, 1)JT | O | (J \mp 1, 1)JT \rangle \sin^2 \tilde{\theta}_J(r) \\
 \mp \langle (J \mp 1, 1)JT | O | (J \mp 1, 1)JT \rangle \cos \tilde{\theta}_J(r) \sin \tilde{\theta}_J(r) \\
 \left. \pm \langle (J \pm 1, 1)JT | O | (J \pm 1, 1)JT \rangle \sin \tilde{\theta}_J(r) \cos \tilde{\theta}_J(r) \right] .
 \end{aligned} \tag{2.47}$$

Hence, for the evaluation of the matrix elements we have to calculate the integrals of the radial wave functions as well as the matrix elements of the operators O in LS -coupled angular momentum states. The off-diagonal matrix elements on the right-hand-side of Eqs. (2.46) and (2.47) vanish for all operators except for the standard tensor operator $S_{12}(\frac{\mathbf{r}}{r}, \frac{\mathbf{r}}{r})$ which simplifies these relations significantly.

The correlated matrix elements reveal the effect of the tensor correlator leading to an admixture of components with $\Delta L = \pm 2$ to the states, as we have already seen in Section 2.2.2.

For the radial momentum the full unitary transformation is applied to the operator

$$V_{qr} = \frac{1}{2}[q_r^2 V(r) + V(r)q_r^2] , \tag{2.48}$$

since it is given by a closed exact expression. The application of the tensor correlator yields

$$\begin{aligned}
 C_\Omega^\dagger V_{qr} C_\Omega = \frac{1}{2}[q_r^2 V(r) + V(r)q_r^2] + V(r)[\vartheta'(r)S_{12}(\mathbf{r}, \mathbf{q}_\Omega)]^2 \\
 - [q_r V(r)\vartheta'(r) + \vartheta'(r)V(r)q_r]S_{12}(\mathbf{r}, \mathbf{q}_\Omega) .
 \end{aligned} \tag{2.49}$$

After including the central correlations, the following expression is derived for the diagonal matrix elements with $L = L' = J$:

$$\begin{aligned}
 \langle n(JS)JT | C_r^\dagger C_\Omega^\dagger V_{qr} C_\Omega C_r | n'(JS)JT \rangle = \\
 \int dr \left\{ u_{n,J}^*(r) u_{n',J}(r) \left[\tilde{V}(r) W(r) - \tilde{V}'(r) \frac{R_+''(r)}{R_+'(r)^2} \right] \right. \\
 \left. - \frac{1}{2} [u_{n,J}^*(r) u_{n',J}''(r) + u_{n,J}''^*(r) u_{n',J}(r)] \frac{\tilde{V}(r)}{R_+'(r)^2} \right\}
 \end{aligned} \quad (2.50)$$

with $\tilde{V}'(r) = V'(R_+(r))$ and the additional local potential

$$W(r) = \frac{7R_+''(r)^2}{4R_+'(r)^4} - \frac{R_+'''(r)}{2R_+'(r)^3}. \quad (2.51)$$

Again, these matrix elements are only affected by the central correlator. For the diagonal matrix elements with $L = L' = J \mp 1$ one obtains

$$\begin{aligned}
 \langle n(J \mp 1, 1)JT | C_r^\dagger C_\Omega^\dagger V_{qr} C_\Omega C_r | n'(J \mp 1, 1)JT \rangle = \\
 \int dr \left\{ u_{n,J \mp 1}^*(r) u_{n',J \mp 1}(r) \left[\tilde{V}(r) W(r) + \tilde{V}(r) \tilde{\theta}'_J(r)^2 - \tilde{V}'(r) \frac{R_+''(r)}{R_+'(r)^2} \right] \right. \\
 \left. - \frac{1}{2} [u_{n,J \mp 1}^*(r) u_{n',J \mp 1}''(r) + u_{n,J \mp 1}''^*(r) u_{n',J \mp 1}(r)] \frac{\tilde{V}(r)}{R_+'(r)^2} \right\}
 \end{aligned} \quad (2.52)$$

with $\tilde{\theta}'_J(r) = \theta'_J(R_+(r))$. And finally, the off-diagonal matrix elements with $L = J \mp 1$ and $L' = J \pm 1$ are calculated:

$$\begin{aligned}
 \langle n(J \mp 1, 1)JT | C_r^\dagger C_\Omega^\dagger V_{qr} C_\Omega C_r | n'(J \pm 1, 1)JT \rangle = \\
 \pm \int dr [u_{n,J \mp 1}^*(r) u_{n',J \pm 1}'(r) - u_{n,J \mp 1}'^*(r) u_{n',J \pm 1}(r)] \frac{\tilde{V}(r) \tilde{\theta}'_J(r)}{R_+'(r)}. \quad (2.53)
 \end{aligned}$$

Using these relations, the matrix elements for all contributions of the correlated interaction can be constructed, including the matrix elements of the correlated kinetic energy.

2.2.6 Optimal Correlation Functions

The correlation functions describing the radial dependencies of the correlation operators depend on the underlying bare NN potential but they should not depend on the nucleus under consideration. Hence, we have to disentangle the long- and short-range correlations, as already mentioned earlier, in order to construct a state-independent

S	T	Param.	α_c [fm]	β_c [fm]	γ_c [fm]	η
0	0	II	0.7971	1.2638	0.4621	–
0	1	I	1.3793	0.8853	–	0.3724
1	0	I	1.3265	0.8342	–	0.4471
1	1	II	0.5665	1.3888	0.1786	–

Table 2.1: Parameters of the central correlation functions $R_+(r)$ in the different S, T -channels for the Argonne V18 potential (cf. [10]).

unitary transformation. The correlation functions are determined for each spin-isospin channel separately. The most convenient procedure is based on an energy minimization in the two-body system. For each spin-isospin channel we choose the two-body state with the lowest possible angular momentum L and compute the energy expectation value of the correlated energy with the trial state. As the uncorrelated trial state should not contain any of the short-range correlations, one possible choice is to use a free zero-energy scattering solution $\phi_L(r) \propto r^L$ [9, 10, 18].

Different parameterizations for the correlation functions have been investigated. For the central correlation functions two parameterizations with a double-exponential drop-off and different short-range behavior have proven appropriate:

$$\begin{aligned}
 R_+^I(r) &= r + \alpha_c (r/\beta_c)^\eta \exp[-\exp(r/\beta_c)] \\
 R_+^{II}(r) &= r + \alpha_c [1 - \exp(-r/\gamma_c)] \exp[-\exp(r/\beta_c)] ,
 \end{aligned} \tag{2.54}$$

where we choose in each spin-isospin channel the parameterization which yields the lower energy expectation value. The tensor correlation function is described by the following parameterization:

$$\vartheta(r) = \alpha_t [1 - \exp(-r/\gamma_t)] \exp[-\exp(r/\beta_t)] . \tag{2.55}$$

In the $S = 0$ channels we only have to consider the central correlations. The minimization of the energy E_{ST} is performed via the variation of the parameters where the lowest possible angular momenta are $L = 1$ for $T = 0$ and $L = 0$ for $T = 1$, respectively, i.e.:

$$\begin{aligned}
 E_{00} &= \langle \phi_1(10)10 | C_r^\dagger H_{\text{int}} C_r | \phi_1(10)10 \rangle \\
 E_{01} &= \langle \phi_0(00)01 | C_r^\dagger H_{\text{int}} C_r | \phi_0(00)01 \rangle
 \end{aligned} \tag{2.56}$$

with the states $|\phi_L(LS)JT\rangle$. The determination of the central correlation function in the $S = 0, T = 1$ channel is straightforward. The parameters for the central correlation

T	l_ϑ [fm ³]	α_t	β_t [fm]	γ_t [fm]
0	0.04	521.60	1.0367	1000.0
0	0.09	536.67	1.2608	1000.0
0	0.20	450.67	1.6081	1000.0
1	-0.01	-0.1036	1.5869	3.4426
1	-0.03	-0.0569	2.1874	1.4761
1	-0.09	-0.0364	3.2925	0.5473

Table 2.2: Parameters of the tensor correlation functions $\vartheta(r)$ for the Argonne V18 potential with different values for the range-constraint l_ϑ (cf. [10]).

functions are summarized in Table 2.1. In the $S = 0, T = 0$ channel the potential is purely repulsive leading to a correlation function of very long range. Hence, in order to stick to the short-range correlations, we introduce a constraint via

$$I_{R_+} = \int dr r^2 (R_+(r) - r) , \quad (2.57)$$

which is fixed to $I_{R_+} = 0.1 \text{ fm}^4$ in the $S = 0, T = 0$ channel giving a range similar to the values in the other spin-isospin channels.

For $S = 1$ the central and tensor correlation functions have to be determined simultaneously, i.e. for $T = 0$ the energy

$$E_{10} = \langle \phi_0(01)10 | C_r^\dagger C_\Omega^\dagger H_{\text{int}} C_\Omega C_r | \phi_0(01)10 \rangle \quad (2.58)$$

has to be minimized since the lowest possible angular momentum is $L = 0$. For $T = 1$, however, the total angular momentum can be coupled to $J = 0, 1, 2$ as the lowest angular momentum is $L = 1$. We, therefore, choose a superposition of all three energy expectation values with relative weights of $2J + 1$ for the minimization:

$$\begin{aligned} E_{11} &= \frac{1}{9} \langle \phi_1(11)01 | C_r^\dagger H_{\text{int}} C_r | \phi_1(11)01 \rangle \\ &+ \frac{3}{9} \langle \phi_1(11)11 | C_r^\dagger H_{\text{int}} C_r | \phi_1(11)11 \rangle \\ &+ \frac{5}{9} \langle \phi_1(11)21 | C_r^\dagger C_\Omega^\dagger H_{\text{int}} C_\Omega C_r | \phi_1(11)21 \rangle . \end{aligned} \quad (2.59)$$

For the tensor correlator, all correlation functions are of long range as the tensor correlations themselves are long-ranged. However, the aim is to construct a state-independent unitary transformation, i.e. we have to separate the short-range correlations covered by the correlation operators from the long-range correlations which have

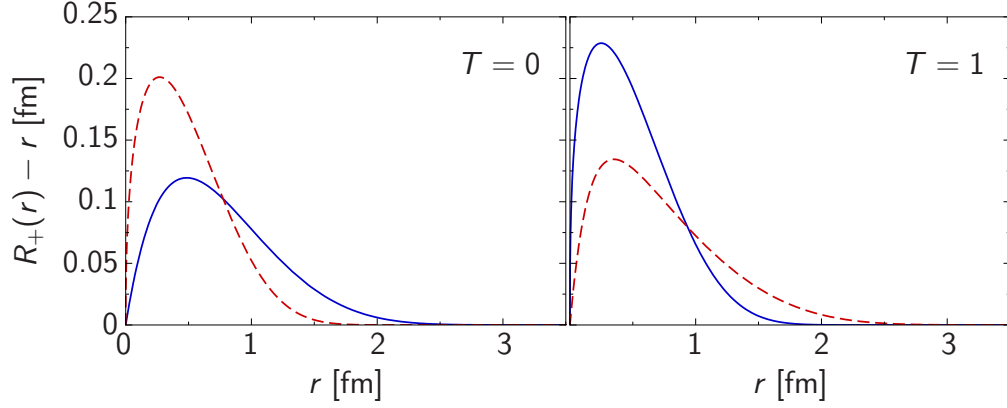


Figure 2.4: Optimal central correlation functions $R_+(r) - r$ for the isospin channels $T = 0$ (left), $T = 1$ (right) and the spins $S = 0$ (—) and $S = 1$ (---) for the Argonne V18 potential (cf. [10]).

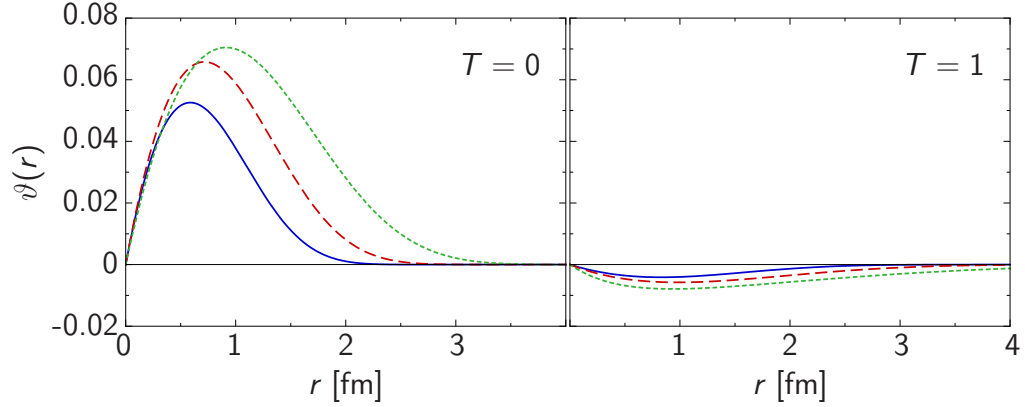


Figure 2.5: Optimal tensor correlation functions $\vartheta(r)$ for the Argonne V18 potential with different values for the range constraint l_ϑ for the isospin channels $T = 0$ with $l_\vartheta = 0.04 \text{ fm}^3$ (—), 0.09 fm^3 (---), and 0.20 fm^3 (····) (left) and $T = 1$ with $l_\vartheta = -0.01 \text{ fm}^3$ (—), -0.03 fm^3 (---), and -0.09 fm^3 (····) (right) (cf. [10]).

to be described by the many-body states. Therefore, we employ a range-constraint for the tensor correlation functions, which is done via the following integral:

$$l_\vartheta = \int dr r^2 \vartheta(r) . \quad (2.60)$$

The optimal parameters for the tensor correlation functions are listed in Table 2.2 for different values of the constraint l_ϑ . The variation of l_ϑ has almost no effect on the central correlation functions, hence, they are chosen to be independent of the tensor correlator range.

In Figure 2.4 the optimal central correlation functions are shown for the Argonne

V18 potential. The correlation functions in the even channels ($(S, T) = (0, 1)$ and $(1, 0)$) decrease rapidly while those in the odd channels ($(S, T) = (0, 0)$ and $(1, 1)$) are weaker and of slightly longer range due to the effect of the centrifugal barrier. The optimal tensor correlation functions are shown in Figure 2.5 for different values of the range constraint. The tensor interaction is significantly weaker in the triplet-odd channel. Therefore, also the correlation functions and the corresponding constraints are much weaker than in the triplet-even channel. The optimal values for the tensor range constraints cannot be determined on the basis of two-body calculations. They can only be fixed including information of few-nucleon systems.

2.3 Similarity Renormalization Group

Another possibility to address short-range correlations induced by the NN interaction is provided by the Similarity Renormalization Group (SRG) [10, 11, 20, 21]. The basic idea of the SRG is to pre-diagonalize a Hamilton matrix with respect to a specific basis. Although the motivations of UCOM and SRG are quite different, they show a couple of similarities as will be discussed in the following sections.

2.3.1 SRG Flow Equation

The initial many-body Hamiltonian H shall be pre-diagonalized by using a continuous similarity transformation:

$$H_\alpha = U_\alpha^\dagger H U_\alpha \quad (2.61)$$

with the unitary transformation operator U_α depending on the flow parameter α . This similarity transformation is equivalent to the renormalization group flow equation

$$\frac{dH_\alpha}{d\alpha} = [\eta_\alpha, H_\alpha], \quad H_{\alpha=0} = H \quad (2.62)$$

containing the anti-hermitian generator η_α , which is connected to the operator U_α via

$$\frac{dU_\alpha}{d\alpha} = -U_\alpha \eta_\alpha. \quad (2.63)$$

All operators one is interested in besides the Hamiltonian have to be transformed in the same way. Therefore, one can either evolve all operators of interest consistently using Equation (2.62) or one can determine the unitary transformation operator U_α using Equation (2.63) with the initial condition $U_{\alpha=0} = 1$ and transform all operators

of interest via Equation (2.61). Since the generator η_α generally depends on the flow parameter in a nontrivial way, the unitary operator is not simply given by an exponential of the generator but can be expressed via a Dyson series.

Before solving the flow equation (2.62) or the similarity transformation (2.61) one has to choose a generator suitable for the specific problem. We will deal with A -nucleon systems leading to evolved operators that contain up to A -body contributions even if starting from a Hamiltonian with two-body operators at most. Therefore, the following approximation is employed, similar to the two-body approximation of the cluster expansion in the UCOM. We use the operator defining the basis with respect to which the Hamiltonian shall be diagonalized, which is a two-body operator in our case, and perform the evolution in two-body space, hence, discarding three-body and higher contributions. The corresponding generator is defined as

$$\eta_\alpha = (2\mu)^2 [T_{\text{int}}, H_\alpha] = 2\mu [\mathbf{q}^2, H_\alpha] \quad (2.64)$$

with the intrinsic kinetic energy $T_{\text{int}} = T - T_{\text{cm}} = \frac{\mathbf{q}^2}{2\mu}$ in the two-body system [10, 11, 21, 22]. The prefactor of the commutator is chosen such that the flow parameter has the dimension $[\alpha] = \text{fm}^4$. It can be understood easily why the commutator with the evolved Hamiltonian is used in the definition of the generator: If the evolved Hamiltonian is diagonal with respect to the eigenbasis of the intrinsic kinetic energy, the commutator vanishes and the flow evolution reaches a trivial fix point. The square of the two-body relative momentum operator can be written as a sum of a radial and an angular part:

$$\mathbf{q}^2 = q_r^2 + \frac{\mathbf{L}^2}{r^2}, \quad q_r = \frac{1}{2} \left(\mathbf{q} \cdot \frac{\mathbf{r}}{r} + \frac{\mathbf{r}}{r} \cdot \mathbf{q} \right). \quad (2.65)$$

Hence, the two-body Hamiltonian H_α is diagonalized in a simultaneous eigenbasis of q_r^2 and $\frac{\mathbf{L}^2}{r^2}$, i.e. in a partial-wave momentum space representation the matrix elements of the Hamiltonian are driven towards a band-diagonal structure with respect to relative momentum (q, q') and orbital angular momentum (L, L') .

2.3.2 Evolution of Two-Body Matrix Elements

We start from a Hamiltonian $H = T_{\text{int}} + V_{\text{NN}}$ consisting of the intrinsic kinetic energy T_{int} and two-body interaction V_{NN} . Similar to the correlated interaction V_{UCOM} the evolved interaction V_α is defined such that it contains all α -dependent terms of the evolved Hamiltonian H_α , which includes the evolved intrinsic kinetic energy:

$$H_\alpha = T_{\text{int}} + V_\alpha. \quad (2.66)$$

Since the intrinsic kinetic energy is chosen such that it is independent of α , the flow evolution of the Hamiltonian is reduced to the evolution of the interaction V_α . With the generator (2.64) the flow equation reads

$$\frac{dH_\alpha}{d\alpha} = \frac{dV_\alpha}{d\alpha} = [\eta_\alpha, H_\alpha] = (2\mu)^2 [[T_{\text{int}}, V_\alpha], T_{\text{int}} + V_\alpha] . \quad (2.67)$$

This flow evolution can most conveniently be evaluated on the level of matrix elements [10, 23]. Since the square of the relative momentum operator \mathbf{q}^2 enters into the generator, we choose the partial-wave momentum eigenbasis $|q(LS)JM_T\rangle$. The projection quantum numbers M and M_T will be omitted for brevity in the following. Thus, we have to derive evolution equations for the matrix elements

$$V_\alpha^{(JLL'ST)}(q, q') = \langle q(LS)JT | V_\alpha | q'(L'S)JT \rangle \quad (2.68)$$

from Equation (2.67). The result can be written in a generic form:

$$\begin{aligned} \frac{dV_\alpha(q, q')}{d\alpha} = & -(q^2 - q'^2)^2 V_\alpha(q, q') \\ & + 2\mu \int dQ Q^2 (q^2 + q'^2 - 2Q^2) V_\alpha(q, Q) V_\alpha(Q, q') , \end{aligned} \quad (2.69)$$

where we simply have

$$V_\alpha(q, q') = V_\alpha^{(JJJST)}(q, q') \quad (2.70)$$

for non-coupled partial waves with $L = L' = J$.

For $S = 1$, angular momenta with $\Delta L = \pm 2$ are coupled due to the tensor force. Thus, for the flow equations in the coupled channels, the $V_\alpha(q, q')$ are defined as 2×2 matrices

$$V_\alpha(q, q') = \begin{pmatrix} V_\alpha^{(JLLST)}(q, q') & V_\alpha^{(JLL'ST)}(q, q') \\ V_\alpha^{(JL'LST)}(q, q') & V_\alpha^{(JL'L'ST)}(q, q') \end{pmatrix} \quad (2.71)$$

containing the matrix elements with the possible combinations of the orbital angular momenta $L = J-1$ and $L' = J+1$. Due to the properties of the generator (2.64), each non-coupled partial wave and each set of coupled partial waves evolves independently of the other channels.

As mentioned above, not only the Hamiltonian but all operators of interest have to be evolved in the same way. The evolution of all operators has to be done simultaneously since they are coupled to the evolution of the Hamiltonian via the generator.

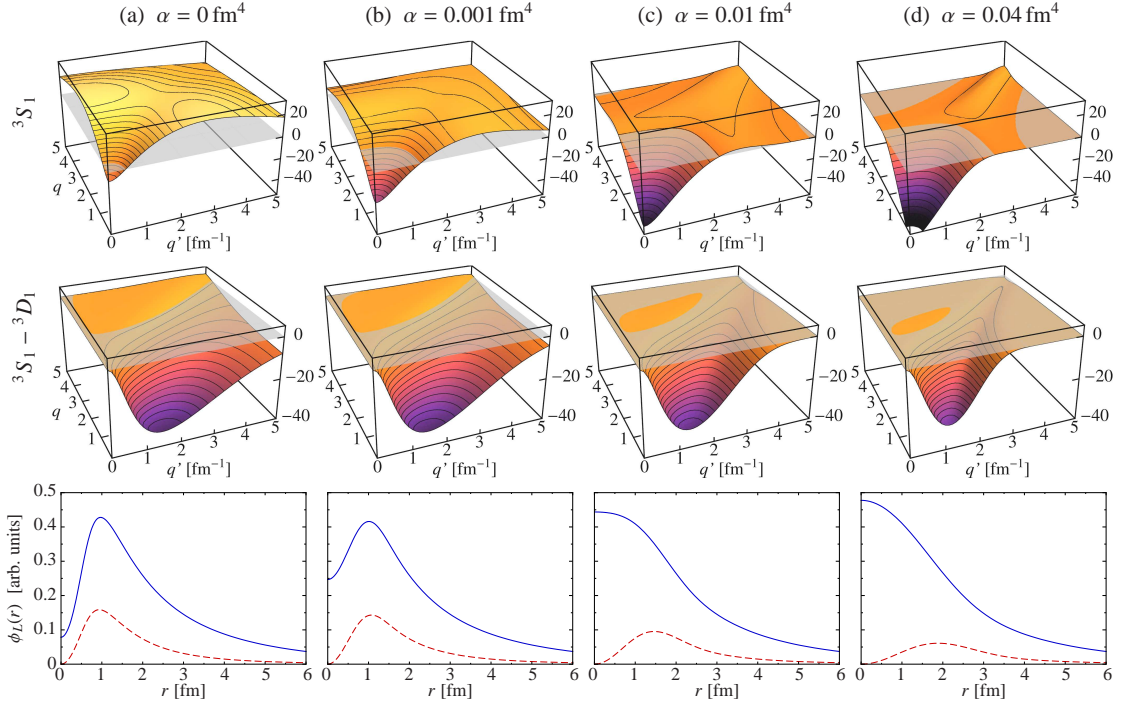


Figure 2.6: SRG evolution of momentum-space matrix elements in the 3S_1 and ${}^3S_1 - {}^3D_1$ partial waves in units of MeV fm^3 starting from the Argonne V18 potential in the upper two rows for flow parameters $\alpha = 0 \text{ fm}^4$, 0.001 fm^4 , 0.01 fm^4 , 0.04 fm^4 from left to right. The bottom row shows the S - (—) and D -wave (---) radial wave functions of the deuteron ground-state obtained with the respective SRG-evolved interaction (taken from [23]).

2.3.3 Evolved Wave Functions and Matrix Elements

In this section, some properties of the SRG evolution are illustrated using momentum-space matrix elements and the deuteron wave function as example [10, 23, 24]. Figure 2.6 depicts the momentum-space matrix elements of the 3S_1 and ${}^3S_1 - {}^3D_1$ partial waves in the upper two rows as well as the S - and D -wave components of the radial deuteron wave function in the lower row. Starting from the Argonne V18 potential in the left column the SRG evolution is performed up to a flow parameter $\alpha = 0.04 \text{ fm}^4$. Inspection of the matrix elements reveals that the initial interaction has large off-diagonal contributions for both considered partial waves. The application of the SRG evolution leads to a strong suppression of the off-diagonal matrix elements already for very small values of the flow parameter (column (b)). The evolution finally yields momentum-space matrices with a pronounced band-diagonal structure (column (d)). At the same time the correlation effects being present in the initial deuteron wave func-

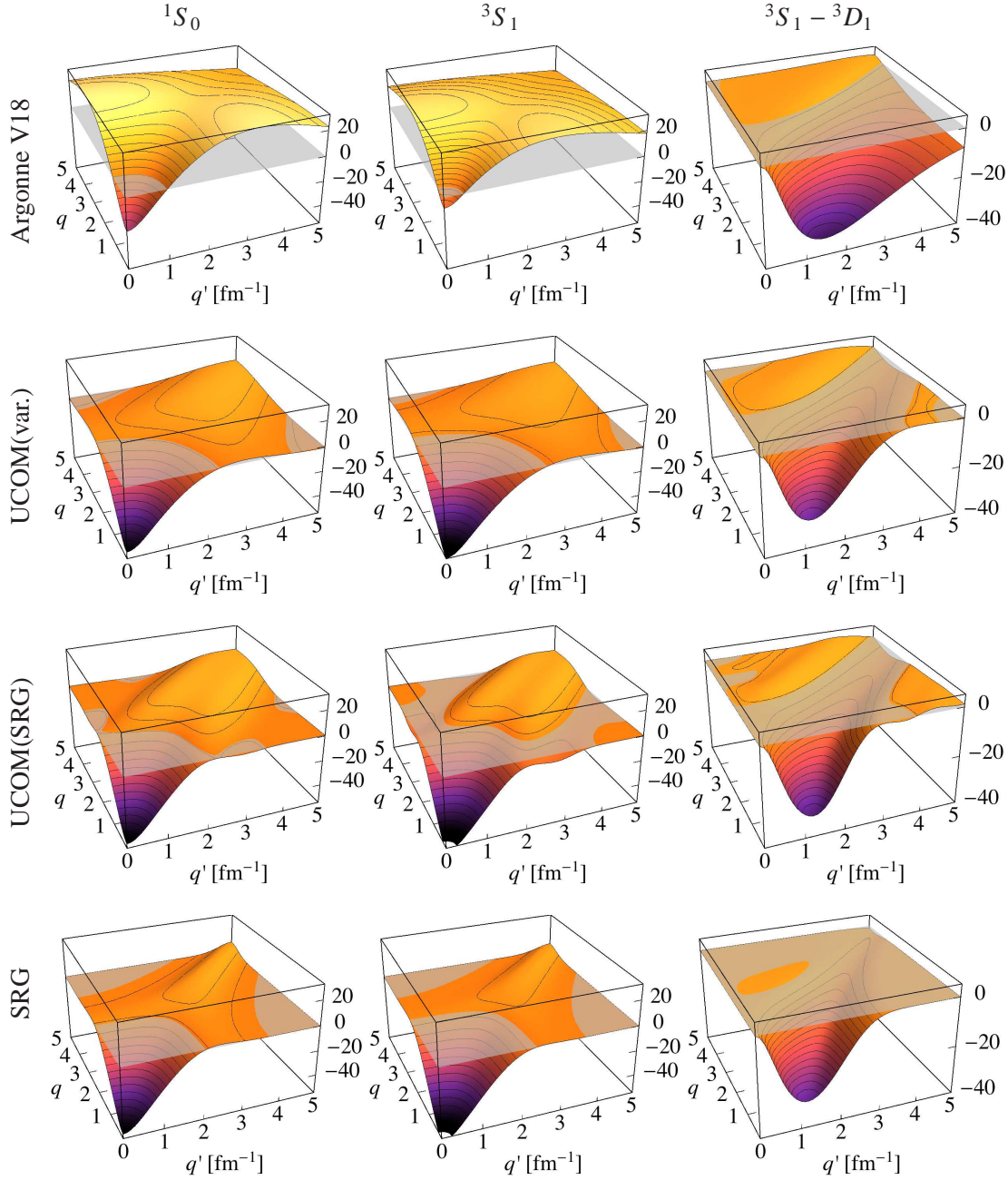


Figure 2.7: Momentum-space matrix elements in units of MeV fm^3 for the 1S_0 , 3S_1 and $^3S_1 - ^3D_1$ partial waves of the bare Argonne V18 potential (upper row), the UCOM transformed AV18 using variationally optimized correlation functions with $l_{\vartheta}^{(10)} = 0.09 \text{ fm}^3$ (second row), the UCOM transformed AV18 using SRG-generated correlation functions with $\alpha = 0.04 \text{ fm}^4$ (third row) and the SRG-evolved AV18 with $\alpha = 0.03 \text{ fm}^4$ (bottom row) (taken from [10]).

tion are eliminated throughout the SRG evolution, i.e. the correlation hole at small interparticle distances caused by the repulsive core vanishes and the D-wave admixture due to the tensor force becomes much weaker. Hence, the SRG flow evolution resembles the application of the UCOM central and tensor correlators discussed in Section 2.2.2 (Fig. 2.3).

Finally, we compare the momentum-space matrix elements of the different interactions obtained via the UCOM and SRG transformations. Figure 2.7 shows matrix elements using the 1S_0 , 3S_1 and $^3S_1 - ^3D_1$ partial waves as an example. The main features are comparable in all partial waves. The upper row shows the matrix elements of the initial Argonne V18 potential, which show large off-diagonal contributions in all considered partial waves. The two middle rows show the AV18 transformed via the UCOM using correlation functions obtained via energy minimization, and using SRG-generated correlation functions, and the bottom row shows the SRG-evolved AV18. All three transformed interactions show some common features that are also manifested in the momentum space matrix elements. In all partial waves, the off-diagonal contributions are suppressed while the low-momentum parts are enhanced yielding a band-diagonal structure. In other words, all unitary transformations lead to a decoupling of low-momentum and high-momentum states, which in turn improves the convergence properties of the unitarily transformed interactions compared to the initial bare interaction.

On the other hand, the investigation of the momentum-space matrix elements also reveals some differences between the approaches. The SRG evolution yields almost perfect band-diagonal matrices, while the UCOM transformations lead to a broader band falling off more slowly with increasing distance from the diagonal. Here, using the variationally optimized correlation functions produces an even broader plateau of non-vanishing matrix elements along the diagonal regarding the 1S_0 and 3S_1 partial waves than the application of SRG-generated correlation functions. The band-diagonal structure being not as perfect as for the SRG-evolved interaction is due to the limited flexibility of the UCOM approach compared to the SRG (cf. Sec. 2.3.4).

2.3.4 Connections between UCOM and SRG

The UCOM and the SRG both aim at the construction of soft interactions. Though their starting points are quite different, there are also some connections between the two approaches [10, 22–25]. Firstly, both methods use unitary transformations to construct a manifold of interactions that are all phase-shift equivalent to the underlying potential. In the course of the transformations, both approaches generate irreducible

many-body operators even if starting from a pure two-body potential. For computational reasons we have restricted both approaches to two-body operators. However, different many-body calculations reveal that the neglected higher-order contributions play an important role if we want to describe properties of nuclei beyond the lightest isotopes [10, 13, 18, 19, 23]. The evaluation of the three-body contributions of the UCOM and SRG transformations is in principle possible but very involved [26]. Hence, for first investigations of the importance of the omitted higher orders we will introduce phenomenological three-body forces, which can be included in the calculations more easily and demand less computing time.

Further similarities between the UCOM and the SRG are manifested if we compare the UCOM generators g_r and g_Ω with the initial SRG generator η_0 . We consider an interaction

$$V = \sum_p v_p(r) O_p \quad (2.72)$$

that contains the operators of the charge-independent part of the Argonne V18 potential (cf. Eq. (2.26)). The evaluation of the generator at $\alpha = 0$ using this interaction yields

$$\eta_0 = \frac{i}{2} (q_r S(r) + S(r) q_r) + i \Theta(r) S_{12}(\mathbf{r}, \mathbf{q}_\Omega) \quad (2.73)$$

with the operator-valued functions

$$S(r) = -\frac{1}{\mu} \left(\sum_p v'_p(r) O_p \right), \quad \Theta(r) = -\frac{2}{\mu} \frac{v_t(r)}{r^2}. \quad (2.74)$$

Therefore, one finds the same operator structure for the initial SRG generator as for the sum of the UCOM generators g_r and g_Ω (Eqs. (2.9) and (2.12)). This means that both methods deal with the same kind of short-range correlations induced by the nuclear interaction, although they start from different motivations: the SRG aims at a pre-diagonalization of the Hamilton matrix while the UCOM explicitly addresses the short-range central and tensor correlations. Furthermore, we can deduce from this connection, that the most important terms are covered by the UCOM correlators.

A closer look at Eqs. (2.73) and (2.74) also reveals some differences between the two approaches. The UCOM correlation functions $s(r)$ and $\vartheta(r)$ only depend on the respective spin-isospin channel while the operator valued function $S(r)$ also depends on the respective partial wave. Hence, the UCOM generators represent a simplification compared to the SRG generator. The UCOM generators could also be made more flexible by introducing separate correlation functions for each partial wave. Nevertheless, the SRG evolution drives the Hamiltonian towards a band-diagonal structure more

efficiently than the UCOM transformation since the SRG uses a dynamical generator that changes its structure during the evolution in order to perform the diagonalization in an optimal way (cf. Sec. 2.3.3). In contrast, the UCOM performs only one unitary transformation using static generators.

2.3.5 SRG-Generated UCOM Correlation Functions

In view of the connections between UCOM and SRG discussed in the previous section, one is prompted to extract UCOM correlation functions from the SRG evolution. This is achieved by the following procedure [10, 23, 25]: Starting from a given interaction, the SRG flow equations are solved up to a specific flow parameter α yielding the momentum space matrix elements $V_\alpha(q, q')$ for a certain partial wave. Subsequently, a set of coordinate-space wave functions is determined by solving the two-body problem based on the evolved matrix elements. Finally, the correlation functions are derived via a mapping of the two-body wave function of the SRG-evolved interaction onto the corresponding wave function of the initial interaction.

To illustrate the mapping procedure, we start with the two-body eigenstate $|\varphi^{(\alpha)}\rangle$ of the evolved interaction and the corresponding state $|\varphi^{(0)}\rangle$ of the initial interaction, both having the same energy eigenvalue. The correlation functions of the correlation operator C are determined such that they map these two states onto each other:

$$|\varphi^{(0)}\rangle = C|\varphi^{(\alpha)}\rangle = C_\Omega C_r |\varphi^{(\alpha)}\rangle . \quad (2.75)$$

First, we consider non-coupled partial waves with $L = J$, where the two-body states can be written as

$$\begin{aligned} |\varphi^{(0)}\rangle &= |\phi^{(0)}(LS)JT\rangle \\ |\varphi^{(\alpha)}\rangle &= |\phi^{(\alpha)}(LS)JT\rangle . \end{aligned} \quad (2.76)$$

In this case we only have to consider central correlations. Using the relations for the central correlated two-body wave functions derived in Section 2.2.2 (Eq. (2.13)), we find the following equation for the determination of the central correlation function $R_-(r)$:

$$\phi^{(0)}(r) = \frac{R_-(r)}{r} \sqrt{R'_-(r)} \phi^{(\alpha)}(R_-(r)) . \quad (2.77)$$

The wave functions are assumed to be real-valued. By formal integration we can deduce an implicit integral equation:

$$R_-(r)^3 = 3 \int_0^r d\xi \xi^2 \frac{\phi^{(0)}(\xi)^2}{\phi^{(\alpha)}(R_-(\xi))^2} , \quad (2.78)$$

which is solved iteratively for the partial wave under consideration. The corresponding correlation function $R_+(r)$ is obtained by numerical inversion.

For coupled partial waves we use the following ansatz for the two-body eigenstates of the initial and evolved interaction, respectively:

$$\begin{aligned} |\varphi^{(0)}\rangle &= |\phi_L^{(0)}(LS)JT\rangle + |\phi_{L'}^{(0)}(L'S)JT\rangle \\ |\varphi^{(\alpha)}\rangle &= |\phi_L^{(\alpha)}(LS)JT\rangle + |\phi_{L'}^{(\alpha)}(L'S)JT\rangle \end{aligned} \quad (2.79)$$

with $L = J - 1$ and $L' = J + 1$. In these channels central as well as tensor correlation functions have to be determined, since both types of correlations appear. Using the coordinate space representation of the central and tensor correlated wave functions (Eq. (2.18)), we obtain a system of coupled equations

$$\begin{pmatrix} \phi_L^{(0)}(r) \\ \phi_{L'}^{(0)}(r) \end{pmatrix} = \frac{R_-(r)}{r} \sqrt{R'_-(r)} \begin{pmatrix} \cos \theta_J(r) & \sin \theta_J(r) \\ -\sin \theta_J(r) & \cos \theta_J(r) \end{pmatrix} \begin{pmatrix} \phi_L^{(\alpha)}(R_-(r)) \\ \phi_{L'}^{(\alpha)}(R_-(r)) \end{pmatrix} \quad (2.80)$$

containing the correlation functions $R_-(r)$ and $\vartheta(r) = \frac{\theta_J(r)}{3\sqrt{J(J+1)}}$. By considering the sum of the squares of the two orbital components of the initial wave function, we obtain an equation independent of the tensor correlation function:

$$\phi_L^{(0)}(r)^2 + \phi_{L'}^{(0)}(r)^2 = \frac{R_-(r)^2}{r^2} R'_-(r) \{ \phi_L^{(\alpha)}(R_-(r))^2 + \phi_{L'}^{(\alpha)}(R_-(r))^2 \}. \quad (2.81)$$

From this the central correlation function can be obtained, analogously to the uncoupled partial waves, via

$$R_-(r)^3 = 3 \int_0^r d\xi \xi^2 \frac{\phi_L^{(0)}(\xi)^2 + \phi_{L'}^{(0)}(\xi)^2}{\phi_L^{(\alpha)}(R_-(\xi))^2 + \phi_{L'}^{(\alpha)}(R_-(\xi))^2}. \quad (2.82)$$

Subsequently, the tensor correlation function can be determined numerically via the solution of Equation (2.80).

In practical applications, the SRG evolution of the matrix elements for the required partial wave is performed on a momentum-space grid. After the solution of the two-body problem on the same momentum-space grid using the evolved matrix elements, the resulting wave functions are transformed into coordinate representation. Applying the mapping procedure to the ground-state wave functions finally yields the discretized correlation functions.

Although it would be straightforward, we do not introduce separate correlation functions for each partial wave, but stay as close as possible to the scheme already used

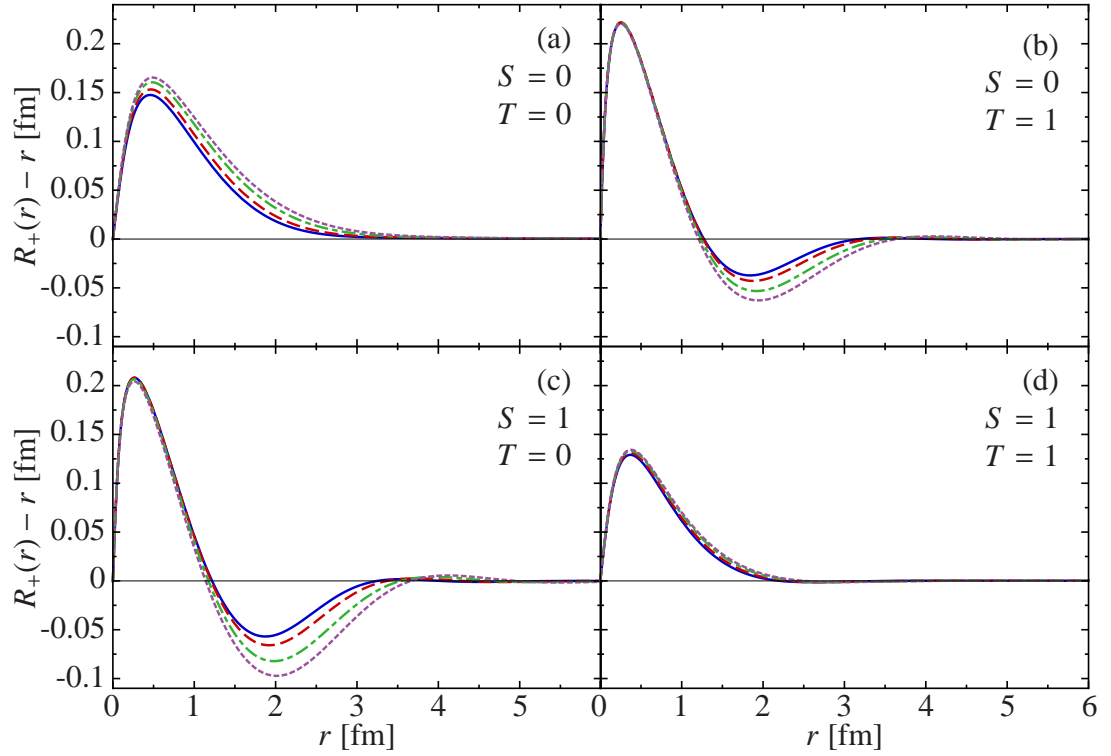


Figure 2.8: SRG-generated central correlation functions $R_+(r) - r$ for the AV18 potential in the four spin-isospin channels for different values of the flow parameter: $\alpha = 0.03 \text{ fm}^4$ (—), $\alpha = 0.04 \text{ fm}^4$ (---), $\alpha = 0.06 \text{ fm}^4$ (-·-·-), $\alpha = 0.08 \text{ fm}^4$ (·····) (taken from [10]).

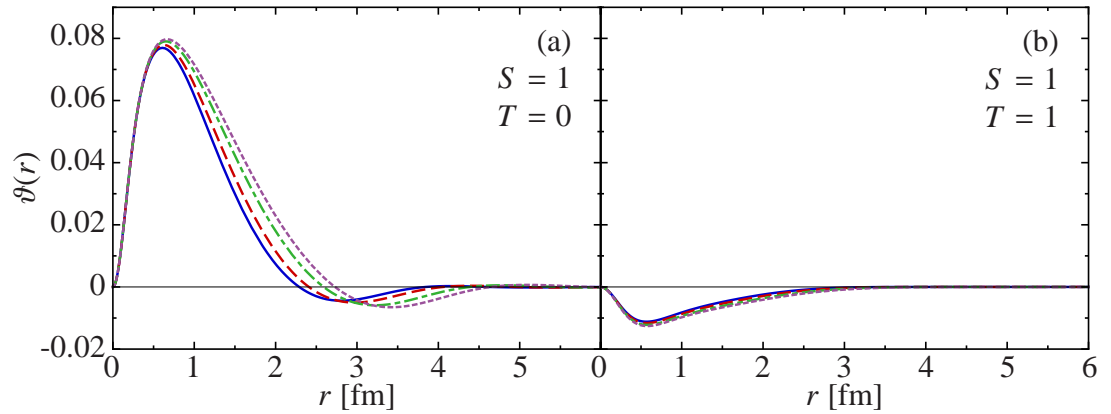


Figure 2.9: SRG-generated tensor correlation functions $\vartheta(r)$ for the AV18 potential in the two spin-isospin channels for different values of the flow parameter: $\alpha = 0.03 \text{ fm}^4$ (—), $\alpha = 0.04 \text{ fm}^4$ (---), $\alpha = 0.06 \text{ fm}^4$ (-·-·-), $\alpha = 0.08 \text{ fm}^4$ (·····) (taken from [10]).

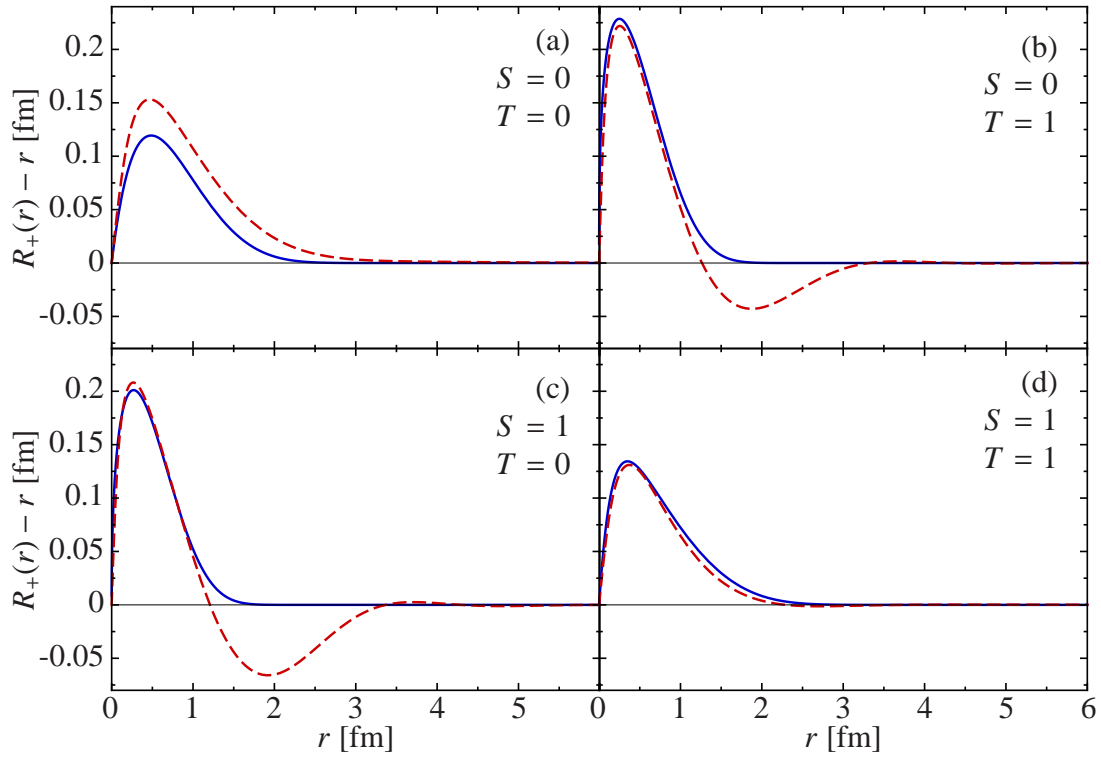


Figure 2.10: Comparison of variationally determined central correlation functions $R_+(r) - r$ (—) and SRG-generated ones with $\alpha = 0.04 \text{ fm}^4$ (---) for the AV18 potential in the four spin-isospin channels (taken from [10]).

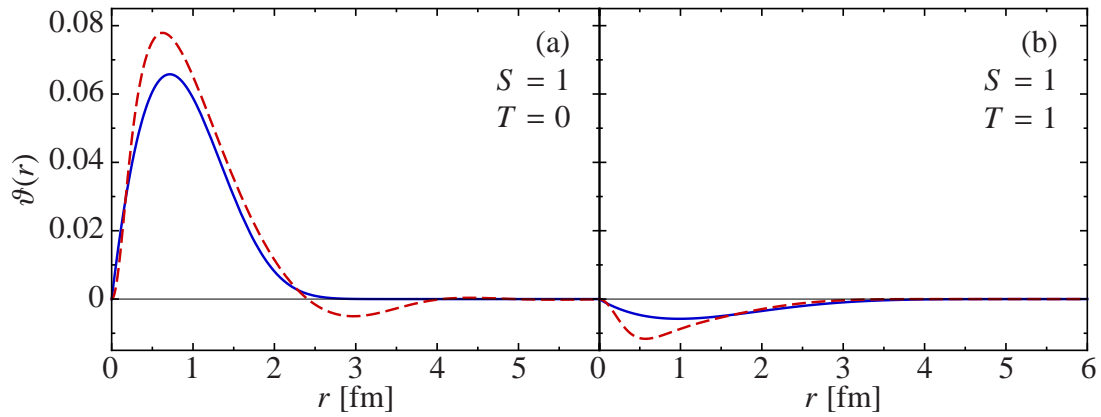


Figure 2.11: Comparison of variationally determined tensor correlation functions $\vartheta(r)$ with constraints $I_\vartheta^{(10)} = 0.09 \text{ fm}^3$, $I_\vartheta^{(11)} = -0.03 \text{ fm}^3$ (—) and SRG-generated ones with $\alpha = 0.04 \text{ fm}^4$ (---) for the AV18 potential in the two spin-isospin channels (taken from [10]).

for the variationally determined correlation functions. That means, that we distinguish the possible spin-isospin channels and only consider the lowest angular momenta in the respective channel [10]. Hence, for the determination of the central correlation functions in the spin-singlet channels we use the 1S_0 partial wave for $T = 1$ and the 1P_1 partial wave for $T = 0$. In the spin-triplet channel, both central and tensor correlation functions have to be calculated. For $T = 0$ this is straightforward by using the deuteron solution in the coupled $^3S_1 - ^3D_1$ partial wave. But for $T = 1$ the lowest allowed angular momentum is $L = 1$ so that the total angular momentum can be coupled to $J = 0, 1, 2$. There are several possibilities to deal with this ambiguity, currently the most convenient scheme is to create a pseudo interaction by averaging the 3P_0 , 3P_1 and 3P_2 partial waves with a relative weight $2J+1$ and use its eigenstates for the mapping procedure. We extract the correlation functions of the SRG evolution by using the energetically lowest states in the respective spin-isospin channel.

Contrary to the correlation functions determined via an energy minimization we do not have to introduce additional range constraints. The only parameter is the flow parameter α that enters the central and tensor correlation functions in a consistent way.

In Figs. 2.8 and 2.9 we show the dependencies of the central and tensor correlation functions on the flow parameter, respectively. The range of all correlation functions increases with increasing flow parameter. This can be understood in the following way: The flow evolution starts by suppressing the matrix elements at high-lying momenta, i.e. small inter-particle distances. With increasing flow parameter, also the matrix elements involving lower momenta are driven towards a band-diagonal structure, i.e. in coordinate space the wave functions are modified at larger distances, leading to longer-ranged correlation functions.

The SRG-generated central and tensor correlation functions are compared to those determined via an energy minimization in Figs. 2.10 and 2.11, respectively. The parameters were chosen such that both sets of correlators yield approximately the same ground-state energy of ^4He in a No-Core Shell Model calculation, i.e. $\alpha = 0.04 \text{ fm}^4$ for the SRG-generated correlation functions and for the variationally optimized tensor correlation functions the range constraints are $l_\vartheta = 0.09 \text{ fm}^3$ for $T = 0$ and $l_\vartheta = -0.03 \text{ fm}^3$ for $T = 1$. In the $S = 0, T = 0$ channel the shapes of both central correlation functions are very similar, but the variationally optimized correlation function is somewhat weaker and of smaller range, which can be explained by the additional constraint introduced in Section 2.2.6. In the even channels ($S = 0, T = 1$ and $S = 1, T = 0$), where the dominant central correlations appear, the correlation functions nicely agree at small distances. But the SRG-generated functions have a negative

contribution around 2 fm while the variationally optimized correlation functions simply fall off to zero. The behavior of the latter is caused by the chosen parameterization which does not allow for negative parts. Possibly, the agreement at intermediate distances could be improved if one would apply parameterizations that are more flexible. The shape of the SRG-generated correlation functions reveals that the attractive region of the interaction is exploited by shifting probability amplitude of both smaller and larger inter-particle distances towards the potential minimum. Finally, in the odd $S = 1$, $T = 1$ channel both types of central correlation functions agree very well.

Figure 2.11 shows that the agreement of the tensor correlation functions is not as good as for the central correlation functions. This is again explained by the artificial range constraints of the variationally optimized tensor correlation functions. For $T = 0$ the SRG-generated correlation function shows a negative part, which is much weaker than for the corresponding central correlation function.

Chapter 3

Many-Body Calculations

As a starting point to characterize the properties of the unitarily transformed two-body interactions discussed in Chapter 2 we will apply the Hartree-Fock method to calculate binding energies and charge radii across the whole nuclear chart. The derivation of the general Hartree-Fock equations applied to a Hamiltonian containing a two-body and a three-body interaction is summarized in Appendix A, in Section 3.1 we will discuss the practical application of the Hartree-Fock method adapted to our specific requirements. Subsequently, we will examine the properties of different two-body interactions by considering HF ground-state energies and charge radii of selected closed-shell nuclei in Section 3.2 and single-particle spectra in Section 3.3.

To estimate the importance of long-range correlations we apply low-order many-body perturbation theory on top of the Hartree-Fock results. We will derive the second-order energy correction in Section 3.4, again on the basis of a two- plus three-body interaction. To conclude the discussion based on pure two-body interactions, we will investigate the perturbative energy corrections for the different two-body interactions in Section 3.5.

3.1 The Hartree-Fock Method

In the Hartree-Fock approximation the many-body state is represented by a single Slater determinant [13]:

$$|\text{HF}\rangle = \mathcal{A}(|\varphi_{\alpha_1}\rangle \otimes |\varphi_{\alpha_2}\rangle \otimes \cdots \otimes |\varphi_{\alpha_A}\rangle), \quad (3.1)$$

where \mathcal{A} denotes the antisymmetrization operator acting on the A -body product state $|\varphi_{\alpha_1}\rangle \otimes |\varphi_{\alpha_2}\rangle \otimes \cdots \otimes |\varphi_{\alpha_A}\rangle$. The minimization of the energy expectation value is performed by using the single-particle states $|\varphi_{\alpha}\rangle$ as variational degrees of freedom.

Since this simple many-body state is not capable of describing the complex correlations induced by the nuclear interaction, it is crucial to employ an appropriate unitarily transformed NN interaction in connection with the HF method incorporating at least parts of the correlations. The Hamiltonian entering the HF equations consists of the kinetic energy T , a transformed NN interaction V_{NN} and a phenomenological 3N interaction $V_{3\text{N}}$ [13, 19, 27]:

$$\begin{aligned} H_{\text{int}} &= T - T_{\text{cm}} + V_{\text{NN}} + V_{3\text{N}} = \\ &= T_{\text{int}} + V_{\text{NN}} + V_{3\text{N}} = H_{\text{int}}^{(2)} + V_{3\text{N}} . \end{aligned} \quad (3.2)$$

The unitarily transformed interaction V_{NN} includes all Coulomb and charge-dependent terms. In order to approximately account for the center-of-mass contribution to the energy, the center-of-mass kinetic energy T_{cm} has been subtracted yielding the intrinsic kinetic energy T_{int} , which can be written as a pure two-body operator:

$$T_{\text{int}} = \frac{1}{A\mu} \sum_{i < j}^A \mathbf{q}_{ij}^2 \quad (3.3)$$

with the reduced nucleon mass $\mu = m_N/2$ and the relative two-body momentum operator \mathbf{q} . Thus, the Hamiltonian only contains two- and three-body operators.

We choose the eigenstates $|nljmm_t\rangle$ of the spherical harmonic oscillator as basis for the calculations. The HF single-particle states can be expanded in the following way:

$$|\varphi_{\alpha}\rangle = |\nu l j m m_t\rangle = \sum_n C_n^{(\nu l j m m_t)} |nljmm_t\rangle , \quad (3.4)$$

where only states with the same quantum numbers l, j and m can contribute as we assume spherical symmetry. Furthermore, we will only consider nuclei with closed j -shells in the following, i.e. the expansion coefficients can be chosen to be independent of the projection quantum number m : $C_n^{(\nu l j m m_t)} = C_n^{(\nu l j m_t)}$. These expansion coefficients are used as variational parameters for the minimization of the energy expectation value. Thus, the HF equations can be written as

$$\sum_{n'_1} h_{m_1 n'_1}^{(l j_1 m_{t_1})} C_{n'_1}^{(\nu_1 l j_1 m_{t_1})} = \varepsilon_{(\nu_1 l j_1 m_{t_1})} C_{m_1}^{(\nu_1 l j_1 m_{t_1})} \quad (3.5)$$

with the single-particle energies $\varepsilon^{(\nu l j m_t)}$. The matrix elements of the single-particle Hamiltonian

$$\begin{aligned}
h_{n_1 n'_1}^{(l_1 j_1 m_{t_1})} &= \sum_{l_2 j_2 m_{t_2}} \sum_{n_2 n'_2} H_{n_1 n_2, n'_1 n'_2}^{(l_1 j_1 m_{t_1}, l_2 j_2 m_{t_2})} \varrho_{n'_2 n_2}^{(l_2 j_2 m_{t_2})} \\
&+ \frac{1}{2} \sum_{l_2 j_2 m_{t_2}} \sum_{l_3 j_3 m_{t_3}} \sum_{n_2 n_3 n'_2 n'_3} V_{3N, n_1 n_2 n_3, n'_1 n'_2 n'_3}^{(l_1 j_1 m_{t_1}, l_2 j_2 m_{t_2}, l_3 j_3 m_{t_3})} \varrho_{n'_2 n_2}^{(l_2 j_2 m_{t_2})} \varrho_{n'_3 n_3}^{(l_3 j_3 m_{t_3})}
\end{aligned} \quad (3.6)$$

consist of the matrix elements $H_{n_1 n_2, n'_1 n'_2}^{(l_1 j_1 m_{t_1}, l_2 j_2 m_{t_2})}$ of the two-body part of the Hamiltonian $H_{\text{int}}^{(2)} = T_{\text{int}} + V_{\text{NN}}$ and the matrix elements of the three-body interaction $V_{3N, n_1 n_2 n_3, n'_1 n'_2 n'_3}^{(l_1 j_1 m_{t_1}, l_2 j_2 m_{t_2}, l_3 j_3 m_{t_3})}$. The one-body density matrix ϱ is defined by

$$\varrho_{n' n}^{(l j m_t)} = \sum_{\nu} (2j + 1) C_{n'}^{(\nu l j m_t)^*} C_n^{(\nu l j m_t)}, \quad (3.7)$$

The single-particle Hamiltonian itself depends on the coefficients $C_n^{(\nu l j m_t)}$ via the one-body density matrix revealing the non-linearity of the HF equations.

The m -averaged antisymmetric matrix elements of the two-body part of the Hamiltonian entering into the eigenvalue problem (3.5) can be expressed by using uncoupled two-body matrix elements:

$$\begin{aligned}
H_{n_1 n_2, n'_1 n'_2}^{(l_1 j_1 m_{t_1}, l_2 j_2 m_{t_2})} &= \frac{1}{(2j_1 + 1)(2j_2 + 1)} \\
&\times \sum_{m_1 m_2} \langle n_1 l_1 j_1 m_1 m_{t_1}, n_2 l_2 j_2 m_2 m_{t_2} | H_{\text{int}}^{(2)} | n'_1 l_1 j_1 m_1 m_{t_1}, n'_2 l_2 j_2 m_2 m_{t_2} \rangle.
\end{aligned} \quad (3.8)$$

However, it is more convenient to start from jj -coupled two-body matrix elements:

$$\begin{aligned}
H_{n_1 n_2, n'_1 n'_2}^{(l_1 j_1 m_{t_1}, l_2 j_2 m_{t_2})} &= \sum_{JTM_T} \frac{(2J + 1)}{(2j_1 + 1)(2j_2 + 1)} c \left(\begin{array}{cc} \frac{1}{2} & \frac{1}{2} \\ m_{t_1} & m_{t_2} \end{array} \middle| \begin{array}{c} T \\ M_T \end{array} \right)^2 \\
&\times \langle n_1 l_1 j_1, n_2 l_2 j_2; JTM_T | H_{\text{int}}^{(2)} | n'_1 l_1 j_1, n'_2 l_2 j_2; JTM_T \rangle
\end{aligned} \quad (3.9)$$

with the Clebsch-Gordan coefficient $c \left(\begin{array}{cc} \frac{1}{2} & \frac{1}{2} \\ m_{t_1} & m_{t_2} \end{array} \middle| \begin{array}{c} T \\ M_T \end{array} \right)$.

The matrix elements of the two-body interactions are most conveniently calculated in a basis of LS -coupled relative two-body states and they have to be transformed into jj -coupled matrix elements for the application in Hartree-Fock and other methods.

In addition the matrix elements of the three-body interaction are required. They will be calculated in Chapter 4 for a finite-range three-body interaction with Gaussian shape and in Chapter 5 for a regularized three-body contact interaction. In the following, we will discuss HF calculations based on pure two-body interactions.

3.2 Ground-State Energies and Charge Radii

We start by discussing some results obtained with pure unitarily transformed two-body interactions. While the properties of the transformed interactions were studied in Section 2.3.3 by considering momentum-space matrix elements, we now perform many-body calculations to investigate some other aspects of the pure two-body interactions before including three-body forces.

The matrix elements of the transformed two-body interaction as well as those of any other observables, especially the intrinsic kinetic energy and the charge radius, are computed beforehand for each basis size and oscillator parameter separately and stored to disk. This procedure allows for an efficient solution of the Hartree-Fock eigenvalue problem on the one hand and on the other hand the matrix elements can be used as input for different many-body methods without calculating them again. The solution of the HF equations is performed in an iterative fashion until full self-consistency is reached.

In the following, we will consider ground-state energies (cf. Eq. (A.33)) as well as charge radii for selected nuclei across the whole nuclear chart. In order to preserve spherical symmetry only closed-shell nuclei are investigated. The operators of the mean-square radii can be written in a translationally invariant form [24, 28]:

$$r_{\text{ms}} = \frac{1}{A} \sum_i (\mathbf{x}_i - \mathbf{x}_{\text{cm}})^2 = \frac{1}{2A^2} \sum_{ij} \mathbf{r}_{ij}^2 \quad (3.10)$$

$$r_{\text{ms}}^p = \frac{1}{AZ} \sum_{ij} \mathbf{r}_{ij}^2 \Pi_p - \frac{1}{2A^2} \sum_{ij} \mathbf{r}_{ij}^2 \quad (3.11)$$

$$r_{\text{ms}}^n = \frac{1}{AN} \sum_{ij} \mathbf{r}_{ij}^2 \Pi_n - \frac{1}{2A^2} \sum_{ij} \mathbf{r}_{ij}^2, \quad (3.12)$$

where r_{ms} denotes the radius operator for a nucleon and $r_{\text{ms}}^{p/n}$ for a proton/neutron. The point root-mean-square (rms) radius r_{rms} is obtained by calculating the square-root of the expectation value of the mean-square radius operator for the HF ground-state. In principle, one would have to use the unitarily transformed radius operators. For the UCOM transformation using variationally optimized correlators, however, it was shown that the difference between the correlated and the uncorrelated charge radii is marginal [13]. Therefore, we will discuss uncorrelated charge radii in the following. The impact of the SRG transformation on the charge radii has not yet been investigated, but we neglect it nonetheless.

UCOM(SRG)	standard UCOM using SRG-generated correlation functions
S-UCOM(SRG)	S-wave only UCOM using SRG-generated correlation functions
SRG	standard SRG
S-SRG	S-wave only SRG

Table 3.1: Acronyms for the four different families of unitarily transformed interactions.

To obtain the charge radius r_{ch} one has to add the standard corrections for proton and neutron size:

$$r_{\text{ch}} = \sqrt{r_{\text{p,rms}}^2 + r_{\text{p,ch}}^2 + \frac{N}{Z} r_{\text{n,ch}}^2}, \quad (3.13)$$

where we use

$$r_{\text{p,ch}} = 0.8768 \text{ fm}, \quad r_{\text{n,ch}}^2 = -0.116 \text{ fm}^2 \quad (3.14)$$

for the proton and neutron charge radii [29].

We employ the UCOM and the SRG to obtain a manifold of phase-shift equivalent transformed NN potentials depending on one parameter. When applying the standard SRG evolution all partial waves are transformed consistently. However, it is also possible to restrict the SRG evolution to the relative S-partial waves, i.e. the 1S_0 and the coupled $^3S_1 - ^3D_1$ partial waves, since the short-range correlations are most dominant in these channels. For higher angular momenta the wave functions are suppressed at short distances due to the centrifugal barrier, i.e. the effects of short-range correlations are not as pronounced as in the S-wave channels.

For the UCOM transformation we use correlation functions obtained from the SRG evolution. In each spin-isospin channel the lowest partial waves are considered for the determination of the correlation functions. Subsequently, these correlation functions are used to transform all partial waves consistently. In contrast to this standard UCOM, we can also correlate the S-partial waves only, i.e. the 1S_0 and the coupled $^3S_1 - ^3D_1$ partial waves, in analogy to the restricted SRG evolution. Note that in this case already the SRG evolution is restricted to the S-partial waves as the higher partial waves are not required for the determination of the correlation functions.

In the following we will consider these four different classes of unitarily transformed two-body interactions, the corresponding acronyms are listed in Table 3.1.

The harmonic-oscillator basis is truncated with respect to the major oscillator quantum number $e = 2n + l \leq e_{\text{max}}$. Additional constraints for the radial quantum number n or the orbital angular momentum l are possible. A truncation at $e_{\text{max}} = 10$ is sufficient to obtain converged Hartree-Fock results (cf. Sec. 3.5).

Isotope	⁴ He	¹⁶ O	²⁴ O	³⁴ Si	⁴⁰ Ca	⁴⁸ Ca	⁴⁸ Ni	⁵⁶ Ni	⁶⁰ Ni
a_{HO} [fm]	1.3	1.8	1.9	1.9	2.0	2.0	2.0	2.0	2.0
Isotope	⁷⁸ Ni	⁸⁸ Sr	⁹⁰ Zr	¹⁰⁰ Sn	¹¹⁴ Sn	¹³² Sn	¹⁴⁶ Gd	²⁰⁸ Pb	
a_{HO} [fm]	2.1	2.2	2.2	2.2	2.2	2.2	2.2	2.4	

Table 3.2: Optimal oscillator lengths for the considered closed-shell nuclei.

To perform the Hartree-Fock calculations we, first of all, have to choose the oscillator parameter a_{HO} defining the width of the oscillator potential. In former applications the oscillator parameter was fixed for each nucleus separately by minimizing the HF energy. However, when perturbative corrections are included, the oscillator lengths can no longer be determined via an energy minimization, since perturbation theory does not obey the variational principle. Therefore, we will apply a different scheme for the determination of the oscillator lengths, i.e. instead of ground-state energies we consider charge radii. We choose the oscillator parameter such that the experimental charge radius is approximately reproduced by a Slater determinant which is built of the harmonic-oscillator single-particle states with the lowest energies. For those nuclei, where no experimental value for the charge radius is available, we have to estimate the oscillator parameter. The advantage of this procedure is that the oscillator parameter is independent of the respective two- and three-body interactions. Hence, we can stick to the once determined set of oscillator parameters throughout all following calculations. The resulting values are summarized in Table 3.2.

Figures 3.1 and 3.2 show the ground-state energies per nucleon (upper panel) and the charge radii (lower panel) for selected closed-shell nuclei across the whole nuclear chart obtained from HF calculations based on the UCOM(SRG) and S-UCOM(SRG) interactions, respectively. The different symbols indicate different values of the flow parameter. In both cases, the smallest value of the flow parameter, i.e. $\alpha = 0.04 \text{ fm}^4$, is chosen such that the experimental ⁴He ground-state energy is reproduced in converged No-Core Shell Model (NCSM) calculations. Therefore, calculations with the pure two-body interaction are performed using this flow parameter. Nonetheless, we investigate the influence of the flow parameter, and especially examine the properties of two-body interactions with larger flow parameters as they will be required when including a repulsive three-body interaction. Figures 3.1 and 3.2 show that the HF ground-state energies calculated with $\alpha = 0.04 \text{ fm}^4$ reproduce the systematics of the experimental data except for an almost constant shift. In case of the UCOM(SRG) interaction all nuclei are underbound by about 2.5 to 3.5 MeV per nucleon, while for the S-UCOM(SRG) interaction the ground-state energies per nucleon differ from experiment

3.2 · Ground-State Energies and Charge Radii

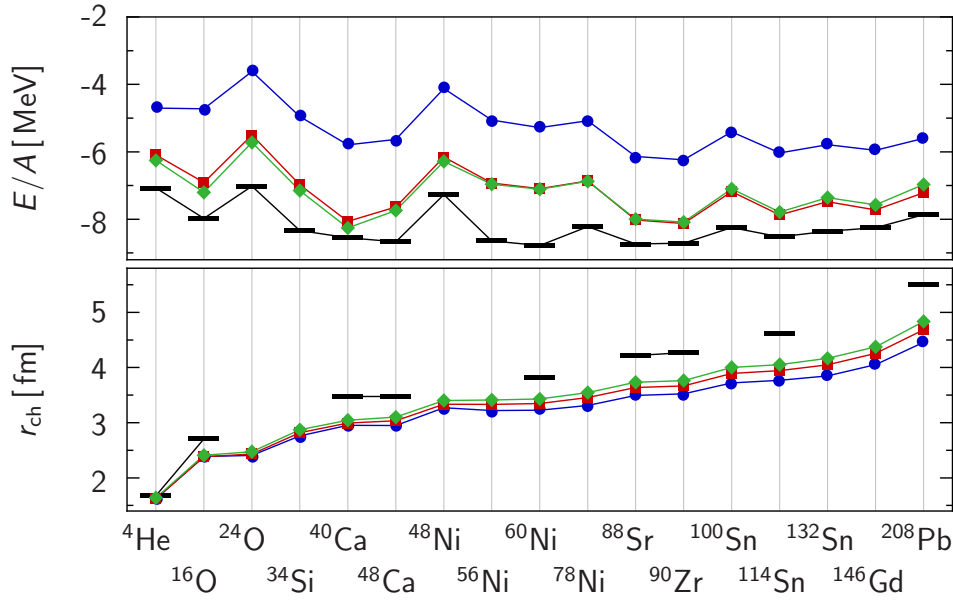


Figure 3.1: Ground-state energies per nucleon and charge radii of selected closed-shell nuclei resulting from HF calculations for the UCOM(SRG) interaction for $e_{\max} = 10$ and different flow parameters: (●) $\alpha = 0.04 \text{ fm}^4$, (■) $\alpha = 0.12 \text{ fm}^4$, (◆) $\alpha = 0.16 \text{ fm}^4$. The bars indicate the experimental values [30, 31].

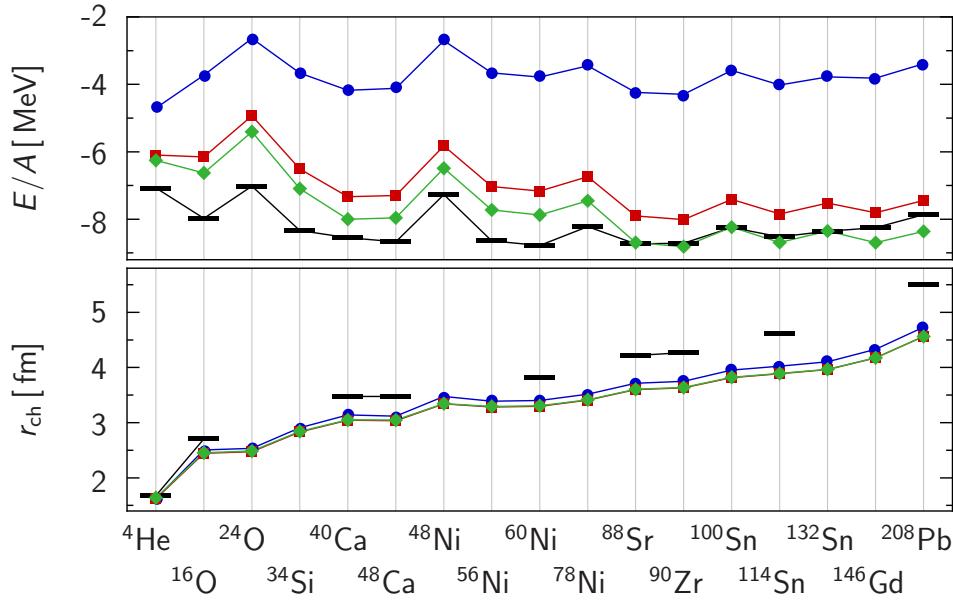


Figure 3.2: Same as in Figure 3.1 for the S-UCOM(SRG) interaction with $e_{\max} = 10$ and (●) $\alpha = 0.04 \text{ fm}^4$, (■) $\alpha = 0.12 \text{ fm}^4$, (◆) $\alpha = 0.16 \text{ fm}^4$.

by about 4 to 5 MeV. With increasing flow parameter the difference to the experimental binding energies diminishes, in case of the S-UCOM(SRG) interaction the trend of the experimental energies is no longer reproduced, i.e. the light nuclei are underbound while the heaviest nuclei are already overbound for the largest flow parameter. The gain of binding energy with increasing flow parameter can be understood by considering the meaning of the flow parameter. With increasing flow parameter, the range of the derived correlation functions increases as well. Hence, correlations of longer range are covered by the UCOM transformation and are thus included effectively already on the HF level leading to an improved reproduction of the experimental binding energies. Nonetheless, for calculations based on the pure two-body interaction one chooses the flow parameter $\alpha = 0.04 \text{ fm}^4$ for the above-mentioned reason. Furthermore, missing long-range correlations can be included by using second-order many-body perturbation theory on top of the HF results, which will entail a lowering of the ground-state energies (cf. Sec. 3.5).

Figure 3.1 reveals a further interesting feature of the UCOM(SRG) interaction. If we compare the ground-state energies calculated with the flow parameter $\alpha = 0.16 \text{ fm}^4$ to those calculated with $\alpha = 0.12 \text{ fm}^4$, we find that for light nuclei the trend to lower energies is confirmed while we observe the opposite trend for the heaviest nuclei. With increasing flow parameter correlations of longer range are included in the UCOM transformation, but only the short-range correlations are state-independent. Hence, for $\alpha = 0.16 \text{ fm}^4$ the UCOM transformation obviously becomes state-dependent due to the long range of the correlation functions, which is reflected in the trend of the binding energies.

The charge radii shown in the lower parts of Figures 3.1 and 3.2 are significantly smaller than the experimental values for both the UCOM(SRG) and the S-UCOM(SRG) interaction. The variation of the charge radii with increasing flow parameter is much weaker than in case of the ground-state energies. For the UCOM(SRG) interaction the charge radii slightly increase with increasing flow parameter. In contrast, the radii decrease with increasing flow parameter in case of the S-UCOM(SRG) interaction.

In Figures 3.3 and 3.4 the ground-state energies and charge radii obtained with the SRG and S-SRG interaction for different flow parameters are displayed. Again, the smallest flow parameter is chosen such that the experimental ${}^4\text{He}$ ground-state energy is reproduced in a converged NCSM calculation, which is $\alpha = 0.03 \text{ fm}^4$ for these interactions. For the SRG interaction the binding energy per nucleon increases rapidly with increasing mass number leading to a strong overbinding of intermediate and heavy nuclei. With increasing flow parameter this systematic deviation is even more dramatic. At the same time the charge radii are significantly too small, e.g. for

3.2 · Ground-State Energies and Charge Radii

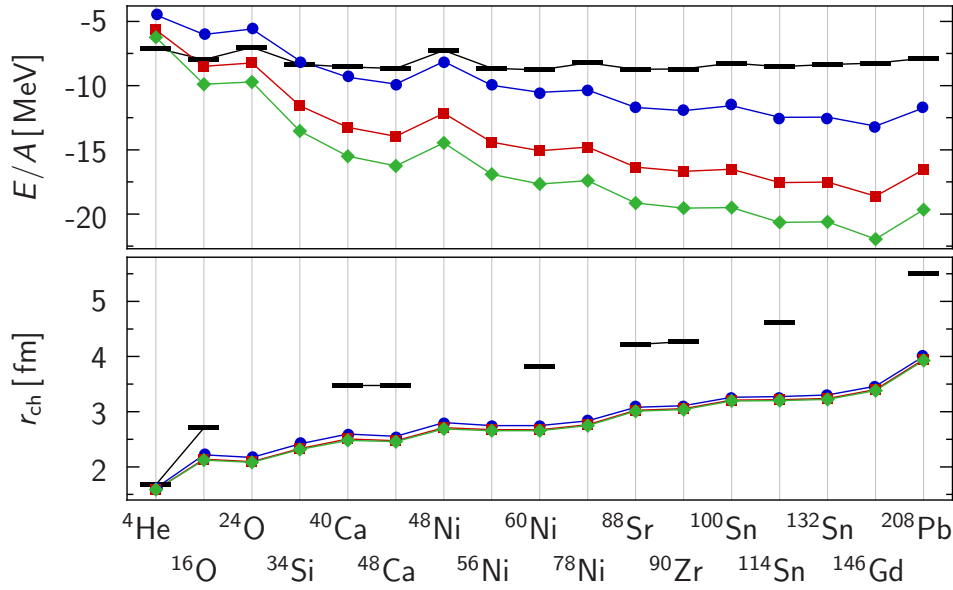


Figure 3.3: Ground-state energies per nucleon and charge radii of selected closed-shell nuclei resulting from HF calculations for the SRG interaction for $e_{\max} = 10$ and different flow parameters: (●) $\alpha = 0.03 \text{ fm}^4$, (■) $\alpha = 0.06 \text{ fm}^4$, (◆) $\alpha = 0.10 \text{ fm}^4$. The bars indicate the experimental values [30,31].

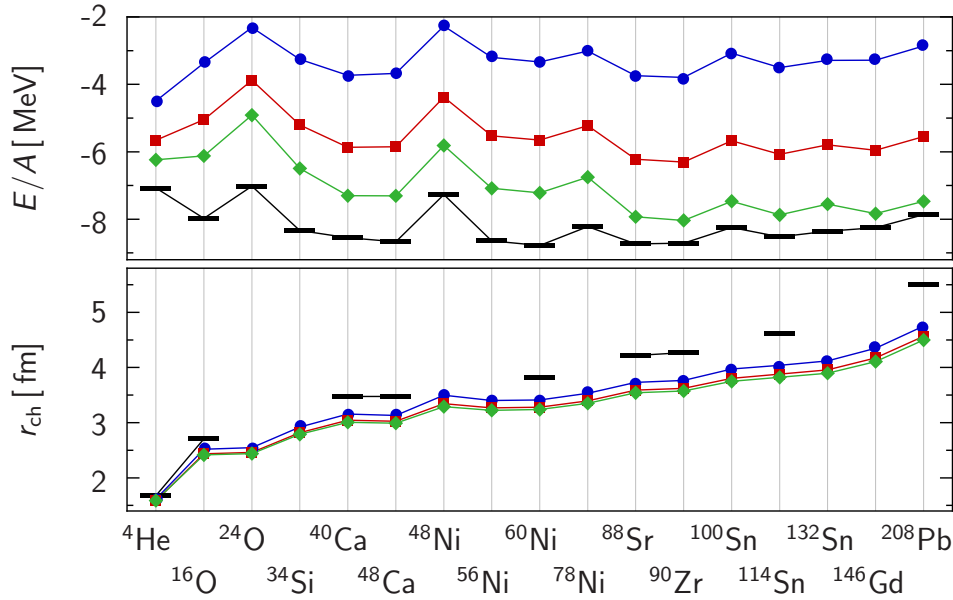


Figure 3.4: Same as in Figure 3.3 for the S-SRG interaction with $e_{\max} = 10$ and (●) $\alpha = 0.03 \text{ fm}^4$, (■) $\alpha = 0.06 \text{ fm}^4$, (◆) $\alpha = 0.10 \text{ fm}^4$.

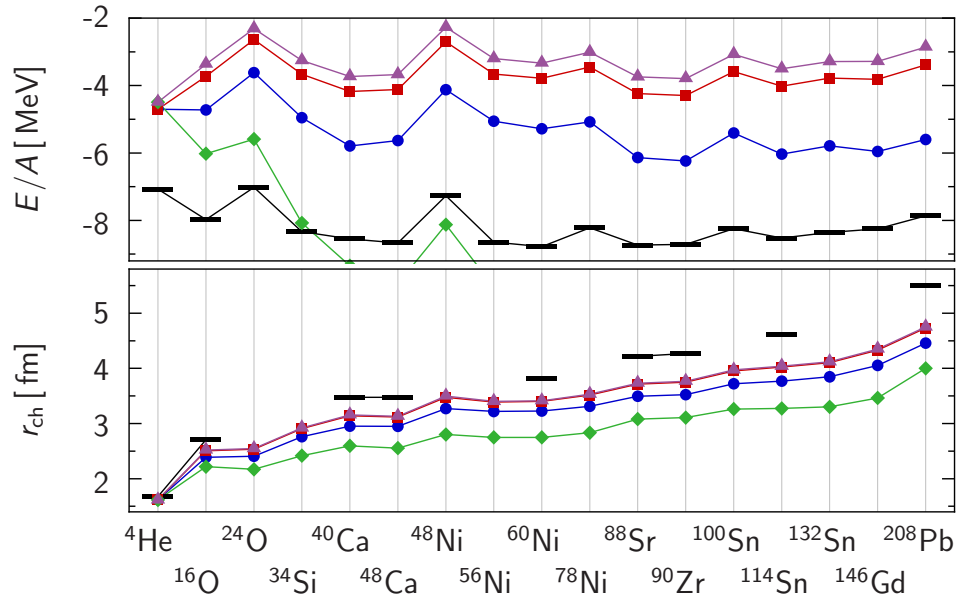


Figure 3.5: Ground-state energies per nucleon and charge radii of selected closed-shell nuclei resulting from HF calculations for different two-body interactions with $e_{\text{max}} = 10$: (●) UCOM(SRG), $\alpha = 0.04 \text{ fm}^4$; (■) S-UCOM(SRG), $\alpha = 0.04 \text{ fm}^4$; (◆) SRG, $\alpha = 0.03 \text{ fm}^4$; (▲) S-SRG, $\alpha = 0.03 \text{ fm}^4$. The bars indicate the experimental values [30, 31].

${}^{208}\text{Pb}$ the difference to experiment reaches 1.5 fm. The radii are almost independent of the flow parameter. This behavior shows that for the SRG transformation the induced three-body and higher many-body forces do not cancel genuine three-body forces, i.e. the net three-body forces have a significant impact on the results. Hence, we expect that the three-body interaction has to be strong compared to the other cases in order to reproduce the experimental data.

For the S-SRG interaction, the systematic of the ground-state energies is again reproduced, as seen in Figure 3.4. For the smallest flow parameter the values differ by about 4.5 to 5.5 MeV per nucleon from experiment, for the larger flow parameters this difference decreases. The charge radii are again smaller than in experiment and depend only weakly on the flow parameter.

It is obvious that the energies as well as the charge radii will increase, if one adds a repulsive three-body interaction. The additional repulsion shifts the nucleons apart, which increases the radius and reduces the binding energy at the same time. Fortunately, the dependence of the radii on the flow parameter is weak, so we can determine the strength of the three-body interaction such that the experimental charge radii are reproduced. Subsequently, the flow parameter is used to adjust the ground-state energies.

Figure 3.5 shows a comparison of the results of the four different interactions, each with the flow parameter one uses for calculations with the pure two-body interaction, in order to emphasize the differences between these interactions. First we compare the UCOM(SRG) with the SRG interactions, which have some inherent differences as seen from the HF ground-state energies and charge radii. The UCOM transformation is designed to describe short-range correlations which are most dominant in the lowest partial waves. Hence, the higher partial waves are not treated in an optimal way by the UCOM transformation. Since short-range correlations are more and more suppressed in higher partial waves due to the centrifugal barrier, this non-optimal pre-diagonalization of the higher partial waves only leads to minor effects. In contrast, in SRG each partial wave is evolved separately leading to an optimal pre-diagonalization also for higher partial waves resulting in faster convergence than in case of the UCOM(SRG) interaction [10]. Evidently, this entails larger contributions from three- and many-body forces which in turn yields strongly overbound nuclei with small radii as shown in Figure 3.5.

Next, we compare the UCOM(SRG) and SRG interactions with S-UCOM(SRG) and S-SRG, respectively. As mentioned above, UCOM aims at the description of short-range correlations which are most dominant in the lowest partial waves. Therefore, the higher partial waves are not correlated in an optimal manner. The UCOM transformation generates repulsion in higher partial waves, which is not evident from Figure 3.5, but becomes apparent for larger flow parameters. Consequently, we will need a weaker three-body force to supplement the UCOM(SRG) interaction than for S-UCOM(SRG) as we will discuss in Chapter 5.

In the S-SRG approach only the S-partial waves are evolved as well. Compared to the HF results of the SRG interaction this also leads to an improved description of the charge radii. As the nuclei are strongly overbound when using the SRG interaction, the S-SRG interaction yields also an improvement in the description of ground-state energies.

The S-UCOM(SRG) and the S-SRG interaction both yield very similar results for ground-state energies and charge radii in the HF approximation.

Considering the UCOM(SRG), S-UCOM(SRG) and S-SRG interactions, the ground-state energies of all considered closed-shell nuclei differ from experiment, but their description can be improved by including long-range correlations, e.g. in the framework of many-body perturbation theory. The charge radii are systematically smaller than the experimental values for all four types of two-body interactions. However, this discrepancy cannot be covered by the inclusion of long-range correlations but is an evidence for the omitted three- and many-body forces of the respective interaction.

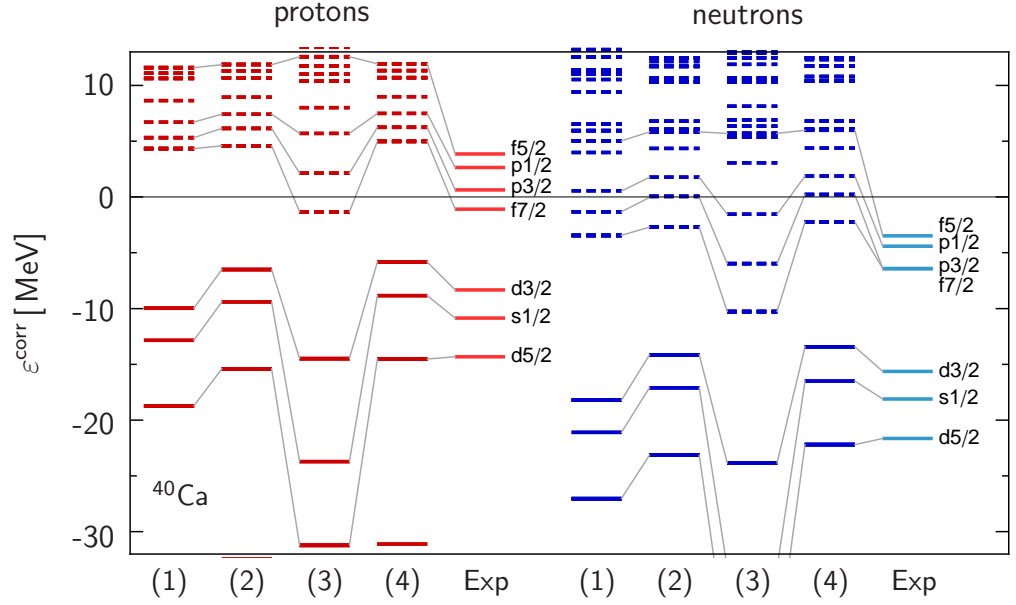


Figure 3.6: Single-particle spectra of ^{40}Ca for the different two-body interactions with $e_{\text{max}} = 10$: (1) UCOM(SRG), $\alpha = 0.04 \text{ fm}^4$; (2) S-UCOM(SRG), $\alpha = 0.04 \text{ fm}^4$; (3) SRG, $\alpha = 0.03 \text{ fm}^4$; (4) S-SRG, $\alpha = 0.03 \text{ fm}^4$; compared to experimental data [32]. Solid and dashed lines indicate occupied and unoccupied states of the HF solutions, respectively.

Hence, for an improved description of the charge radii one has to include a repulsive three-body interaction.

3.3 Single-Particle Spectra

Besides ground-state energies and charge radii the HF calculations provide an estimate for single-particle spectra. The single-particle energies being physical observables are defined via many-body energy differences of neighboring nuclei. However, in HF calculations based on the intrinsic kinetic energy calculating the energy difference $E_A - E_{A-1}(\beta \text{ removed})$, where the energy expectation value of the Slater determinant with removed state $|\beta\rangle$ is subtracted from the expectation value of the full A -body Slater determinant, does not directly yield the single-particle energy of a hole state $|\beta\rangle$; but one obtains two additional terms leading to the corrected single-particle energy, which can be compared to data extracted from experiment [13]:

$$\varepsilon_{\beta}^{\text{corr}} = E_A - E_{A-1}(\beta \text{ removed}) = \varepsilon_{\beta} - \frac{\langle T_{\text{int}} \rangle}{A-1} + \frac{2}{mA(A-1)} \sum_{\alpha}^{\leq \varepsilon_F} \langle \alpha\beta | \mathbf{q}^2 | \alpha\beta \rangle, \quad (3.15)$$

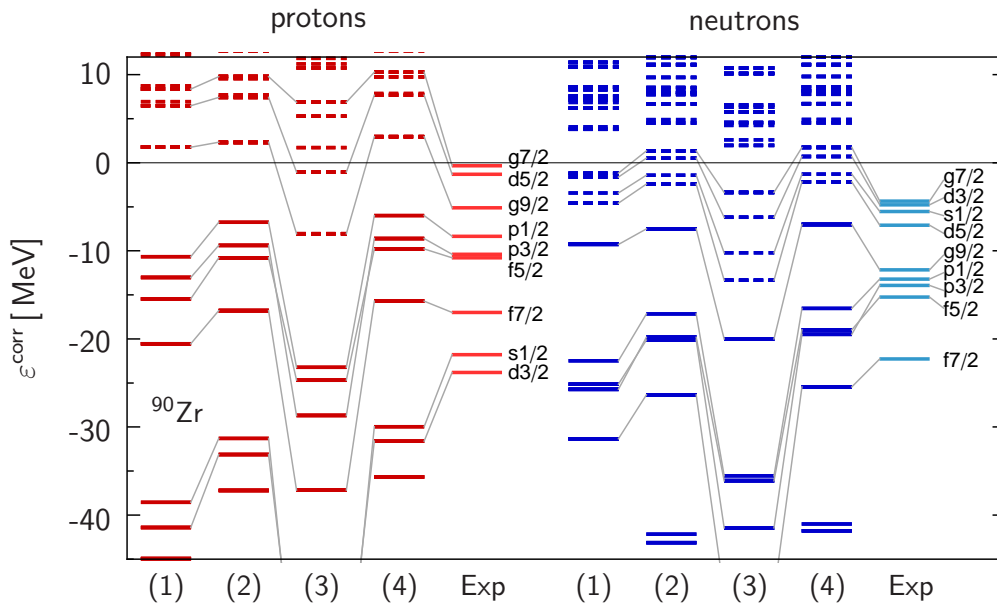


Figure 3.7: Single-particle spectra of ^{90}Zr for same interactions used in Figure 3.6. Experimental data taken from Refs. [33, 34].

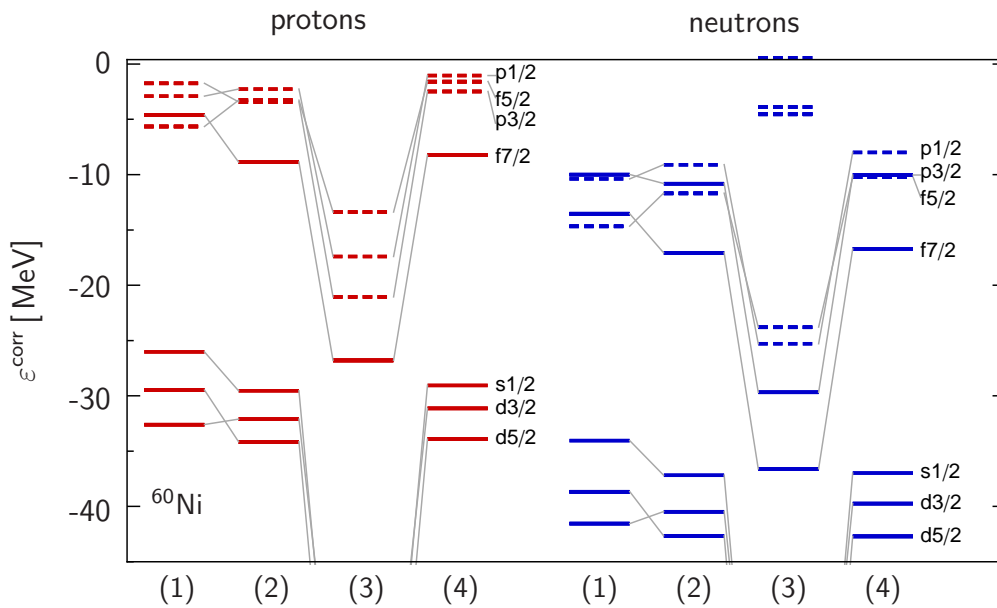


Figure 3.8: Single-particle spectra of ^{60}Ni for the different two-body interactions with $e_{\text{max}} = 10$: (1) UCOM(SRG), $\alpha = 0.16 \text{ fm}^4$; (2) S-UCOM(SRG), $\alpha = 0.16 \text{ fm}^4$; (3) SRG, $\alpha = 0.10 \text{ fm}^4$; (4) S-SRG, $\alpha = 0.10 \text{ fm}^4$. Solid and dashed lines indicate occupied and unoccupied states of the HF solutions, respectively.

where $\langle T_{\text{int}} \rangle$ is the expectation value of the intrinsic kinetic energy. For particle states the single-particle energy reads

$$\varepsilon_{\beta}^{\text{corr}} = E_{A+1}(\beta \text{ added}) - E_A = \varepsilon_{\beta} - \frac{\langle T_{\text{int}} \rangle}{A+1} - \frac{2}{mA(A+1)} \sum_{\alpha}^{\leq \varepsilon_F} \langle \alpha\beta | \mathbf{q}^2 | \alpha\beta \rangle . \quad (3.16)$$

We can use these corrected single-particle energies to investigate the properties of the four different two-body interactions introduced in the previous section. However, one has to be careful with the interpretation of single-particle spectra since they are no direct experimental observable.

Figure 3.6 shows the single-particle spectra for ^{40}Ca obtained with the four different two-body interactions in comparison to experimental estimates for the single-particle energies. The order of the levels is in nice agreement with experiment. But for all four interaction types the Fermi gap is overestimated and especially the spectra calculated with the SRG interaction are spread too wide compared with experiment. As a second example, the single-particle spectra of ^{90}Zr are shown in Figure 3.7, where one can observe similar features as for ^{40}Ca . The level ordering is mainly reproduced by the UCOM(SRG), S-UCOM(SRG) and S-SRG interactions, while there are some interchanged levels in case of the SRG interaction. The level spacings are overestimated by all four interactions, especially by the SRG interaction. This behavior shows the connection between radii and level spacings of single-particle spectra: On the basis of the SRG interaction the smallest radii were observed, which entails the largest level spacings.

The single-particle spectra of most of the other considered nuclei show a similar behavior, hence, they are not displayed here.

Like in the case of ground-state energies and charge radii, the S-UCOM(SRG) and the S-SRG interactions yield very similar single-particle spectra which confirms that these two interactions have a number of common properties.

It is expected that the inclusion of a repulsive three-body interaction will improve the description of the single-particle spectra. The additional repulsion will shift the nucleons apart from each other which results in larger radii as well as a reduction of the level spacings.

On the other hand, increasing the flow parameter may also lead to unintentional effects. As an example, the spectra of ^{60}Ni are shown in Figure 3.8 using the largest flow parameters for each two-body interaction. For both the proton and the neutron spectra one can observe, that the Fermi gap collapses and even occupied and unoccupied levels are interchanged. These effects are most pronounced in the spectra calculated with the UCOM(SRG) interaction. They are observed also in the spectra of several other

nuclei, but the corresponding spectra are not shown here. The collapse of the Fermi gap as well as the interchanging of particle and hole states might lead to problems, when applying many-body perturbation theory on top of these HF results. We will come back to this point in Section 3.5 and in Chapter 5, where the three-body contact interaction is considered.

3.4 *Low-Order Many-Body Perturbation Theory*

As discussed in the previous sections, the Hartree-Fock method is not capable of describing correlations. The short-range correlations are included by the unitarily transformed NN interactions while the long-range correlations have to be covered by the many-body states. The single Slater determinant used in the Hartree-Fock method cannot describe these correlations. One possibility to include long-range correlations is to apply many-body perturbation theory on top of the HF results. This approach will allow us to disentangle the effects of long-range correlations from the impact of three-body forces.

The basic concept of general perturbation theory is summarized in Appendix B. In the following, we will illustrate the formalism of many-body perturbation theory (MBPT) including two- and three-body interactions.

As we apply MBPT on top of the HF results, we start from the same intrinsic Hamiltonian

$$H_{\text{int}} = T_{\text{int}} + V_{\text{NN}} + V_{3\text{N}} = H_{\text{int}}^{(2)} + V_{3\text{N}} \quad (3.17)$$

containing the intrinsic kinetic energy T_{int} , a transformed two-body interaction V_{NN} and a phenomenological three-body interaction $V_{3\text{N}}$. In order to apply perturbation theory, we have to find a decomposition of the Hamiltonian of the form

$$H_{\text{int}} = H_0 + W, \quad (3.18)$$

with the unperturbed Hamiltonian H_0 , whose eigensystem has already been solved, and the perturbation W . In the HF eigenbasis only the diagonal matrix elements of the Hamiltonian contribute when calculating the HF energy. Hence, the unperturbed Hamiltonian H_0 can be expressed via the creation and annihilation operators a^\dagger and a , respectively, in the following way [27]:

$$\begin{aligned}
 H_0 &= \frac{1}{2} \sum_{\nu_1 \nu_2} \langle \nu_1 \nu_2 | H_{\text{int}}^{(2)} | \nu_1 \nu_2 \rangle a_{\nu_1}^\dagger a_{\nu_2}^\dagger a_{\nu_2} a_{\nu_1} \\
 &+ \frac{1}{6} \sum_{\nu_1 \nu_2 \nu_3} \langle \nu_1 \nu_2 \nu_3 | V_{3N} | \nu_1 \nu_2 \nu_3 \rangle a_{\nu_1}^\dagger a_{\nu_2}^\dagger a_{\nu_3}^\dagger a_{\nu_3} a_{\nu_2} a_{\nu_1} ,
 \end{aligned} \tag{3.19}$$

where the matrix elements are understood to be antisymmetrized. Thus, the perturbation W consists of the off-diagonal part of the Hamiltonian H_{int} in HF basis:

$$\begin{aligned}
 W &= \frac{1}{4} \sum_{\substack{\nu_1 \nu_2 \\ \kappa_1 \kappa_2}} \langle \nu_1 \nu_2 | H_{\text{int}}^{(2)} | \kappa_1 \kappa_2 \rangle a_{\nu_1}^\dagger a_{\nu_2}^\dagger a_{\kappa_2} a_{\kappa_1} \\
 &+ \frac{1}{36} \sum_{\substack{\nu_1 \nu_2 \nu_3 \\ \kappa_1 \kappa_2 \kappa_3}} \langle \nu_1 \nu_2 \nu_3 | V_{3N} | \kappa_1 \kappa_2 \kappa_3 \rangle a_{\nu_1}^\dagger a_{\nu_2}^\dagger a_{\nu_3}^\dagger a_{\kappa_3} a_{\kappa_2} a_{\kappa_1} ,
 \end{aligned} \tag{3.20}$$

where the antisymmetric two-body states $|\nu_1 \nu_2\rangle$ and $|\kappa_1 \kappa_2\rangle$ as well as the three-body states $|\nu_1 \nu_2 \nu_3\rangle$ and $|\kappa_1 \kappa_2 \kappa_3\rangle$ must differ in at least one single-particle state, respectively.

Since we start from the HF solution, the unperturbed ground-state energy is the HF energy: $E_0^{(0)} = E_{\text{HF}}$, while the first-order correction vanishes: $E_1^{(0)} = 0$. Thus the second order provides the leading correction to the HF ground-state energy. The generic form of the second-order energy correction can be written as (cf. Eq. (B.14)):

$$E_0^{(2)} = \sum_{\substack{n \\ n \neq 0}} \frac{|\langle \Psi_0^{(0)} | W | \Psi_n^{(0)} \rangle|^2}{E_0^{(0)} - E_n^{(0)}} , \tag{3.21}$$

where the unperturbed state $|\Psi_0^{(0)}\rangle$ is the HF ground-state and the states $|\Psi_n^{(0)}\rangle$ are n -particle- n -hole (n pn h , $n = 1, 2, 3, \dots$) excitations of the HF ground-state.

The HF Hamiltonian is constructed such that it does not connect the HF ground-state with 1p1h excitations [35]:

$$\langle \text{HF} | H_{\text{int}} | \text{HF}_h^p \rangle = 0 , \tag{3.22}$$

where $|\text{HF}_h^p\rangle$ denotes the HF state with one particle removed from state $|h\rangle$ below the Fermi energy (hole state) and one particle added to state $|p\rangle$ above the Fermi energy (particle state). Since the Hamiltonian contains up to three-body operators we have to consider 2p2h as well as 3p3h excitations of the HF ground-state. For the derivation of the second order energy correction we consider the two-body part of the Hamiltonian $H_{\text{int}}^{(2)}$ and the three-body interaction V_{3N} separately.

Energy Correction for $H_{int}^{(2)}$

Considering the two-body part of the Hamiltonian we only have to take into account 2p2h excitations written as $|HF_{hh'}^{pp'}\rangle$. Thus, the second order energy correction reads

$$E_0^{(2)}(H_{int}^{(2)}) = \frac{1}{4} \sum_{hh'}^{<\varepsilon_F} \sum_{pp'}^{>\varepsilon_F} \frac{|\langle HF | H_{int}^{(2)} | HF_{hh'}^{pp'} \rangle|^2}{E_{HF} - E_{HF_{hh'}^{pp'}}}, \quad (3.23)$$

where the summations cover the holes h, h' below the Fermi energy ε_F and the particles p, p' above the Fermi energy. The energy denominator can be approximated via the single-particle energies of the respective particle and hole states:

$$E_{HF} - E_{HF_{hh'}^{pp'}} \approx \varepsilon_h + \varepsilon_{h'} - \varepsilon_p - \varepsilon_{p'}. \quad (3.24)$$

The 2p2h excitation is generated via the application of the creation and annihilation operators to the HF ground-state:

$$|HF_{hh'}^{pp'}\rangle = a_p^\dagger a_{p'}^\dagger a_{h'} a_h |HF\rangle. \quad (3.25)$$

Together with the two-body part of the Hamiltonian written in second quantization

$$H_{int}^{(2)} = \frac{1}{4} \sum_{\substack{\nu_1 \nu_2 \\ \kappa_1 \kappa_2}} \langle \nu_1 \nu_2 | H_{int}^{(2)} | \kappa_1 \kappa_2 \rangle a_{\nu_1}^\dagger a_{\nu_2}^\dagger a_{\kappa_2} a_{\kappa_1} \quad (3.26)$$

we obtain the following expression for the energy correction:

$$E_0^{(2)}(H_{int}^{(2)}) = \frac{1}{64} \sum_{hh'}^{<\varepsilon_F} \sum_{pp'}^{>\varepsilon_F} \sum_{\substack{\nu_1 \nu_2 \\ \kappa_1 \kappa_2}} \frac{|\langle \nu_1 \nu_2 | H_{int}^{(2)} | \kappa_1 \kappa_2 \rangle \langle HF | a_{\nu_1}^\dagger a_{\nu_2}^\dagger a_{\kappa_2} a_{\kappa_1} a_p^\dagger a_{p'}^\dagger a_{h'} a_h | HF \rangle|^2}{\varepsilon_h + \varepsilon_{h'} - \varepsilon_p - \varepsilon_{p'}}. \quad (3.27)$$

Since the HF ground-state is given by a Slater determinant, the numerator can be evaluated to

$$\begin{aligned} & \sum_{\substack{\nu_1 \nu_2 \\ \kappa_1 \kappa_2}} \langle \nu_1 \nu_2 | H_{int}^{(2)} | \kappa_1 \kappa_2 \rangle \langle HF | a_{\nu_1}^\dagger a_{\nu_2}^\dagger a_{\kappa_2} a_{\kappa_1} a_p^\dagger a_{p'}^\dagger a_{h'} a_h | HF \rangle \\ &= \sum_{\substack{\nu_1 \nu_2 \\ \kappa_1 \kappa_2}} \langle \nu_1 \nu_2 | H_{int}^{(2)} | \kappa_1 \kappa_2 \rangle \{ \delta_{\nu_1 h} \delta_{\nu_2 h'} \delta_{\kappa_2 p'} \delta_{\kappa_1 p} - \delta_{\nu_1 h'} \delta_{\nu_2 h} \delta_{\kappa_2 p'} \delta_{\kappa_1 p} \\ & \quad - \delta_{\nu_1 h} \delta_{\nu_2 h'} \delta_{\kappa_2 p} \delta_{\kappa_1 p'} + \delta_{\nu_1 h'} \delta_{\nu_2 h} \delta_{\kappa_2 p} \delta_{\kappa_1 p'} \} \\ &= \langle hh' | H_{int}^{(2)} | pp' \rangle - \langle h'h | H_{int}^{(2)} | pp' \rangle \\ & \quad - \langle hh' | H_{int}^{(2)} | p'p \rangle + \langle h'h | H_{int}^{(2)} | p'p \rangle. \end{aligned} \quad (3.28)$$

Inserting this relation, the final expression for the second order energy correction emerging from the two-body part of the Hamiltonian is obtained [13]:

$$E_0^{(2)}(H_{\text{int}}^{(2)}) = \frac{1}{4} \sum_{hh'}^{<\varepsilon_F} \sum_{pp'}^{>\varepsilon_F} \frac{|\langle hh' | H_{\text{int}}^{(2)} | pp' \rangle|^2}{\varepsilon_h + \varepsilon_{h'} - \varepsilon_p - \varepsilon_{p'}}. \quad (3.29)$$

Energy Correction for V_{3N}

For the second-order energy correction emerging from the three-body interaction, we have to consider 2p2h as well as 3p3h excitations of the HF ground-state:

$$E_0^{(2)}(V_{3N}) = \frac{1}{4} \sum_{hh'}^{<\varepsilon_F} \sum_{pp'}^{>\varepsilon_F} \frac{|\langle \text{HF} | V_{3N} | \text{HF}_{hh'}^{pp'} \rangle|^2}{E_{\text{HF}} - E_{\text{HF}_{hh'}^{pp'}}} + \frac{1}{36} \sum_{hh'h''}^{<\varepsilon_F} \sum_{pp'p''}^{>\varepsilon_F} \frac{|\langle \text{HF} | V_{3N} | \text{HF}_{hh'h''}^{pp'p''} \rangle|^2}{E_{\text{HF}} - E_{\text{HF}_{hh'h''}^{pp'p''}}}. \quad (3.30)$$

In analogy to the 2p2h excitations, the 3p3h excitations of the HF state are expressed as

$$|\text{HF}_{hh'h''}^{pp'p''}\rangle = a_p^\dagger a_{p'}^\dagger a_{p''}^\dagger a_{h''} a_{h'} a_h |\text{HF}\rangle, \quad (3.31)$$

and the three-body interaction is written in second quantization

$$V_{3N} = \frac{1}{36} \sum_{\substack{\nu_1 \nu_2 \nu_3 \\ \kappa_1 \kappa_2 \kappa_3}} \langle \nu_1 \nu_2 \nu_3 | V_{3N} | \kappa_1 \kappa_2 \kappa_3 \rangle a_{\nu_1}^\dagger a_{\nu_2}^\dagger a_{\nu_3}^\dagger a_{\kappa_3} a_{\kappa_2} a_{\kappa_1}. \quad (3.32)$$

Performing the analogous steps as discussed in the previous passage, the energy correction can be reformulated to

$$E_0^{(2)}(V_{3N}) = \frac{1}{4} \sum_{hh'}^{<\varepsilon_F} \sum_{pp'}^{>\varepsilon_F} \frac{\left| \sum_{\bar{h}}^{<\varepsilon_F} \langle hh'\bar{h} | V_{3N} | pp'\bar{h} \rangle \right|^2}{\varepsilon_h + \varepsilon_{h'} - \varepsilon_p - \varepsilon_{p'}} + \frac{1}{36} \sum_{hh'h''}^{<\varepsilon_F} \sum_{pp'p''}^{>\varepsilon_F} \frac{|\langle hh'h'' | V_{3N} | pp'p'' \rangle|^2}{\varepsilon_h + \varepsilon_{h'} + \varepsilon_{h''} - \varepsilon_p - \varepsilon_{p'} - \varepsilon_{p''}}. \quad (3.33)$$

Combining Eqs. (3.29) and (3.33) the final expression for the full second order energy correction is obtained [19, 27]:

$$\begin{aligned}
E_0^{(2)} = & \frac{1}{4} \sum_{hh'}^{\leq \varepsilon_F} \sum_{pp'}^{\geq \varepsilon_F} \frac{\left| \langle hh' | H_{\text{int}}^{(2)} | pp' \rangle + \sum_{\bar{h}}^{\leq \varepsilon_F} \langle hh'\bar{h} | V_{3N} | pp'\bar{h} \rangle \right|^2}{\varepsilon_h + \varepsilon_{h'} - \varepsilon_p - \varepsilon_{p'}} \\
& + \frac{1}{36} \sum_{hh'h''}^{\leq \varepsilon_F} \sum_{pp'p''}^{\geq \varepsilon_F} \frac{|\langle hh'h'' | V_{3N} | pp'p'' \rangle|^2}{\varepsilon_h + \varepsilon_{h'} + \varepsilon_{h''} - \varepsilon_p - \varepsilon_{p'} - \varepsilon_{p''}}.
\end{aligned} \tag{3.34}$$

First of all, it is obvious that this expression reduces to the energy correction for a pure two-body Hamiltonian (Eq. (3.29)) if all three-body matrix elements are set to zero.

The additional computational effort of calculating the second-order energy correction in many-body perturbation theory including a three-body interaction compared to the effort using a pure two-body interaction can be roughly estimated by having a closer look at Equation (3.34). There is one additional sum over three-body matrix elements in the term for the 2p2h excitations. As this sum only runs over occupied states with respect to the HF ground-state, the required computing time will be moderate under the assumption that the three-body matrix elements are calculated beforehand, in analogy to the handling of the two-body matrix elements. But for the 3p3h term there are in addition to the three sums over occupied states also three sums over unoccupied states which make the computation very time-consuming.

3.5 Second-Order Energy Corrections

In this section we will investigate the perturbative energy corrections for the Hartree-Fock results obtained with the pure two-body interactions discussed in Section 3.2. We will consider the same set of closed-shell nuclei with the same oscillator lengths.

We consider only the second order energy correction of many-body perturbation theory as the calculation of higher orders would become too time-consuming when including a three-body interaction. For the UCOM interaction using variationally optimized correlators it was shown for some light nuclei that the third order MBPT corrections are small [13]. However, one has to be careful with the interpretation of the second order MBPT corrections as they provide only an estimate of the influence of long-range correlations as the convergence of higher orders is not guaranteed [36].

As mentioned in Section 3.3 some properties of the HF solutions, revealed in the single-particle spectra, might lead to problems when calculating the second-order en-

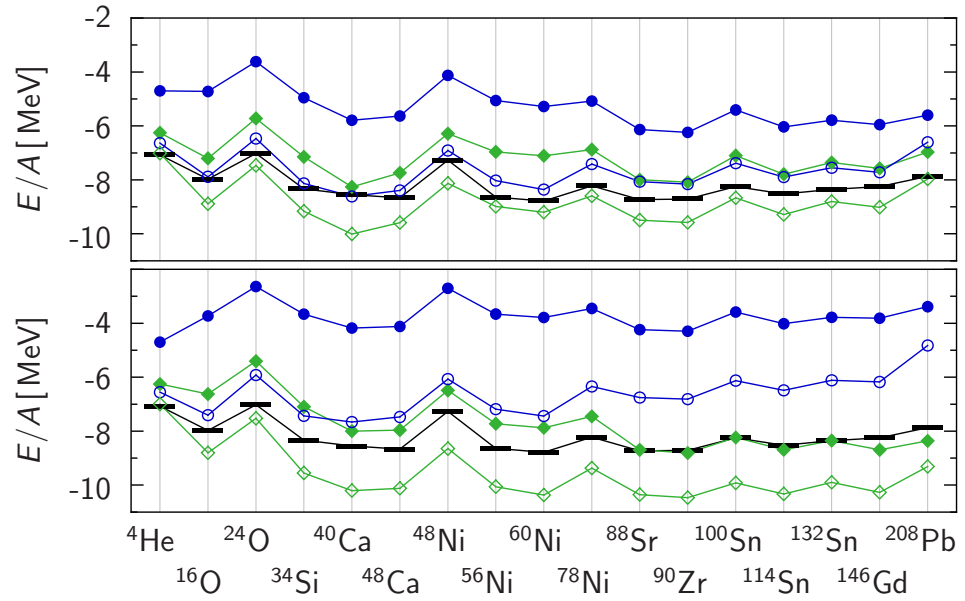


Figure 3.9: Ground-state energies per nucleon based on the UCOM(SRG) interaction (upper panel) and the S-UCOM(SRG) interaction (lower panel) resulting from HF+MBPT calculations for $e_{\text{max}} = 10$ and different flow parameters: (\bullet, \circ) $\alpha = 0.04 \text{ fm}^4$, (\blacklozenge, \diamond) $\alpha = 0.16 \text{ fm}^4$. Filled symbols indicate the HF energies, open symbols include the MBPT corrections. The bars indicate the experimental values [30].

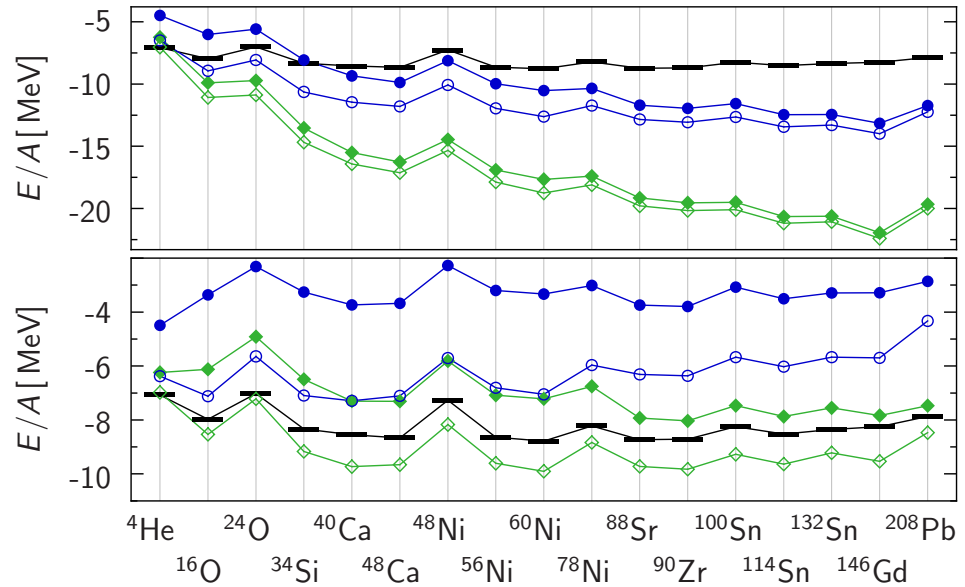


Figure 3.10: Same as in Figure 3.9 for the SRG and the S-SRG interactions with $e_{\text{max}} = 10$ and (\bullet, \circ) $\alpha = 0.03 \text{ fm}^4$, (\blacklozenge, \diamond) $\alpha = 0.10 \text{ fm}^4$.

ergy correction. Especially a collapse of the Fermi gap and interchanged particle and hole states can cause divergent terms because the energy denominator becomes very small (Eq. (3.29)). In order to identify and eliminate these divergent terms we introduce a cut-off κ_R , which is defined via the square of the first-order correction to the states, and is growing linearly with the particle number:

$$\left(\frac{\langle hh' | H_{\text{int}}^{(2)} | pp' \rangle}{\varepsilon_h + \varepsilon_{h'} - \varepsilon_p - \varepsilon_{p'}} \right)^2 \leq A \kappa_R . \quad (3.35)$$

This cut-off is used to check each single term contributing to the energy correction. The cut-off is set to $\kappa_R = 0.0001$ for all calculations. The perturbative energy corrections are computed with and without cut-off simultaneously. Thus, by comparing the results one can easily identify the nuclei, for which divergent terms occur. Fortunately, these are only individual cases. Throughout all calculations, divergent terms in the second-order energy correction were only observed for some nuclei calculated with the UCOM(SRG) interaction, also when including the three-body contact interaction. In the following figures the perturbative corrections obtained with the cut-off are shown. One has to be careful with the interpretation of the results anyway, because we have no information about the behavior of higher orders, and especially for the UCOM(SRG) interaction.

Figure 3.9 shows the HF ground-state energies together with the second-order MBPT energies for the UCOM(SRG) interaction in the upper panel and for the S-UCOM(SRG) interaction in the lower panel for different values of the flow parameter. The corresponding results for the SRG and the S-SRG interactions are displayed in the upper and lower panel of Figure 3.10, respectively. These calculations were performed using 11 major oscillator shells, which does not yield fully converged MBPT corrections as we will discuss below.

In all four cases one can observe that the second-order energy correction decreases with increasing flow parameter. This can be understood intuitively: For larger flow parameters correlations of longer range are already included on the HF level, entailing a lowering of the ground-state energy, and reducing the remaining difference to experimental data that has to be covered by MBPT.

For the UCOM(SRG) interaction systematics of the experimental ground-state energies is nicely reproduced for the light nuclei with the small value of the flow parameter, while the heavier isotopes are still slightly underbound, as seen in Figure 3.9. But one has to keep in mind, that these energies are not yet converged. Increasing the basis size will entail a further lowering of the ground-state energies. For the larger flow parameter almost all nuclei are overbound already in this small model space. In case

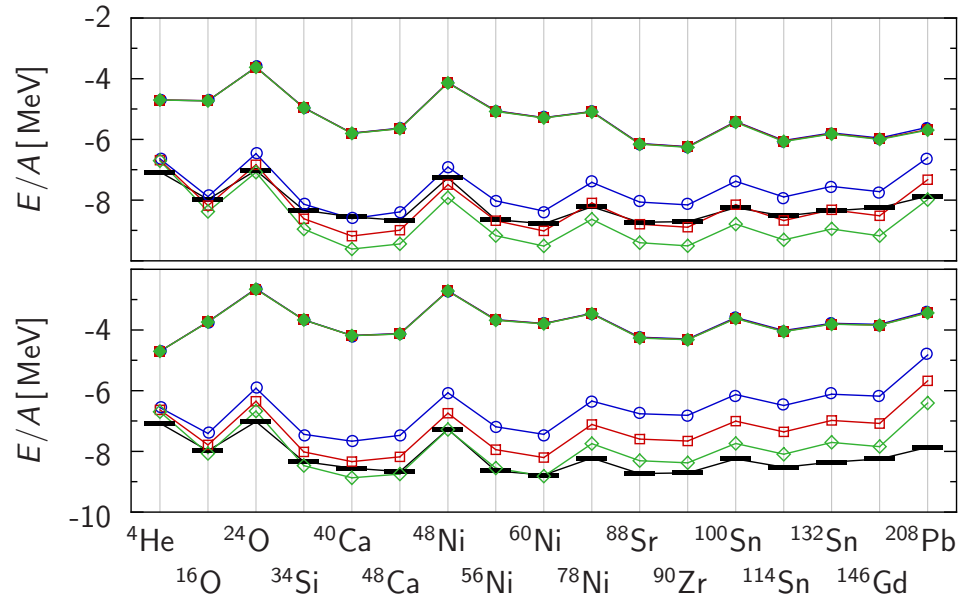


Figure 3.11: Ground-state energies per nucleon based on the UCOM(SRG) interaction (upper panel) and the S-UCOM(SRG) interaction (lower panel) resulting from HF+MBPT calculations for $\alpha = 0.04 \text{ fm}^4$ and different model space sizes: (\bullet, \circ) $e_{\max} = 10$; (\blacksquare, \square) $e_{\max} = 12$, $l_{\max} = 10$; (\blacklozenge, \lozenge) $e_{\max} = 14$, $l_{\max} = 10$. Filled symbols indicate the HF energies, open symbols include the MBPT corrections. The bars indicate the experimental values [30].

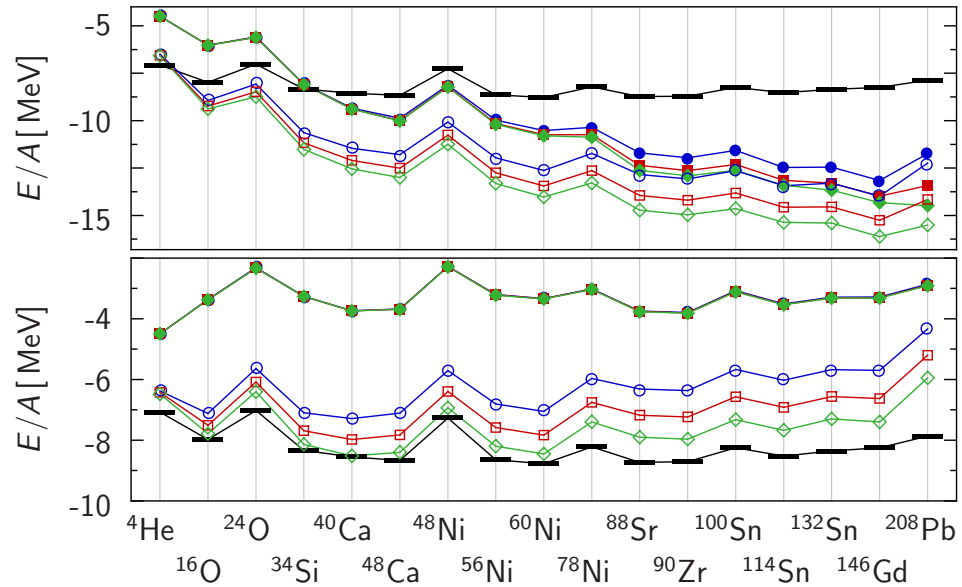


Figure 3.12: Same as in Figure 3.11 for the SRG and the S-SRG interactions with $\alpha = 0.03 \text{ fm}^4$ and (\bullet, \circ) $e_{\max} = 10$; (\blacksquare, \square) $e_{\max} = 12$, $l_{\max} = 10$; (\blacklozenge, \lozenge) $e_{\max} = 14$, $l_{\max} = 10$.

of the S-UCOM(SRG) and the S-SRG interaction the nuclei are still underbound when using the small flow parameter and overbound for the larger flow parameter (Figs. 3.9 and 3.10). The energies calculated with the SRG interaction are significantly too low already on the HF level, the second-order MBPT corrections cannot improve this trend (Fig. 3.10).

Finally, we investigate the dependence of the second-order MBPT energy corrections on the basis size e_{\max} . Therefore, we consider three model spaces, the smallest with $e_{\max} = 10$, the second with $e_{\max} = 12$ with an additional truncation of the orbital angular momentum at $l_{\max} = 10$, and the largest considered model space is $e_{\max} = 14$, $l_{\max} = 10$.

Figure 3.11 shows the ground-state energies calculated with the UCOM(SRG) and S-UCOM(SRG) interactions in the upper and lower part, respectively, using the flow parameter $\alpha = 0.04 \text{ fm}^4$ and the basis sizes mentioned above. The HF energies are fully converged while the perturbative corrections are not yet converged, even for the largest model space. In case of the UCOM(SRG) interaction the lowering of the ground-state energies with increasing model space leads to a slight overbinding for most nuclei. For the S-UCOM(SRG) interaction a reasonable agreement with experimental data is achieved for the largest basis size, where one has to keep in mind that these energies are not yet converged.

The ground-state energies obtained with the SRG and S-SRG interactions are shown in Figure 3.12 using the flow parameter $\alpha = 0.03 \text{ fm}^4$. For the SRG interaction even the HF energies of the heaviest nuclei are not converged. Hence, the perturbative corrections are not converged either. The results of the S-SRG interaction exhibit an agreement with experiment which is comparable to those of the S-UCOM(SRG) interaction keeping in mind the same limitations.

Regarding the UCOM(SRG), S-UCOM(SRG) and S-SRG interactions it is possible to achieve reasonable agreement with experimental data when calculating the ground-state energies in the HF approximation and adding the second-order perturbative corrections. The charge radii have not been considered in this section as it was shown that the influence of many-body perturbation theory on charge radii is only marginal [13]. Hence, to improve the description of charge radii we have to include a repulsive three-body interaction in our calculations. We will then exploit the fact that the considered nuclei are overbound on the basis of HF plus MBPT for larger values of the flow parameter as a repulsive three-body interaction will counteract this trend.

Chapter 3 · Many-Body Calculations

Chapter 4

Gaussian Three-Body Interaction

In Chapter 3 we have discussed some properties of pure two-body interactions. The investigation of ground-state energies and charge radii on the basis of HF plus MBPT calculations has revealed that a three-body interaction is necessary for a quantitative description of nuclear properties. We, therefore, introduce a finite-range three-body interaction of Gaussian shape. First, the matrix elements of the Gaussian three-body interaction are calculated in Section 4.1 and are then included in the HF approximation (Sec. 4.2) and in many-body perturbation theory (Sec. 4.3).

4.1 Calculation of Matrix Elements

A Gaussian three-body interaction is a simple interaction of finite range, which can be written as

$$V_{3N}^G = C_{3N}^G \exp\left\{-\frac{1}{a_{3N}^2}\{(\mathbf{r}_1 - \mathbf{r}_2)^2 + (\mathbf{r}_2 - \mathbf{r}_3)^2 + (\mathbf{r}_3 - \mathbf{r}_1)^2\}\right\} \quad (4.1)$$

with variable strength C_{3N}^G and range a_{3N} .

The matrix elements are calculated in the harmonic-oscillator basis. In coordinate space representation the matrix elements can be evaluated in spherical or cartesian coordinates. Using spherical coordinates, it is convenient to calculate the matrix elements in relative states. Since for various many-body methods the matrix elements need to be calculated with respect to single-particle states a double Talmi-Moshinsky transformation [37, 38], which is numerically costly, has to be applied. When calculating

the matrix elements in cartesian coordinates one has to perform a transformation into the spherical single-particle quantum numbers, which is time-consuming, too. Since the latter option is computationally less costly, we evaluate the three-body matrix elements in cartesian single-particle coordinates and apply a transformation into spherical coordinates subsequently.

4.1.1 Cartesian Matrix Elements

To evaluate the three-body matrix elements in the eigenbasis of the cartesian harmonic oscillator, we start by considering three-body product states and perform the antisymmetrization at the end. With the cartesian harmonic-oscillator quantum numbers n_x , n_y and n_z the matrix elements read in coordinate representation:

$$\begin{aligned}
 & \langle n_{x_1} n_{y_1} n_{z_1}, n_{x_2} n_{y_2} n_{z_2}, n_{x_3} n_{y_3} n_{z_3} | V_{3N}^G | n'_{x_1} n'_{y_1} n'_{z_1}, n'_{x_2} n'_{y_2} n'_{z_2}, n'_{x_3} n'_{y_3} n'_{z_3} \rangle \\
 &= \int d^3 r_1 d^3 r_2 d^3 r_3 \Phi_{n_{x_1} n_{y_1} n_{z_1}}^*(\mathbf{r}_1) \Phi_{n_{x_2} n_{y_2} n_{z_2}}^*(\mathbf{r}_2) \Phi_{n_{x_3} n_{y_3} n_{z_3}}^*(\mathbf{r}_3) \\
 & \quad \times C_{3N}^G \exp \left\{ -\frac{1}{a_{3N}^2} \{ (\mathbf{r}_1 - \mathbf{r}_2)^2 + (\mathbf{r}_2 - \mathbf{r}_3)^2 + (\mathbf{r}_3 - \mathbf{r}_1)^2 \} \right\} \\
 & \quad \times \Phi_{n'_{x_1} n'_{y_1} n'_{z_1}}(\mathbf{r}_1) \Phi_{n'_{x_2} n'_{y_2} n'_{z_2}}(\mathbf{r}_2) \Phi_{n'_{x_3} n'_{y_3} n'_{z_3}}(\mathbf{r}_3) .
 \end{aligned} \tag{4.2}$$

The coordinate representation of the eigenstates of the harmonic oscillator $\Phi_{n_x n_y n_z}(\mathbf{r})$ can be written as a product of three independent functions:

$$\Phi_{n_x n_y n_z}(\mathbf{r}) = \varphi_{n_x}(x) \varphi_{n_y}(y) \varphi_{n_z}(z) , \tag{4.3}$$

where the one-dimensional wave function is given by

$$\varphi_{n_x}(x) = N_{n_x} H_{n_x} \left(\frac{x}{a_{\text{HO}}} \right) \exp \left\{ -\frac{x^2}{2a_{\text{HO}}^2} \right\} \tag{4.4}$$

with the oscillator length a_{HO} , the normalization factor $N_{n_x} = (\sqrt{\pi} a_{\text{HO}} 2^{n_x} n_x!)^{-1/2}$, and the Hermite polynomials $H_{n_x}(x)$ [39]. Inserting the harmonic-oscillator wave functions (4.3) into the expression for the matrix element, we can separate the three

cartesian dimensions:

$$\begin{aligned}
& \langle n_{x_1} n_{y_1} n_{z_1}, n_{x_2} n_{y_2} n_{z_2}, n_{x_3} n_{y_3} n_{z_3} | V_{3N}^G | n'_{x_1} n'_{y_1} n'_{z_1}, n'_{x_2} n'_{y_2} n'_{z_2}, n'_{x_3} n'_{y_3} n'_{z_3} \rangle \\
&= C_{3N}^G \int dx_1 dx_2 dx_3 \varphi_{n_{x_1}}(x_1) \varphi_{n_{x_2}}(x_2) \varphi_{n_{x_3}}(x_3) \varphi_{n'_{x_1}}(x_1) \varphi_{n'_{x_2}}(x_2) \varphi_{n'_{x_3}}(x_3) \\
&\quad \times \exp \left\{ -\frac{1}{a_{3N}^2} \{ (x_1 - x_2)^2 + (x_2 - x_3)^2 + (x_3 - x_1)^2 \} \right\} \\
&\quad \times \int dy_1 dy_2 dy_3 \varphi_{n_{y_1}}(y_1) \varphi_{n_{y_2}}(y_2) \varphi_{n_{y_3}}(y_3) \varphi_{n'_{y_1}}(y_1) \varphi_{n'_{y_2}}(y_2) \varphi_{n'_{y_3}}(y_3) \\
&\quad \times \exp \left\{ -\frac{1}{a_{3N}^2} \{ (y_1 - y_2)^2 + (y_2 - y_3)^2 + (y_3 - y_1)^2 \} \right\} \\
&\quad \times \int dz_1 dz_2 dz_3 \varphi_{n_{z_1}}(z_1) \varphi_{n_{z_2}}(z_2) \varphi_{n_{z_3}}(z_3) \varphi_{n'_{z_1}}(z_1) \varphi_{n'_{z_2}}(z_2) \varphi_{n'_{z_3}}(z_3) \\
&\quad \times \exp \left\{ -\frac{1}{a_{3N}^2} \{ (z_1 - z_2)^2 + (z_2 - z_3)^2 + (z_3 - z_1)^2 \} \right\} \\
&\equiv C_{3N}^G I_{\{n_x\}}(x_1, x_2, x_3) I_{\{n_y\}}(y_1, y_2, y_3) I_{\{n_z\}}(z_1, z_2, z_3). \tag{4.5}
\end{aligned}$$

Hence, the matrix element is split into a product of three equivalent integrals. For the further discussion we consider the integral $I_{\{n_x\}}(x_1, x_2, x_3)$. By inserting the one-dimensional wave functions (4.4) we can reformulate the integral:

$$\begin{aligned}
& I_{\{n_x\}}(x_1, x_2, x_3) \\
&= N \int dx_1 dx_2 dx_3 H_{n_{x_1}} \left(\frac{x_1}{a_{HO}} \right) H_{n_{x_2}} \left(\frac{x_2}{a_{HO}} \right) H_{n_{x_3}} \left(\frac{x_3}{a_{HO}} \right) \\
&\quad \times H_{n'_{x_1}} \left(\frac{x_1}{a_{HO}} \right) H_{n'_{x_2}} \left(\frac{x_2}{a_{HO}} \right) H_{n'_{x_3}} \left(\frac{x_3}{a_{HO}} \right) \exp \left\{ -\frac{1}{a_{HO}^2} (x_1^2 + x_2^2 + x_3^2) \right\} \\
&\quad \times \exp \left\{ -\frac{1}{a_{3N}^2} \{ (x_1 - x_2)^2 + (x_2 - x_3)^2 + (x_3 - x_1)^2 \} \right\} \\
&= N \int dx_1 H_{n_{x_1}} \left(\frac{x_1}{a_{HO}} \right) H_{n'_{x_1}} \left(\frac{x_1}{a_{HO}} \right) \exp \left\{ -\left(\frac{1}{a_{HO}^2} + \frac{2}{a_{3N}^2} \right) x_1^2 \right\} \\
&\quad \times \int dx_2 H_{n_{x_2}} \left(\frac{x_2}{a_{HO}} \right) H_{n'_{x_2}} \left(\frac{x_2}{a_{HO}} \right) \exp \left\{ -\left(\frac{1}{a_{HO}^2} + \frac{2}{a_{3N}^2} \right) x_2^2 + \frac{2x_1}{a_{3N}^2} x_2 \right\} \\
&\quad \times \int dx_3 H_{n_{x_3}} \left(\frac{x_3}{a_{HO}} \right) H_{n'_{x_3}} \left(\frac{x_3}{a_{HO}} \right) \exp \left\{ -\left(\frac{1}{a_{HO}^2} + \frac{2}{a_{3N}^2} \right) x_3^2 + \frac{2(x_1 + x_2)}{a_{3N}^2} x_3 \right\}
\end{aligned}$$

with the normalization factor $N = N_{n_{x_1}} N_{n_{x_2}} N_{n_{x_3}} N_{n'_{x_1}} N_{n'_{x_2}} N_{n'_{x_3}}$. We are not able to provide an analytic solution for these integrals in a closed expression. Therefore, we calculate them numerically and ensure the agreement with analytical values for some

chosen sets of quantum numbers. The numerical calculation of a three-dimensional integral is rather elaborate. Fortunately, these integrals can be computed by performing three one-dimensional integrations. We start with the innermost integral and consider $(x_1 + x_2)$ as a parameter, i.e. we solve the integral for a set of values for this parameter. The result is inserted in the next integral, where we take x_1 as parameter and follow the same procedure. Finally, by using these results we can solve the outermost integral.

The numerical integration is performed via the application of the trapezoidal rule. The program Mathematica [40] is capable of providing an exact solution of the three-dimensional integral $I_{\{n_x\}}(x_1, x_2, x_3)$ if the quantum numbers are sufficiently small. We are thus able to guarantee a sufficient accuracy of the numerical calculation.

For applications in many-body methods we have to perform a transformation of these matrix elements from the cartesian harmonic oscillator into the spherical one.

4.1.2 Coordinate Transformation

In order to convert the three-body matrix elements the single-particle states of the cartesian harmonic oscillator have to be transformed into spherical ones:

$$|nlm_l\rangle = \sum_{n_x n_y n_z} |n_x n_y n_z\rangle \langle n_x n_y n_z | nlm_l\rangle, \quad (4.6)$$

where the eigenstates of the spherical harmonic oscillator are defined via the principal quantum number n and angular momentum l with projection m_l . The transformation coefficients $\langle n_x n_y n_z | nlm_l\rangle$ can be determined using the generating functions of the harmonic oscillator wave functions [41]. The generating function of the three-dimensional cartesian harmonic oscillator reads

$$\begin{aligned} F(x, y, z; x_0, y_0, z_0) &= \sum_{n_x=0}^{\infty} \sum_{n_y=0}^{\infty} \sum_{n_z=0}^{\infty} \frac{1}{n_x! n_y! n_z!} \exp\left\{-\frac{x^2 + y^2 + z^2}{2a_{\text{HO}}^2}\right\} \\ &\times H_{n_x}\left(\frac{x}{a_{\text{HO}}}\right) H_{n_y}\left(\frac{y}{a_{\text{HO}}}\right) H_{n_z}\left(\frac{z}{a_{\text{HO}}}\right) \left(\frac{x_0}{a_{\text{HO}}}\right)^{n_x} \left(\frac{y_0}{a_{\text{HO}}}\right)^{n_y} \left(\frac{z_0}{a_{\text{HO}}}\right)^{n_z}. \end{aligned} \quad (4.7)$$

The eigenfunctions of the cartesian harmonic oscillator can be obtained by deriving the generating function with respect to x_0 , y_0 , and z_0 and evaluating the derivation at $x_0 = y_0 = z_0 = 0$. The generating function for the spherical harmonic oscillator is

given by

$$\begin{aligned}
& F(r, \vartheta, \varphi; r_0, \vartheta_0, \varphi_0) \\
&= \sum_{n=0}^{\infty} \sum_{l=0}^{\infty} \sum_{m_l=-l}^l \frac{2\pi^{3/2}(-1)^n}{\Gamma(n+l+\frac{3}{2})} \exp\left\{-\frac{r^2}{2a_{\text{HO}}^2}\right\} \left(\frac{r}{a_{\text{HO}}}\right)^l \\
&\quad \times L_n^{[l+\frac{1}{2}]} \left(\frac{r^2}{a_{\text{HO}}^2}\right) Y_{lm_l}(\vartheta, \varphi) Y_{lm_l}^*(\vartheta_0, \varphi_0) \left(\frac{r_0}{a_{\text{HO}}}\right)^{2n+l}. \quad (4.8)
\end{aligned}$$

The coordinate representation of the eigenfunctions of the spherical harmonic oscillator can again be obtained out of the derivatives of the corresponding generating function with respect to r_0 , ϑ_0 , and φ_0 and reads

$$\psi_{nlm_l}(r, \vartheta, \varphi) = N_{nl} \exp\left\{-\frac{r^2}{2a_{\text{HO}}^2}\right\} \left(\frac{r}{a_{\text{HO}}}\right)^l L_n^{[l+\frac{1}{2}]} \left(\frac{r^2}{a_{\text{HO}}^2}\right) Y_{lm_l}(\vartheta, \varphi) \quad (4.9)$$

with the normalization factor $N_{nl} = \sqrt{\frac{2n!}{a_{\text{HO}}^3 \Gamma(n+l+\frac{3}{2})}}$, the Laguerre polynomials $L_n^{[l+\frac{1}{2}]} \left(\frac{r^2}{a_{\text{HO}}^2}\right)$, and the spherical harmonics $Y_{lm_l}(\vartheta, \varphi)$.

Identifying these eigenfunctions in Equation (4.8) as well as the eigenfunctions (4.4) of the cartesian harmonic oscillator in Equation (4.7), we find the following relation:

$$\begin{aligned}
& \sum_{n_x=0}^{\infty} \sum_{n_y=0}^{\infty} \sum_{n_z=0}^{\infty} \frac{1}{n_x! n_y! n_z! N_{n_x} N_{n_y} N_{n_z}} |n_x n_y n_z\rangle x_0^{n_x} y_0^{n_y} z_0^{n_z} \\
&= \sum_{n=0}^{\infty} \sum_{l=0}^{\infty} \sum_{m_l=-l}^l \frac{2\pi^{3/2}(-1)^n}{\Gamma(n+l+\frac{3}{2}) N_{nl}} |nlm_l\rangle Y_{lm_l}^*(\vartheta_0, \varphi_0) r_0^{2n+l}, \quad (4.10)
\end{aligned}$$

where we use the ket representation of the wave functions as we aim at the derivation of the transformation coefficients $\langle n_x n_y n_z | nlm_l \rangle$. For this purpose we have to express the spherical coordinates in cartesian ones. Therefore, we need the binomial formula

$$(x+y)^n = \sum_{k=0}^n \binom{n}{k} x^{n-k} y^k, \quad (4.11)$$

and the spherical harmonics in cartesian coordinates [42]

$$\begin{aligned}
r^l Y_{lm_l}(x, y, z) &= \sqrt{\frac{2l+1}{4\pi}} (l+m_l)!(l-m_l)! \\
&\quad \times \sum_{pqs} \frac{1}{p! q! s!} \left(-\frac{x+iy}{2}\right)^p \left(\frac{x-iy}{2}\right)^q z^s \quad (4.12)
\end{aligned}$$

with $p+q+s = l$ and $p-q = m_l$. These equations can be reformulated to $q = p - m_l$, $s = l + m_l - 2p$, and $p = 0, \dots, l$. Then, Equation (4.12) reads

$$r^l Y_{lm_l}(x, y, z) = \sqrt{\frac{2l+1}{4\pi}} (l+m_l)!(l-m_l)! \times \sum_{p=0}^l (p!(p-m_l)!(l+m_l-2p)!)^{-1} \times \left(-\frac{x+iy}{2}\right)^p \left(\frac{x-iy}{2}\right)^{p-m_l} z^{l+m_l-2p}. \quad (4.13)$$

Using Eqs. (4.13) and (4.11), we can deduce the following relation between spherical and cartesian coordinates

$$Y_{lm_l}^*(\vartheta_0, \varphi_0) r_0^{2n+l} = (-1)^{m_l} r_0^l Y_{l-m_l}(\vartheta_0, \varphi_0) (r_0^2)^n = \sum_{n_x=0}^{\infty} \sum_{n_y=0}^{\infty} \sum_{n_z=0}^{\infty} C_{n_x n_y n_z}^{nlm_l} x_0^{n_x} y_0^{n_y} z_0^{n_z} \quad (4.14)$$

with the transformation constant

$$C_{n_x n_y n_z}^{nlm_l} = \sqrt{\frac{2l+1}{4\pi}} (l+m_l)!(l-m_l)! \times \sum_{a=0}^n \sum_{p=0}^{\lfloor (l-m_l)/2 \rfloor} \sum_{b=0}^p \frac{(-1)^{n-n_x-a-b} i^{m_l-n_x}}{p!(p+m_l)!(l-m_l-2p)! 2^{2p+m_l}} \times \binom{n}{a} \binom{a}{(n_z+2p-l+m_l)/2} \binom{p}{b} \binom{p+m_l}{2n+2p-2a+m_l-n_x-b}. \quad (4.15)$$

By multiplying Equation (4.10) from the left with $\langle n'l'm_l|$ and inserting Equation (4.14) we finally arrive at the transformation coefficients

$$\langle nlm_l|n_x n_y n_z\rangle = \frac{2\pi^{3/2}(-1)^n}{\Gamma(n+l+3/2)N_{nl}} n_x! n_y! n_z! N_{n_x} N_{n_y} N_{n_z} C_{n_x n_y n_z}^{nlm_l}. \quad (4.16)$$

For the computation of each three-body matrix element, six single-particle states have to be transformed, which requires 18 summations involving the coefficients (4.16). This coordinate transformation is the most demanding part regarding computing time during the calculation of the three-body matrix elements.

So far, we have only considered coordinate-space matrix elements, for the full matrix elements we also have to take into account spin and isospin. The Gaussian three-body interaction only acts in coordinate space, i.e. the spin-isospin part of the

matrix element is simply given by Kronecker deltas for the spin and isospin projection quantum numbers m_s and m_t , respectively:

$$\begin{aligned}
& \langle n_1 l_1 m_{l_1} m_{s_1} m_{t_1}, n_2 l_2 m_{l_2} m_{s_2} m_{t_2}, n_3 l_3 m_{l_3} m_{s_3} m_{t_3} | \\
& \quad \times V_{3N}^G | n'_1 l'_1 m'_{l_1} m'_{s_1} m'_{t_1}, n'_2 l'_2 m'_{l_2} m'_{s_2} m'_{t_2}, n'_3 l'_3 m'_{l_3} m'_{s_3} m'_{t_3} \rangle \\
& = \langle n_1 l_1 m_{l_1}, n_2 l_2 m_{l_2}, n_3 l_3 m_{l_3} | V_{3N}^G | n'_1 l'_1 m'_{l_1}, n'_2 l'_2 m'_{l_2}, n'_3 l'_3 m'_{l_3} \rangle \\
& \quad \times \delta_{m_{s_1} m'_{s_1}} \delta_{m_{s_2} m'_{s_2}} \delta_{m_{s_3} m'_{s_3}} \delta_{m_{t_1} m'_{t_1}} \delta_{m_{t_2} m'_{t_2}} \delta_{m_{t_3} m'_{t_3}} .
\end{aligned} \tag{4.17}$$

For brevity, we have omitted the quantum numbers $s = \frac{1}{2}$ and $t = \frac{1}{2}$ for spin and isospin, respectively. In the next step, the single-particle angular momenta l and single-particle spins are coupled to total single-particle angular momenta j with projection quantum numbers m using Clebsch-Gordan coefficients. Finally, the matrix elements have to be antisymmetrized explicitly.

The calculation of the matrix elements is very time-consuming due to the coordinate transformation involving a large number of summations. Thus, it is not feasible to compute the full matrix elements during the many-body calculation. Therefore, the coordinate space matrix elements with respect to the spherical harmonic-oscillator basis are precomputed and stored for each set of oscillator length a_{HO} and three-body range a_{3N} . The inclusion of spin and isospin, the j -coupling and the antisymmetrization are then done on-the-fly during the many-body calculation. Due to the large number of non-vanishing matrix elements, we are restricted to small model spaces. Currently, we are able to handle the three-body matrix elements for a model space including seven major oscillator shells with an additional truncation of the orbital angular momentum at $l_{\max} = 4$.

4.2 Ground-State Energies and Charge Radii

As starting point, the impact of the Gaussian three-body interaction is investigated in the framework of the Hartree-Fock approximation. The parameters of the three-body interaction – the strength C_{3N}^G and the range a_{3N} – have to be determined, and the flow parameter of the respective two-body interaction has to be adjusted accordingly. As we are only able to handle small model spaces, we can only provide an estimate for the strength C_{3N}^G and the range a_{3N} , the choice of the parameters would have to be verified in model spaces sufficiently large to reach convergence.

In the following, we consider a set of closed-shell nuclei from ${}^4\text{He}$ to ${}^{90}\text{Zr}$. The heaviest nuclei included in Chapter 3 are not considered here, since one cannot obtain reliable results in such small model spaces. We use again the oscillator parameters

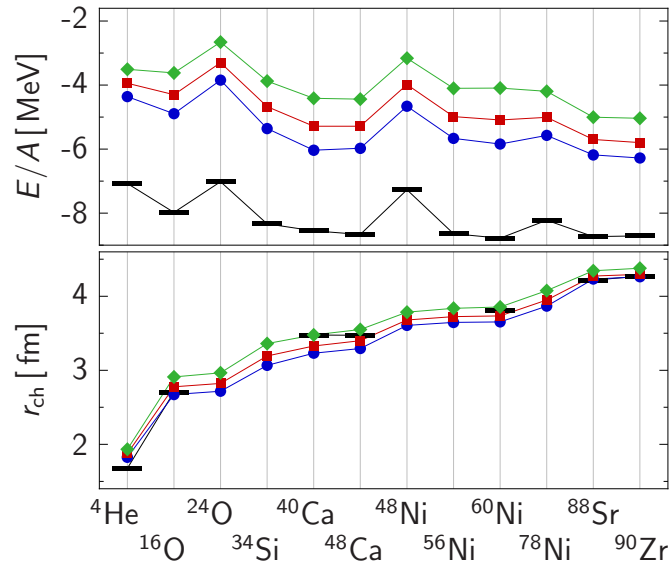


Figure 4.1: Ground-state energies per nucleon and charge radii of selected closed-shell nuclei resulting from HF calculations for the S-UCOM(SRG) interaction for $\alpha = 0.16 \text{ fm}^4$, $e_{\text{max}} = 4$, $C_{3N} = 100 \text{ MeV}$ and different three-body ranges: (●) $a_{3N} = 1.22 \text{ fm}$, (■) $a_{3N} = 1.26 \text{ fm}$, (◆) $a_{3N} = 1.30 \text{ fm}$. The bars indicate the experimental values [30, 31].

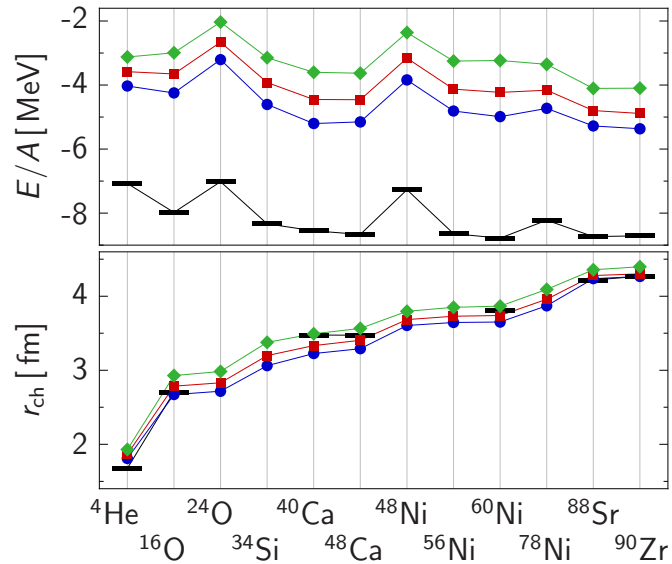


Figure 4.2: Same as in Figure 4.1 for the S-SRG interaction with $\alpha = 0.10 \text{ fm}^4$, $e_{\text{max}} = 4$, $C_{3N} = 100 \text{ MeV}$, and (●) $a_{3N} = 1.22 \text{ fm}$, (■) $a_{3N} = 1.26 \text{ fm}$, (◆) $a_{3N} = 1.30 \text{ fm}$.

4.2 · Ground-State Energies and Charge Radii

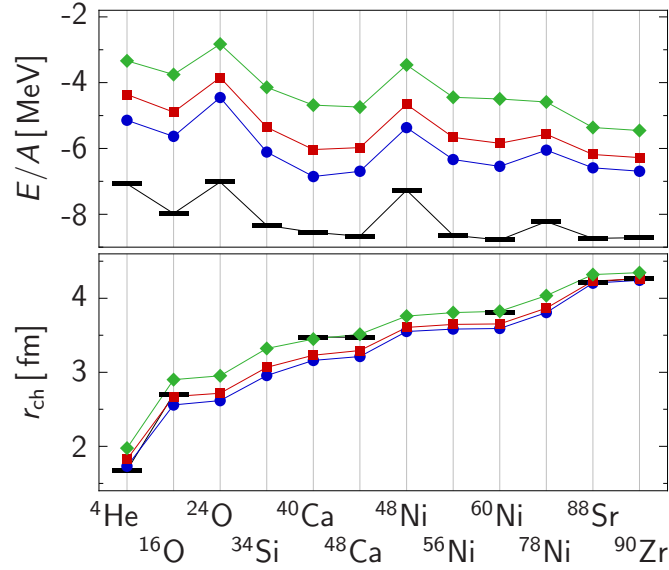


Figure 4.3: Ground-state energies per nucleon and charge radii of selected closed-shell nuclei resulting from HF calculations for the S-UCOM(SRG) interaction for $\alpha = 0.16 \text{ fm}^4$, $e_{\max} = 4$, $a_{3N} = 1.22 \text{ fm}$ and different three-body strengths: (●) $C_{3N} = 50 \text{ MeV}$, (■) $C_{3N} = 100 \text{ MeV}$, (◆) $C_{3N} = 200 \text{ MeV}$. The bars indicate the experimental values [30, 31].

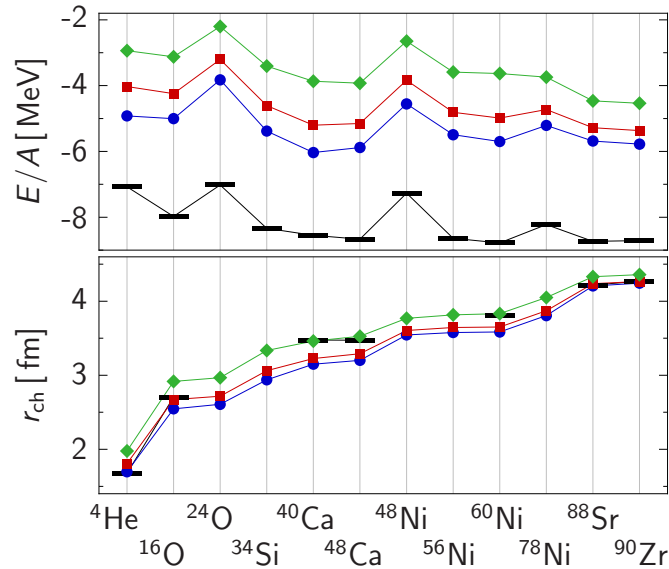


Figure 4.4: Same as in Figure 4.3 for the S-SRG interaction with $\alpha = 0.10 \text{ fm}^4$, $e_{\max} = 4$, $a_{3N} = 1.22 \text{ fm}$, and (●) $C_{3N} = 50 \text{ MeV}$, (■) $C_{3N} = 100 \text{ MeV}$, (◆) $C_{3N} = 200 \text{ MeV}$.

listed in Table 3.2. The following calculations will be performed in a model space with $e_{\max} = 4$. In this chapter we do not consider all four two-body interactions introduced in Chapter 3 but restrict ourselves to S-UCOM(SRG) and S-SRG.

First, the influence of the three-body range a_{3N} is studied. In Figure 4.1 the ground-state energies per nucleon (upper panel) and the charge radii (lower panel) are shown for different values of a_{3N} using the S-UCOM(SRG) interaction with the flow parameter $\alpha = 0.16 \text{ fm}^4$. The systematics of the experimental ground-state energies is reproduced except for an almost constant shift. With increasing three-body range the energies increase as well, for the smallest value $a_{3N} = 1.22 \text{ fm}$ they differ by about 2.5 MeV from experiment and for $a_{3N} = 1.30 \text{ fm}$ by about 3.5 MeV. The charge radii are in reasonable agreement with data. The dependence of the charge radii on the three-body range is weaker than for the ground-state energies. Increasing the range a_{3N} of the three-body interaction shifts apart the nucleons, which results in larger, weaker bound nuclei. However, one cannot find one value for a_{3N} that fits all nuclei perfectly, e.g. for the smallest value, the radii of the intermediate nuclei are slightly underestimated while the light and the heavy ones are in nice agreement with experimental data.

The corresponding results for the S-SRG interaction (Fig. 4.2) using the flow parameter $\alpha = 0.10 \text{ fm}^4$ and the same parameters for the three-body interaction are very similar. In the following, we will use $a_{3N} = 1.22 \text{ fm}$ for both interactions.

In Figures 4.3 and 4.4 the dependence on the three-body strength is shown for the S-UCOM(SRG) and the S-SRG interactions. The influence of the strength is similar to the one of the range. With increasing three-body strength the ground-state energies as well as the charge radii increase. This behavior can be understood intuitively. As the three-body interaction is purely repulsive, increasing the strength leads to weaker bound nuclei with larger charge radii. Again, it is not possible to find one parameter that describes all considered nuclei with the same accuracy. For the following calculations we will use $C_{3N}^G = 100 \text{ MeV}$. Although we refer to the parameter C_{3N}^G as three-body strength, a more accurate measure for the strength of the interaction would be an integral over the three-body interaction, which clearly connects the two parameters a_{3N} and C_{3N}^G with each other.

Next, we investigate the influence of the flow parameter in Figures 4.5 and 4.6. For both interactions the ground-state energies decrease with increasing flow parameter for the same reason as discussed in Section 3.2. In contrast to the results obtained with the pure two-body interactions, the systematics of the experimental data is reproduced by all flow parameters, which is due to the inclusion of a repulsive three-body interaction. The charge radii depend only weakly on the flow parameter. However, using the smallest flow parameters, i.e. $\alpha = 0.04 \text{ fm}^4$ for the S-UCOM(SRG) interaction and

4.2 · Ground-State Energies and Charge Radii

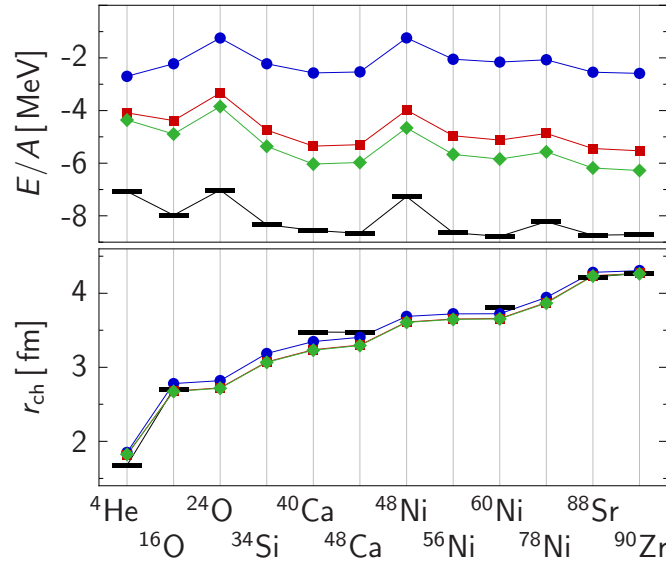


Figure 4.5: Ground-state energies per nucleon and charge radii of selected closed-shell nuclei resulting from HF calculations for the S-UCOM(SRG) interaction for $e_{\max} = 4$, $a_{3N} = 1.22 \text{ fm}$, $C_{3N} = 100 \text{ MeV}$ and different flow parameters: (●) $\alpha = 0.04 \text{ fm}^4$, (■) $\alpha = 0.12 \text{ fm}^4$, (◆) $\alpha = 0.16 \text{ fm}^4$. The bars indicate the experimental values [30, 31].

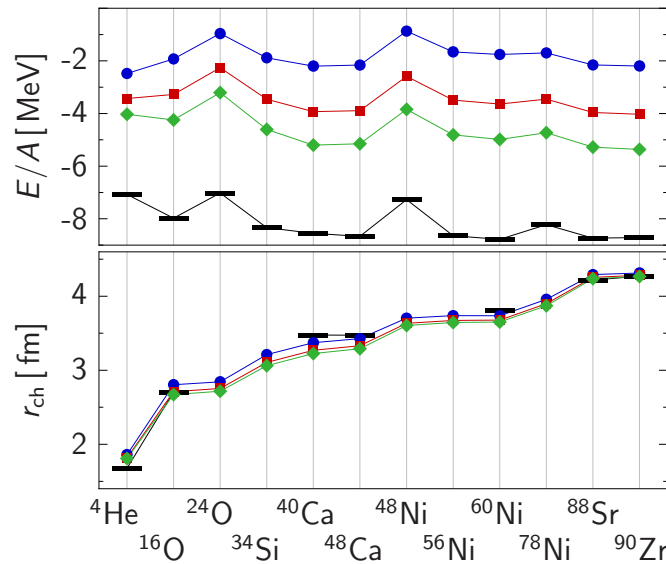


Figure 4.6: Same as in Figure 4.5 for the S-SRG interaction with $e_{\max} = 4$, $a_{3N} = 1.22 \text{ fm}$, $C_{3N} = 100 \text{ MeV}$, and (●) $\alpha = 0.03 \text{ fm}^4$, (■) $\alpha = 0.06 \text{ fm}^4$, (◆) $\alpha = 0.10 \text{ fm}^4$.

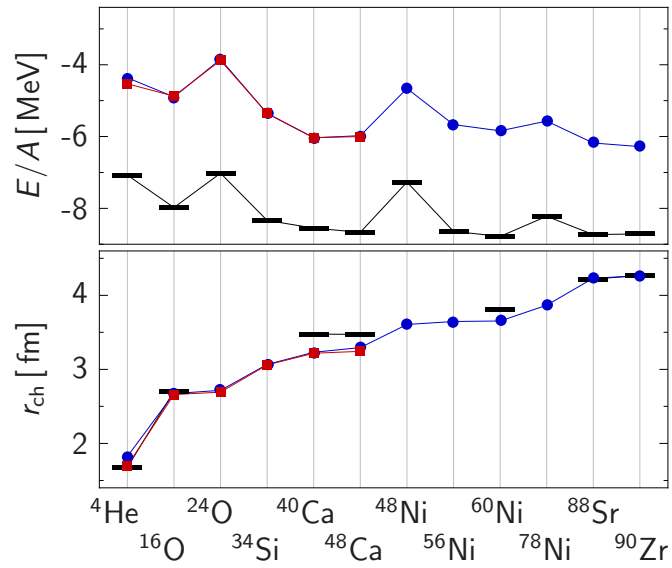


Figure 4.7: Ground-state energies per nucleon and charge radii of selected closed-shell nuclei resulting from HF calculations for the S-UCOM(SRG) interaction for $\alpha = 0.16 \text{ fm}^4$, $a_{3\text{N}} = 1.22 \text{ fm}$, $C_{3\text{N}}^{\text{G}} = 100 \text{ MeV}$ and different basis sizes: (\bullet) $e_{\text{max}} = 4$ (optimal a_{HO}), (\blacksquare) $e_{\text{max}} = 6$, $l_{\text{max}} = 4$ ($a_{\text{HO}} = 1.9 \text{ fm}$). The bars indicate the experimental values [30, 31].

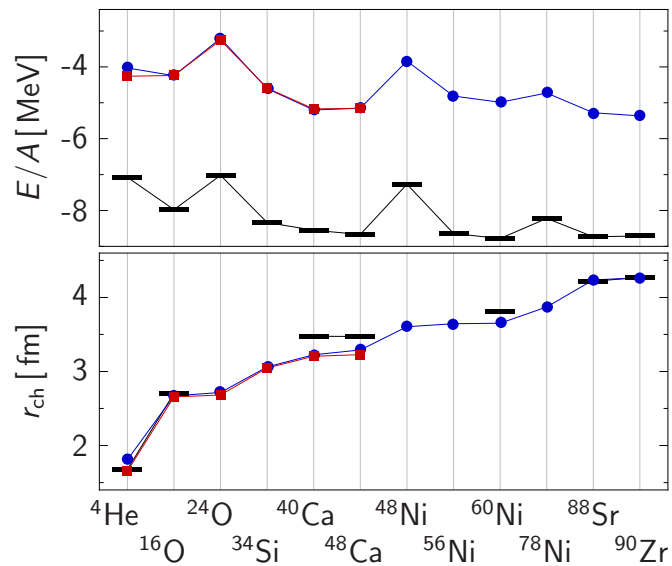


Figure 4.8: Same as in Figure 4.7 for the S-SRG interaction with $\alpha = 0.10 \text{ fm}^4$, $a_{3\text{N}} = 1.22 \text{ fm}$, $C_{3\text{N}}^{\text{G}} = 100 \text{ MeV}$, and (\bullet) $e_{\text{max}} = 4$ (optimal a_{HO}), (\blacksquare) $e_{\text{max}} = 6$, $l_{\text{max}} = 4$ ($a_{\text{HO}} = 1.9 \text{ fm}$).

$\alpha = 0.03 \text{ fm}^4$ for S-SRG, leads to a slightly improved overall description of the charge radii. On the other hand, the ground-state energies calculated with the small flow parameters are significantly larger than those obtained with the larger flow parameters. One can, therefore, choose the flow parameters such that either the ground-state energies are closer to experiment or the charge radii. We prefer a better description of the energies, i.e. we use $\alpha = 0.16 \text{ fm}^4$ for the S-UCOM(SRG) interaction and $\alpha = 0.10 \text{ fm}^4$ for S-SRG, as the effect is rather weak for the charge radii.

Finally, the convergence of the HF results is examined by increasing the model space size. The number of three-body matrix elements can only be stored up to a basis size of $e_{\text{max}} = 6$ with an additional constraint for the orbital angular momentum of $l_{\text{max}} = 4$. The calculation of the matrix elements for this basis size is very time-consuming. As the matrix elements have to be calculated for each oscillator parameter separately, we choose an average oscillator length of $a_{\text{HO}} = 1.9 \text{ fm}$ for all nuclei for the calculation in the larger model space. Consequently, we only have to calculate one set of three-body matrix elements.

The results obtained in this model space are compared to the previous ones with $e_{\text{max}} = 4$ in Figure 4.7 for the S-UCOM(SRG) interaction and in Figure 4.8 for the S-SRG interaction. As we do not expect to obtain reliable results for the heavier nuclei using the oscillator length $a_{\text{HO}} = 1.9 \text{ fm}$, the energies and radii are only shown up to ^{48}Ca . The ground-state energies as well as the charge radii are almost identical in both model spaces suggesting convergence. The small deviations observed for ^4He can be explained by the non-optimal oscillator length. However, one has to keep in mind, that the larger model space only takes into account few additional single-particle states as the largest possible orbital angular momentum is the same as for the small model space, i.e. $l_{\text{max}} = 4$.

4.3 *Perturbative Energy Corrections*

In this section the impact of the second-order energy correction is studied. We only consider the energy corrections emerging from the two-body part of the Hamiltonian (Eq. (3.29)) as the correction emerging from the three-body interaction is marginal at least in such small model spaces: it does not exceed 1.5% for $e_{\text{max}} = 4$. Furthermore, the calculation of the energy correction emerging from the three-body interaction is very time-consuming and is therefore not feasible in larger model spaces. As discussed in Section 3.5 we study the energy corrections obtained with the cut-off $\kappa_R = 0.0001$, although it has almost no effect on the results discussed in this section. Figure 4.9

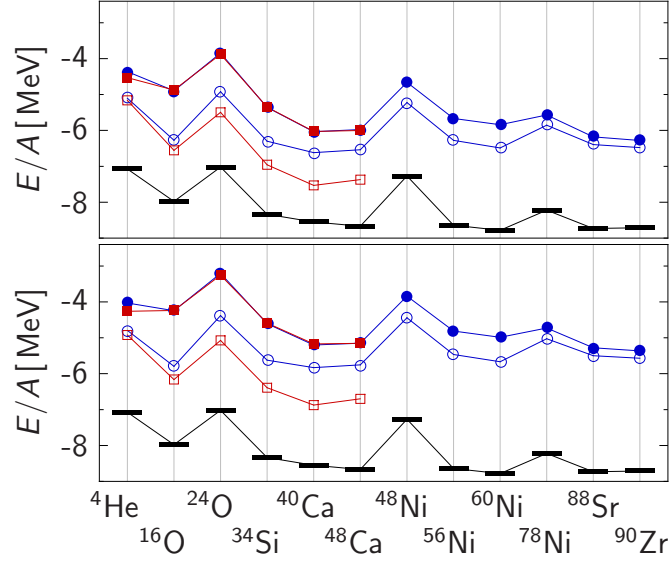


Figure 4.9: Ground-state energies per nucleon based on the S-UCOM(SRG) interaction with $\alpha = 0.16 \text{ fm}^4$ (upper panel) and the S-SRG interaction with $\alpha = 0.10 \text{ fm}^4$ (lower panel) resulting from HF+MBPT calculations for $a_{3N} = 1.22 \text{ fm}$, $C_{3N}^G = 100 \text{ MeV}$, and different model space sizes: (\bullet, \circ) $e_{\text{max}} = 4$ (optimal a_{HO}), (\blacksquare, \square) $e_{\text{max}} = 6$, $l_{\text{max}} = 4$ ($a_{\text{HO}} = 1.9 \text{ fm}$). Filled symbols indicate the HF energies, open symbols include the MBPT corrections. The bars indicate the experimental values [30].

shows the HF ground-state energies as well as the perturbative energy corrections for the S-UCOM(SRG) interaction (upper panel) and the S-SRG interaction (lower panel), where the results obtained with the basis size $e_{\text{max}} = 4$ are compared to those obtained with $e_{\text{max}} = 6$, $l_{\text{max}} = 4$. As already discussed in the previous section, for the calculations in the larger model space only one oscillator parameter was used for all nuclei due to the computational effort of the matrix element calculation. While the difference of the HF energies is only marginal in the two model spaces, the perturbative corrections are significantly larger in the larger model space, especially for intermediate nuclei. On the basis of these results it is impossible to make a statement about the convergence behavior. For this purpose it would be necessary to further increase the model space size.

A more illuminating aspect is revealed by the comparison of the finite-range three-body interaction of Gaussian shape with the regularized contact interaction, which will be introduced in the following chapter. For the contact interaction we use the parameters that are determined in Chapter 5. Note, that the optimal parameters are different for the S-UCOM(SRG) and the S-SRG interaction. In Figures 4.10 and

4.3 · Perturbative Energy Corrections

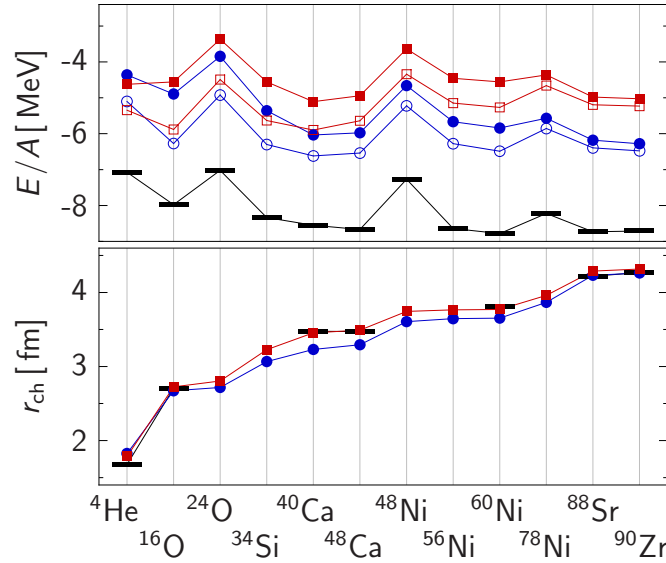


Figure 4.10: Ground-state energies per nucleon and charge radii based on the S-UCOM(SRG) interaction resulting from HF+MBPT calculations for $\alpha = 0.16 \text{ fm}^4$, $e_{\text{max}} = 4$, and comparing the three-body interactions: (\bullet, \circ) Gaussian interaction with $a_{3N} = 1.22 \text{ fm}$, $C_{3N}^G = 100 \text{ MeV}$; (\blacksquare, \square) regularized contact interaction with $C_{3N} = 2200 \text{ MeV fm}^6$, $e_{3N} = 20$. Filled symbols indicate the HF energies, open symbols include the MBPT corrections. The bars indicate the experimental values [30].

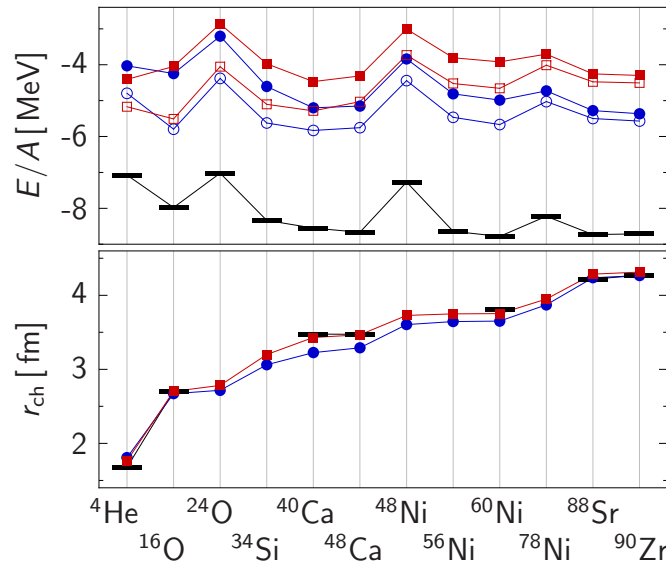


Figure 4.11: Same as in Figure 4.10 for the S-SRG interaction with $\alpha = 0.10 \text{ fm}^4$, $e_{\text{max}} = 4$, and (\bullet, \circ) Gaussian interaction with $a_{3N} = 1.22 \text{ fm}$, $C_{3N}^G = 100 \text{ MeV}$; (\blacksquare, \square) regularized contact interaction with $C_{3N} = 2000 \text{ MeV fm}^6$, $e_{3N} = 20$.

4.11 the HF ground-state energies together with the perturbative corrections emerging from the two-body Hamiltonian and the charge radii are shown for the S-UCOM(SRG) and the S-SRG interactions in a model space including five major oscillator shells. The comparison of the Gaussian three-body interaction with the regularized contact interaction reveals that the latter yields slightly less binding energy for intermediate and heavy nuclei on the HF level. This discrepancy could be reduced by an adjustment of the parameters. The perturbative energy corrections are almost identical for both interactions across the whole nuclear chart, which is not surprising as the corrections are only calculated for the two-body interactions being the same in both cases. The calculated charge radii are similar for both three-body interactions, but the overall agreement with experimental data is slightly better for the contact interaction. The results are very similar for both underlying two-body interactions.

On the basis of these results, we can motivate the following strategy: The Gaussian three-body interaction is the most simple finite-range three-body interaction, but we can only handle it in very small model spaces. The calculation of the matrix elements of the regularized three-body contact interaction is much more efficient and this interaction can also be included in larger model spaces. We have shown that both three-body interactions yield comparable results in small model spaces. We will, therefore, perform further studies on the basis of the regularized contact interaction. As this three-body interaction can be included in various many-body methods and in sufficiently large model spaces, this procedure allows for reliable investigations.

Chapter 5

Three-Body Contact Interaction

In Chapter 4 we have seen that already the most simple finite-range three-body force of Gaussian shape proves to be an enormous computational challenge. In this case, it was not possible to perform calculations in sufficiently large Hilbert spaces allowing for reliable converged calculations. In order to investigate the impact of three-body forces and to develop strategies for the handling of three-body matrix elements we introduce a three-body contact interaction. In this chapter we discuss the calculation of the matrix elements of a regularized three-body contact interaction in Section 5.1. Subsequently, the Hartree-Fock method is used to calculate ground-state energies and charge radii in Section 5.2 as well as single-particle spectra in Section 5.3. In Section 5.4 the second-order energy corrections emerging from many-body perturbation theory are discussed.

5.1 Calculation of Matrix Elements

In the following, we discuss the calculation of the matrix elements of a three-body contact interaction which is supplemented by a cut-off introduced at the end of this section. The three-body contact interaction can be written as

$$V_{3N} = C_{3N} \delta^{(3)}(\mathbf{x}_1 - \mathbf{x}_2) \delta^{(3)}(\mathbf{x}_1 - \mathbf{x}_3) \quad (5.1)$$

with variable strength C_{3N} , and $\delta^{(3)}(\mathbf{x})$ being the Dirac delta distribution in three dimensions. The strength C_{3N} of the three-body interaction will be positive since the interaction has to be repulsive in order to increase the charge radii (cf. Sec. 3.2).

Considering general three-body interactions it is common to calculate the matrix elements in a basis that is based on Jacobi coordinates. But for applications in many-body methods the matrix elements have to be transformed into the m-scheme, i.e. using independent single-particle states, which is computationally very demanding for a three-body interaction. In contrast, the matrix elements of a contact interaction can be directly evaluated in the m-scheme, which is of great advantage compared to general three-body forces. The calculation of these matrix elements has already been discussed in my diploma thesis [27], but since it is the most essential ingredient for the following investigations it will be recapitulated in this section.

The matrix elements are calculated in the harmonic-oscillator basis. We start with three-body product states in coordinate space. Since the three-body contact interaction does not affect spin and isospin, we will neglect these quantum numbers for the moment. The antisymmetrization will be performed explicitly in the end. Introducing the coordinate-space representation of the harmonic-oscillator states, the matrix elements can be expressed as

$$\begin{aligned}
 & \langle n_1 l_1 m_1, n_2 l_2 m_2, n_3 l_3 m_3 | V_{3N} | n'_1 l'_1 m'_1, n'_2 l'_2 m'_2, n'_3 l'_3 m'_3 \rangle \\
 &= \int d^3 x_1 d^3 x_2 d^3 x_3 \langle n_1 l_1 m_1 | \mathbf{x}_1 \rangle \langle n_2 l_2 m_2 | \mathbf{x}_2 \rangle \langle n_3 l_3 m_3 | \mathbf{x}_3 \rangle \\
 & \quad \times C_{3N} \delta^{(3)}(\mathbf{x}_1 - \mathbf{x}_2) \delta^{(3)}(\mathbf{x}_1 - \mathbf{x}_3) \langle \mathbf{x}_1 | n'_1 l'_1 m'_1 \rangle \langle \mathbf{x}_2 | n'_2 l'_2 m'_2 \rangle \langle \mathbf{x}_3 | n'_3 l'_3 m'_3 \rangle
 \end{aligned} \tag{5.2}$$

with the principal quantum number n , angular momentum l and projection quantum number m_l of the harmonic oscillator states. By introducing the relative coordinates $\mathbf{r}_{12} = \mathbf{x}_1 - \mathbf{x}_2$ and $\mathbf{r}_{13} = \mathbf{x}_1 - \mathbf{x}_3$ we can directly exploit the properties of the delta distributions and evaluate six of the nine integrals:

$$\begin{aligned}
 & \int d^3 x_1 d^3 x_2 d^3 x_3 \langle n_1 l_1 m_1 | \mathbf{x}_1 \rangle \langle n_2 l_2 m_2 | \mathbf{x}_2 \rangle \langle n_3 l_3 m_3 | \mathbf{x}_3 \rangle \\
 & \quad \times C_{3N} \delta^{(3)}(\mathbf{x}_1 - \mathbf{x}_2) \delta^{(3)}(\mathbf{x}_1 - \mathbf{x}_3) \langle \mathbf{x}_1 | n'_1 l'_1 m'_1 \rangle \langle \mathbf{x}_2 | n'_2 l'_2 m'_2 \rangle \langle \mathbf{x}_3 | n'_3 l'_3 m'_3 \rangle \\
 &= \int d^3 x_1 d^3 r_{12} d^3 r_{13} \langle n_1 l_1 m_1 | \mathbf{x}_1 \rangle \langle n_2 l_2 m_2 | \mathbf{x}_1 - \mathbf{r}_{12} \rangle \langle n_3 l_3 m_3 | \mathbf{x}_1 - \mathbf{r}_{13} \rangle \\
 & \quad \times C_{3N} \delta^{(3)}(\mathbf{r}_{12}) \delta^{(3)}(\mathbf{r}_{13}) \langle \mathbf{x}_1 | n'_1 l'_1 m'_1 \rangle \langle \mathbf{x}_1 - \mathbf{r}_{12} | n'_2 l'_2 m'_2 \rangle \langle \mathbf{x}_1 - \mathbf{r}_{13} | n'_3 l'_3 m'_3 \rangle \\
 &= C_{3N} \int d^3 x_1 \langle n_1 l_1 m_1 | \mathbf{x}_1 \rangle \langle n_2 l_2 m_2 | \mathbf{x}_1 \rangle \langle n_3 l_3 m_3 | \mathbf{x}_1 \rangle \\
 & \quad \times \langle \mathbf{x}_1 | n'_1 l'_1 m'_1 \rangle \langle \mathbf{x}_1 | n'_2 l'_2 m'_2 \rangle \langle \mathbf{x}_1 | n'_3 l'_3 m'_3 \rangle .
 \end{aligned} \tag{5.3}$$

In coordinate space, the harmonic-oscillator eigenfunctions are composed of a real-valued radial part $R_{nl}(x)$ and an angular part represented by the spherical harmonics

$Y_{lm_l}(\Omega)$ [39]:

$$\langle \mathbf{x} | nlm_l \rangle = R_{nl}(x) Y_{lm_l}(\Omega) . \quad (5.4)$$

Inserting this representation into Equation (5.3) one arrives at

$$\begin{aligned} & \langle n_1 l_1 m_{l_1}, n_2 l_2 m_{l_2}, n_3 l_3 m_{l_3} | V_{3N} | n'_1 l'_1 m'_{l_1}, n'_2 l'_2 m'_{l_2}, n'_3 l'_3 m'_{l_3} \rangle \\ &= C_{3N} \int dx_1 x_1^2 R_{n_1 l_1}(x_1) R_{n_2 l_2}(x_1) R_{n_3 l_3}(x_1) R_{n'_1 l'_1}(x_1) R_{n'_2 l'_2}(x_1) R_{n'_3 l'_3}(x_1) \\ & \quad \times \int d\Omega Y_{l_1 m_{l_1}}^*(\Omega) Y_{l_2 m_{l_2}}^*(\Omega) Y_{l_3 m_{l_3}}^*(\Omega) Y_{l'_1 m'_{l_1}}(\Omega) Y_{l'_2 m'_{l_2}}(\Omega) Y_{l'_3 m'_{l_3}}(\Omega) . \end{aligned} \quad (5.5)$$

The integral over the six radial wavefunctions has to be calculated numerically while the integral over the six spherical harmonics can be evaluated analytically. The product of three spherical harmonics can be reduced to one spherical harmonic:

$$\begin{aligned} & Y_{l_1 m_{l_1}}(\Omega) Y_{l_2 m_{l_2}}(\Omega) Y_{l_3 m_{l_3}}(\Omega) \\ &= \sum_{L_1 M_{L_1}} \sqrt{\frac{(2l_1+1)(2l_2+1)}{4\pi(2L_1+1)}} c \left(\begin{array}{cc|c} l_1 & l_2 & L_1 \\ 0 & 0 & 0 \end{array} \right) c \left(\begin{array}{cc|c} l_1 & l_2 & L_1 \\ m_{l_1} & m_{l_2} & M_{L_1} \end{array} \right) Y_{L_1 M_{L_1}}(\Omega) Y_{l_3 m_{l_3}}(\Omega) \\ &= \sum_{L_1 M_{L_1}} \sqrt{\frac{(2l_1+1)(2l_2+1)}{4\pi(2L_1+1)}} c \left(\begin{array}{cc|c} l_1 & l_2 & L_1 \\ 0 & 0 & 0 \end{array} \right) c \left(\begin{array}{cc|c} l_1 & l_2 & L_1 \\ m_{l_1} & m_{l_2} & M_{L_1} \end{array} \right) \\ & \quad \times \sum_{L_2 M_{L_2}} \sqrt{\frac{(2L_1+1)(2l_3+1)}{4\pi(2L_2+1)}} c \left(\begin{array}{cc|c} L_1 & l_3 & L_2 \\ 0 & 0 & 0 \end{array} \right) c \left(\begin{array}{cc|c} L_1 & l_3 & L_2 \\ M_{L_1} & m_{l_3} & M_{L_2} \end{array} \right) Y_{L_2 M_{L_2}}(\Omega) \end{aligned} \quad (5.6)$$

with the Clebsch-Gordan coefficients $c \left(\begin{array}{cc|c} l_1 & l_2 & L \\ m_{l_1} & m_{l_2} & M_L \end{array} \right)$. Using this relation we can eval-

uate the angular part of the integral:

$$\begin{aligned}
 & \int d\Omega Y_{l_1 m_1}^*(\Omega) Y_{l_2 m_2}^*(\Omega) Y_{l_3 m_3}^*(\Omega) Y_{l'_1 m'_1}(\Omega) Y_{l'_2 m'_2}(\Omega) Y_{l'_3 m'_3}(\Omega) \\
 &= \sum_{\substack{L_1 M_{L_1} \\ L_2 M_{L_2}}} \sqrt{\frac{(2l_1+1)(2l_2+1)}{4\pi(2L_1+1)}} \sqrt{\frac{(2L_1+1)(2l_3+1)}{4\pi(2L_2+1)}} \\
 & \quad \times c \left(\begin{array}{cc|c} l_1 & l_2 & L_1 \\ 0 & 0 & 0 \end{array} \right) c \left(\begin{array}{cc|c} l_1 & l_2 & L_1 \\ m_1 & m_2 & M_{L_1} \end{array} \right) c \left(\begin{array}{cc|c} L_1 & l_3 & L_2 \\ 0 & 0 & 0 \end{array} \right) c \left(\begin{array}{cc|c} L_1 & l_3 & L_2 \\ M_{L_1} & m_3 & M_{L_2} \end{array} \right) \\
 & \quad \times \sum_{\substack{L'_1 M'_{L_1} \\ L'_2 M'_{L_2}}} \sqrt{\frac{(2l'_1+1)(2l'_2+1)}{4\pi(2L'_1+1)}} \sqrt{\frac{(2L'_1+1)(2l'_3+1)}{4\pi(2L'_2+1)}} \\
 & \quad \times c \left(\begin{array}{cc|c} l'_1 & l'_2 & L'_1 \\ 0 & 0 & 0 \end{array} \right) c \left(\begin{array}{cc|c} l'_1 & l'_2 & L'_1 \\ m'_1 & m'_2 & M'_{L_1} \end{array} \right) c \left(\begin{array}{cc|c} L'_1 & l'_3 & L'_2 \\ 0 & 0 & 0 \end{array} \right) c \left(\begin{array}{cc|c} L'_1 & l'_3 & L'_2 \\ M'_{L_1} & m'_3 & M'_{L_2} \end{array} \right) \\
 & \quad \times \underbrace{\int d\Omega Y_{L_2 M_{L_2}}^*(\Omega) Y_{L'_2 M'_{L_2}}(\Omega)}_{=\delta_{L_2 L'_2} \delta_{M_{L_2} M'_{L_2}}} \\
 &= \sum_{\substack{L_1 L_2 L'_1 \\ M_{L_1} M_{L_2} M'_{L_1}}} \frac{\sqrt{(2l_1+1)(2l_2+1)(2l_3+1)(2l'_1+1)(2l'_2+1)(2l'_3+1)}}{16\pi^2(2L_2+1)} \\
 & \quad \times c \left(\begin{array}{cc|c} l_1 & l_2 & L_1 \\ 0 & 0 & 0 \end{array} \right) c \left(\begin{array}{cc|c} l_1 & l_2 & L_1 \\ m_1 & m_2 & M_{L_1} \end{array} \right) c \left(\begin{array}{cc|c} L_1 & l_3 & L_2 \\ 0 & 0 & 0 \end{array} \right) c \left(\begin{array}{cc|c} L_1 & l_3 & L_2 \\ M_{L_1} & m_3 & M_{L_2} \end{array} \right) \\
 & \quad \times c \left(\begin{array}{cc|c} l'_1 & l'_2 & L'_1 \\ 0 & 0 & 0 \end{array} \right) c \left(\begin{array}{cc|c} l'_1 & l'_2 & L'_1 \\ m'_1 & m'_2 & M'_{L_1} \end{array} \right) c \left(\begin{array}{cc|c} L'_1 & l'_3 & L'_2 \\ 0 & 0 & 0 \end{array} \right) c \left(\begin{array}{cc|c} L'_1 & l'_3 & L'_2 \\ M'_{L_1} & m'_3 & M'_{L_2} \end{array} \right) . \quad (5.7)
 \end{aligned}$$

Hence, the calculation of the angular integral is reduced to six summations over a number of Clebsch-Gordan coefficients.

For the complete matrix element we have to include spin and isospin degrees of freedom. As the three-body contact interaction only acts in coordinate space, the evaluation of matrix elements simply yields Kronecker deltas for the spin and isospin projection quantum numbers m_s and m_t , respectively:

$$\begin{aligned}
 & \langle n_1 l_1 m_1 m_{s_1} m_{t_1}, n_2 l_2 m_2 m_{s_2} m_{t_2}, n_3 l_3 m_3 m_{s_3} m_{t_3} | \\
 & \quad \times V_{3N} | n'_1 l'_1 m'_1 m'_{s_1} m'_{t_1}, n'_2 l'_2 m'_2 m'_{s_2} m'_{t_2}, n'_3 l'_3 m'_3 m'_{s_3} m'_{t_3} \rangle \\
 &= \langle n_1 l_1 m_1, n_2 l_2 m_2, n_3 l_3 m_3 | V_{3N} | n'_1 l'_1 m'_1, n'_2 l'_2 m'_2, n'_3 l'_3 m'_3 \rangle \\
 & \quad \times \delta_{m_{s_1} m'_{s_1}} \delta_{m_{s_2} m'_{s_2}} \delta_{m_{s_3} m'_{s_3}} \delta_{m_{t_1} m'_{t_1}} \delta_{m_{t_2} m'_{t_2}} \delta_{m_{t_3} m'_{t_3}} . \quad (5.8)
 \end{aligned}$$

5.1 · Calculation of Matrix Elements

For brevity, we have omitted the quantum numbers $s = \frac{1}{2}$ and $t = \frac{1}{2}$ for spin and isospin, respectively.

For the practical application of the three-body interaction in various many-body methods, the single-particle angular momenta l_i and spins s_i have to be coupled to total single-particle angular momenta j_i . This is achieved by inserting a number of Clebsch-Gordan coefficients yielding the j-coupled three-body matrix elements

$$\begin{aligned}
& \langle n_1 l_1 j_1 m_1 m_{t_1}, n_2 l_2 j_2 m_2 m_{t_2}, n_3 l_3 j_3 m_3 m_{t_3} | \\
& \quad \times \mathbb{V}_{3N} | n'_1 l'_1 j'_1 m'_1 m'_{t_1}, n'_2 l'_2 j'_2 m'_2 m'_{t_2}, n'_3 l'_3 j'_3 m'_3 m'_{t_3} \rangle \\
= & \sum_{\substack{m_1 \dots m'_3 \\ m_{s_1} \dots m_{s_3}}} c \left(\begin{array}{c} l_1 \quad \frac{1}{2} \\ m_1 \quad m_{s_1} \end{array} \middle| \begin{array}{c} j_1 \\ m_1 \end{array} \right) c \left(\begin{array}{c} l_2 \quad \frac{1}{2} \\ m_2 \quad m_{s_2} \end{array} \middle| \begin{array}{c} j_2 \\ m_2 \end{array} \right) c \left(\begin{array}{c} l_3 \quad \frac{1}{2} \\ m_3 \quad m_{s_3} \end{array} \middle| \begin{array}{c} j_3 \\ m_3 \end{array} \right) \\
& \quad \times c \left(\begin{array}{c} l'_1 \quad \frac{1}{2} \\ m'_1 \quad m'_{s_1} \end{array} \middle| \begin{array}{c} j'_1 \\ m'_1 \end{array} \right) c \left(\begin{array}{c} l'_2 \quad \frac{1}{2} \\ m'_2 \quad m'_{s_2} \end{array} \middle| \begin{array}{c} j'_2 \\ m'_2 \end{array} \right) c \left(\begin{array}{c} l'_3 \quad \frac{1}{2} \\ m'_3 \quad m'_{s_3} \end{array} \middle| \begin{array}{c} j'_3 \\ m'_3 \end{array} \right) \\
& \quad \times \langle n_1 l_1 m_1 m_{s_1} m_{t_1}, n_2 l_2 m_2 m_{s_2} m_{t_2}, n_3 l_3 m_3 m_{s_3} m_{t_3} | \\
& \quad \times \mathbb{V}_{3N} | n'_1 l'_1 m'_1 m'_{s_1} m'_{t_1}, n'_2 l'_2 m'_2 m'_{s_2} m'_{t_2}, n'_3 l'_3 m'_3 m'_{s_3} m'_{t_3} \rangle \\
= & \sum_{\substack{m_1 \dots m'_3 \\ m_{s_1} \dots m_{s_3}}} c \left(\begin{array}{c} l_1 \quad \frac{1}{2} \\ m_1 \quad m_{s_1} \end{array} \middle| \begin{array}{c} j_1 \\ m_1 \end{array} \right) c \left(\begin{array}{c} l_2 \quad \frac{1}{2} \\ m_2 \quad m_{s_2} \end{array} \middle| \begin{array}{c} j_2 \\ m_2 \end{array} \right) c \left(\begin{array}{c} l_3 \quad \frac{1}{2} \\ m_3 \quad m_{s_3} \end{array} \middle| \begin{array}{c} j_3 \\ m_3 \end{array} \right) \\
& \quad \times c \left(\begin{array}{c} l'_1 \quad \frac{1}{2} \\ m'_1 \quad m'_{s_1} \end{array} \middle| \begin{array}{c} j'_1 \\ m'_1 \end{array} \right) c \left(\begin{array}{c} l'_2 \quad \frac{1}{2} \\ m'_2 \quad m'_{s_2} \end{array} \middle| \begin{array}{c} j'_2 \\ m'_2 \end{array} \right) c \left(\begin{array}{c} l'_3 \quad \frac{1}{2} \\ m'_3 \quad m'_{s_3} \end{array} \middle| \begin{array}{c} j'_3 \\ m'_3 \end{array} \right) \\
& \quad \times C_{3N} \int dx x^2 R_{n_1 l_1}(x) R_{n_2 l_2}(x) R_{n_3 l_3}(x) R_{n'_1 l'_1}(x) R_{n'_2 l'_2}(x) R_{n'_3 l'_3}(x) \\
& \quad \times \frac{1}{16\pi^2} \sqrt{(2l_1 + 1)(2l_2 + 1)(2l_3 + 1)(2l'_1 + 1)(2l'_2 + 1)(2l'_3 + 1)} \\
& \quad \times \sum_{\substack{L_1 L_2 L'_1 \\ M_{L_1} M_{L_2} M'_{L_1}}} \frac{1}{(2L_2 + 1)} c \left(\begin{array}{c} l_1 \quad l_2 \\ 0 \quad 0 \end{array} \middle| \begin{array}{c} L_1 \\ 0 \end{array} \right) c \left(\begin{array}{c} L_1 \quad l_3 \\ 0 \quad 0 \end{array} \middle| \begin{array}{c} L_2 \\ 0 \end{array} \right) c \left(\begin{array}{c} l'_1 \quad l'_2 \\ 0 \quad 0 \end{array} \middle| \begin{array}{c} L'_1 \\ 0 \end{array} \right) c \left(\begin{array}{c} L'_1 \quad l'_3 \\ 0 \quad 0 \end{array} \middle| \begin{array}{c} L_2 \\ 0 \end{array} \right) \\
& \quad \times c \left(\begin{array}{c} l_1 \quad l_2 \\ m_1 \quad m_2 \end{array} \middle| \begin{array}{c} L_1 \\ M_{L_1} \end{array} \right) c \left(\begin{array}{c} L_1 \quad l_3 \\ M_{L_1} \quad m_3 \end{array} \middle| \begin{array}{c} L_2 \\ M_{L_2} \end{array} \right) c \left(\begin{array}{c} l'_1 \quad l'_2 \\ m'_1 \quad m'_2 \end{array} \middle| \begin{array}{c} L'_1 \\ M'_{L_1} \end{array} \right) c \left(\begin{array}{c} L'_1 \quad l'_3 \\ M'_{L_1} \quad m'_3 \end{array} \middle| \begin{array}{c} L_2 \\ M_{L_2} \end{array} \right) \\
& \quad \times \delta_{m_{s_1} m'_{s_1}} \delta_{m_{s_2} m'_{s_2}} \delta_{m_{s_3} m'_{s_3}} \delta_{m_{t_1} m'_{t_1}} \delta_{m_{t_2} m'_{t_2}} \delta_{m_{t_3} m'_{t_3}} . \tag{5.9}
\end{aligned}$$

For an efficient calculation of the three-body matrix elements it is advantageous to evaluate as many as possible of these 18 sums analytically. Therefore, one can evaluate the Kronecker deltas and exploit the condition $m_1 + m_2 = M$ in the Clebsch-Gordan

coefficients $c \left(\begin{smallmatrix} j_1 & j_2 \\ m_1 & m_2 \end{smallmatrix} \middle| \begin{smallmatrix} J \\ M \end{smallmatrix} \right)$. Thus, 12 sums can be eliminated:

$$\begin{aligned}
 & \langle n_1 l_1 j_1 m_1 m_{t_1}, n_2 l_2 j_2 m_2 m_{t_2}, n_3 l_3 j_3 m_3 m_{t_3} | \\
 & \quad \times V_{3N} | n'_1 l'_1 j'_1 m'_1 m'_{t_1}, n'_2 l'_2 j'_2 m'_2 m'_{t_2}, n'_3 l'_3 j'_3 m'_3 m'_{t_3} \rangle \\
 & = C_{3N} \delta_{m_{t_1} m'_{t_1}} \delta_{m_{t_2} m'_{t_2}} \delta_{m_{t_3} m'_{t_3}} \\
 & \quad \times \frac{1}{16\pi^2} \sqrt{(2l_1 + 1)(2l_2 + 1)(2l_3 + 1)(2l'_1 + 1)(2l'_2 + 1)(2l'_3 + 1)} \\
 & \quad \times \int dx x^2 R_{n_1 l_1}(x) R_{n_2 l_2}(x) R_{n_3 l_3}(x) R_{n'_1 l'_1}(x) R_{n'_2 l'_2}(x) R_{n'_3 l'_3}(x) \\
 & \quad \times \sum_{m_{s_1} m_{s_2} m_{s_3}} c \left(\begin{smallmatrix} l_1 & \frac{1}{2} \\ m_1 - m_{s_1} & m_{s_1} \end{smallmatrix} \middle| \begin{smallmatrix} j_1 \\ m_1 \end{smallmatrix} \right) c \left(\begin{smallmatrix} l_2 & \frac{1}{2} \\ m_2 - m_{s_2} & m_{s_2} \end{smallmatrix} \middle| \begin{smallmatrix} j_2 \\ m_2 \end{smallmatrix} \right) c \left(\begin{smallmatrix} l_3 & \frac{1}{2} \\ m_3 - m_{s_3} & m_{s_3} \end{smallmatrix} \middle| \begin{smallmatrix} j_3 \\ m_3 \end{smallmatrix} \right) \\
 & \quad \times c \left(\begin{smallmatrix} l'_1 & \frac{1}{2} \\ m'_1 - m_{s_1} & m_{s_1} \end{smallmatrix} \middle| \begin{smallmatrix} j'_1 \\ m'_1 \end{smallmatrix} \right) c \left(\begin{smallmatrix} l'_2 & \frac{1}{2} \\ m'_2 - m_{s_2} & m_{s_2} \end{smallmatrix} \middle| \begin{smallmatrix} j'_2 \\ m'_2 \end{smallmatrix} \right) c \left(\begin{smallmatrix} l'_3 & \frac{1}{2} \\ m'_3 - m_{s_3} & m_{s_3} \end{smallmatrix} \middle| \begin{smallmatrix} j'_3 \\ m'_3 \end{smallmatrix} \right) \\
 & \quad \times \sum_{L_1 L_2 L'_1} \frac{1}{(2L_2 + 1)} c \left(\begin{smallmatrix} l_1 & l_2 \\ 0 & 0 \end{smallmatrix} \middle| \begin{smallmatrix} L_1 \\ 0 \end{smallmatrix} \right) c \left(\begin{smallmatrix} L_1 & l_3 \\ 0 & 0 \end{smallmatrix} \middle| \begin{smallmatrix} L_2 \\ 0 \end{smallmatrix} \right) c \left(\begin{smallmatrix} l'_1 & l'_2 \\ 0 & 0 \end{smallmatrix} \middle| \begin{smallmatrix} L'_1 \\ 0 \end{smallmatrix} \right) c \left(\begin{smallmatrix} L'_1 & l'_3 \\ 0 & 0 \end{smallmatrix} \middle| \begin{smallmatrix} L_2 \\ 0 \end{smallmatrix} \right) \\
 & \quad \times c \left(\begin{smallmatrix} l_1 & l_2 \\ m_1 - m_{s_1} & m_2 - m_{s_2} \end{smallmatrix} \middle| \begin{smallmatrix} L_1 \\ M_{L_1} \end{smallmatrix} \right) c \left(\begin{smallmatrix} L_1 & l_3 \\ M_{L_1} & m_3 - m_{s_3} \end{smallmatrix} \middle| \begin{smallmatrix} L_2 \\ M_{L_2} \end{smallmatrix} \right) \\
 & \quad \times c \left(\begin{smallmatrix} l'_1 & l'_2 \\ m'_1 - m_{s_1} & m'_2 - m_{s_2} \end{smallmatrix} \middle| \begin{smallmatrix} L'_1 \\ M'_{L_1} \end{smallmatrix} \right) c \left(\begin{smallmatrix} L'_1 & l'_3 \\ M'_{L_1} & m'_3 - m_{s_3} \end{smallmatrix} \middle| \begin{smallmatrix} L_2 \\ M_{L_2} \end{smallmatrix} \right) , \tag{5.10}
 \end{aligned}$$

where the following conditions must be fulfilled:

$$\begin{aligned}
 M_{L_1} & = m_1 + m_2 - m_{s_1} - m_{s_2} , \\
 M_{L_2} & = m_1 + m_2 + m_3 - m_{s_1} - m_{s_2} - m_{s_3} \\
 & = m'_1 + m'_2 + m'_3 - m_{s_1} - m_{s_2} - m_{s_3} , \\
 M'_{L_1} & = m'_1 + m'_2 - m_{s_1} - m_{s_2} .
 \end{aligned} \tag{5.11}$$

Finally, these matrix elements have to be antisymmetrized explicitly.

In order to facilitate calculations in large model spaces, the radial integrals (see Eq. (5.5)) as well as the angular integrals (5.7) are precomputed and stored. The inclusion of the spin and isospin quantum numbers, the j-coupling and the antisymmetrization are then done on the fly during the many-body calculation [19].

The calculation of these matrix elements is simple compared to more general three-body forces. But a pure contact interaction is not of physical character and leads to difficulties, e.g. in the framework of many-body perturbation theory [27]. Hence, a regularization of the three-body interaction is inevitable. As we want to preserve the simplicity of the matrix element calculation, momentum-space cut-offs are out of

question. Instead, we introduce an energy cut-off parameter e_{3N} which is defined via $(2n_1 + l_1) + (2n_2 + l_2) + (2n_3 + l_3) \leq e_{3N}$ as an upper limit for the total oscillator energy of the three-particle state [19]. This cut-off is implemented consistently for all calculations.

5.2 Ground-State Energies and Charge Radii

For first investigations the regularized contact interaction is included in Hartree-Fock calculations. We consider the same set of closed-shell nuclei as in Chapter 3 with the same oscillator parameters. To obtain converged HF results it is sufficient to include 11 major oscillator shells. In the following, the parameters of the three-body interaction, i.e. the strength C_{3N} and the cut-off e_{3N} , have to be determined. In addition, the flow parameters of the different two-body interactions have to be adjusted. The strength of the three-body interaction will be chosen such that the experimental charge radii are reproduced while the flow parameter is used to adjust the ground-state energies as the dependence of the charge radii on the flow parameter is weak.

We consider the same types of two-body interactions as in Chapter 3, i.e. the UCOM(SRG) and the S-UCOM(SRG) interactions as well as the SRG and the S-SRG interactions.

In Figure 5.1 the ground-state energies per nucleon (upper panel) and the charge radii (lower panel) for the S-UCOM(SRG) interaction using the flow parameter $\alpha = 0.16 \text{ fm}^4$ and different three-body strengths C_{3N} are shown. The systematics of the experimental ground-state energies is reproduced by all considered two- plus three-body interactions except for an almost constant shift. The considered nuclei are underbound by about 2.5 to 3.5 MeV per nucleon for the weakest three-body force up to 3.5 to 4.5 MeV per nucleon for the strongest one, since the three-body interaction is purely repulsive and, therefore, reduces the binding energies. As in case of pure two-body interactions this discrepancy can be reduced by including the effect of long-range correlations via many-body perturbation theory (cf. Sec. 5.4). The charge radii also increase with increasing three-body strength which is again due to the repulsive character of the three-body interaction pushing the nucleons apart. For the strongest three-body interaction the experimental radii are almost perfectly reproduced. However, we will choose the intermediate value $C_{3N} = 2.2 \text{ GeV fm}^6$ as we have to keep in mind that minor corrections to the charge radii emerge from many-body perturbation theory although they are not calculated here. Furthermore, we have not transformed the corresponding operator, which would also result in minor corrections.

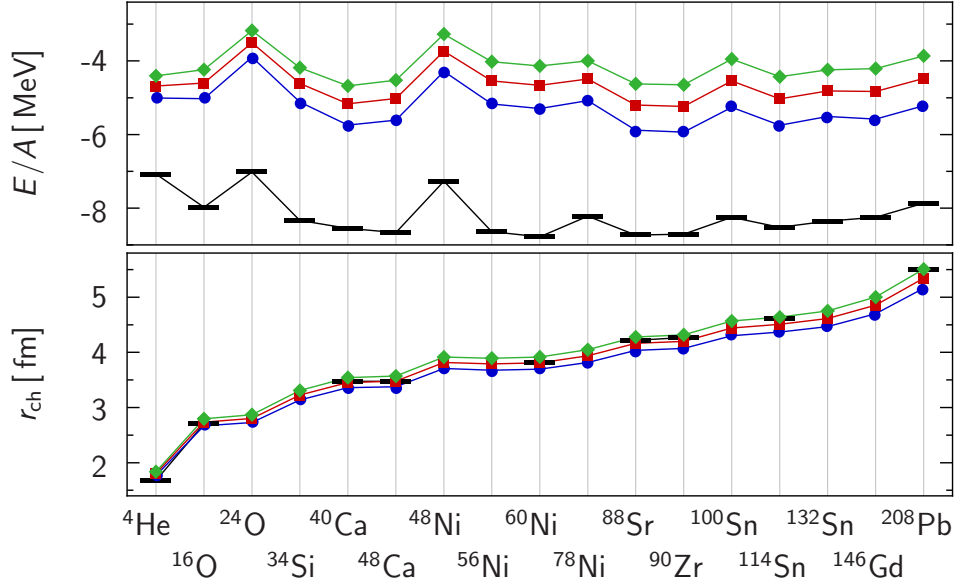


Figure 5.1: Ground-state energies per nucleon and charge radii of selected closed-shell nuclei resulting from HF calculations for the S-UCOM(SRG) interaction with $\alpha = 0.16 \text{ fm}^4$, $e_{\text{max}} = 10$, $e_{3N} = 20$, and different three-body strengths: (●) $C_{3N} = 1.6 \text{ GeV fm}^6$, (■) $C_{3N} = 2.2 \text{ GeV fm}^6$, (◆) $C_{3N} = 2.8 \text{ GeV fm}^6$. The bars indicate the experimental values [30, 31].

The dependencies on the strength of the three-body interaction are similar for all four two-body interactions. Therefore, they are not all shown here but can be found in Appendix E. The optimal values for the strengths of the three-body interactions supplementing the two-body interactions are: $C_{3N} = 1.6 \text{ GeV fm}^6$ for the UCOM(SRG) interaction, $C_{3N} = 4.3 \text{ GeV fm}^6$ for the SRG interaction, and $C_{3N} = 2.0 \text{ GeV fm}^6$ for the S-SRG interaction (cf. Tab. 5.1). The three-body strengths for the UCOM(SRG), S-UCOM(SRG) and S-SRG interactions are in the same range while the three-body force supplementing the SRG interaction has to be significantly stronger in order to compensate the strong overbinding and the significantly smaller charge radii observed in Section 3.2 (Fig. 3.3).

Next, we investigate the dependence of the two- plus three-body interactions on the flow parameter. Figures 5.2 and 5.3 show the ground-state energies per nucleon and the charge radii for the UCOM(SRG) interaction with $C_{3N} = 1.6 \text{ GeV fm}^6$ and the S-UCOM(SRG) interaction with $C_{3N} = 2.2 \text{ GeV fm}^6$, for different values of the flow parameter. In both cases, the ground-state energies decrease with increasing flow parameter. The step from the smallest flow parameter $\alpha = 0.04 \text{ fm}^4$ to $\alpha = 0.12 \text{ fm}^4$ is connected with a substantial gain of binding energy while going further to $\alpha = 0.16 \text{ fm}^4$ leads only to slightly stronger bound nuclei. In contrast, the charge radii are almost

5.2 · Ground-State Energies and Charge Radii

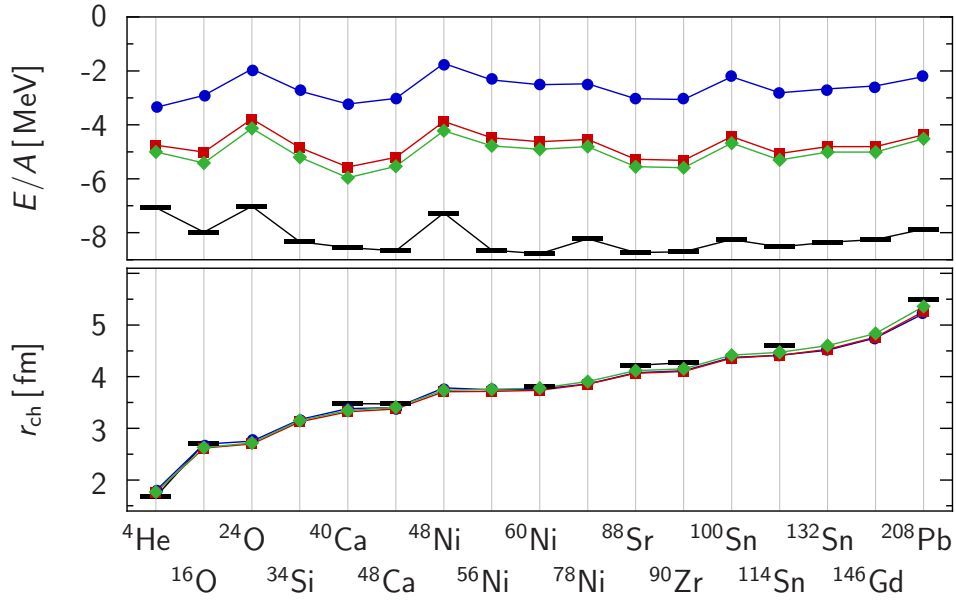


Figure 5.2: Ground-state energies per nucleon and charge radii of selected closed-shell nuclei resulting from HF calculations for the UCOM(SRG) interaction with $e_{\max} = 10$, $C_{3N} = 1.6 \text{ GeV fm}^6$, $e_{3N} = 20$, and different flow parameters: (●) $\alpha = 0.04 \text{ fm}^4$, (■) $\alpha = 0.12 \text{ fm}^4$, (◆) $\alpha = 0.16 \text{ fm}^4$. The bars indicate the experimental values [30, 31].

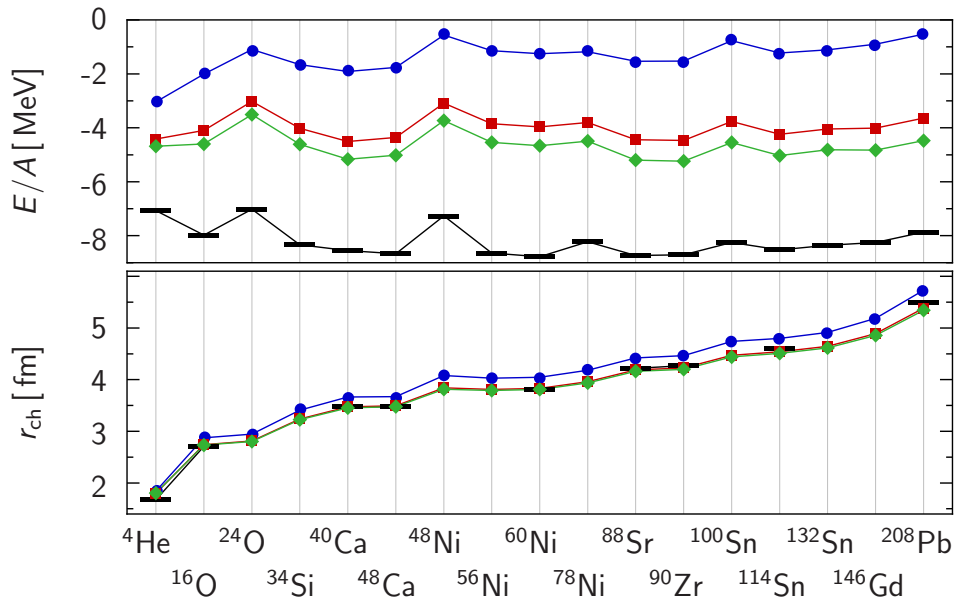


Figure 5.3: Same as in Figure 5.2 for the S-UCOM(SRG) interaction with $e_{\max} = 10$, $C_{3N} = 2.2 \text{ GeV fm}^6$, $e_{3N} = 20$, and (●) $\alpha = 0.04 \text{ fm}^4$, (■) $\alpha = 0.12 \text{ fm}^4$, (◆) $\alpha = 0.16 \text{ fm}^4$.

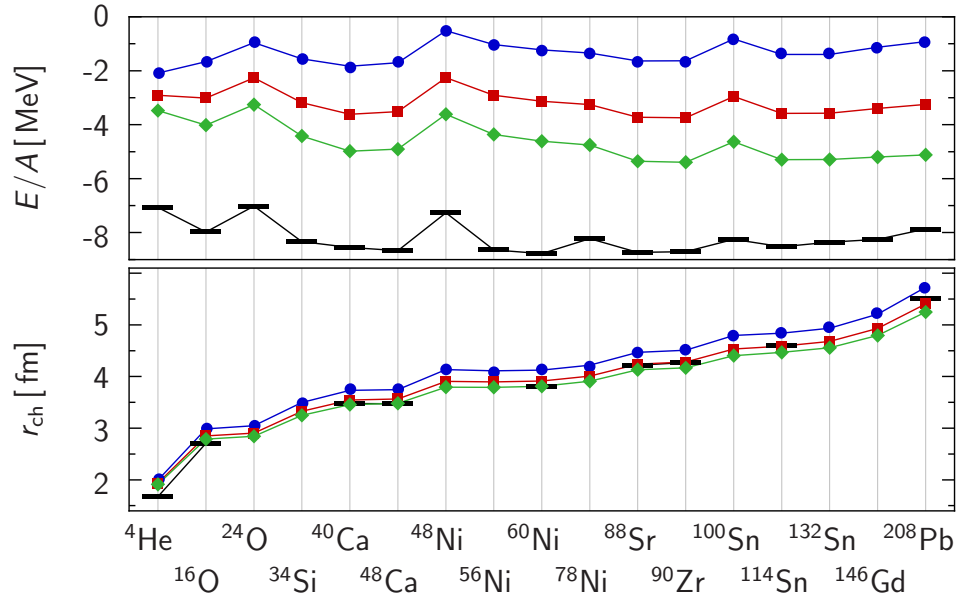


Figure 5.4: Same as in Figure 5.2 for the SRG interaction with $e_{\max} = 10$, $C_{3N} = 4.3 \text{ GeV fm}^6$, $e_{3N} = 20$, and $(\bullet) \alpha = 0.03 \text{ fm}^4$, $(\blacksquare) \alpha = 0.06 \text{ fm}^4$, $(\blacklozenge) \alpha = 0.10 \text{ fm}^4$.

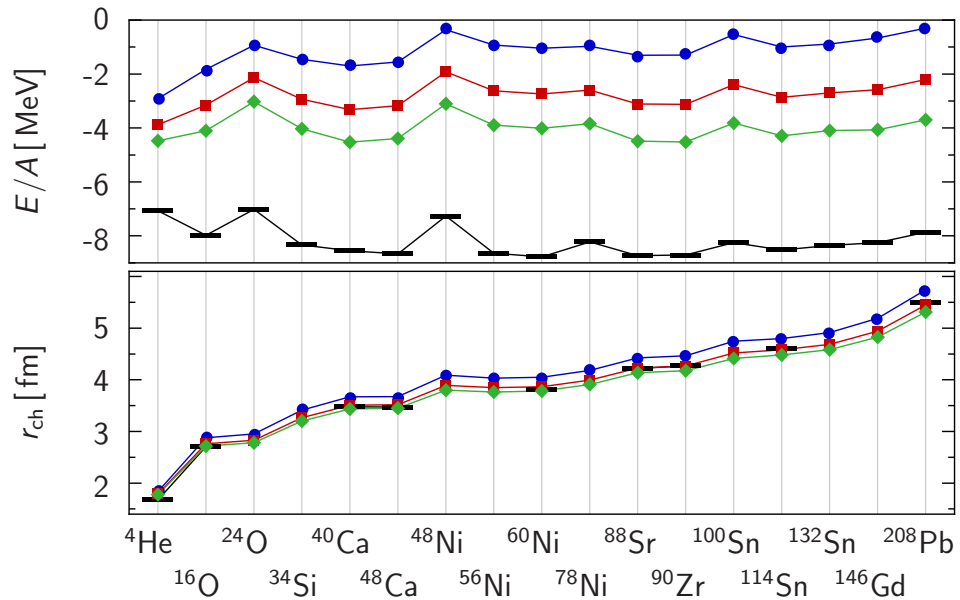


Figure 5.5: Same as in Figure 5.2 for the S-SRG interaction with $e_{\max} = 10$, $C_{3N} = 2.0 \text{ GeV fm}^6$, $e_{3N} = 20$, and $(\bullet) \alpha = 0.03 \text{ fm}^4$, $(\blacksquare) \alpha = 0.06 \text{ fm}^4$, $(\blacklozenge) \alpha = 0.10 \text{ fm}^4$.

	α [fm ⁴]	C_{3N} [GeV fm ⁶]
UCOM(SRG)	0.16	1.6
S-UCOM(SRG)	0.16	2.2
SRG	0.10	4.3
S-SRG	0.10	2.0

Table 5.1: Optimal parameter sets for the different two- plus three-body interactions.

independent of the flow parameter considering the UCOM(SRG) interaction. In case of the S-UCOM(SRG) interaction the charge radii slightly decrease with increasing flow parameter.

The energies and radii calculated with the SRG interaction with $C_{3N} = 4.3 \text{ GeV fm}^6$ (Fig. 5.4) and the S-SRG interaction with $C_{3N} = 2.0 \text{ GeV fm}^6$ (Fig. 5.5) show a similar behavior. Increasing the flow parameter leads to a significant lowering of the ground-state energies and a slight decrease of the charge radii.

For the following calculations we will use the largest flow parameters, i.e. $\alpha = 0.16 \text{ fm}^4$ for the UCOM(SRG) and the S-UCOM(SRG) interactions and $\alpha = 0.10 \text{ fm}^4$ for the SRG and the S-SRG interactions. The complete optimal parameter sets are listed in Table 5.1.

Finally, in Figure 5.6 are compared the four combinations of two- plus three-body interactions that will be employed in the following. The charge radii of all four interactions are almost identical and reproduce nicely the experimental data while the ground-state energies show some small differences. The remaining difference to the experimental ground-state energies will be covered by including the second-order perturbative corrections (Sec. 5.4).

5.3 Single-Particle Spectra

In this section, single-particle spectra resulting from the HF calculations are investigated. We compare the four two- plus three-body interactions discussed in the previous section using the parameters listed in Table 5.1. The harmonic-oscillator basis is again truncated at $e_{\max} = 10$ and the three-body cut-off is set to $e_{3N} = 20$.

Figure 5.7 shows the corrected single-particle energies of ^{40}Ca for the four interactions compared to data extracted from experiment. For the UCOM(SRG) interaction the order of the $1s_{1/2}$ and the $0p_{3/2}$ levels is interchanged but all other level orderings

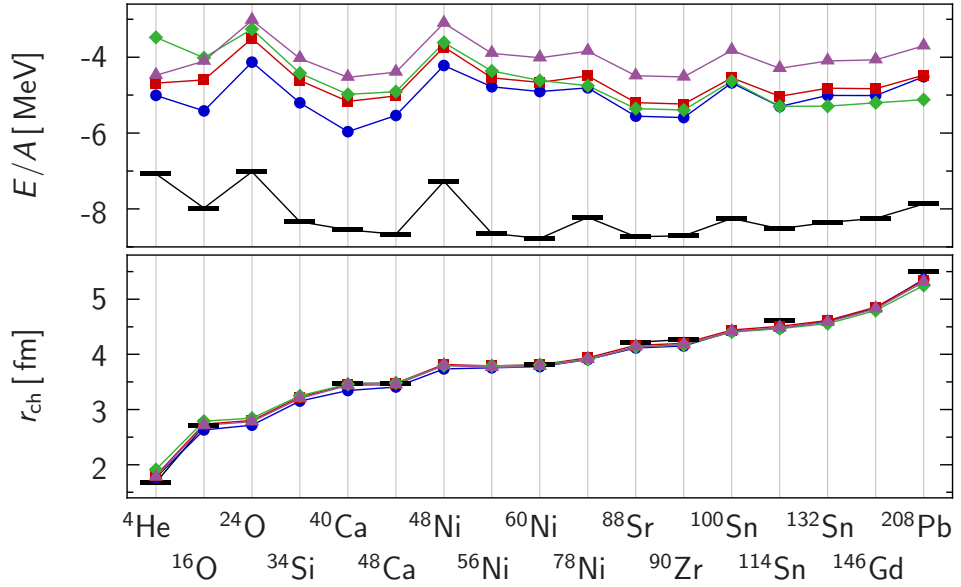


Figure 5.6: Ground-state energies per nucleon and charge radii of selected closed-shell nuclei resulting from HF calculations for different two- plus three-body interactions with $e_{\text{max}} = 10$, $e_{3\text{N}} = 20$: (●) UCOM(SRG), $\alpha = 0.16 \text{ fm}^4$, $C_{3\text{N}} = 1.6 \text{ GeV fm}^6$; (■) S-UCOM(SRG), $\alpha = 0.16 \text{ fm}^4$, $C_{3\text{N}} = 2.2 \text{ GeV fm}^6$; (◆) SRG, $\alpha = 0.10 \text{ fm}^4$, $C_{3\text{N}} = 4.3 \text{ GeV fm}^6$; (▲) S-SRG, $\alpha = 0.10 \text{ fm}^4$, $C_{3\text{N}} = 2.0 \text{ GeV fm}^6$. The bars indicate the experimental values [30, 31].

are nicely reproduced. Furthermore, the level spacings are in reasonable agreement with experiment. There are only minor differences between the spectra calculated with the four different interactions, especially the overestimated level spacings observed for the two-body SRG interaction (cf. Sec. 3.3) are compensated by the inclusion of the appropriate three-body contact interaction.

The single-particle spectra of ${}^{90}\text{Zr}$ (Fig. 5.8) are in reasonable agreement with experiment as well. But for the UCOM(SRG) interaction one observes a collapse of level spacings at several points. Furthermore, considering the single-particle spectra of ${}^{60}\text{Ni}$ (Fig. 5.9) reveals, in addition to collapsed level spacings, that for all four interactions the order of occupied and unoccupied states with respect to the HF ground-state is interchanged at least once. At this point one has to be extremely careful when applying many-body perturbation theory to these nuclei. In the formula for the second-order energy correction the difference of single-particle energies enters in the denominator (Eq. (3.34)). The interchange of occupied and unoccupied levels might lead to a sign change of the term while collapsed level spacings might yield divergent terms. Both effects invalidate the perturbative energy corrections. For most of the heavier nuclei the corresponding single-particle spectra exhibit at least one of the effects, i.e.

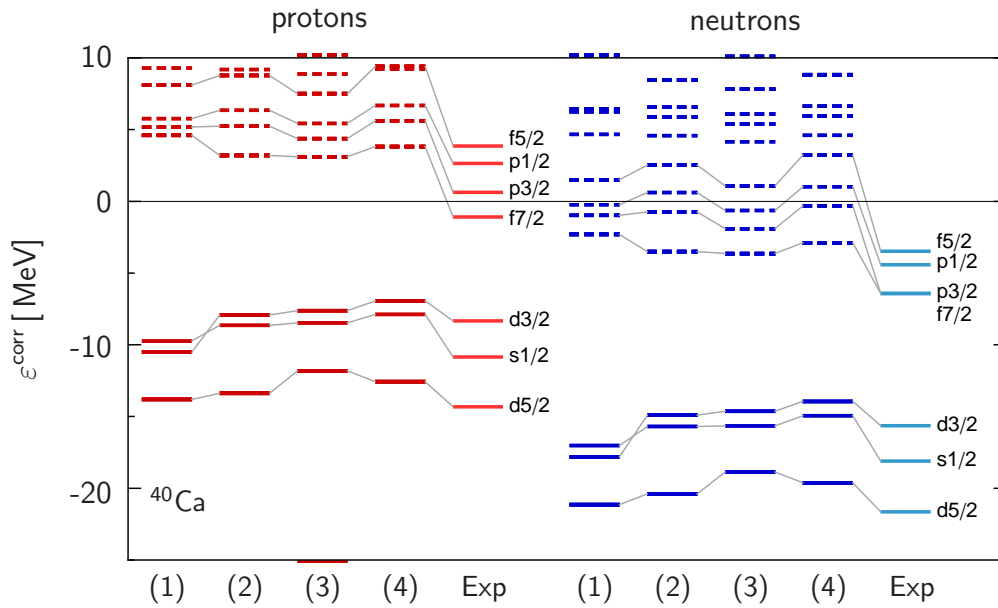


Figure 5.7: Single-particle spectra of ^{40}Ca for the different two- plus three-body interactions with $e_{\text{max}} = 10$, $e_{3\text{N}} = 20$: (1) UCOM(SRG), $\alpha = 0.16 \text{ fm}^4$, $C_{3\text{N}} = 1.6 \text{ GeV fm}^6$; (2) S-UCOM(SRG), $\alpha = 0.16 \text{ fm}^4$, $C_{3\text{N}} = 2.2 \text{ GeV fm}^6$; (3) SRG, $\alpha = 0.10 \text{ fm}^4$, $C_{3\text{N}} = 4.3 \text{ GeV fm}^6$; (4) S-SRG, $\alpha = 0.10 \text{ fm}^4$, $C_{3\text{N}} = 2.0 \text{ GeV fm}^6$; compared to experimental data [32]. Solid and dashed lines indicate occupied and unoccupied states of the HF solutions, respectively.

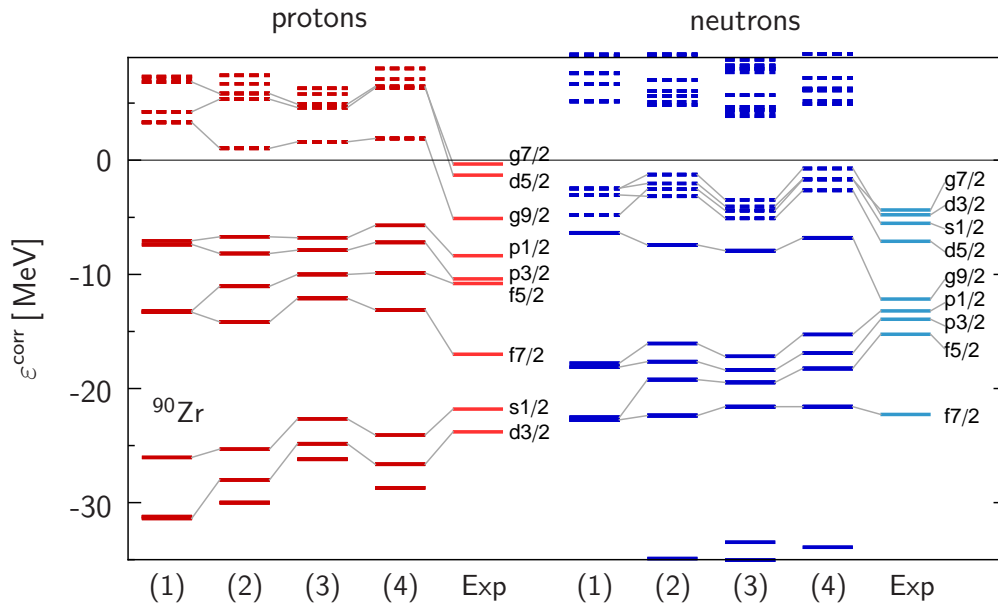
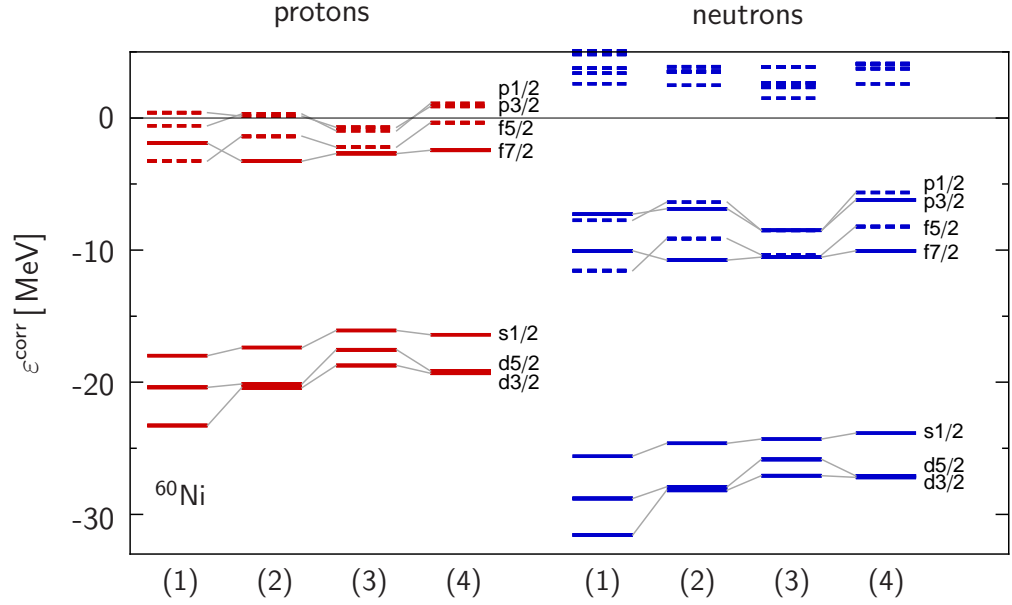


Figure 5.8: Single-particle spectra of ^{90}Zr for the same interactions used in Figure 5.7. Experimental data taken from Refs. [33, 34].


 Figure 5.9: Single-particle spectra of ^{60}Ni for the same interactions used in Figure 5.7.

a collapse of level spacings and/or the interchange of occupied and unoccupied levels.

A procedure to deal with divergent terms in the second-order energy correction in MBPT discussed in Section 3.5 will be used in the following.

5.4 Perturbative Energy Corrections

After the study of different observables on the Hartree-Fock level we will now investigate the impact of long-range correlations by applying many-body perturbation theory on top of the HF results. As a reminder, the second-order energy correction for two-plus three-body interactions (Eq. (3.34)) is repeated:

$$\begin{aligned}
 E_0^{(2)} = & \frac{1}{4} \sum_{hh'}^{<\varepsilon_F} \sum_{pp'}^{>\varepsilon_F} \frac{\left| \langle hh' | H_{\text{int}}^{(2)} | pp' \rangle + \sum_{\bar{h}}^{<\varepsilon_F} \langle hh'\bar{h} | V_{3N} | pp'\bar{h} \rangle \right|^2}{\varepsilon_h + \varepsilon_{h'} - \varepsilon_p - \varepsilon_{p'}} \\
 & + \frac{1}{36} \sum_{hh'h''}^{<\varepsilon_F} \sum_{pp'p''}^{>\varepsilon_F} \frac{|\langle hh'h'' | V_{3N} | pp'p'' \rangle|^2}{\varepsilon_h + \varepsilon_{h'} + \varepsilon_{h''} - \varepsilon_p - \varepsilon_{p'} - \varepsilon_{p''}}.
 \end{aligned} \tag{5.12}$$

The inclusion of a three-body interaction entails two additional terms compared to the expression for a pure two-body interaction [19]. The matrix elements of the two-body

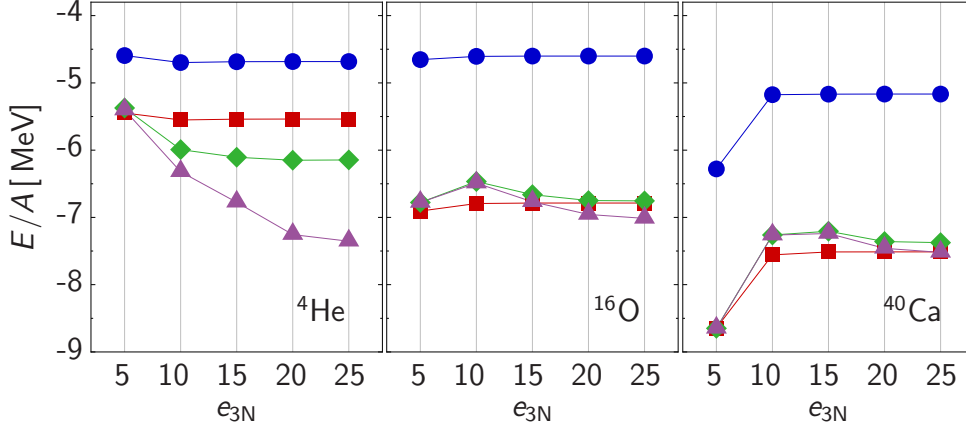


Figure 5.10: Contributions to the ground-state energy resulting from HF plus MBPT based on the S-UCOM(SRG) interaction for $\alpha = 0.16 \text{ fm}^4$, $C_{3N} = 2.2 \text{ GeV fm}^6$, $e_{\text{max}} = 10$ in dependence of the cut-off parameter e_{3N} : (●) HF, (■) HF+MBPT(2b), (◆) HF+MBPT(2b+3bp-ph), (▲) HF+MBPT(2b+3b).

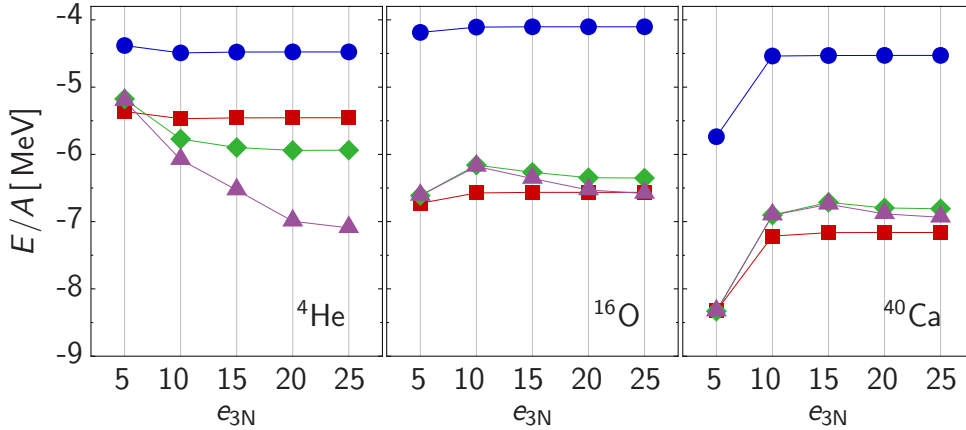


Figure 5.11: Same as in Figure 5.10 for the S-SRG interaction with $\alpha = 0.10 \text{ fm}^4$, $C_{3N} = 2.0 \text{ GeV fm}^6$, $e_{\text{max}} = 10$.

Hamiltonian involving 2p2h excitations are supplemented by an expression that results from a contraction of the third particle index in the three-body matrix elements. The second additional term results from 3p3h excitations involving the pure three-body interaction.

In order to disentangle the effects of these different contributions we introduce three variants of MBPT in the following. The contribution of the two-body Hamiltonian, labeled MBPT(2b), provides the starting point. In the next step, the expression emerging from 2p2h excitations of the three-body interaction is added, i.e. the com-

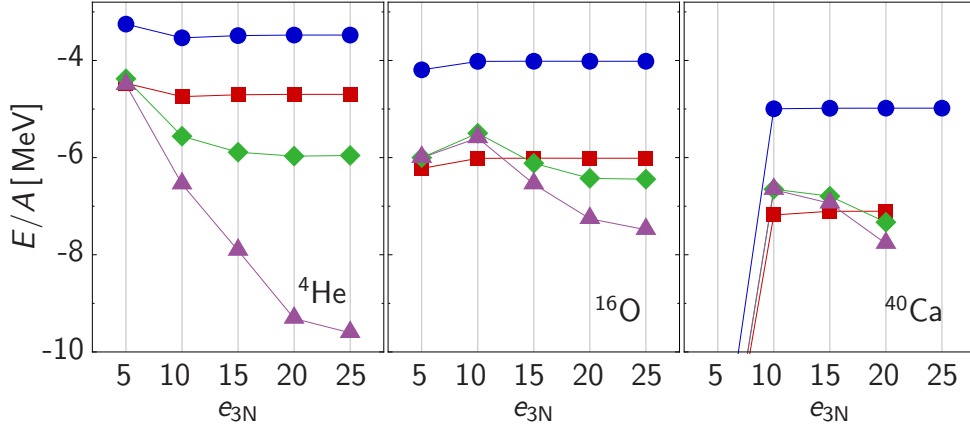


Figure 5.12: Same as in Figure 5.10 for the SRG interaction with $\alpha = 0.10 \text{ fm}^4$, $C_{3N} = 4.3 \text{ GeV fm}^6$, $e_{\text{max}} = 10$. Note the different energy scale.

plete first term, labeled MBPT(2b+3bp-ph). Finally, MBPT(2b+3b) indicates the full expression (5.12). Thus, the difference between MBPT(2b) and MBPT(2b+3bp-ph) indicates the amount of energy correction emerging from the three-body interaction involving 2p2h excitations, while the step from MBPT(2b+3bp-ph) to MBPT(2b+3b) contains the energy gain due to the 3p3h excitations generated by the three-body interaction. Obviously, the difference between MBPT(2b) and MBPT(2b+3b) reveals the overall influence of the three-body interaction.

The different energy contributions are considered exemplarily for the three nuclei ${}^4\text{He}$, ${}^{16}\text{O}$ and ${}^{40}\text{Ca}$ as a function of the three-body cut-off e_{3N} . The ground-state energies resulting from HF, MBPT(2b), MBPT(2b+3bp-ph) and MBPT(2b+3b) are shown in Figure 5.10 for the S-UCOM(SRG) interaction with $\alpha = 0.16 \text{ fm}^4$ and $C_{3N} = 2.2 \text{ MeV fm}^6$, and in Figure 5.11 for the S-SRG interaction with $\alpha = 0.10 \text{ fm}^4$ and $C_{3N} = 2.0 \text{ MeV fm}^6$. The results are very similar for both interactions. Above $e_{3N} = 10$ the HF energies are independent of the cut-off, which confirms that the choice of $e_{3N} = 20$ for the previous calculations is justified.

The inclusion of the energy correction emerging from the two-body Hamiltonian (MBPT(2b)) results in a lowering of the ground-state energies of about 1 MeV per nucleon for ${}^4\text{He}$ and about 2.5 MeV for ${}^{16}\text{O}$ and ${}^{40}\text{Ca}$. This correction has to be almost constant with respect to the cut-off parameter as the two-body Hamiltonian is independent of the cut-off, this term is affected only indirectly via high-lying HF single-particle states. As seen in Figures 5.10 and 5.11 the HF+MBPT(2b) energies essentially depend on e_{3N} via the HF energy, confirming the above consideration.

The energy corrections involving the three-body interaction directly depend on the

cut-off parameter, because the sums over particle states above the Fermi energy probe the high-lying matrix elements. Compared to MBPT(2b), MBPT(2b+3bp-ph) can change the ground-state energy in either direction. In contrast, including also the term containing 3p3h excitations, i.e. MBPT(2b+3b) compared to MBPT(2b+3bp-ph), one always arrives at a lowering of the energy as can be seen in Equation (5.12).

For all three nuclei, the step from MBPT(2b) to MBPT(2b+3b) results in a slight increase of the ground-state energies for the smallest values of the cut-off parameter for both the S-UCOM(SRG) and the S-SRG interaction. Considering ${}^4\text{He}$, increasing the cut-off leads to a significant gain of binding energy of about 2 MeV for the S-UCOM(SRG) interaction and about 1.5 MeV for the S-SRG interaction, where the main contribution results from the matrix elements involving 3p3h excitations. In contrast, comparing MBPT(2b+3b) to MBPT(2b) for ${}^{16}\text{O}$ and ${}^{40}\text{Ca}$ reveals that the ground-state energy is slightly increased for small values of the cut-off, but remains almost unchanged for larger values. These calculations were done in a model space with $e_{\text{max}} = 10$. If the cut-off is further increased beyond $e_{3N} \geq 3e_{\text{max}} = 30$ all energies will become independent of this cut-off.

Figures 5.10 and 5.11 already indicate the systematics of the MBPT(2b+3b) corrections: For most nuclei the contribution emerging from the three-body interaction compared to the full energy correction is small particularly when compared to other uncertainties, e.g. the convergence with respect to the model space (cf. Figs. 5.16 and 5.17). Therefore, and due to the fact that the calculation of the full MBPT(2b+3b) is currently not feasible for heavy nuclei, we will consider only MBPT(2b) using $e_{3N} = 20$ for the following calculations. This restriction allows us to estimate the perturbative corrections up to ${}^{208}\text{Pb}$. However, one has to keep in mind that the full second-order correction MBPT(2b+3b) leads to significant lowering of the ground-state energy compared to MBPT(2b) for very light nuclei, i.e. ${}^4\text{He}$, which improves the agreement with experiment (cf. Figs. 5.16 and 5.17).

For the UCOM(SRG) interaction we obtain similar results, therefore, they are not shown here. For the SRG interaction, however, the picture is somewhat different, which is demonstrated in Figure 5.12. Including the second-order energy corrections emerging from the three-body interaction (MBPT(2b+3b)) leads to a substantial energy gain for larger values of the cut-off e_{3N} compared to MBPT(2b) for all nuclei. For ${}^4\text{He}$ this results in an overbinding. But also for the other nuclei the influence of the three-body interaction on the second-order energy corrections is not negligible. Nonetheless, we will only consider MBPT(2b) as the calculation of MBPT(2b+3b) is not feasible for heavier nuclei, where we have to keep in mind the observed importance of MBPT(2b+3b).

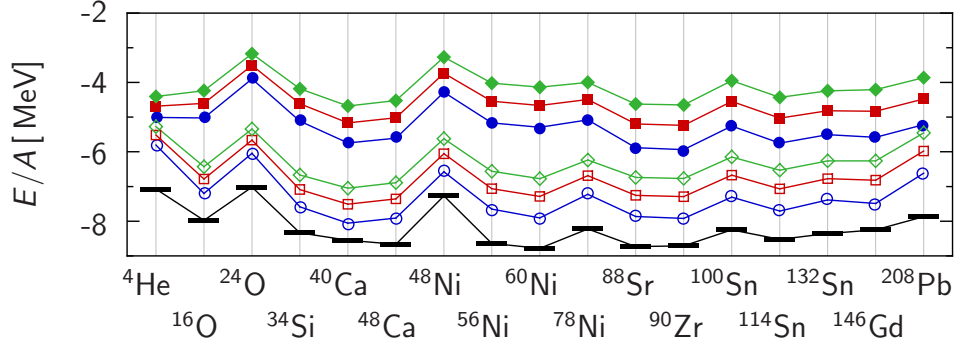


Figure 5.13: Ground-state energies per nucleon based on the S-UCOM(SRG) interaction for $\alpha = 0.16 \text{ fm}^4$, $e_{\text{max}} = 10$, $e_{3N} = 20$, and different three-body strengths: (\bullet, \circ) $C_{3N} = 1.6 \text{ GeV fm}^6$, (\blacksquare, \square) $C_{3N} = 2.2 \text{ GeV fm}^6$, (\blacklozenge, \diamond) $C_{3N} = 2.8 \text{ GeV fm}^6$. Filled symbols indicate the HF energies, open symbols include the MBPT corrections. The bars indicate the experimental values [30].

The dependence of the MBPT(2b) energy corrections on the strength of the three-body interaction, the flow parameter and the model space size will be discussed in the following. Figure 5.13 shows the dependence of the perturbative energy corrections on the strength of the three-body interaction for the S-UCOM(SRG) interaction with $\alpha = 0.16 \text{ fm}^4$. The inclusion of long-range correlations via MBPT leads to a substantial lowering of the ground-state energies across the whole nuclear chart. The energy gain per nucleon with increasing three-body strength is almost constant for all considered nuclei. For the heaviest nuclei the energy gain is slightly smaller, which can be explained by the model space size being not sufficiently large to obtain fully converged results. Furthermore, the perturbative correction for ${}^4\text{He}$ is small compared to the neighboring nuclei. But for this nucleus it was shown that the perturbative corrections emerging from the three-body interaction have a significant effect and their inclusion would yield a further lowering of the ground-state energy. Enhancing the repulsion of the three-body interaction leads to an increase of the HF ground-state energies as well as the HF+MBPT(2b) energies. The amount of energy gain is constant for the different three-body strengths. As they reveal no further insight, the corresponding figures for the UCOM(SRG), SRG and S-SRG interactions are only shown in Appendix E.

In order to emphasize the differences in the dependencies on the flow parameter, the corresponding results are shown for all four interactions in Figures 5.14 and 5.15. In all cases the MBPT(2b) ground-state energies per nucleon are lowered with increasing flow parameter and differ by about 0.5 to 1 MeV from experiment in case of the larger value. Thus, choosing the larger flow parameters, i.e. $\alpha = 0.16 \text{ fm}^4$ for UCOM(SRG) and S-UCOM(SRG) as well as $\alpha = 0.10 \text{ fm}^4$ for SRG and S-SRG (cf. Tab. 5.1),

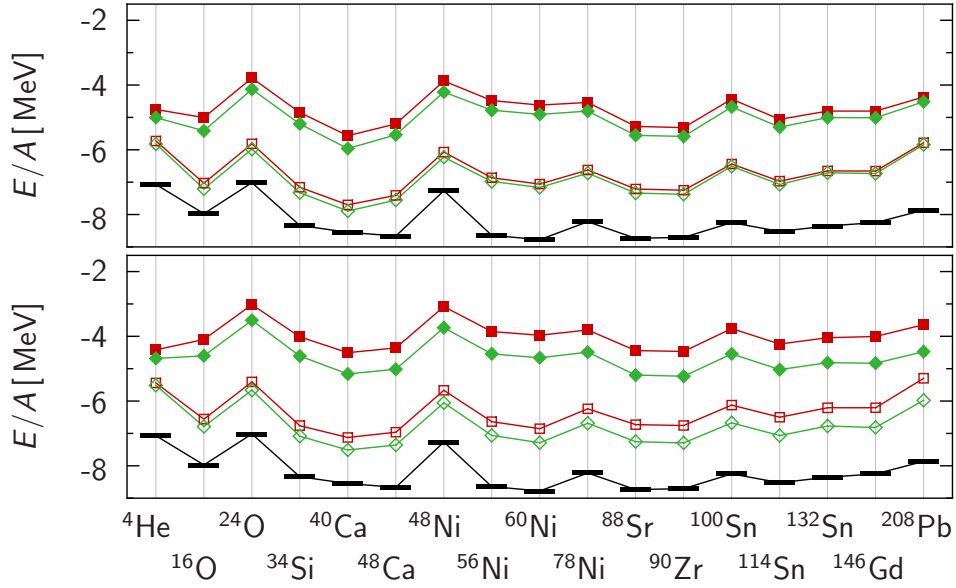


Figure 5.14: Ground-state energies per nucleon based on the UCOM(SRG) interaction with $C_{3N} = 1.6 \text{ GeV fm}^6$ (upper panel) and the S-UCOM(SRG) interaction with $C_{3N} = 2.2 \text{ GeV fm}^6$ (lower panel) for $e_{\text{max}} = 10$, $e_{3N} = 20$, and different flow parameters: (■, □) $\alpha = 0.12 \text{ fm}^4$, (◆, ◇) $\alpha = 0.16 \text{ fm}^4$. Filled symbols indicate the HF energies, open symbols include the MBPT corrections. The bars indicate the experimental values [30].

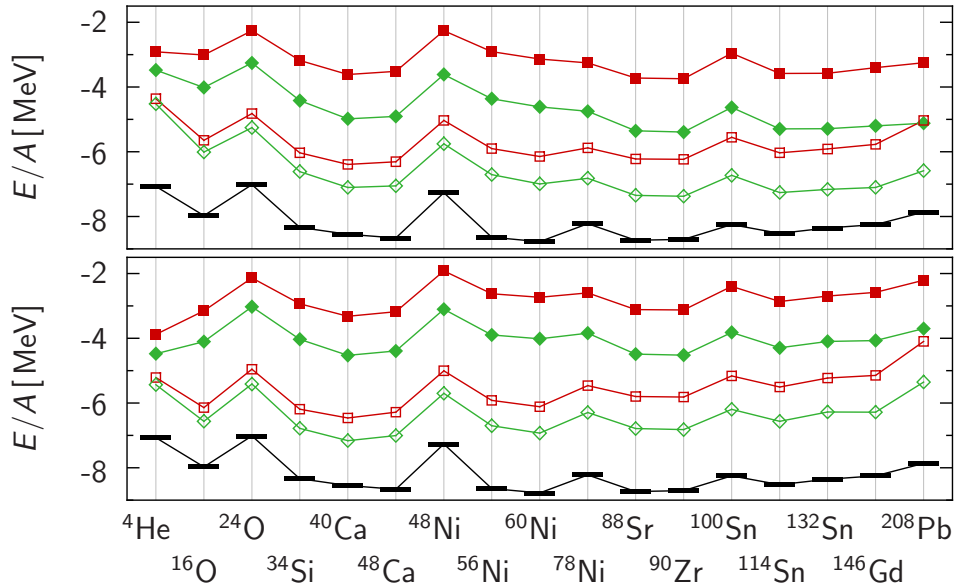


Figure 5.15: Same as in Figure 5.14 for the SRG with $C_{3N} = 4.3 \text{ GeV fm}^6$ (upper panel) and the S-SRG interaction with $C_{3N} = 2.0 \text{ GeV fm}^6$ (lower panel) with $e_{\text{max}} = 10$, $e_{3N} = 20$, and (■, □) $\alpha = 0.06 \text{ fm}^4$, (◆, ◇) $\alpha = 0.10 \text{ fm}^4$.

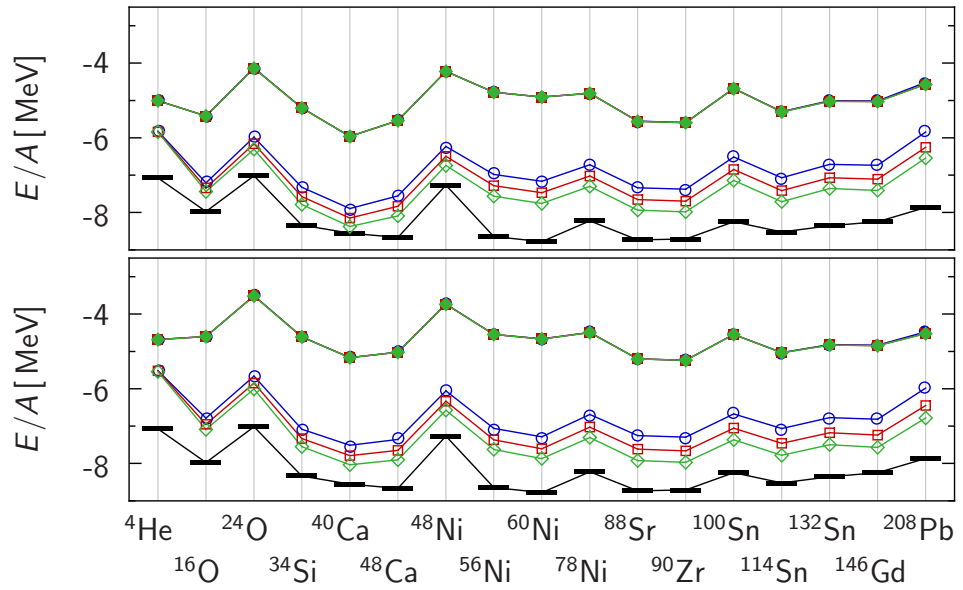


Figure 5.16: Ground-state energies per nucleon based on the UCOM(SRG) interaction with $C_{3N} = 1.6 \text{ GeV fm}^6$ (upper panel) and the S-UCOM(SRG) interaction with $C_{3N} = 2.2 \text{ GeV fm}^6$ (lower panel) for $\alpha = 0.16 \text{ fm}^4$, $e_{3N} = 20$ and different basis sizes: (●,○) $e_{\text{max}} = 10$; (■,□) $e_{\text{max}} = 12, l_{\text{max}} = 10$; (◆,◇) $e_{\text{max}} = 14, l_{\text{max}} = 10$. Filled symbols indicate the HF energies, open symbols include the MBPT corrections. The bars indicate the experimental values [30].

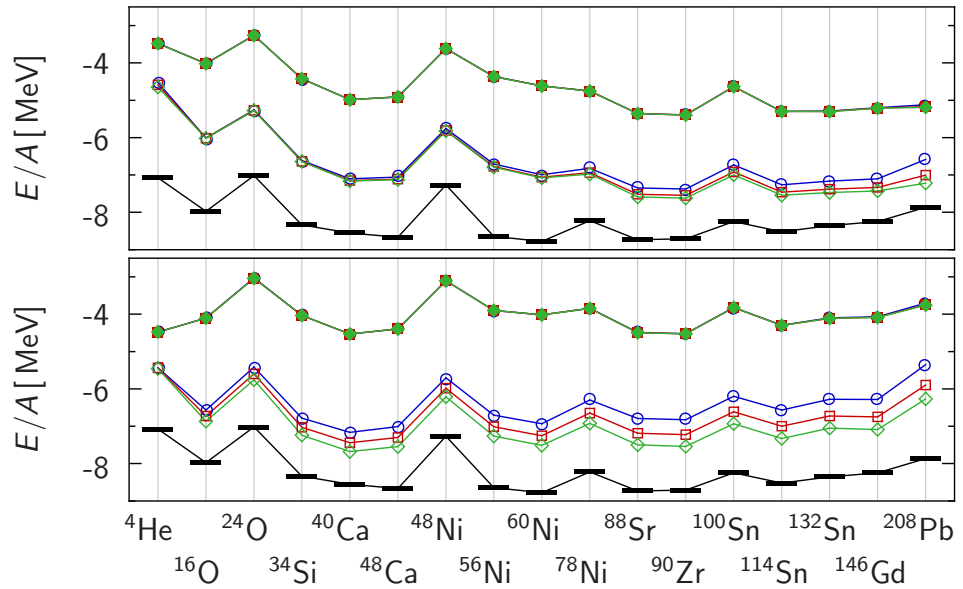


Figure 5.17: Same as in Figure 5.16 for the SRG interaction with $C_{3N} = 4.3 \text{ GeV fm}^6$ (upper panel) and the S-SRG interaction with $C_{3N} = 2.0 \text{ GeV fm}^6$ (lower panel) with $\alpha = 0.10 \text{ fm}^4$, $e_{3N} = 20$ and (●,○) $e_{\text{max}} = 10$; (■,□) $e_{\text{max}} = 12, l_{\text{max}} = 10$; (◆,◇) $e_{\text{max}} = 14, l_{\text{max}} = 10$.

for further investigations seems appropriate. As already observed on the basis of pure two-body interactions the perturbative energy corrections decrease with increasing flow parameter. In contrast to the results obtained with the pure two-body interactions, the respective three-body interaction compensates for the overbinding observed for the larger values of the flow parameter (cf. Sec. 3.5, especially Figures 3.9 and 3.10).

Finally, the convergence of the MBPT(2b) energies is examined by increasing the model space size in Figures 5.16 and 5.17. For the UCOM(SRG), the S-UCOM(SRG) and the S-SRG interactions with the appropriate three-body interactions the MBPT energies are not yet converged, even for the largest basis size. But as the considered nuclei are still slightly underbound an extrapolation to infinite basis sizes would result in a reasonable agreement with the experimental ground-state energies. However, one has to keep in mind that the second-order perturbative energy corrections only serve as an estimate as already discussed in Section 3.5. The picture is somewhat different for the SRG interaction where the MBPT(2b) energies are converged, but still exhibit a significant difference to experiment, especially for the light and intermediate nuclei. But for this interaction we have demonstrated in Figure 5.12 that the influence of the energy corrections emerging from the three-body interaction is significantly larger. Therefore, including these terms would improve the agreement with the experimental ground-state energies.

Chapter 5 · Three-Body Contact Interaction

Chapter 6

Few-Body Calculations

In the previous chapters we have used the Hartree-Fock method and many-body perturbation theory, which both aim at an approximate solution of the nuclear many-body problem. We will now focus on an exact solution in the framework of the No-Core Shell Model (NCSM). We will briefly introduce the NCSM in Section 6.1 and calculate the ${}^4\text{He}$ ground-state energy in Section 6.2.

6.1 The No-Core Shell Model

The No-Core Shell Model [12, 43] aims at an exact numerical solution of the nuclear eigenvalue problem

$$H|\Psi_n\rangle = E_n|\Psi_n\rangle, \quad (6.1)$$

where we again use the Hamiltonian

$$H = T_{\text{int}} + V_{\text{NN}} + V_{3\text{N}} \quad (6.2)$$

consisting of the intrinsic kinetic energy T_{int} , the two-nucleon interaction V_{NN} , and the three-nucleon interaction $V_{3\text{N}}$. The eigenvalue problem is solved by diagonalizing the Hamilton matrix. Therefore, we have to choose a many-body basis, which is given by Slater determinants $|\Phi_\nu\rangle$ built of single-particle harmonic-oscillator eigenstates. The eigenstates of the Hamiltonian are expanded in these Slater determinants:

$$|\Psi_n\rangle = \sum_{\nu} C_{\nu}^n |\Phi_{\nu}\rangle. \quad (6.3)$$

As the number of Slater determinants is infinite one has to truncate the many-body basis to obtain a tractable eigenvalue problem in a finite model space. This is achieved by restricting the maximum number of harmonic-oscillator excitation quanta N_{\max} with respect to the configuration with the lowest possible energy. The specific choice of the basis and the corresponding truncation guarantee that the eigenstates of the Hamiltonian are free of spurious center-of-mass contaminations. Furthermore, the NCSM follows the variational principle, i.e. the energies converge monotonically from above towards the exact value.

The NCSM is a powerful tool to investigate the properties of the applied interactions regarding convergence behavior as well as the agreement of calculated observables with experimental data. However, the model space sizes required to obtain converged results increase factorially with the number of nucleons, which restricts the applicability to light nuclei.

6.2 ${}^4\text{He}$ Ground-State Energy

We use the No-Core Shell Model to calculate the ground-state energy of ${}^4\text{He}$. The oscillator frequency defining the single-particle harmonic-oscillator basis is set to $\hbar\Omega = 28 \text{ MeV}$.

In Figure 6.1 we display the ${}^4\text{He}$ ground-state energy calculated on the basis of the S-UCOM(SRG) interaction with $\alpha = 0.16 \text{ fm}^4$ as function of the model space size N_{\max} for different values of the three-body strength C_{3N} . In these calculations the three-body cut-off e_{3N} is larger than the model space size N_{\max} , i.e. the results are independent of the three-body cut-off. As expected the energies slightly increase with increasing three-body strength. For the calculations including the three-body interaction the largest model space is not sufficient to obtain fully converged results. For comparison the energies obtained with the pure two-body interaction using the same flow parameter are shown, which can be performed in larger model spaces and which show a similar convergence behavior. Thus, the convergence behavior of the energies obtained with the three-body interaction can be deduced from the results obtained with the pure two-body interaction. Moreover, an extrapolation towards infinite model spaces based on the values obtained in the largest three model spaces ($N_{\max} = 6, 8, 10$) is carried out, the resulting values are indicated by horizontal lines. Even the weakest three-body interaction leads to underbinding of 1.1 MeV. In the framework of the Hartree-Fock approximation (cf. Sec. 5.2, Tab. 5.1) we have seen, that the charge radii are best reproduced using $C_{3N} = 2.2 \text{ GeV fm}^6$. But the difference between the respective ${}^4\text{He}$

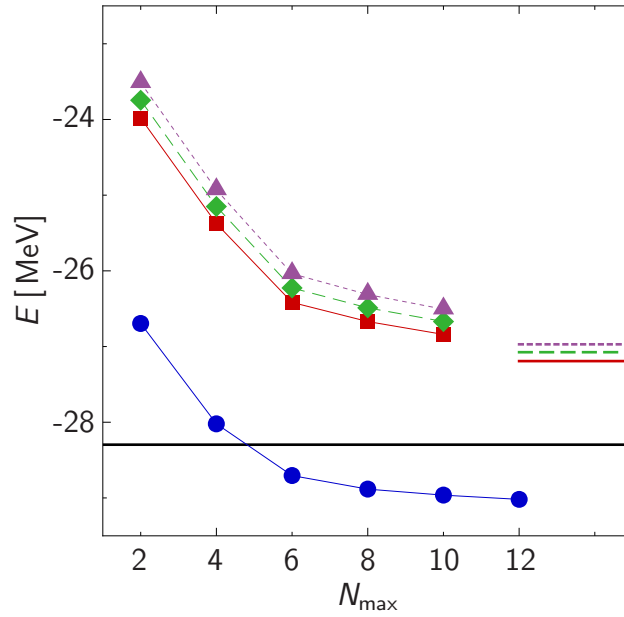


Figure 6.1: Ground-state energy of ${}^4\text{He}$ as function of the model space size based on the S-UCOM(SRG) interaction with $\alpha = 0.16 \text{ fm}^4$, $e_{\max} = 12$, and different three-body strengths: (■) $C_{3N} = 2.0 \text{ GeV fm}^6$, (◆) $C_{3N} = 2.2 \text{ GeV fm}^6$, (▲) $C_{3N} = 2.4 \text{ GeV fm}^6$. The horizontal lines indicate the corresponding energies obtained by extrapolating $N_{\max} \rightarrow \infty$. For comparison the results obtained with the pure two-body interaction (●) as well as the experimental value [30] (—) are shown.

ground-state energies is only 120 keV. Adding the second-order perturbative energy correction resulting from the full two- plus three-body interaction to the HF ground-state energy, one arrives at an overbinding of 1.1 MeV. Thus, the difference to the experimental ${}^4\text{He}$ ground-state energy is the same in the framework of the NCSM and HF plus MBPT, but the NCSM leads to an underbinding while HF plus MBPT yields an overbinding of ${}^4\text{He}$.

Figure 6.2 shows the corresponding results obtained with the S-SRG interaction using $\alpha = 0.10 \text{ fm}^4$. The energies show a similar behavior as observed for the S-UCOM(SRG) interaction except that they show a slightly faster convergence resulting in a larger deviation from the experimental value of 1.9 MeV for the weakest three-body interaction. In this case, the values obtained in the three largest model spaces do not exhibit an exponential convergence behavior. Therefore, the extrapolation was performed using four energies ($N_{\max} = 4, 6, 8, 10$). The ${}^4\text{He}$ ground-state energy obtained from HF plus MBPT differs only slightly from the experimental energy, i.e. including the full two- plus three-body second-order energy correction leads to an

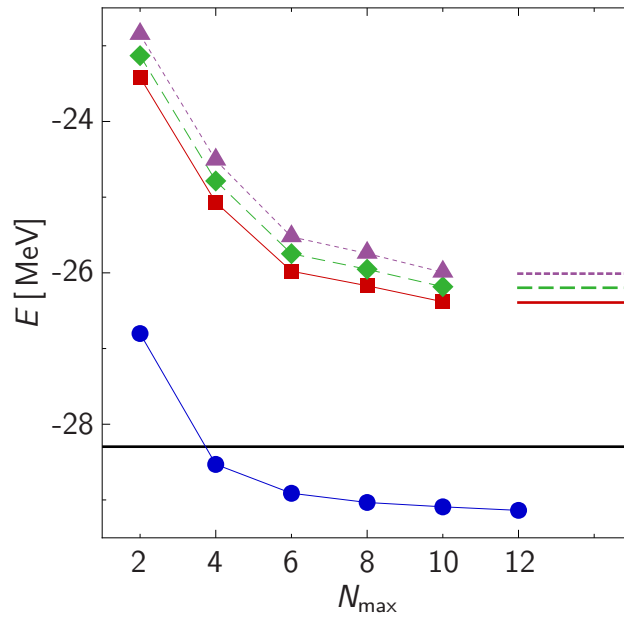


Figure 6.2: Same as in Figure 6.1 for the S-SRG interaction with $\alpha = 0.10 \text{ fm}^4$, $e_{\max} = 12$, and (■) $C_{3N} = 2.0 \text{ GeV fm}^6$, (◆) $C_{3N} = 2.2 \text{ GeV fm}^6$, (▲) $C_{3N} = 2.4 \text{ GeV fm}^6$. For comparison: (●) pure two-body interaction, (—) experiment [30].

overbinding of 130 keV.

For a consistent study one would also have to investigate the dependencies of the ${}^4\text{He}$ ground-state energy on the flow parameter α and the oscillator frequency Ω , where the dependence on the oscillator frequency is expected to be weak [10].

In summary, the ${}^4\text{He}$ ground-state energies obtained with the three-body contact interaction differ from the experimental value by 1 to 2 MeV, which is a promising result but still leaves room for improvement. In principle, it is possible to choose the parameters such that the experimental ${}^4\text{He}$ ground-state energy is reproduced, but obviously this would also change the results for the charge radii on the basis of the HF approximation.

Chapter 7

Collective Excitations

In the previous chapters we have studied ground-state properties of nuclei across the whole nuclear chart. In this chapter we will focus on excited states, particularly collective excitations. On the one hand the investigation of collective excitations provides valuable information about the underlying interaction. On the other hand, a detailed knowledge especially of giant resonances provides information on properties of nuclear matter and is important for various applications, e.g. in nuclear astrophysics for the understanding of supernovae. A suitable method for the investigation of collective excitation modes is the Random Phase Approximation (RPA) based self-consistently on a Hartree-Fock calculation. The general RPA equations are derived in Appendix C. In the following we will outline the RPA on the basis of unitarily transformed two-body interactions in Section 7.1, where the three-body contact interaction is replaced by a density-dependent two-body interaction. After introducing multipole transition operators in Section 7.2, we will discuss the energy-weighted sum rules in Section 7.3 to ensure the proper implementation of the RPA. Finally, the response functions obtained for three different excitation modes will be investigated in detail in Section 7.4.

7.1 Random Phase Approximation

The Random Phase Approximation is based on Hartree-Fock single-particle states. Therefore, as in the HF method, we would prefer to use the intrinsic Hamiltonian H_{int} containing the intrinsic kinetic energy $T_{\text{int}} = T - T_{\text{cm}}$, the unitarily transformed two-body interaction V_{NN} as well as the phenomenological three-body interaction $V_{3\text{N}}$. The

inclusion of the full three-body interaction in RPA calculations is, however, very time-extensive. Fortunately, for Hartree-Fock calculations of even-even nuclei the three-body contact interaction (without regularization) is equivalent to a density-dependent two-body interaction [44, 45]

$$V_{\text{NN}}[\varrho] = \frac{C_{3\text{N}}}{6} (1 + P_\sigma) \varrho \left(\frac{\mathbf{r}_1 + \mathbf{r}_2}{2} \right) \delta^{(3)}(\mathbf{r}_1 - \mathbf{r}_2) \quad (7.1)$$

with the spin-exchange operator P_σ . This equivalence holds also for RPA [46]. The Hamiltonian thus reads

$$H_{\text{int}} = T_{\text{int}} + V_{\text{NN}} + V_{\text{NN}}[\varrho] . \quad (7.2)$$

Note, that for the HF calculations providing the basis for RPA the density-dependent two-body interaction is employed instead of the three-body contact interaction for consistency. The only difference is that in this way the three-body interaction enters without the cut-off $e_{3\text{N}}$ in the HF method. In the following we will refer to the three-body interaction although it is technically included as density-dependent two-body interaction.

As already in the previous chapters, we will restrict our studies to spherically symmetric nuclei so that the single-particle angular momenta can be coupled to good total angular momentum J indicating the multipolarity of the respective collective state. The excited states are generated by the operators $Q_{\nu, JM}^\dagger$ (cf. Eq. (C.2)):

$$Q_{\nu, JM}^\dagger |\Psi_0\rangle = |\Psi_\nu\rangle , \quad Q_{\nu, JM} |\Psi_0\rangle = 0 \quad (7.3)$$

with the RPA ground-state $|\Psi_0\rangle = |\text{RPA}\rangle$. The excitation operators are formulated in the coupled representation [47, 48]

$$Q_{\nu, JM}^\dagger = \sum_{\text{ph}} (X_{\text{ph}}^{\nu, JM} A_{\text{ph}}^{J, M^\dagger} - (-1)^{J-M} Y_{\text{ph}}^{\nu, JM} A_{\text{ph}}^{J, -M}) , \quad (7.4)$$

where the summation includes all particle-hole (ph) excitations of the HF ground-state, and

$$A_{\text{ph}}^{J, M^\dagger} = \sum_{m_p m_h} c \left(\begin{matrix} j_p & j_h & J \\ m_p & m_h & M \end{matrix} \right) (-1)^{j_h - m_h} a_{j_p m_p}^\dagger a_{j_h m_h} \quad (7.5)$$

represents the ph-creation operator built of the single-particle creation and annihilation operators a_{jm}^\dagger and a_{jm} , respectively. The RPA equations are written as

$$\begin{pmatrix} A^J & B^J \\ B^{J^*} & A^{J^*} \end{pmatrix} \begin{pmatrix} X^{\nu, JM} \\ Y^{\nu, JM} \end{pmatrix} = \hbar\omega_\nu \begin{pmatrix} 1 & 0 \\ 0 & -1 \end{pmatrix} \begin{pmatrix} X^{\nu, JM} \\ Y^{\nu, JM} \end{pmatrix} \quad (7.6)$$

with the amplitudes $X_{\text{ph}}^{\nu, JM}$ and $Y_{\text{ph}}^{\nu, JM}$, and the RPA eigenvalues $\hbar\omega_\nu$. For the derivation of this eigenvalue problem one has to exploit the quasi-boson approximation, and the RPA ground-state is approximated by the HF ground-state (cf. Appendix C). Thus, the matrices A^J and B^J are obtained from

$$\begin{aligned} A_{\text{php}'h'}^J &= \langle \text{HF} | \left[[A_{\text{ph}}^{J,M}, H_{\text{int}}], A_{\text{p}'h'}^{J,M\dagger} \right] | \text{HF} \rangle \\ B_{\text{php}'h'}^J &= - \langle \text{HF} | \left[[A_{\text{ph}}^{J,M}, H_{\text{int}}], (-1)^{J-M} A_{\text{p}'h'}^{J,-M} \right] | \text{HF} \rangle . \end{aligned} \quad (7.7)$$

7.2 Multipole Transitions

In the following, we will investigate the impact of the three-body contact interaction on electric multipole transitions. The reduced transition probability

$$B^T(EJ, J_0 \rightarrow J_\nu) = B_J^T(\omega_\nu) = \frac{1}{2J_0 + 1} |\langle \nu | Q_J^T | 0 \rangle|^2 \quad (7.8)$$

describes the response on these excitation modes [14, 48]. The reduced matrix element $\langle \nu | Q_J^T | 0 \rangle$ connects the initial state $|0\rangle$, which is the ground-state in our case, with the final state $|\nu\rangle$ via the multipole transition operator Q_J^T . In the following we will consider isoscalar monopole (ISM) excitations for which the transition operator is given by

$$Q_{00}^0 = \sum_{i=1}^A x_i^2 Y_{00}(\vartheta_i, \varphi_i) , \quad (7.9)$$

isovector dipole (IVD) excitations with the transition operator

$$Q_{1M}^1 = e \sum_{i=1}^A \tau_3^{(i)} x_i Y_{1M}(\vartheta_i, \varphi_i) , \quad (7.10)$$

as well as the isoscalar quadrupole (ISQ) excitation operator

$$Q_{2M}^0 = e \sum_{i=1}^A x_i^2 Y_{2M}(\vartheta_i, \varphi_i) \quad (7.11)$$

with the elementary charge e , the third component of the isospin τ_3 and the spherical harmonics $Y_{JM}(\vartheta, \varphi)$. As unitarily transformed NN potentials enter in the Hamiltonian, the transition operators should be transformed consistently. However, for the UCOM

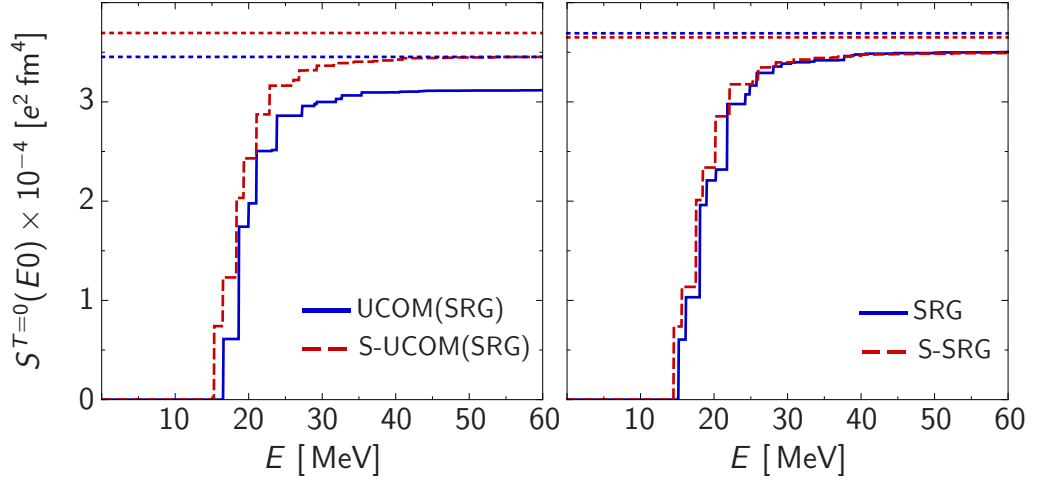


Figure 7.1: Cumulative energy-weighted sum of the isoscalar monopole transition strengths for ^{40}Ca as function of the excitation energy based on calculations including the density-dependent two-body interaction compared to the classical sum rule (dotted lines).

transformation it was shown that the difference between the response functions calculated with transformed and initial operators is marginal [14]. It is expected that the effect of the SRG transformation is small as well. Therefore, we will work with the bare transition operators (7.9) to (7.11) for the following studies.

7.3 Sum Rules

The transition operators introduced in the previous section satisfy sum rules, which provide a useful test of the RPA. For electromagnetic transitions the energy-weighted sum rule [49]

$$S = \sum_{\nu>0} \hbar\omega_{\nu} |\langle \nu | Q | 0 \rangle|^2 = \frac{1}{2} \langle 0 | [Q, [H, Q]] | 0 \rangle \quad (7.12)$$

is of special interest. We will only consider electric multipole transitions for which the energy-weighted sum rule is given by [14, 24]

$$S^T(EJ) = \sum_{\nu>0} \hbar\omega_{\nu} B_J^T(\omega_{\nu}) . \quad (7.13)$$

This energy-weighted sum of transition strengths can be compared to the classical sum rules, which are derived by evaluating the double commutator in Equation (7.12) under the assumption of a local interaction without any exchange terms. In this case

	UCOM(SRG)		S-UCOM(SRG)		SRG		S-SRG		
	(a)	(b)	(a)	(b)	(a)	(b)	(a)	(b)	
α [fm ⁴]	0.04	0.16	0.04	0.16	0.03	0.10	0.03	0.10	
C_{3N} [GeV fm ⁶]	–	1.6	–	2.2	–	4.3	–	2.0	
ISM	¹⁶ O	98.7	90.4	98.3	92.2	99.8	94.7	98.8	94.6
	⁴⁰ Ca	97.7	90.5	98.4	93.7	100.8	95.1	99.1	95.8
	⁹⁰ Zr	99.0	92.8	99.5	95.4	117.8	95.9	100.1	97.0
	²⁰⁸ Pb	101.7	95.7	100.6	97.4	158.8	97.1	100.9	98.4
IVD	¹⁶ O	180.1	193.2	175.4	179.8	173.4	160.9	172.9	174.7
	⁴⁰ Ca	194.1	209.0	183.9	188.5	187.9	168.3	180.9	182.4
	⁹⁰ Zr	205.6	218.9	192.3	195.1	207.7	173.4	188.9	188.4
	²⁰⁸ Pb	211.8	223.8	195.4	198.4	235.7	176.9	191.8	191.3
ISQ	¹⁶ O	103.0	104.3	101.0	100.2	102.2	100.3	101.3	100.7
	⁴⁰ Ca	102.2	102.9	100.8	100.0	102.8	100.1	101.1	100.6
	⁹⁰ Zr	102.1	102.0	100.9	100.0	110.1	100.0	101.2	100.5
	²⁰⁸ Pb	101.1	99.9	99.6	98.5	127.6	98.4	99.7	98.9

Table 7.1: Exhaustion of the energy-weighted sum rules, i.e. $S^T(EJ)/S_{\text{class}}^T(EJ)$ in percent for (a) the pure two-body interaction, (b) including the three-body interaction.

only the kinetic energy contributes to the commutator and we obtain for isoscalar monopole excitations

$$S_{\text{class}}^{T=0}(E0) = \frac{2\hbar^2 e^2}{m} (N\langle r_n^2 \rangle + Z\langle r_p^2 \rangle) \quad (7.14)$$

with the neutron and proton root-mean-square radii $r_{n/p}$. Considering the isovector dipole excitation operator one arrives at the Thomas-Reiche-Kuhn sum rule:

$$S_{\text{class}}^{T=1}(E1) = \frac{\hbar^2 e^2}{2m} \frac{9}{4\pi} \frac{NZ}{A} . \quad (7.15)$$

Finally, the classical sum rule for isoscalar quadrupole excitations is given by

$$S_{\text{class}}^{T=0}(E2) = \frac{25\hbar^2 e^2}{4\pi m} (N\langle r_n^2 \rangle + Z\langle r_p^2 \rangle) . \quad (7.16)$$

The UCOM and SRG transformed interactions are not purely local but contain non-local contributions as well as exchange terms. This will lead to an enhancement of the energy-weighted sum rules. Hence, the overestimation of the classical sum rules

is a measure for the non-locality of the applied interaction. Especially the model-independent Thomas-Reiche-Kuhn sum rule is expected to be exceeded by 40 – 80%. On the other hand a significant underestimation of the classical sum rules hints at instabilities in the RPA, e.g. incomplete convergence with respect to the model space size or unstable ground-state.

A typical example for the cumulative energy-weighted sum of the transition strengths is shown in Figure 7.1 for the isoscalar monopole response of ^{40}Ca calculated with the four different two-body interactions including the three-body interaction and compared to the classical sum rule. For all four interactions the sums converge to their final values above 50 MeV but underestimate the classical sum rules by up to 10%.

The exhaustion of the sum rules is listed in Table 7.1 using all four interactions for the three excitation modes in ^{16}O , ^{40}Ca , ^{90}Zr and ^{208}Pb . The values obtained with the pure two-body interactions (columns (a)) are compared to those obtained after including the three-body interaction (columns (b)). For the isoscalar monopole excitation the deviation from the classical sum rule does not exceed 2.3% for the pure two-body UCOM(SRG), S-UCOM(SRG) and S-SRG interactions. For the SRG interaction, however, the sum rule is significantly overestimated for the heavy isotopes. For illustration, the cumulative energy-weighted sum of the transition strengths is shown in Figure 7.2 comparing the four pure two-body interactions for ^{208}Pb . For the UCOM(SRG), the S-UCOM(SRG) and the S-SRG interactions the sums converge above 50 MeV to their final values, which are in nice agreement with the classical sum rule. For the SRG interaction, however, the cumulative energy-weighted sum increases far beyond the classical sum rule.

When including the three-body interaction the deviation of the classical monopole sum rule reaches up to 10%, but on the other hand, the strong overestimation by the SRG interaction is suppressed. Since density-dependent interactions do not affect the sum rules [46], this effect is due to the variation of the flow parameter. Increasing the flow parameter on the one hand generates nonlocal contributions to the respective interaction, on the other hand the HF single-particle spectra, which provide the starting point for RPA, obtained with the pure two-body interactions are spread wider, i.e. discrepancies to experimental data are increased. These effects lead to a larger deviation of the classical sum rule for the UCOM(SRG), S-UCOM(SRG), and S-SRG interactions and for the light nuclei calculated with the SRG interaction. For the heavy nuclei calculated with the SRG interaction the HF calculations yield a strong overbinding of up to 20 MeV per nucleon for $\alpha = 0.10 \text{ fm}^4$. Therefore, one cannot expect to obtain a stable ground-state suitable for the application in RPA. The corresponding values for the ISM sum rule reveal this unphysical behavior [50].

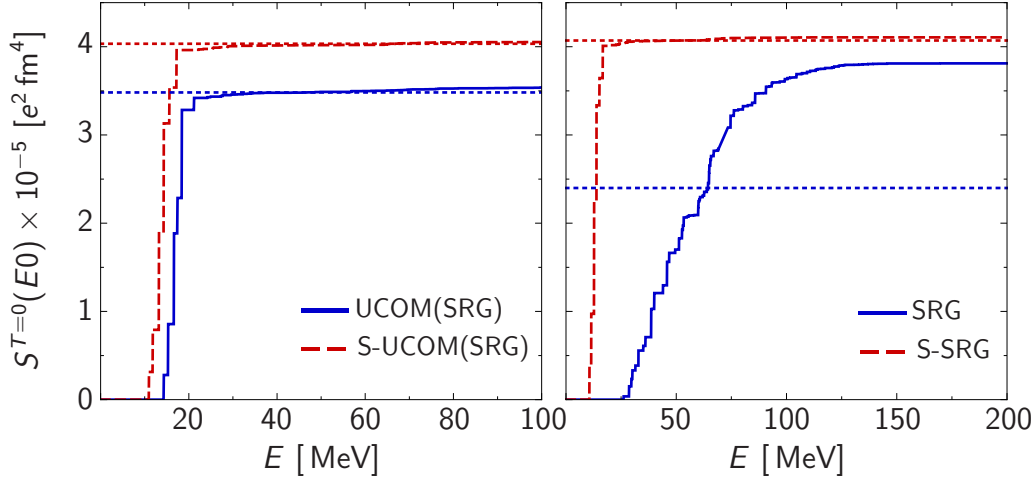


Figure 7.2: Cumulative energy-weighted sum of the isoscalar monopole transition strengths for ^{208}Pb as function of the excitation energy based on the pure two-body interactions compared to the classical sum rule (dotted lines). Note the different energy scales.

For the isovector dipole excitations one observes an enhancement of the Thomas-Reiche-Kuhn sum rule of at least 60% reaching up to more than 100%. As mentioned above, an enhancement of the isovector dipole sum rule in this magnitude is expected due to the non-localities of the applied interactions.

Finally, the deviations of the classical isoscalar quadrupole sum rule are small for the pure two-body interactions as well as for the interactions including the three-body interaction. The monopole and dipole resonances are excitation modes involving essential all nucleons, while the giant quadrupole resonance is a vibration of the surface of the nucleus. Therefore, one expects the dependence on the flow parameter to be weaker, which is confirmed by the sum rules listed in Table 7.1. The only exceptions are, like for the monopole excitations, the heavy isotopes calculated with the pure two-body SRG interaction, which can be explained with the same arguments.

In summary, the cumulative energy-weighted sums of the transition strengths are mainly in reasonable agreement with the classical sum rules for the monopole and quadrupole excitations and reproduce the expected enhancement for the dipole resonances.

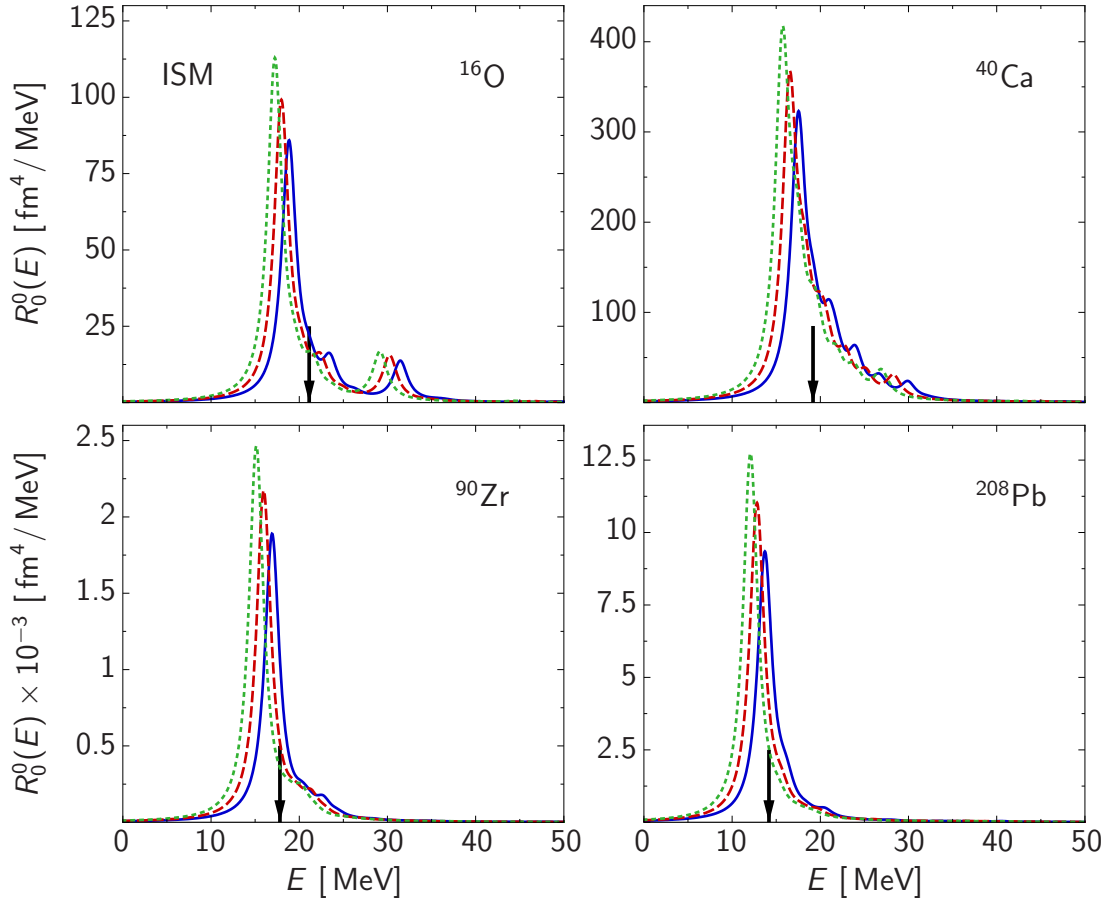


Figure 7.3: Isoscalar monopole response based on the S-UCOM(SRG) interaction with $\alpha = 0.16 \text{ fm}^4$, $e_{\text{max}} = 10$ for different three-body strengths: (—) $C_{3N} = 1.6 \text{ GeV fm}^6$, (---) $C_{3N} = 2.2 \text{ GeV fm}^6$, (⋯) $C_{3N} = 2.8 \text{ GeV fm}^6$. Centroid energies extracted from experiment [51–53] are indicated by arrows.

7.4 Giant Resonances

After the study of sum rules, we will now investigate the corresponding response functions. For ease of presentation, the calculated discrete strength distributions are convolved with a Lorentzian function yielding continuous strength functions in dependence of the excitation energy [14]:

$$R_J^T(E) = \sum_{\nu} B_J^T(\omega_{\nu}) \frac{1}{\pi} \frac{\Gamma/2}{(E - \omega_{\nu})^2 + (\Gamma/2)^2}, \quad (7.17)$$

where the width Γ of the Lorentzian distribution is set arbitrarily to 2 MeV. The Lorentzian function is chosen such that the energy-weighted sum rule is equal for the

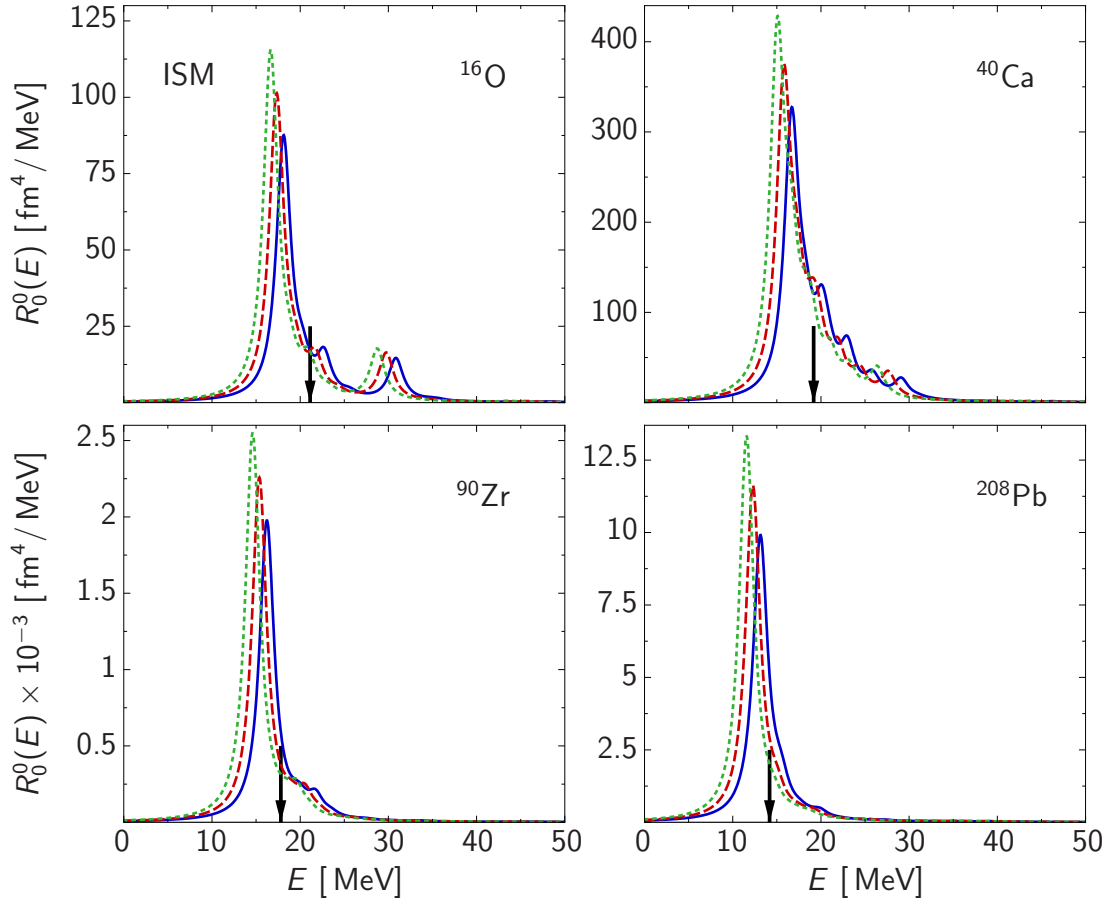


Figure 7.4: Same as in Figure 7.3 for the S-SRG interaction with $\alpha = 0.10 \text{ fm}^4$, $\epsilon_{\text{max}} = 10$, and (—) $C_{3N} = 1.5 \text{ GeV fm}^6$, (---) $C_{3N} = 2.0 \text{ GeV fm}^6$, (····) $C_{3N} = 2.5 \text{ GeV fm}^6$.

discrete distribution and the continuous strength function:

$$S_J^T = \sum_{\nu} E_{\nu} B_J^T(\omega_{\nu}) = \int dE E R_J^T(E). \quad (7.18)$$

7.4.1 Isoscalar Giant Monopole Resonance

First, we study the isoscalar giant monopole resonance, which is understood as a spherically symmetric compressional oscillation of the nucleus. As this mode is isoscalar protons and neutrons move in phase. This excitation mode is also known as breathing mode and is an important element in the investigation of various astrophysical scenarios, such as supernovae and neutron stars, as it is related to the compressibility of nuclear matter.

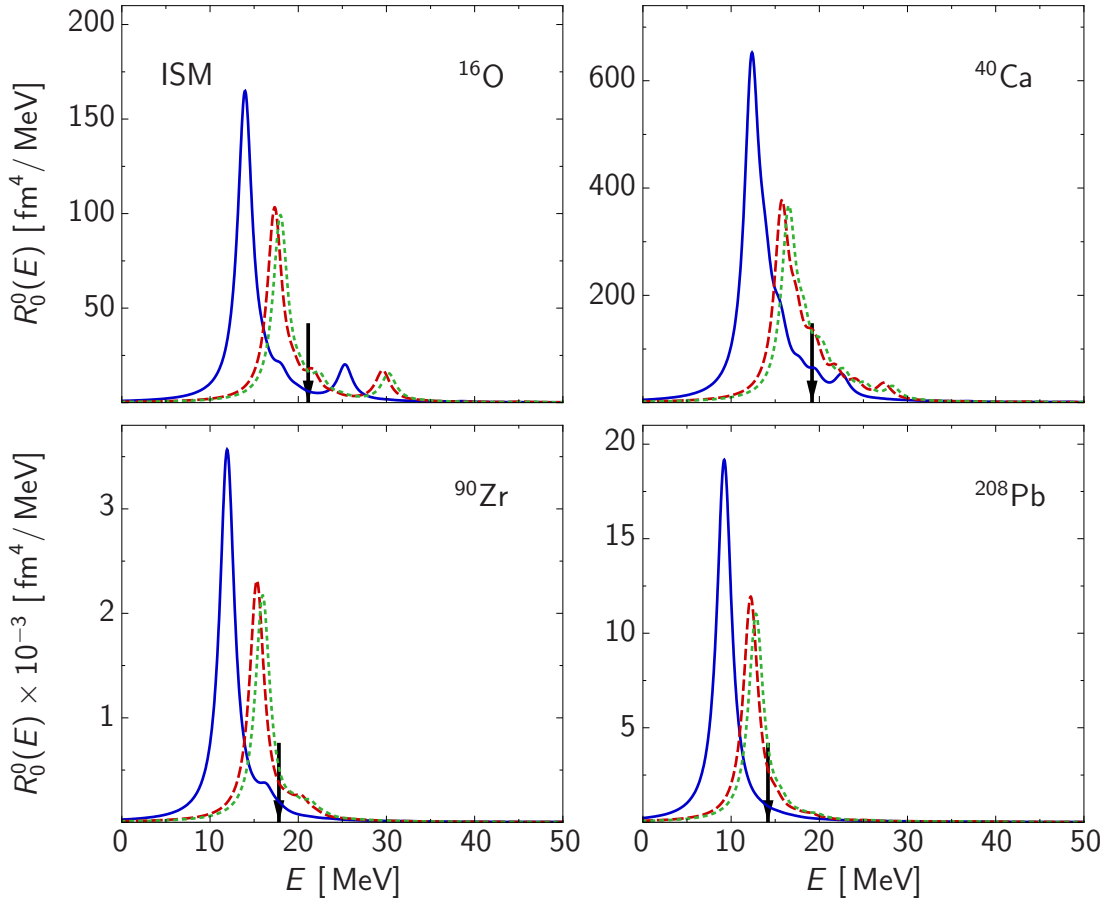


Figure 7.5: Isoscalar monopole response based on the S-UCOM(SRG) interaction with $C_{3N} = 2.2 \text{ GeV fm}^6$, $e_{\text{max}} = 10$ for different flow parameters: (—) $\alpha = 0.04 \text{ fm}^4$, (---) $\alpha = 0.12 \text{ fm}^4$, (⋯) $\alpha = 0.16 \text{ fm}^4$. Centroid energies extracted from experiment [51–53] are indicated by arrows.

In the following the four nuclei ^{16}O , ^{40}Ca , ^{90}Zr , and ^{208}Pb with the oscillator parameters listed in Table 3.2 are considered. The optimal parameter set for each of the four two- plus three-body interactions was determined in Chapter 5. The strength parameters C_{3N} were chosen on the basis of the three-body contact interaction. As this interaction is approximately equivalent to the density-dependent two-body interaction applied in the RPA, we will use the same values for C_{3N} . Nonetheless, we want to investigate the influence of the parameters on the giant monopole resonance. As the effects are similar for all four interactions only the S-UCOM(SRG) and the S-SRG interactions are shown here, the corresponding figures for the UCOM(SRG) and the SRG interactions can be found in Appendix E.3.

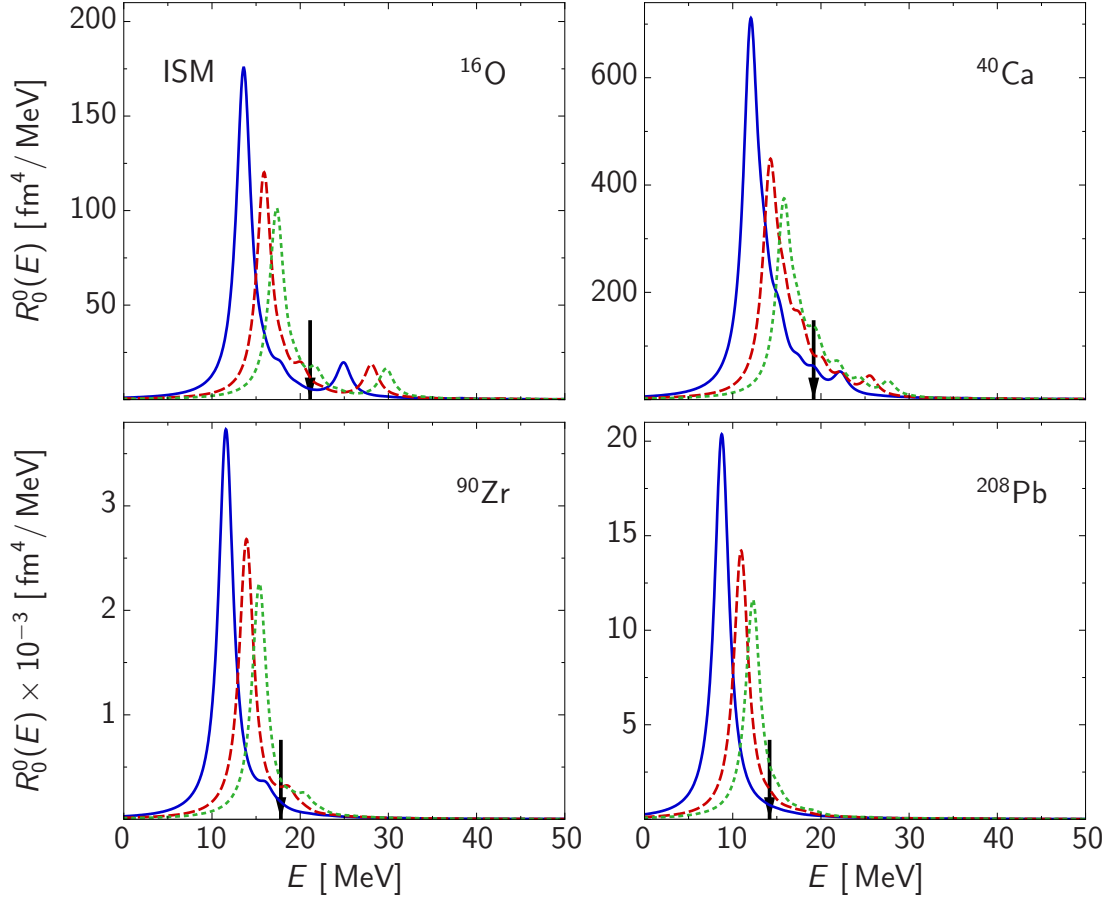


Figure 7.6: Same as in Figure 7.5 for the S-SRG interaction with $C_{3N} = 2.0 \text{ GeV fm}^6$, $e_{\text{max}} = 10$, and (—) $\alpha = 0.03 \text{ fm}^4$, (---) $\alpha = 0.06 \text{ fm}^4$, (····) $\alpha = 0.10 \text{ fm}^4$.

Figures 7.3 and 7.4 show the isoscalar monopole response for the S-UCOM(SRG) and the S-SRG interactions for different values of the strength C_{3N} . The arrows indicate the centroid energies extracted from experiment. The results are very similar for both interactions. The main peak of the response function of ^{16}O lies slightly below the experimental centroid with a second smaller peak at higher energies. For the other three nuclei the experimental centroids lie within the calculated response functions. Especially for the heavy nuclei ^{90}Zr and ^{208}Pb the response is concentrated in one strongly collective peak. In all cases, increasing the strength C_{3N} leads to a shift towards lower excitation energies, while the response is concentrated in a narrower peak. With increasing three-body strength the level density of the single-particle spectra increases, which leads to a lowering of the excitation energies.

The dependencies on the flow parameter are illustrated in Figures 7.5 and 7.6

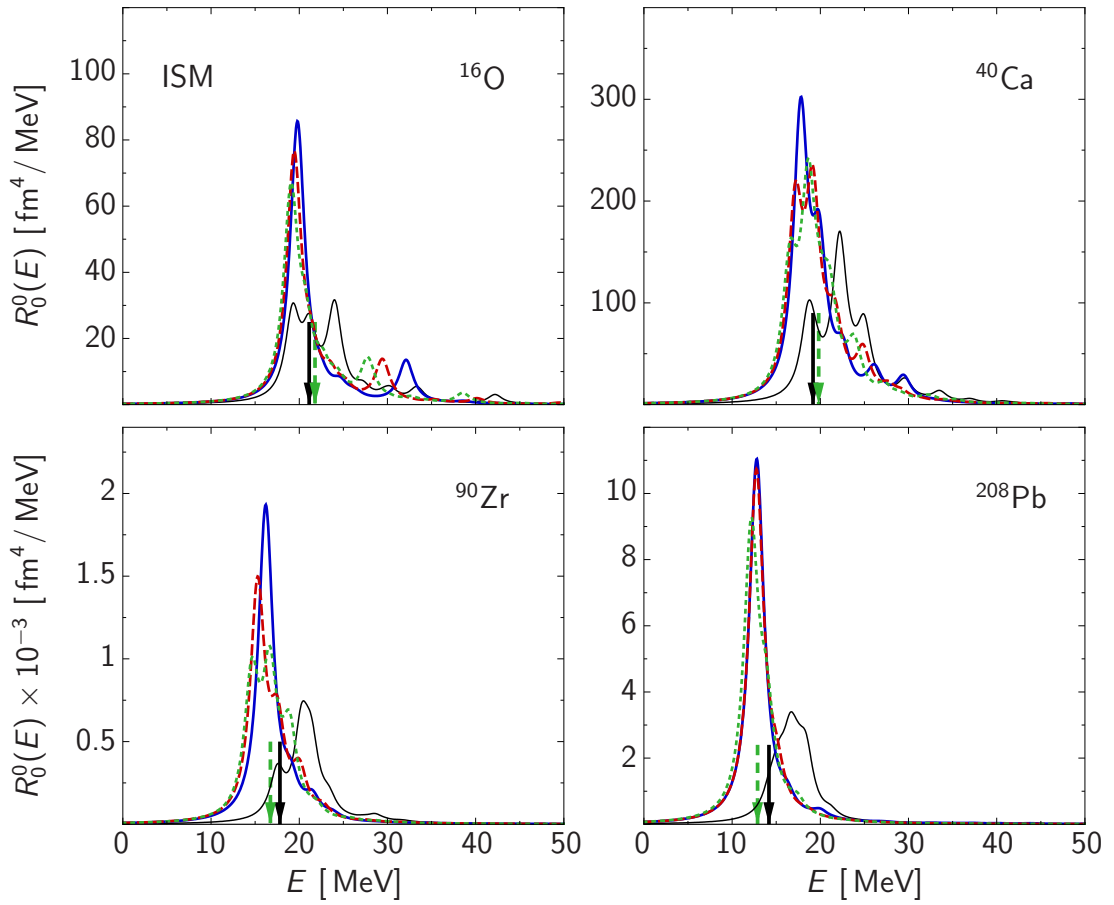


Figure 7.7: Isoscalar monopole response based on the UCOM(SRG) interaction with $\alpha = 0.16 \text{ fm}^4$, $C_{3N} = 1.6 \text{ GeV fm}^6$ for different model spaces sizes: (—) $e_{\text{max}} = 10$; (---) $e_{\text{max}} = 12$, $l_{\text{max}} = 10$; (⋯) $e_{\text{max}} = 14$, $l_{\text{max}} = 10$. For comparison: (—) response function obtained with the pure transformed two-body interaction with $\alpha = 0.04 \text{ fm}^4$, $e_{\text{max}} = 14$, $l_{\text{max}} = 10$. Calculated centroid energies are indicated by dashed arrows, experimental centroids [51–53] by solid arrows.

for the S-UCOM(SRG) and the S-SRG interactions, which are again similar for both interactions. For the smallest flow parameters the main peaks lie significantly below the experimental centroids for all nuclei. With increasing flow parameter the response is shifted to higher excitation energies and spread over a wider range. The influence of the flow parameter on single-particle spectra is opposite to the one of the strength: With increasing flow parameter the level density is reduced, the spectra are spread wider, which entails an increase of the excitation energy.

Finally, the isoscalar monopole resonance is studied in dependence on the model-

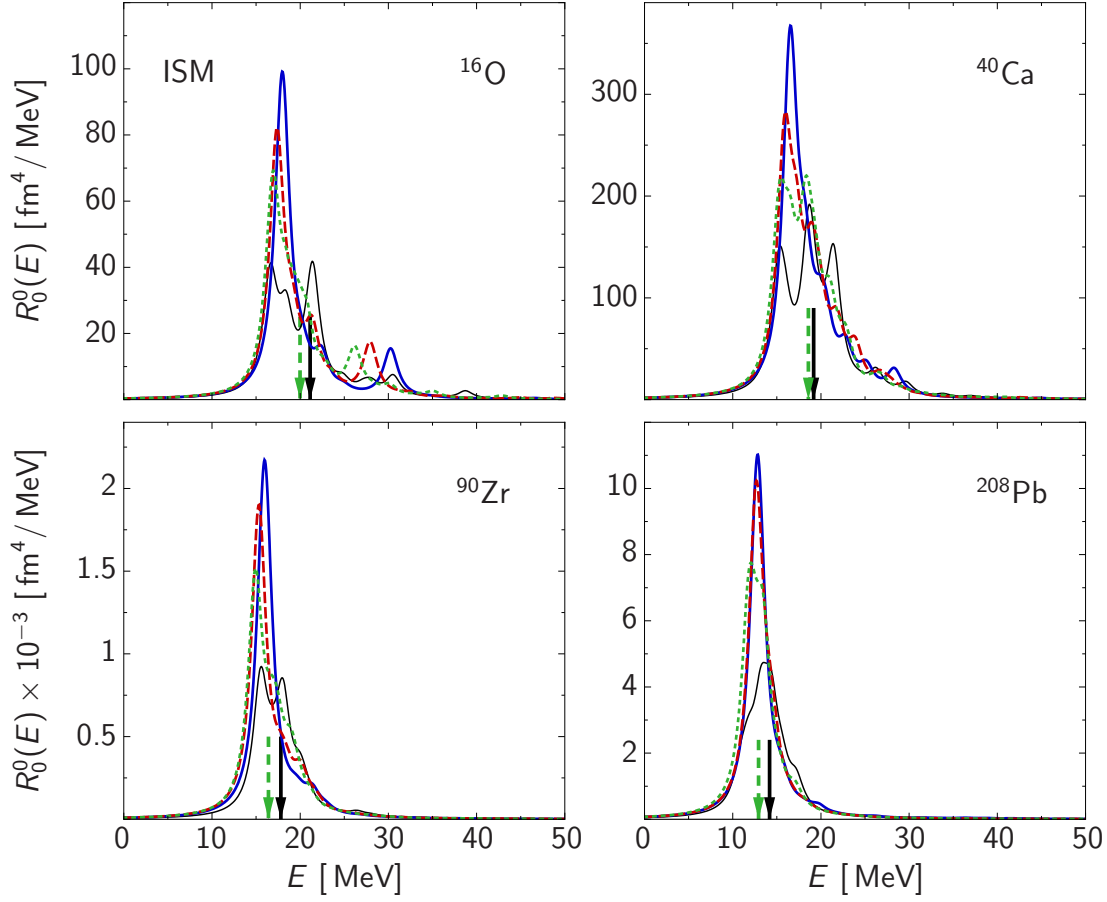


Figure 7.8: Same as in Figure 7.7 for the S-UCOM(SRG) interaction with $\alpha = 0.16$ fm⁴, $C_{3N} = 2.2$ GeV fm⁶, and (—) $e_{\text{max}} = 10$; (---) $e_{\text{max}} = 12$, $l_{\text{max}} = 10$; (-.-.-) $e_{\text{max}} = 14$, $l_{\text{max}} = 10$. For comparison: (—) $\alpha = 0.04$ fm⁴, $e_{\text{max}} = 14$, $l_{\text{max}} = 10$.

space size for all four interactions. In Figure 7.7 the response functions calculated with the UCOM(SRG) interaction in three different model spaces are compared to the response obtained with the pure two-body interaction for $\alpha = 0.04$ fm⁴ in the largest model space. The monopole resonances obtained with the three-body interaction show a stronger fragmentation with increasing model-space size, while the centroids remain essentially unchanged for all considered nuclei. For ^{16}O one observes that the second small peak at higher excitation energies moves towards the main peak. The fragmentation shows that the giant resonance is spread over several RPA excitations and is not concentrated on one single excitation. This behavior agrees with experimental observations. Furthermore, the calculated response functions agree nicely with the experimental centroids. The comparison with the results obtained with the pure two-

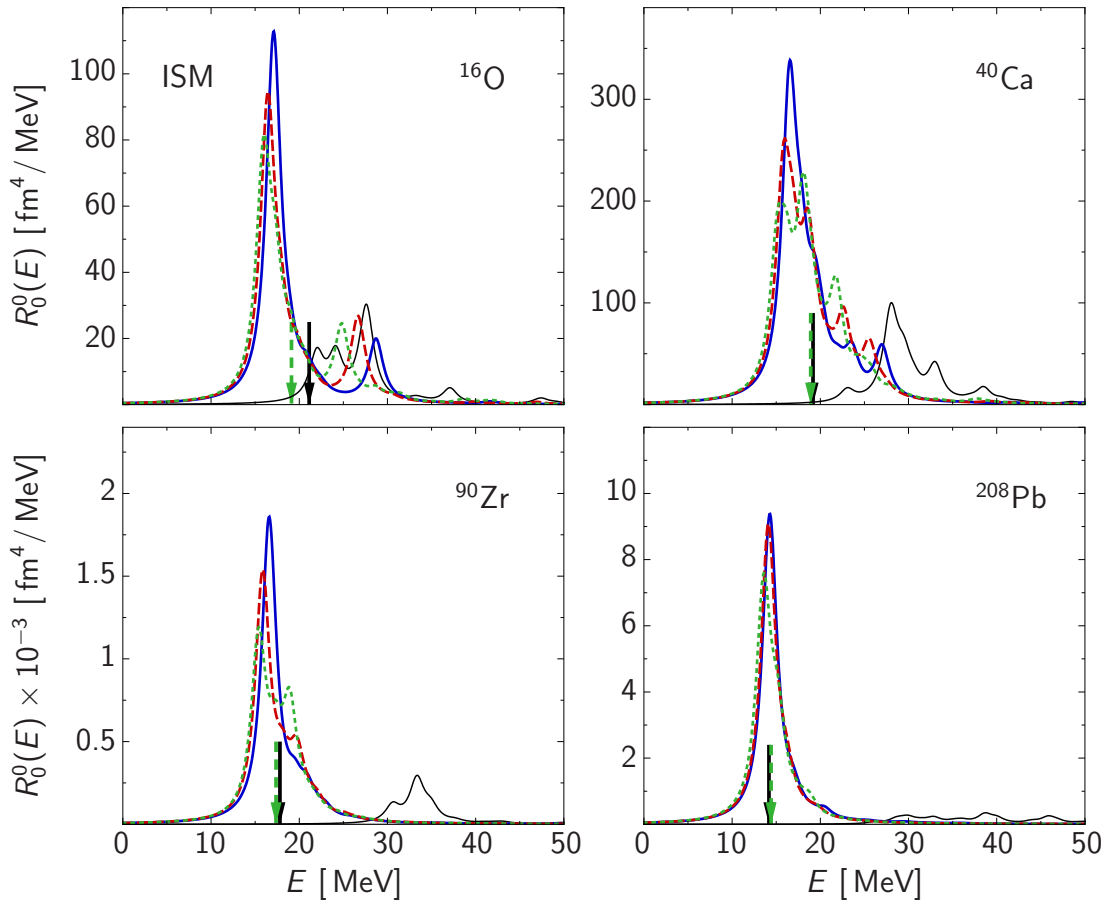


Figure 7.9: Same as in Figure 7.7 for the SRG interaction with $\alpha = 0.10 \text{ fm}^4$, $C_{3N} = 4.3 \text{ GeV fm}^6$, and (—) $e_{\text{max}} = 10$; (---) $e_{\text{max}} = 12$, $l_{\text{max}} = 10$; (····) $e_{\text{max}} = 14$, $l_{\text{max}} = 10$. For comparison: (—) $\alpha = 0.03 \text{ fm}^4$, $e_{\text{max}} = 14$, $l_{\text{max}} = 10$.

body interaction reveals that these response functions are even more fragmented for all nuclei and the calculated centroids slightly overestimate the experimental ones (cf. Tab. 7.2).

Figure 7.8 shows the corresponding data obtained with the S-UCOM(SRG) interaction. One can again observe a fragmentation of the response functions with increasing basis size and the experimental centroids are again reproduced. The response functions obtained without three-body interaction are again more fragmented and the centroids nicely reproduce the experimental ones for all nuclei.

In Figures 7.9 and 7.10 the response functions calculated with the SRG and the S-SRG interactions are shown. For both interactions the already discussed fragmentation is observed. For the SRG interaction the centroid of the monopole resonance of

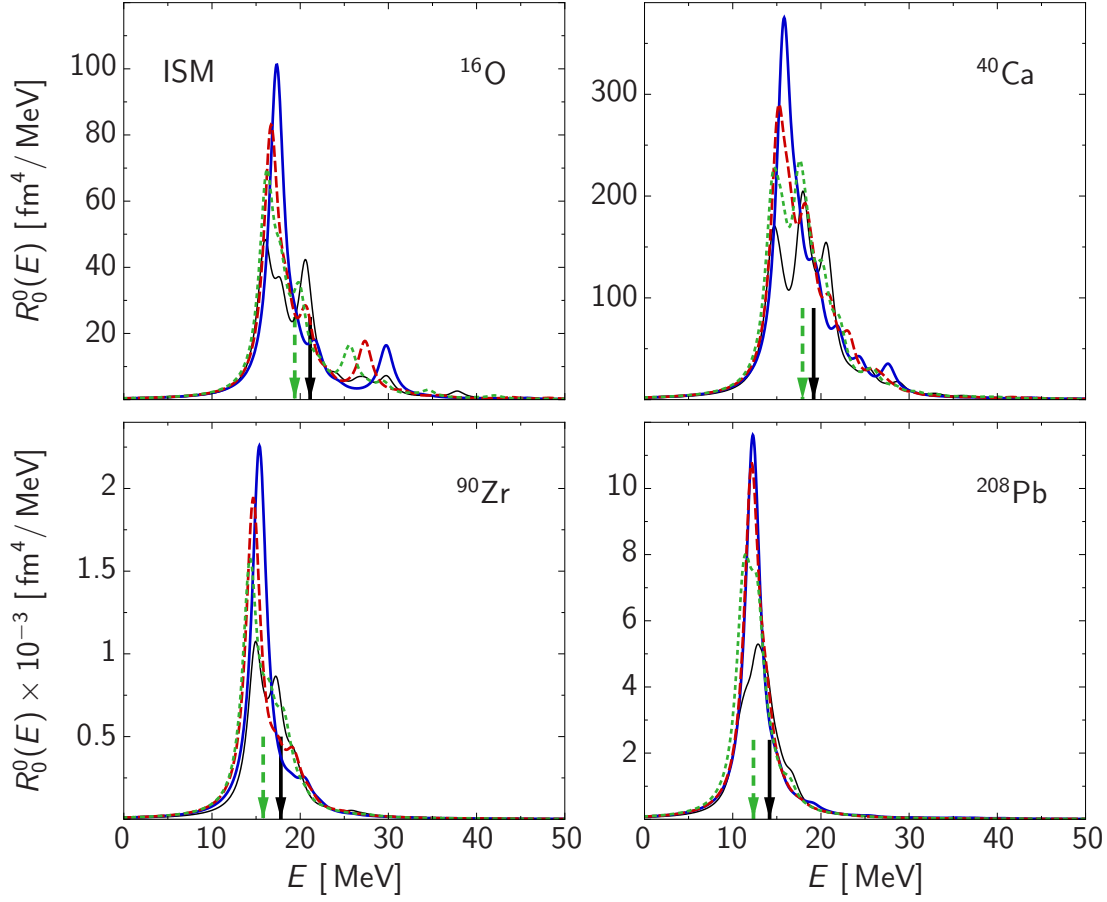


Figure 7.10: Same as in Figure 7.7 for the S-SRG interaction with $\alpha = 0.10 \text{ fm}^4$, $C_{3N} = 2.0 \text{ GeV fm}^6$, and (—) $e_{\text{max}} = 10$; (---) $e_{\text{max}} = 12$, $l_{\text{max}} = 10$; (- - - -) $e_{\text{max}} = 14$, $l_{\text{max}} = 10$. For comparison: (—) $\alpha = 0.03 \text{ fm}^4$, $e_{\text{max}} = 14$, $l_{\text{max}} = 10$.

^{16}O is underestimated by 2 MeV but the centroids of ^{40}Ca , ^{90}Zr , and ^{208}Pb are almost perfectly reproduced. In contrast, the response functions obtained with the pure transformed two-body interaction with $\alpha = 0.03 \text{ fm}^4$ overestimate the monopole resonances of ^{16}O and ^{40}Ca . For ^{90}Zr the response is weak and lies at very high excitation energies. Finally, for ^{208}Pb no collective excitation is found at all. In contrast, the corresponding response functions obtained with the S-SRG interaction nicely agree with the experimental centroids. After including the three-body interaction the experimental ISM centroids are underestimated by roughly 2 MeV for all four nuclei (cf. Tab. 7.3).

In summary, the isoscalar giant monopole resonances of the considered nuclei are nicely reproduced by all four interactions including the three-body contact interaction. In contrast, considering the pure two-body interactions only the centroids calculated

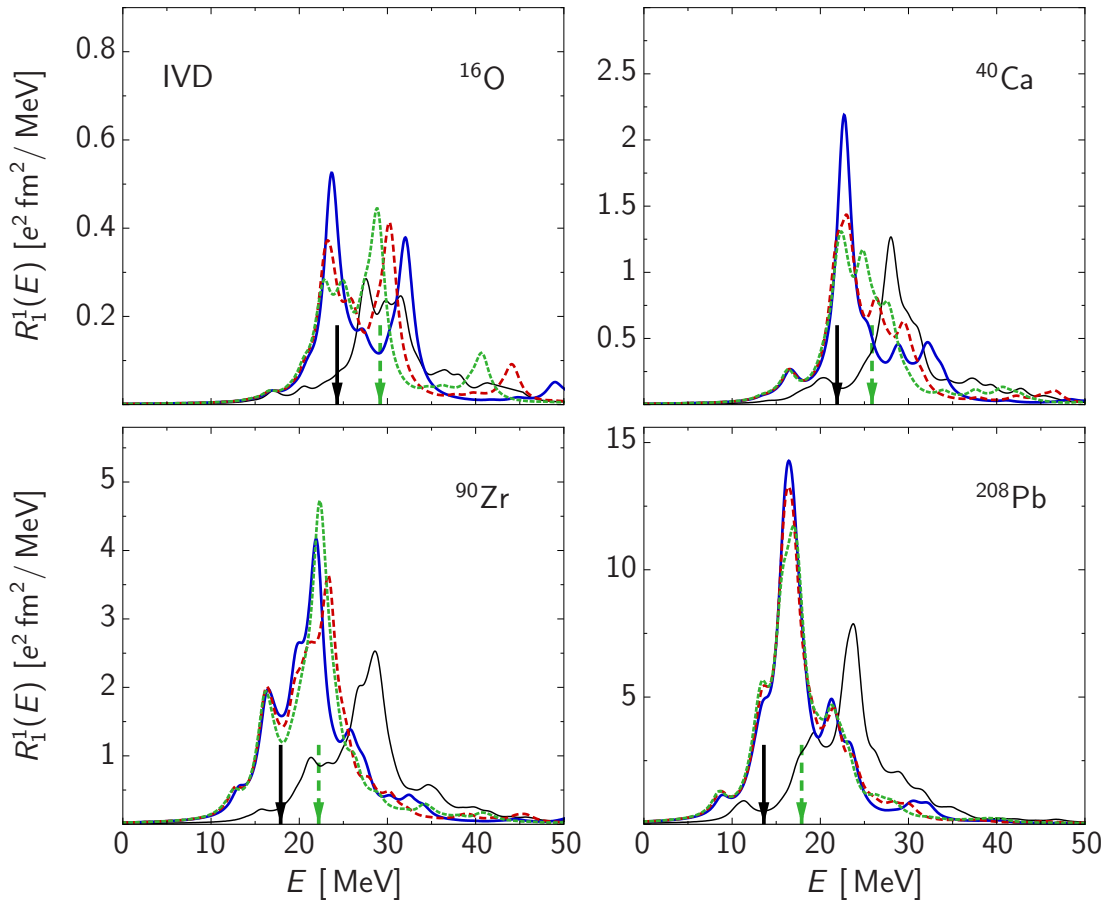


Figure 7.11: Isovector dipole response based on the UCOM(SRG) interaction with $\alpha = 0.16 \text{ fm}^4$, $C_{3N} = 1.6 \text{ GeV fm}^6$ for different model space sizes: (—) $e_{\text{max}} = 10$; (---) $e_{\text{max}} = 12$, $l_{\text{max}} = 10$; (⋯) $e_{\text{max}} = 14$, $l_{\text{max}} = 10$. For comparison: (—) response function obtained with the pure transformed two-body interaction with $\alpha = 0.04 \text{ fm}^4$, $e_{\text{max}} = 14$, $l_{\text{max}} = 10$. Calculated centroid energies are indicated by dashed arrows, experimental centroids [54–57] by solid arrows.

with the S-UCOM(SRG) and the S-SRG interactions agree with the experimental data.

7.4.2 Isovector Giant Dipole Resonance

The isovector giant dipole resonance is an excitation mode where protons and neutrons move out-of-phase. The dependencies of the isovector dipole response functions on the strength C_{3N} and the flow parameter α are similar to those observed for the isoscalar monopole excitations, therefore, they are not discussed here.

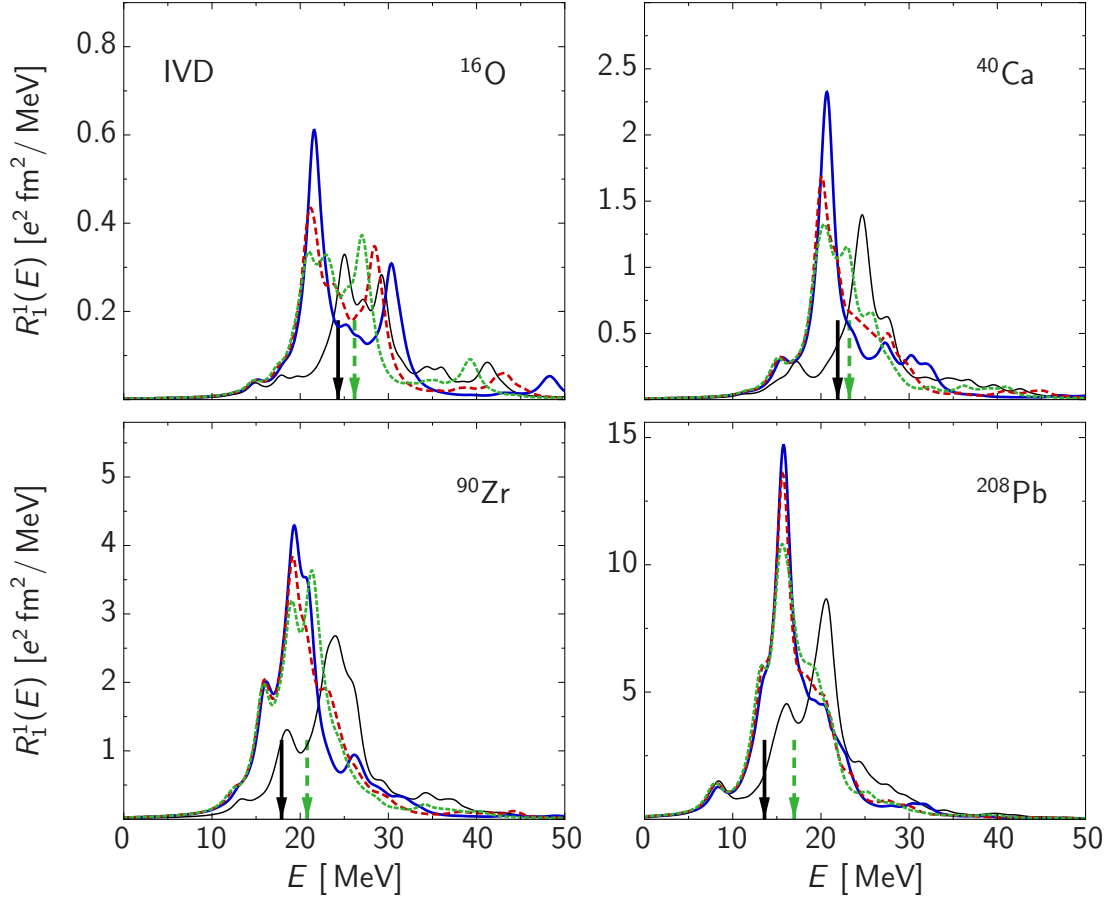


Figure 7.12: Same as in Figure 7.11 for the S-UCOM(SRG) interaction with $\alpha = 0.16 \text{ fm}^4$, $C_{3N} = 2.2 \text{ GeV fm}^6$, and (—) $e_{\text{max}} = 10$; (---) $e_{\text{max}} = 12$, $l_{\text{max}} = 10$; (⋯) $e_{\text{max}} = 14$, $l_{\text{max}} = 10$. For comparison: (—) $\alpha = 0.04 \text{ fm}^4$, $e_{\text{max}} = 14$, $l_{\text{max}} = 10$.

Beginning with the UCOM(SRG) interaction in Figure 7.11 the isovector dipole response functions are shown for different model-space sizes. The response functions of the dipole excitations are broader than for the monopole resonances and divided into several peaks for all four nuclei. For ^{16}O one observes two main peaks and a smaller one at higher excitation energies. With increasing basis size the high-lying main peak moves towards the low-lying one, which remains at the same energy. For ^{40}Ca the response is redistributed with increasing model space size from one main peak with several smaller maxima into one broader peak without changing the position of the centroid. The response functions of ^{90}Zr develop one main peak with one smaller peak at lower excitation energies with increasing basis size. Finally, the response functions of ^{208}Pb show only minor variations with increasing model space size. For all four nuclei

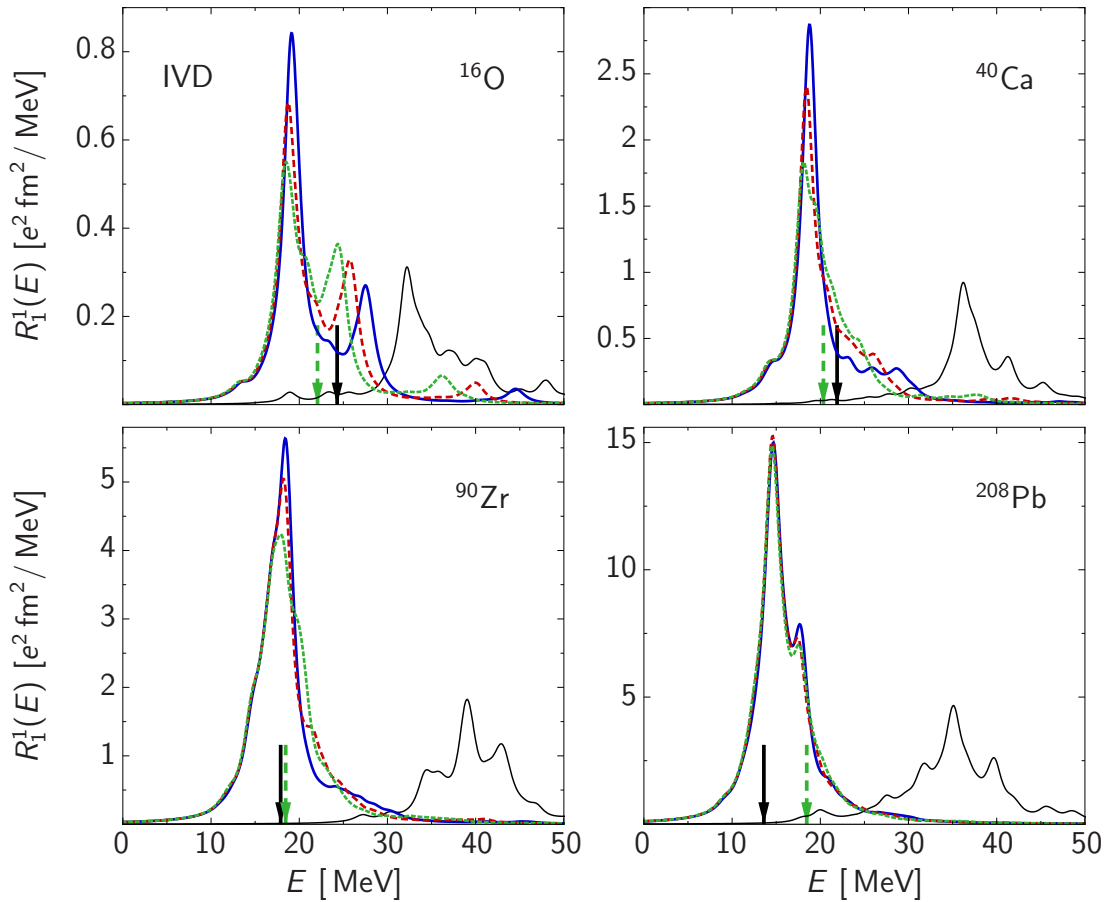


Figure 7.13: Same as in Figure 7.11 for the SRG interaction with $\alpha = 0.10 \text{fm}^4$, $C_{3N} = 4.3 \text{GeV fm}^6$, and (—) $e_{\text{max}} = 10$; (---) $e_{\text{max}} = 12$, $l_{\text{max}} = 10$; (---) $e_{\text{max}} = 14$, $l_{\text{max}} = 10$. For comparison: (—) $\alpha = 0.03 \text{fm}^4$, $e_{\text{max}} = 14$, $l_{\text{max}} = 10$.

the experimental centroids lie within the range of the response functions, but the calculated centroids overestimate the experimental ones by 4 to 5 MeV (cf. Tab. 7.2). The overestimation of the experimental centroids is even more pronounced on the basis of the pure two-body interaction.

The isovector dipole strengths obtained with the S-UCOM(SRG) are shown in Figure 7.12. The response functions exhibit a similar behavior as observed for the UCOM(SRG) interaction, and their centroids still overestimate the experimental ones by 2 to 3 MeV. The centroids of the strength distributions obtained with the pure two-body interaction are closer to experiment than in case of the UCOM(SRG) interaction, but the overestimation is stronger than for the two- plus three-body S-UCOM(SRG) interaction.

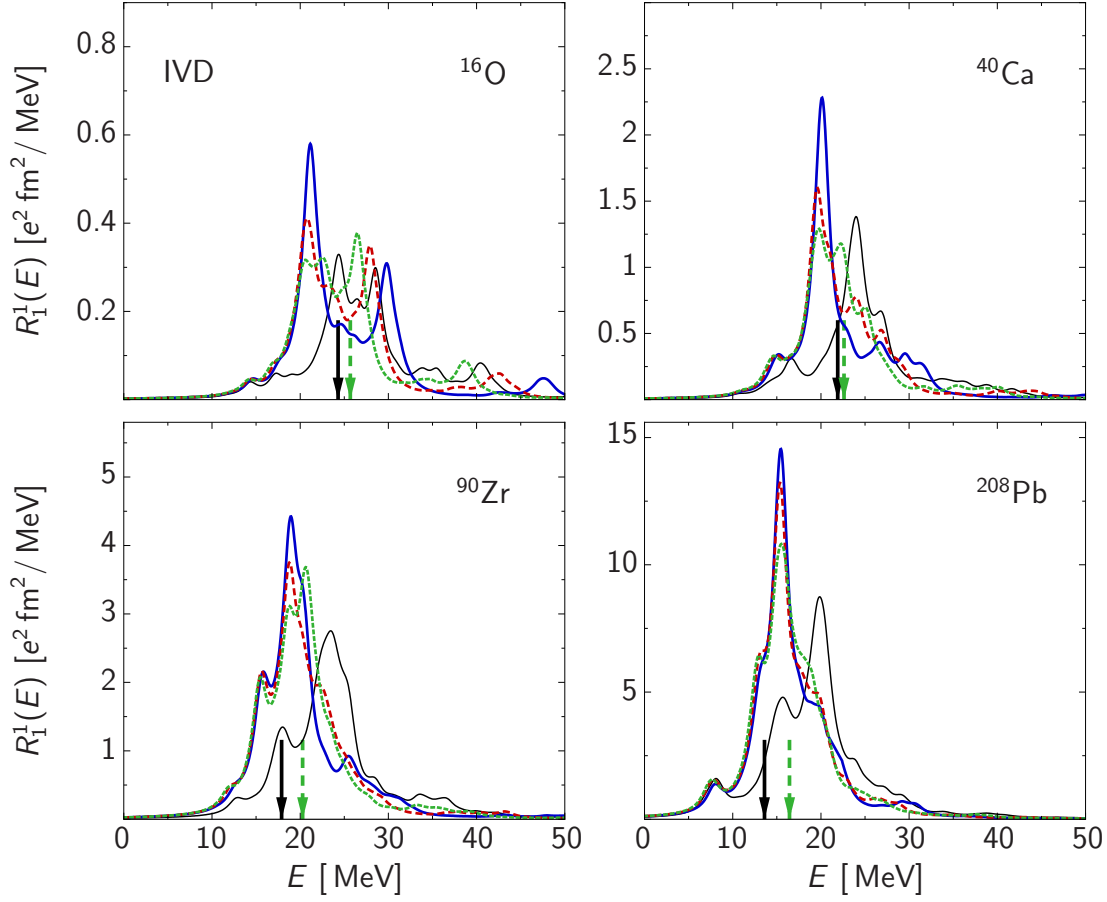


Figure 7.14: Same as in Figure 7.11 for the S-SRG interaction with $\alpha = 0.10 \text{ fm}^4$, $C_{3N} = 2.0 \text{ GeV fm}^6$, and (—) $e_{\text{max}} = 10$; (---) $e_{\text{max}} = 12$, $l_{\text{max}} = 10$; (- - -) $e_{\text{max}} = 14$, $l_{\text{max}} = 10$. For comparison: (—) $\alpha = 0.03 \text{ fm}^4$, $e_{\text{max}} = 14$, $l_{\text{max}} = 10$.

In Figure 7.13 the isovector dipole strengths calculated with the SRG interaction are shown. Compared to the results obtained with the other interactions the response is concentrated in one or two strongly collective peaks. For ^{16}O and ^{40}Ca the experimental centroids are slightly underestimated while they are reproduced for ^{90}Zr and significantly overestimated for ^{208}Pb . The response functions obtained without the three-body interaction lie at unphysically high excitation energies for all four nuclei.

The isovector dipole resonances of the S-SRG interaction (Fig. 7.14) are very similar to those obtained with the S-UCOM(SRG) interaction (Fig. 7.12) in all aspects.

In summary, the experimental isovector giant dipole resonance is overestimated by the pure two-body interactions in most cases, especially by the SRG interaction. The inclusion of the three-body contact interaction leads to a reasonable overall agreement

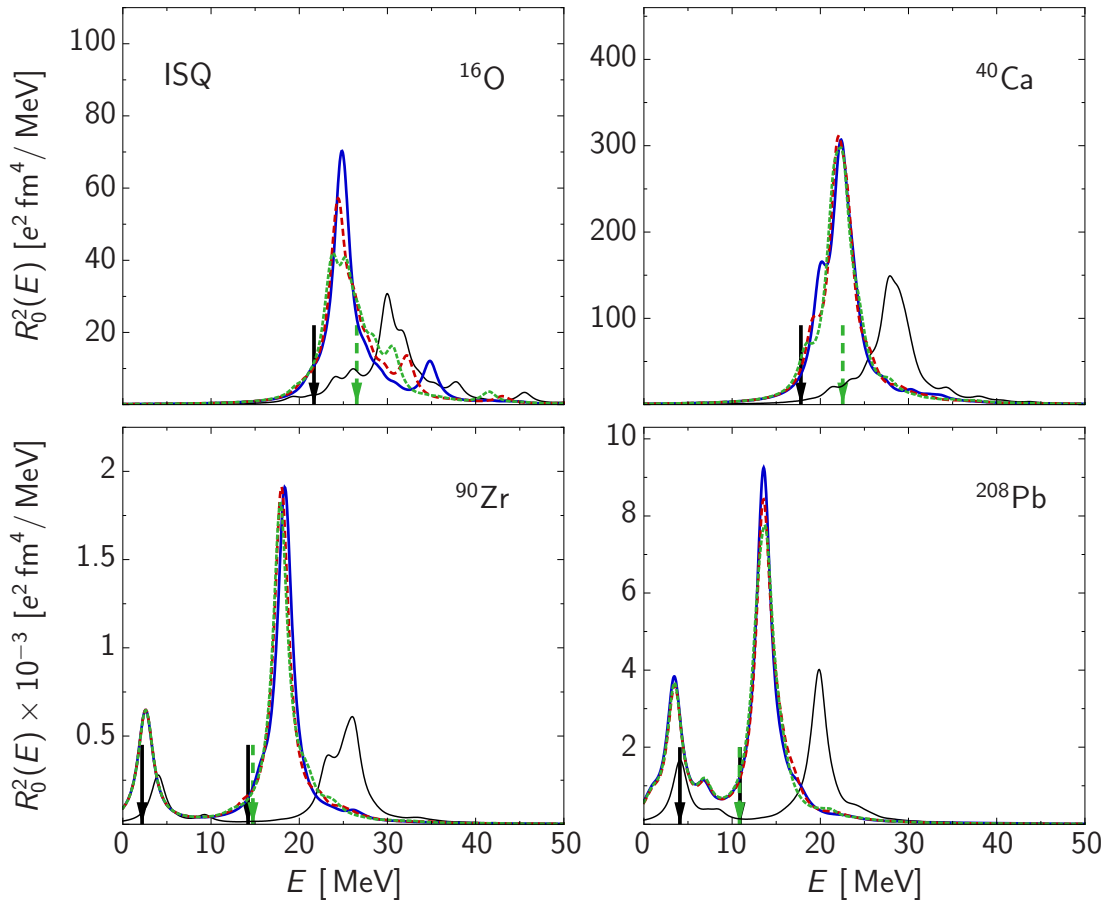


Figure 7.15: Isoscalar quadrupole response based on the UCOM(SRG) interaction with $\alpha = 0.16 \text{ fm}^4$, $C_{3N} = 1.6 \text{ GeV fm}^6$ for different model space sizes (—) $e_{\text{max}} = 10$; (---) $e_{\text{max}} = 12$, $l_{\text{max}} = 10$; (····) $e_{\text{max}} = 14$, $l_{\text{max}} = 10$. For comparison: (—) response function obtained with the pure transformed two-body interaction with $\alpha = 0.04 \text{ fm}^4$, $e_{\text{max}} = 14$, $l_{\text{max}} = 10$. Calculated centroid energies are indicated by dashed arrows, experimental centroids [51, 52, 58–60] by solid arrows.

for all four interactions and all considered nuclei.

7.4.3 Isoscalar Giant Quadrupole Resonance

Finally, the isoscalar quadrupole response is investigated. The calculated strength distributions are shown in Figures 7.15 to 7.18 for the four different interactions. For all nuclei the strength is concentrated in narrow strongly collective peaks. The influence of increasing model space size is similar for all four interactions. For ^{16}O a slight

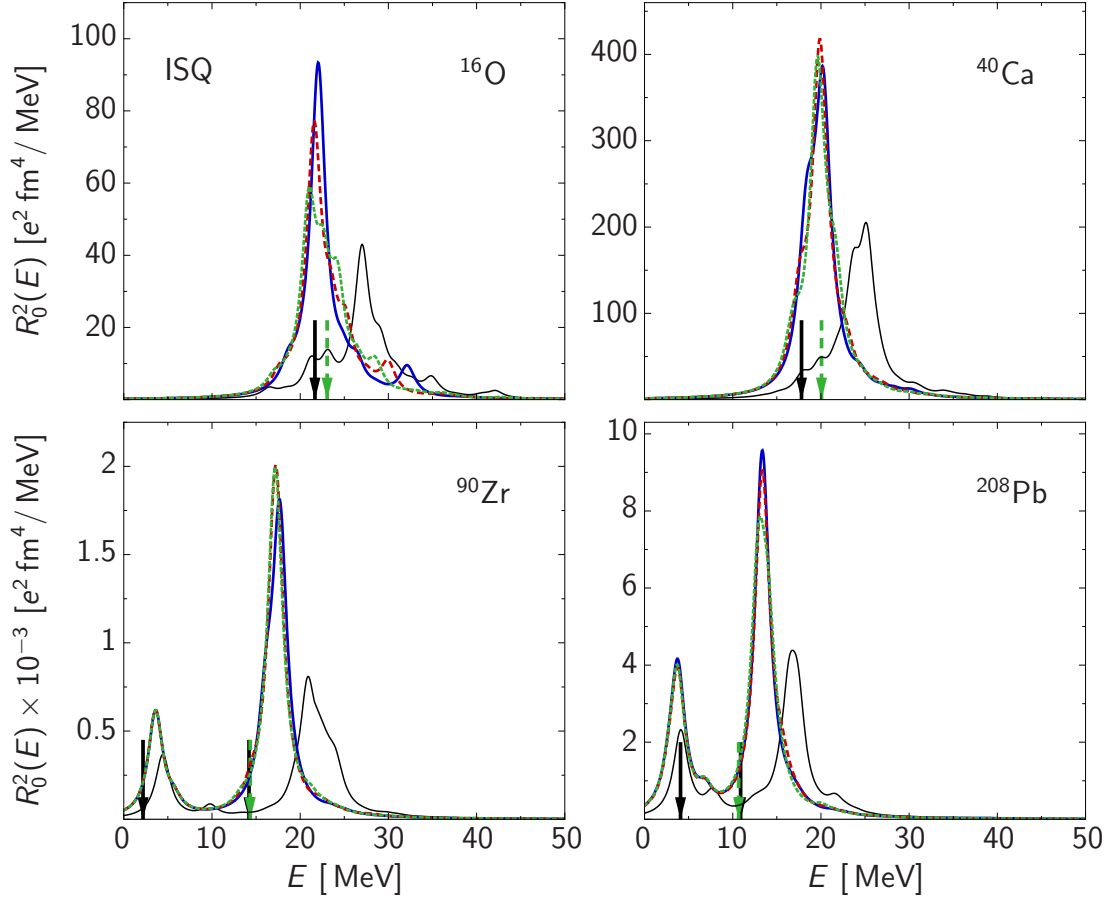


Figure 7.16: Same as in Figure 7.15 for the S-UCOM(SRG) interaction with $\alpha = 0.16 \text{ fm}^4$, $C_{3N} = 2.2 \text{ GeV fm}^6$, and (—) $e_{\text{max}} = 10$; (---) $e_{\text{max}} = 12$, $l_{\text{max}} = 10$; (- - -) $e_{\text{max}} = 14$, $l_{\text{max}} = 10$. For comparison: (—) $\alpha = 0.04 \text{ fm}^4$, $e_{\text{max}} = 14$, $l_{\text{max}} = 10$.

fragmentation is observed while the response functions remain essentially unchanged for ^{40}Ca , ^{90}Zr and ^{208}Pb . For the heavy nuclei one observes a low-lying 2^+ excitation in addition to the giant quadrupole resonance.

For the pure two-body UCOM(SRG) interaction only the centroid of the low-lying 2^+ excitation of ^{208}Pb is reproduced, but all giant quadrupole resonances as well as the low-lying 2^+ excitation of ^{90}Zr are significantly overestimated. The inclusion of the three-body interaction leads to a nice description of both low-lying excitations. The response peaks of the giant resonances move towards lower energies but still lie slightly above the experimental centroids for ^{16}O and ^{40}Ca while they perfectly reproduce the centroids for ^{90}Zr and ^{208}Pb .

The description of the isoscalar quadrupole resonances using the pure two-body

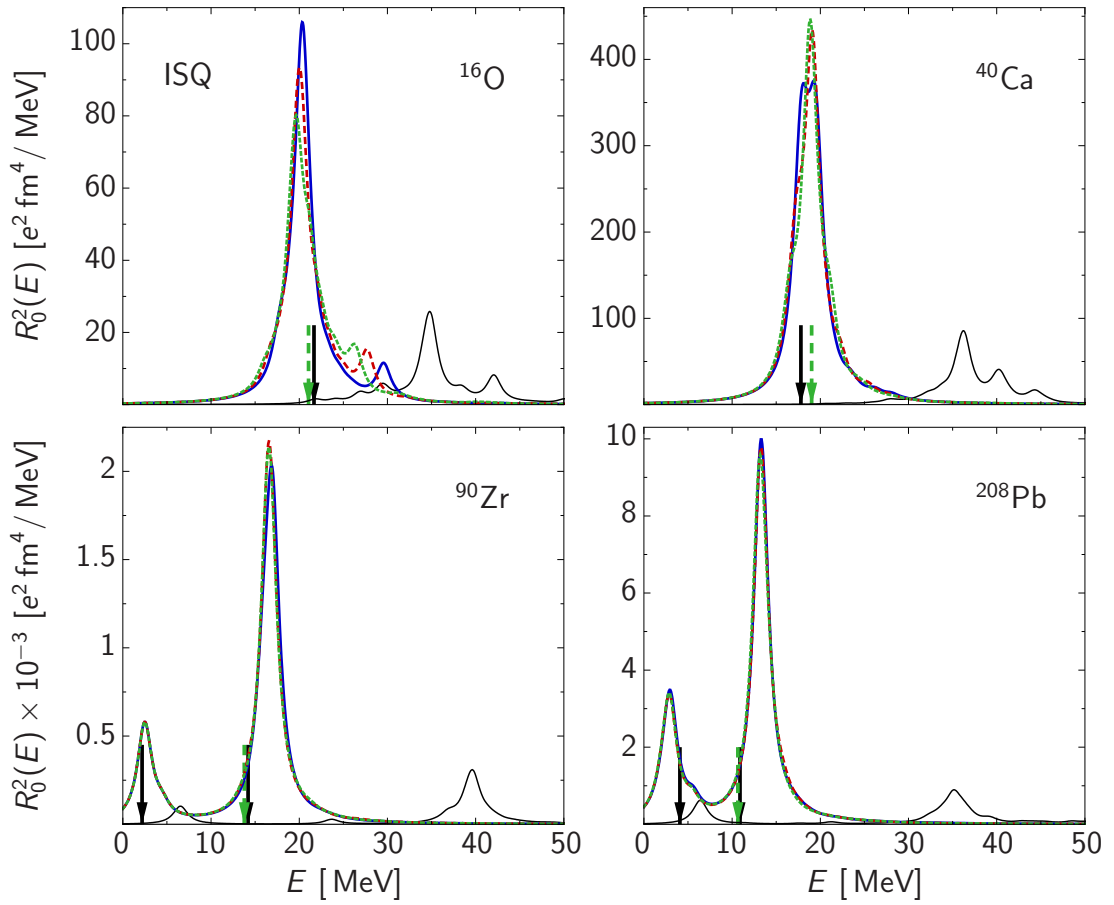


Figure 7.17: Same as in Figure 7.15 for the SRG interaction with $\alpha = 0.10 \text{ fm}^4$, $C_{3N} = 4.3 \text{ GeV fm}^6$, and (—) $e_{\text{max}} = 10$; (---) $e_{\text{max}} = 12$, $l_{\text{max}} = 10$; (- - -) $e_{\text{max}} = 14$, $l_{\text{max}} = 10$. For comparison: (—) $\alpha = 0.03 \text{ fm}^4$, $e_{\text{max}} = 14$, $l_{\text{max}} = 10$.

S-UCOM(SRG) interaction (Fig. 7.16) is of similar quality as for the UCOM(SRG) interaction. The excitation energies of the giant resonances are slightly lowered but they still overestimate the experiment. Including the three-body interaction leads to an agreement of the calculated giant resonances of ^{90}Zr and ^{208}Pb with the experimental centroids. The giant resonances of ^{16}O and ^{40}Ca as well as the low-lying excitation of ^{90}Zr are overestimated by about 1.5 to 2 MeV.

For the SRG interaction (Fig. 7.17) the response functions obtained without the three-body interaction exhibit only weak resonances at very high excitation energies as was already observed for the isoscalar monopole and the isovector dipole resonances. In contrast, including the three-body interaction leads to an almost perfect agreement of all calculated centroids with the experimental ones.

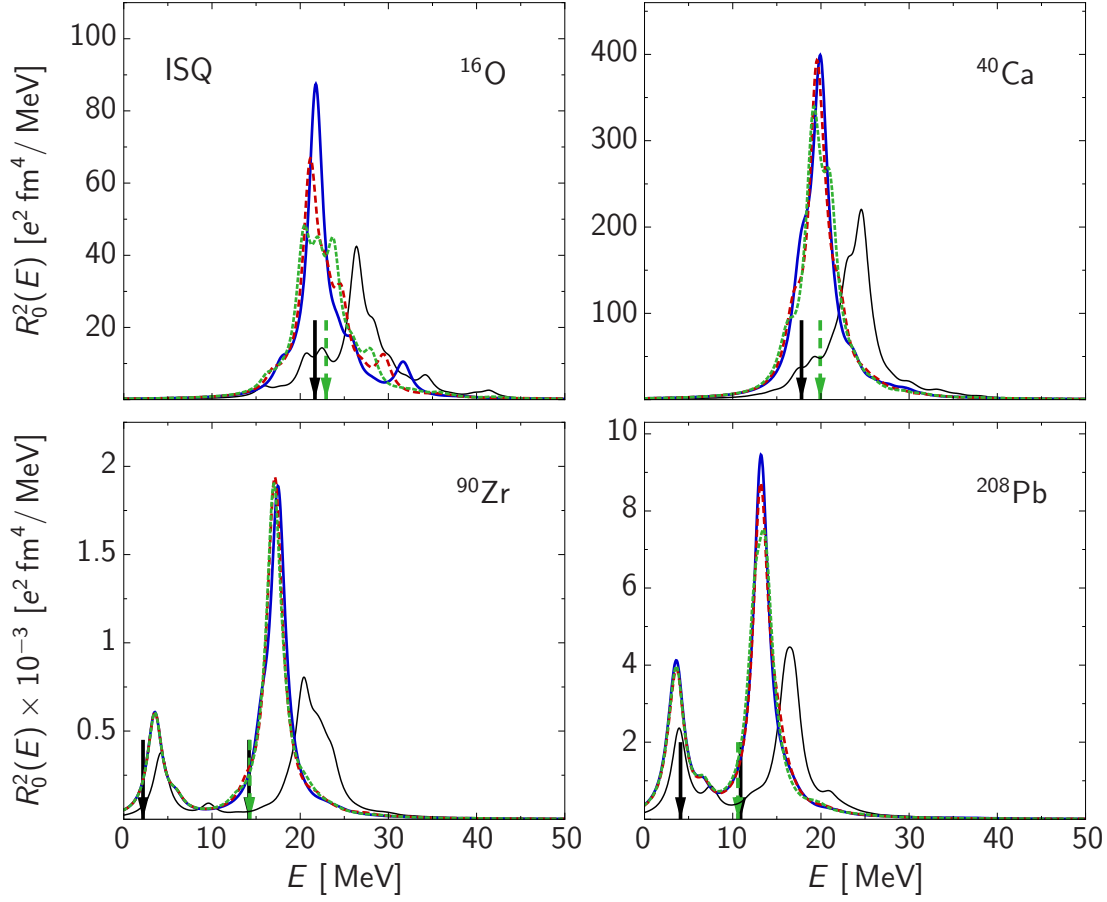


Figure 7.18: Same as in Figure 7.15 for the S-SRG interaction with $\alpha = 0.10 \text{ fm}^4$, $C_{3N} = 2.0 \text{ GeV fm}^6$, and (—) $e_{\text{max}} = 10$; (---) $e_{\text{max}} = 12$, $l_{\text{max}} = 10$; (- - - -) $e_{\text{max}} = 14$, $l_{\text{max}} = 10$. For comparison: (—) $\alpha = 0.03 \text{ fm}^4$, $e_{\text{max}} = 14$, $l_{\text{max}} = 10$.

As was already seen in case of the giant dipole resonances, the S-SRG and the S-UCOM(SRG) interactions (Figs. 7.18 and 7.15) yield very similar response functions that are in agreement with the experimental centroids for the giant quadrupole resonances of ^{90}Zr and ^{208}Pb and the low-lying 2^+ excitation of ^{208}Pb while the giant resonances of ^{16}O and ^{40}Ca as well as the low-lying excitation of ^{90}Zr are only slightly overestimated.

In summary, the inclusion of the three-body interaction leads to an improved description of all considered isoscalar quadrupole excitations, compared to the response functions obtained without the three-body interaction, and in many cases yield nice agreement with the experimental centroids.

		UCOM(SRG)		S-UCOM(SRG)		Exp.
		(a)	(b)	(a)	(b)	
α [fm ⁴]	C_{3N} [GeV fm ⁶]	0.04	0.16	0.04	0.16	
		–	1.6	–	2.2	
ISM	¹⁶ O	23.83	21.78	20.87	19.98	21.13
	⁴⁰ Ca	23.02	19.81	19.40	18.57	19.18
	⁹⁰ Zr	21.02	16.73	17.63	16.40	17.81
	²⁰⁸ Pb	17.20	12.88	13.87	12.93	14.18
IVD	¹⁶ O	33.43	29.17	30.24	26.16	24.3
	⁴⁰ Ca	31.10	25.86	26.88	23.22	21.9
	⁹⁰ Zr	28.86	22.20	24.94	20.79	17.9
	²⁰⁸ Pb	24.00	17.88	19.91	16.96	13.6
ISQ	¹⁶ O	31.17	26.51	27.32	23.05	21.67
	⁴⁰ Ca	28.52	22.54	24.30	20.06	17.8
	⁹⁰ Zr	20.93	14.74	18.15	14.33	14.2
	²⁰⁸ Pb	16.02	10.84	13.53	10.67	10.9

Table 7.2: Centroid energies in MeV obtained for the UCOM(SRG) and S-UCOM(SRG) interactions based on (a) the pure two-body interaction, (b) including the three-body interaction, compared to experimental values [51–58].

7.4.4 Comparison of Giant Resonances

The inclusion of a simple phenomenological three-body contact interaction leads to a substantial improvement in the description of collective excitations. For comparison the centroid energies calculated with the pure two-body and the two- plus three-body interactions are listed in Tables 7.2 and 7.3 together with the experimental values for all discussed excitation modes in ¹⁶O, ⁴⁰Ca, ⁹⁰Zr, and ²⁰⁸Pb. Considering the agreement or disagreement with the experiment one finds several connections with earlier discussed results.

As it is an instructive example, we consider ²⁰⁸Pb calculated with the pure two-body SRG interaction. On the Hartree-Fock level this nucleus is overbound by 11 MeV per nucleon for $\alpha = 0.03$ fm⁴, with increasing flow parameter the overbinding is even more enhanced. Considering the single-particle spectra of ²⁰⁸Pb one observes a strongly underestimated level density, which is connected to the small charge radius differing by 1.5 fm from the experimental value. The RPA is built on the HF single-particle spectra, i.e. it is sensitive to the reproduction of the experimental single-particle levels

		SRG		S-SRG		Exp.
		(a)	(b)	(a)	(b)	
α [fm ⁴]		0.03	0.10	0.03	0.10	
C_{3N} [GeV fm ⁶]		–	4.3	–	2.0	
ISM	¹⁶ O	27.57	19.12	19.85	19.38	21.13
	⁴⁰ Ca	31.02	18.91	18.48	17.92	19.18
	⁹⁰ Zr	40.27	17.37	16.82	15.81	17.81
	²⁰⁸ Pb	49.56	14.41	13.19	12.35	14.18
IVD	¹⁶ O	37.88	22.07	29.29	25.68	24.3
	⁴⁰ Ca	39.92	20.34	25.98	22.61	21.9
	⁹⁰ Zr	42.16	18.46	24.16	20.27	17.9
	²⁰⁸ Pb	37.16	15.72	19.25	16.44	13.6
ISQ	¹⁶ O	36.01	21.04	26.70	22.94	21.67
	⁴⁰ Ca	37.88	19.02	23.76	19.92	17.8
	⁹⁰ Zr	35.89	13.77	17.79	14.28	14.2
	²⁰⁸ Pb	34.42	10.65	13.23	10.59	10.9

Table 7.3: Centroid energies in MeV obtained for the SRG and S-SRG interactions based on (a) the pure two-body interaction, (b) including the three-body interaction, compared to experimental values [51–58].

especially in the region of the Fermi energy [50]. Consequently, for ²⁰⁸Pb a significant deviation from the expected exhaustion of the classical sum rules is observed for all collective excitation modes (cf. Tab. 7.1). Finally, no giant monopole resonance is generated at all for ²⁰⁸Pb on the basis of the SRG interaction, and the dipole and quadrupole resonances are found at unphysically high excitation energies, which is also reflected in the corresponding centroid energies.

Including the three-body contact interaction, which is the most simple phenomenological three-body interaction, cures all these effects. It especially improves the description of the single-particle spectra, which entails a nice reproduction of the giant resonances.

On the other the experimental ground-state energies are not reproduced by any of the applied two-body or two- plus three-body interactions on the HF level. Instead a reasonable agreement is achieved after including the second-order perturbative energy correction. Hence, an improper description of the ground-state energy on the HF level does not exclude a good description of giant resonances in RPA [61]. As mentioned above, a more important measure is the reproduction of single-particle levels in the

region of the Fermi energy.

The additional repulsion of the three-body interaction increases the level density of single-particle spectra on the Hartree-Fock level, which entails a lowering of the excitation energies of the isovector dipole and the isoscalar quadrupole giant resonances, and in part of the isoscalar monopole giant resonance compared to the response functions obtained with the pure two-body interactions. This results in an improved agreement of calculated centroid energies with the experimental ones for the dipole and quadrupole giant resonances. The giant monopole resonances are already nicely reproduced by the pure two-body S-UCOM(SRG) and S-SRG interactions. This agreement is maintained after including the three-body interaction.

The impact of the three-body contact interaction is especially pronounced in case of the SRG interaction. But one has to be careful with these results, because the three-body strength is roughly twice as large as for the other interactions and might lead to problems when considering other observables.

Up to now only centroid energies were compared with experimental data. A more sophisticated insight could be obtained by comparing the experimental response functions with the calculated ones.

Chapter 8

Conclusions

The importance of three-nucleon interactions is demonstrated in various nuclear structure investigations based on pure nucleon-nucleon interactions. As a first step towards the consistent inclusion of realistic three-body forces we study simple phenomenological three-body interactions. We develop an appropriate scheme for the handling of three-body matrix elements and derive the formal application of three-body forces in various many-body methods.

The nuclear interaction induces complex correlations, such as the strong short-range repulsion and tensor correlations. Due to these correlations large model spaces are required to reach convergence. To facilitate calculations in tractable model spaces the Unitary Correlation Operator Method and the Similarity Renormalization Group are discussed as two different approaches to generate soft phase-shift equivalent interactions via unitary transformations. Although the motivations of both methods are quite different, the resulting interactions show a number of similarities, e.g. they exhibit a band-diagonal structure with respect to momentum space matrix elements. These methods are used to obtain four different classes of two-body interactions out of the realistic Argonne V18 potential. Beside the standard UCOM(SRG) and SRG interactions, where all partial waves are transformed consistently, we employ the S-UCOM(SRG) and S-SRG interactions, where only the S-waves undergo the respective unitary transformations.

To investigate ground-state energies and charge radii of selected closed-shell nuclei across the whole nuclear chart the four different two-body interactions are used in the Hartree-Fock approximation. While the systematics of the experimental ground-state energies is reproduced by the UCOM(SRG), S-UCOM(SRG) and S-SRG interactions

except for a constant shift, the SRG interaction leads to a strong overbinding of intermediate and heavy nuclei. The charge radii are systematically underestimated by all four interactions. The HF ground-state is described by a single Slater determinant, which is not capable of describing any correlations. The short-range correlations are covered by the unitary transformations while the long-range correlations have to be described by the many-body states, e.g., by applying many-body perturbation theory on top of the HF results. Including the second-order perturbative corrections leads to a reasonable agreement with experimental ground-state energies for the UCOM(SRG), S-UCOM(SRG) and S-SRG interactions, while the perturbative corrections to the charge radii are negligible. For the SRG interaction most nuclei are already overbound on the HF level, and second-order perturbation theory cannot improve these results.

On the level of the HF approximation also single-particle spectra are examined. The general description of the level ordering agrees rather well with experimental spectra, but the level spacings, and especially the Fermi gap, are significantly overestimated.

The flow parameters used for these calculations are determined for each interaction such that the experimental ${}^4\text{He}$ ground-state energy is reproduced in a No-Core Shell Model calculation, i.e. the flow parameter is chosen considering a four-nucleon system only. Therefore, it is a remarkable result, that the systematics of the experimental ground-state energies is reproduced across the whole nuclear chart on the basis of HF plus MBPT calculations. Nonetheless, the results obtained with the pure two-body interactions show some systematic deviations from experimental data, e.g. the charge radii cannot be accurately reproduced by pure two-body interactions and the description of single-particle spectra leaves room for improvement. To reduce these deviations introducing a repulsive three-body interaction is inevitable.

The first ansatz for a phenomenological three-body interaction is a finite-range interaction of Gaussian shape. The matrix elements are most conveniently calculated in a basis of cartesian harmonic oscillator eigenstates and subsequently transformed into a basis of spherical harmonic oscillator eigenstates. Only the S-UCOM and the S-SRG interactions are supplemented by the Gaussian three-body interaction. The free parameters, the strength and the range, are determined on the basis of HF calculations such that the experimental charge radii are approximately reproduced across the whole nuclear chart. Unfortunately, the matrix element calculation is very time-consuming restricting the applicability of the Gaussian three-body interaction to small model spaces. Since the influence of the Gaussian interaction on the second-order energy corrections is only marginal, we consider only the corrections obtained with the two-body interactions. The small model spaces avoid the convergence of the HF plus MBPT results. But we are able to show that the ground-state energies and charge radii obtained with

the Gaussian three-body interaction are similar to the corresponding results obtained with a regularized three-body contact interaction.

The matrix elements of the three-body contact interaction can directly be calculated in a basis of spherical harmonic-oscillator eigenstates. The structure of the regularized contact interaction entails that the matrix element computation is very efficient compared to the Gaussian three-body interaction. Thus, the contact interaction is also manageable in large model spaces. The contact interaction is employed in connection with all four unitarily transformed two-body interactions. For each underlying two-body interaction the three-body strength is again chosen such that the HF charge radii are in agreement with the experimental ones. For the SRG interaction the three-body strength is roughly twice as large as for the other three two-body interactions. After the inclusion of the three-body interaction the trend of the experimental ground-state energies is reproduced except for an almost constant shift on the basis of all four two-body interactions. Furthermore, in the description of single-particle spectra, the level spacings are reduced due to the additional repulsion. Only for the UCOM(SRG) interaction some inaccuracies appear in the description of single-particle spectra. The inclusion of the perturbative corrections yields a reasonable agreement with experimental data, although we have not yet reached complete convergence. However, these results must not be overstated as the perturbative corrections are only calculated for the two-body interactions and one has to keep in mind the inherent limitations of MBPT.

To obtain a reference point from an exact diagonalization of the Hamilton matrix we include the regularized contact interaction in the No-Core Shell Model. Using the parameter sets optimized to reproduce experimental charge radii across the whole nuclear chart, NCSM calculations based on the S-UCOM(SRG) and S-SRG interactions result in an underbinding of ${}^4\text{He}$ of about 1 to 2 MeV.

As giant resonances are of direct interest for applications in nuclear astrophysics, the influence of the three-body contact interaction on these collective excitation modes is investigated. The Random Phase Approximation provides a suitable framework for the investigation of collective excitations. As including the full three-body interaction in the RPA would be too time-consuming we replace it by a density-dependent two-body contact interaction, which is equivalent in this case except for the regularization. We study extensively isoscalar monopole, isovector dipole, and isoscalar quadrupole excitations. Considering the pure two-body interactions, especially the SRG interaction, strongly overestimates the experimental excitation energies of the considered giant resonances. The giant monopole resonance is generally in agreement with the experimental centroids for the pure two-body interactions while the giant

dipole and giant quadrupole resonances are significantly overestimated. The inclusion of the three-body contact via the density-dependent two-body interaction leads to a reasonable description of all three excitation modes for all four interactions.

Summarizing the preceding studies one can conclude that the UCOM(SRG) interaction shows problems in the description of single-particle spectra and accordingly in the application of MBPT. The SRG interaction has to be supplemented by a stronger three-body interaction in order to compensate the strong overbinding observed on the HF plus MBPT level. As the regularized contact interaction is a phenomenological interaction with a simple structure, e.g. no spin-isospin dependence, one would prefer it to be as weak as possible. The S-UCOM(SRG) and the S-SRG interactions both yield very similar results in all aspects of nuclear properties and, furthermore, their results agree well with experimental data in the framework of various many-body methods for nuclei across the whole nuclear chart. Therefore, one would choose one of these interactions for further investigations, e.g. predictions for exotic nuclei. To perform the next step towards the study of exotic nuclei a number of further important and interesting investigations remain to be examined.

First of all, there are some minor aspects related to the calculation of charge radii. The three-body strength can be chosen such that the radii are in almost perfect agreement with experimental data for all considered nuclei. Therefore, it is worthwhile to examine also minor corrections to the radii, which are the unitary transformation of the radius operator and the calculation of the perturbative corrections for the radii.

The studies in the framework of the No-Core Shell Model can be extended to investigate nuclei beside ${}^4\text{He}$ up to the mid p-shell. Beyond this mass region the Importance Truncated No-Core Shell Model can be applied to examine even heavier nuclei [62]. Furthermore, the study of the influence of the three-body interaction on the T_{jon} line is an interesting aspect.

Throughout this thesis only closed-shell nuclei were examined. For a profound understanding one has to extend the studies to open-shell nuclei, e.g. in the framework of the Hartree-Fock-Bogoliubov method and the Quasiparticle Random Phase Approximation [24, 48, 63]; but also degenerate many-body perturbation theory [64] and the (Importance Truncated) No-Core Shell Model can be applied.

Already the handling of the most simple three-body interaction requires an enormous computational effort. But one would like to include three-body interactions in all aspects that are considered on the basis of pure two-body interactions. Furthermore, one would like to study more general three-body interactions, which exhibit a more complex structure, e.g. the chiral interactions. One possibility to derive of an effective two-body interaction is provided by the normal ordering [65]. The three-body

interaction is reformulated into a zero- plus one- plus two-body interaction with a residual three-body interaction, which is discussed in Appendix D. The influence of the residual three-body interaction on various observables is expected to be negligible. This assumption can be verified by using the contact interaction in the framework of many-body perturbation theory and the No-Core Shell Model.

In summary, the investigation of simple phenomenological three-nucleon interactions proves to be a versatile tool to improve the description of various observables across the whole nuclear chart using different many-body methods as well as to develop an efficient procedure for the handling of three-body matrix elements.

Appendix A

Derivation of the Hartree-Fock Equations

For the derivation of the general Hartree-Fock equations, we first discuss the variational principle which is used to deduce an average single-particle potential out of the NN plus 3N interaction.

A.1 The Variational Principle

The solution of the exact Schrödinger equation

$$H|\Psi\rangle = E|\Psi\rangle \quad (\text{A.1})$$

is equivalent to the variation

$$\delta E[|\Psi\rangle] = E[|\Psi\rangle + |\delta\Psi\rangle] - E[|\Psi\rangle] = 0, \quad (\text{A.2})$$

where we regard the energy E as a functional of the state $|\Psi\rangle$ [49, 66]:

$$E[|\Psi\rangle] = \frac{\langle\Psi|H|\Psi\rangle}{\langle\Psi|\Psi\rangle}. \quad (\text{A.3})$$

The state $|\Psi\rangle + |\delta\Psi\rangle$ denotes an infinitesimal but arbitrary variation of the state $|\Psi\rangle$ with $\langle\delta\Psi|\delta\Psi\rangle \ll 1$. Discarding higher orders in $|\delta\Psi\rangle$ the variation leads to

$$\delta E[|\Psi\rangle] = \frac{1}{\langle\Psi|\Psi\rangle} \left\{ \langle\delta\Psi|H|\Psi\rangle + \langle\Psi|H|\delta\Psi\rangle - \frac{\langle\Psi|H|\Psi\rangle}{\langle\Psi|\Psi\rangle} (\langle\delta\Psi|\Psi\rangle + \langle\Psi|\delta\Psi\rangle) \right\}. \quad (\text{A.4})$$

Appendix A · Derivation of the Hartree-Fock Equations

Together with the condition of stationarity the variation reads

$$\langle \delta\Psi | (H - E) | \Psi \rangle + \langle \Psi | (H - E) | \delta\Psi \rangle = 0 . \quad (\text{A.5})$$

Since $|\delta\Psi\rangle$ is arbitrary the variation can be carried out over $i|\delta\Psi\rangle$ as well:

$$-i\langle \delta\Psi | (H - E) | \Psi \rangle + i\langle \Psi | (H - E) | \delta\Psi \rangle = 0 . \quad (\text{A.6})$$

Together with Equation (A.5) this yields the operator equation

$$\langle \delta\Psi | (H - E) | \Psi \rangle = 0 \quad (\text{A.7})$$

which is equivalent to the Schrödinger equation since $|\delta\Psi\rangle$ is an arbitrary state.

In practical applications one is usually restricted to mathematically simple wave functions for the variation. If the exact solution is not contained in the set of trial wave functions the variation yields only an approximation. The variational principle is especially appropriate to determine ground-states since it can be shown that

$$E[|\Psi\rangle] \geq E_0 , \quad (\text{A.8})$$

i.e. the exact ground state energy E_0 is always the lower bound of the variational calculation. To verify this inequality we only have to expand the trial state $|\Psi\rangle$ in the eigenbasis $|n\rangle$ of the Hamiltonian:

$$|\Psi\rangle = \sum_n c_n |n\rangle \quad \text{with} \quad H|n\rangle = E_n |n\rangle . \quad (\text{A.9})$$

Inserting this expansion in the energy expectation value (A.3) yields

$$E[|\Psi\rangle] = \frac{\sum_{n,m} c_n^* c_m \langle n | H | m \rangle}{\sum_n |c_n|^2} = \frac{\sum_n |c_n|^2 E_n}{\sum_n |c_n|^2} \geq \frac{\sum_n |c_n|^2 E_0}{\sum_n |c_n|^2} = E_0 , \quad (\text{A.10})$$

where we have assumed $E_0 \leq E_1 \leq E_2 \leq \dots$. Hence, for the approximation of the ground-state we only have to carry out an energy minimization by varying the trial state.

A.2 The Hartree-Fock Method

In the Hartree-Fock (HF) method, which we use for the description of an A -fermion system, one uses a single Slater determinant

$$|\Phi\rangle = a_1^\dagger a_2^\dagger \dots a_A^\dagger |0\rangle \quad (\text{A.11})$$

as trial state [49, 66]. The energy minimization is performed via the variation of the single-particle states $|\varphi_k\rangle = a_k^\dagger|0\rangle$. We work on the basis of a complete and orthogonal set of single-particle states $\{|\chi_I\rangle\}$ with the corresponding creation operators c_I^\dagger , which are the spherical harmonic-oscillator states in our case. The HF single-particle states are expanded in this basis:

$$|\varphi_k\rangle = \sum_{I=1}^{\infty} D_{Ik} |\chi_I\rangle \quad \text{and} \quad a_k^\dagger = \sum_{I=1}^{\infty} D_{Ik} c_I^\dagger, \quad (\text{A.12})$$

where we have to determine the expansion coefficients D_{Ik} . The transformation D is unitary since both single-particle bases, $\{|\varphi_k\rangle\}$ and $\{|\chi_I\rangle\}$, are complete and orthogonal.

It is not possible to determine the expansion coefficients D_{Ik} in an unambiguous way because Slater determinants are – apart from a phase – invariant under unitary transformations which do not mix particle and hole states. This means that the energy minimization will only mark a single-particle subspace which can be represented more conveniently by the single-particle density matrix $\varrho_{II'}^{(1)} = \langle \chi_I | \varrho^{(1)} | \chi_{I'} \rangle$. We can express the single-particle density via the expansion coefficients as

$$\varrho_{II'}^{(1)} = \langle \Phi | c_{I'}^\dagger c_I | \Phi \rangle = \sum_{k,k'}^{\infty} D_{Ik} D_{I'k'}^* \langle \Phi | a_{k'}^\dagger a_k | \Phi \rangle = \sum_{k=1}^A D_{Ik} D_{I'k}^* \quad (\text{A.13})$$

since $\varrho^{(1)}$ is diagonal in the single-particle basis a_k^\dagger with eigenvalues 1 for occupied and 0 for unoccupied states. Since we have an unambiguous relation between the Slater determinant $|\Phi\rangle$ and the single-particle density $\varrho^{(1)}$ we will use the density matrix elements as variational parameters. The density matrix of a Slater determinant is hermitian and idempotent:

$$(\varrho^{(1)})^\dagger = \varrho^{(1)} \quad \text{and} \quad (\varrho^{(1)})^2 = \varrho^{(1)}, \quad (\text{A.14})$$

i.e. we have to perform the variation under the constraint (A.14).

To carry out the variation we have to express the energy functional via the single-particle density matrix. Therefore, we start with the Hamiltonian in the basis c_I^\dagger

Appendix A · Derivation of the Hartree-Fock Equations

[27, 49, 66]:

$$\begin{aligned}
 H &= \sum_{a\bar{a}}^{\infty} t_{a\bar{a}} c_a^\dagger c_{\bar{a}} \\
 &\quad + \frac{1}{4} \sum_{\substack{ab \\ \bar{a}\bar{b}}}^{\infty} V_{ab,\bar{a}\bar{b}}^{(2)} c_a^\dagger c_b^\dagger c_{\bar{b}} c_{\bar{a}} \\
 &\quad + \frac{1}{36} \sum_{\substack{abc \\ \bar{a}\bar{b}\bar{c}}}^{\infty} V_{abc,\bar{a}\bar{b}\bar{c}}^{(3)} c_a^\dagger c_b^\dagger c_c^\dagger c_{\bar{c}} c_{\bar{b}} c_{\bar{a}} \quad (A.15)
 \end{aligned}$$

with the one-body matrix elements of the kinetic energy

$$t_{a\bar{a}} = \langle \chi_a | \mathbf{T} | \chi_{\bar{a}} \rangle, \quad (A.16)$$

the antisymmetric two-body matrix elements of the NN interaction

$$V_{ab,\bar{a}\bar{b}}^{(2)} = {}_a \langle \chi_a \chi_b | V^{(2)} | \chi_{\bar{a}} \chi_{\bar{b}} \rangle_a, \quad (A.17)$$

and the antisymmetric three-body matrix elements of the 3N interaction

$$V_{abc,\bar{a}\bar{b}\bar{c}}^{(3)} = {}_a \langle \chi_a \chi_b \chi_c | V^{(3)} | \chi_{\bar{a}} \chi_{\bar{b}} \chi_{\bar{c}} \rangle_a. \quad (A.18)$$

Thus, the energy expectation value reads

$$\begin{aligned}
 E[|\Phi\rangle] &= \sum_{a\bar{a}}^{\infty} t_{a\bar{a}} \langle \Phi | c_a^\dagger c_{\bar{a}} | \Phi \rangle \\
 &\quad + \frac{1}{4} \sum_{\substack{ab \\ \bar{a}\bar{b}}}^{\infty} V_{ab,\bar{a}\bar{b}}^{(2)} \langle \Phi | c_a^\dagger c_b^\dagger c_{\bar{b}} c_{\bar{a}} | \Phi \rangle \\
 &\quad + \frac{1}{36} \sum_{\substack{abc \\ \bar{a}\bar{b}\bar{c}}}^{\infty} V_{abc,\bar{a}\bar{b}\bar{c}}^{(3)} \langle \Phi | c_a^\dagger c_b^\dagger c_c^\dagger c_{\bar{c}} c_{\bar{b}} c_{\bar{a}} | \Phi \rangle \\
 &= \sum_{a\bar{a}}^{\infty} t_{a\bar{a}} \varrho_{\bar{a}a}^{(1)} + \frac{1}{4} \sum_{\substack{ab \\ \bar{a}\bar{b}}}^{\infty} V_{ab,\bar{a}\bar{b}}^{(2)} \varrho_{\bar{a}\bar{b},ab}^{(2)} + \frac{1}{36} \sum_{\substack{abc \\ \bar{a}\bar{b}\bar{c}}}^{\infty} V_{abc,\bar{a}\bar{b}\bar{c}}^{(3)} \varrho_{\bar{a}\bar{b}\bar{c},abc}^{(3)} \quad (A.19)
 \end{aligned}$$

with the two-particle density matrix $\varrho^{(2)}$ and the three-particle density matrix $\varrho^{(3)}$ which can be expressed via the single-particle density matrix, since the state $|\Phi\rangle$ is a Slater determinant:

$$\varrho_{\bar{a}\bar{b},ab}^{(2)} = \varrho_{\bar{a}a}^{(1)} \varrho_{\bar{b}b}^{(1)} - \varrho_{\bar{a}b}^{(1)} \varrho_{\bar{b}a}^{(1)} \quad (A.20)$$

$$\begin{aligned}
 \varrho_{\bar{a}\bar{b}\bar{c},abc}^{(3)} &= \varrho_{\bar{a}a}^{(1)} \varrho_{\bar{b}b}^{(1)} \varrho_{\bar{c}c}^{(1)} + \varrho_{\bar{a}c}^{(1)} \varrho_{\bar{b}a}^{(1)} \varrho_{\bar{c}b}^{(1)} + \varrho_{\bar{a}b}^{(1)} \varrho_{\bar{b}c}^{(1)} \varrho_{\bar{c}a}^{(1)} \\
 &\quad - \varrho_{\bar{a}a}^{(1)} \varrho_{\bar{b}c}^{(1)} \varrho_{\bar{c}b}^{(1)} - \varrho_{\bar{a}b}^{(1)} \varrho_{\bar{b}a}^{(1)} \varrho_{\bar{c}c}^{(1)} - \varrho_{\bar{a}c}^{(1)} \varrho_{\bar{b}b}^{(1)} \varrho_{\bar{c}a}^{(1)}. \quad (A.21)
 \end{aligned}$$

Inserting these relations in Equation (A.19) yields the energy as functional of the single-particle density matrix:

$$E[\varrho^{(1)}] = \sum_{a\bar{a}}^{\infty} t_{a\bar{a}} \varrho_{\bar{a}a}^{(1)} + \frac{1}{2} \sum_{\substack{ab \\ \bar{a}\bar{b}}}^{\infty} V_{ab,\bar{a}\bar{b}}^{(2)} \varrho_{\bar{a}a}^{(1)} \varrho_{\bar{b}b}^{(1)} + \frac{1}{6} \sum_{\substack{abc \\ \bar{a}\bar{b}\bar{c}}}^{\infty} V_{abc,\bar{a}\bar{b}\bar{c}}^{(3)} \varrho_{\bar{a}a}^{(1)} \varrho_{\bar{b}b}^{(1)} \varrho_{\bar{c}c}^{(1)}. \quad (\text{A.22})$$

If we take into account only the linear terms in $\delta\varrho^{(1)}$ the variation of the energy functional reads

$$\begin{aligned} \delta E[\varrho^{(1)}] &= \sum_{a\bar{a}}^{\infty} t_{a\bar{a}} \delta\varrho_{\bar{a}a}^{(1)} \\ &+ \frac{1}{2} \sum_{\substack{ab \\ \bar{a}\bar{b}}}^{\infty} V_{ab,\bar{a}\bar{b}}^{(2)} (\delta\varrho_{\bar{a}a}^{(1)} \varrho_{\bar{b}b}^{(1)} + \varrho_{\bar{a}a}^{(1)} \delta\varrho_{\bar{b}b}^{(1)}) \\ &+ \frac{1}{6} \sum_{\substack{abc \\ \bar{a}\bar{b}\bar{c}}}^{\infty} V_{abc,\bar{a}\bar{b}\bar{c}}^{(3)} (\delta\varrho_{\bar{a}a}^{(1)} \varrho_{\bar{b}b}^{(1)} \varrho_{\bar{c}c}^{(1)} + \varrho_{\bar{a}a}^{(1)} \delta\varrho_{\bar{b}b}^{(1)} \varrho_{\bar{c}c}^{(1)} + \varrho_{\bar{a}a}^{(1)} \varrho_{\bar{b}b}^{(1)} \delta\varrho_{\bar{c}c}^{(1)}) \\ &= \sum_{a\bar{a}}^{\infty} \left\{ t_{a\bar{a}} + \sum_{\substack{ab \\ \bar{a}\bar{b}}}^{\infty} V_{ab,\bar{a}\bar{b}}^{(2)} \varrho_{\bar{b}b}^{(1)} + \frac{1}{2} \sum_{\substack{bc \\ \bar{b}\bar{c}}}^{\infty} V_{abc,\bar{a}\bar{b}\bar{c}}^{(3)} \varrho_{\bar{b}b}^{(1)} \varrho_{\bar{c}c}^{(1)} \right\} \delta\varrho_{\bar{a}a}^{(1)}. \quad (\text{A.23}) \end{aligned}$$

In the last equation we can identify the single-particle potential

$$u_{a\bar{a}}[\varrho^{(1)}] = \sum_{\substack{ab \\ \bar{a}\bar{b}}}^{\infty} V_{ab,\bar{a}\bar{b}}^{(2)} \varrho_{\bar{b}b}^{(1)} + \frac{1}{2} \sum_{\substack{bc \\ \bar{b}\bar{c}}}^{\infty} V_{abc,\bar{a}\bar{b}\bar{c}}^{(3)} \varrho_{\bar{b}b}^{(1)} \varrho_{\bar{c}c}^{(1)} \quad (\text{A.24})$$

depending on the single-particle density matrix. Together with the kinetic energy we get the matrix elements of the single-particle Hamiltonian

$$h_{a\bar{a}}[\varrho^{(1)}] = t_{a\bar{a}} + u_{a\bar{a}}[\varrho^{(1)}]. \quad (\text{A.25})$$

The variational equation can thus be written as

$$\delta E[\varrho^{(1)}] = \sum_{a\bar{a}}^{\infty} h_{a\bar{a}}[\varrho^{(1)}] \delta\varrho_{\bar{a}a}^{(1)} = 0. \quad (\text{A.26})$$

Here, we have to remember the constraints (A.14). A small variation of the density matrix $\varrho^{(1)} + \delta\varrho^{(1)}$ still has to describe a Slater determinant, hence it has to be idempotent: $(\varrho^{(1)} + \delta\varrho^{(1)})^2 = \varrho^{(1)} + \delta\varrho^{(1)}$ which leads to the following conditions:

$$\varrho^{(1)} \delta\varrho^{(1)} \varrho^{(1)} = 0 \quad \text{and} \quad (1 - \varrho^{(1)}) \delta\varrho^{(1)} (1 - \varrho^{(1)}) = 0. \quad (\text{A.27})$$

Appendix A · Derivation of the Hartree-Fock Equations

In the Hartree-Fock basis the single-particle density is diagonal, i.e. in order to satisfy the conditions (A.27) the variation can only take place between occupied (hole) and unoccupied (particle) states. This means that the variation is restricted to ph (particle-hole) and hp matrix elements of $\varrho^{(1)}$ in the HF basis. On the other hand, Equation (A.26) reveals that the single-particle Hamiltonian can only consist of non-vanishing pp and hh matrix elements in the HF basis. In other words, the commutator of the single-particle Hamiltonian and the single-particle density has to vanish:

$$[h[\varrho^{(1)}], \varrho^{(1)}] = 0 . \quad (\text{A.28})$$

This means that the single-particle Hamiltonian and the single-particle density have a simultaneous eigenbasis. Hence, instead of solving the commutator equation we can convert Equation (A.28) into the eigenvalue problem:

$$h[\varrho^{(1)}]|\varphi_k\rangle = \varepsilon_k|\varphi_k\rangle , \quad (\text{A.29})$$

which defines the single-particle Hartree-Fock states $|\varphi_k\rangle$ and the corresponding single-particle energies ε_k . Finally, we transform this eigenvalue problem into the basis $|\chi_l\rangle$:

$$\sum_{\bar{a}}^{\infty} h_{a\bar{a}}[\varrho^{(1)}]D_{\bar{a}k} = \varepsilon_k D_{ak} . \quad (\text{A.30})$$

Inserting the single-particle Hamiltonian (A.25) and the density matrix (A.13) we obtain the Hartree-Fock equations

$$\begin{aligned} \sum_{\bar{a}}^{\infty} \left\{ t_{a\bar{a}} + \sum_{i=1}^A \sum_{b\bar{b}}^{\infty} V_{ab,\bar{a}\bar{b}}^{(2)} D_{\bar{b}i} D_{bi}^* \right. \\ \left. + \frac{1}{2} \sum_{i,j=1}^A \sum_{\substack{bc \\ \bar{b}\bar{c}}}^{\infty} V_{abc,\bar{a}\bar{b}\bar{c}}^{(3)} D_{\bar{b}i} D_{bi}^* D_{\bar{c}j} D_{cj}^* \right\} D_{\bar{a}k} = \varepsilon_k D_{ak} . \end{aligned} \quad (\text{A.31})$$

This set of equations represents a nonlinear eigenvalue problem which can be solved by applying an iterative scheme in order to obtain a self-consistent solution for the coefficients D_{lk} .

The A single-particle states with the lowest single-particle energies are used for the construction of the Hartree-Fock ground-state:

$$|\text{HF}\rangle = |\Phi\rangle = a_1^\dagger a_2^\dagger \dots a_A^\dagger |0\rangle , \quad (\text{A.32})$$

which is again a single Slater determinant. The energy expectation value of the HF state is given by

$$\begin{aligned}
 E[|\text{HF}\rangle] &= \langle \text{HF} | H | \text{HF} \rangle \\
 &= \sum_{i=1}^A \langle \varphi_i | T | \varphi_i \rangle + \frac{1}{2} \sum_{i,j=1}^A a \langle \varphi_i \varphi_j | V^{(2)} | \varphi_i \varphi_j \rangle_a \\
 &\quad + \frac{1}{6} \sum_{i,j,k=1}^A a \langle \varphi_i \varphi_j \varphi_k | V^{(3)} | \varphi_i \varphi_j \varphi_k \rangle_a \\
 &= \sum_{i=1}^A \epsilon_i - \frac{1}{2} \sum_{i,j=1}^A a \langle \varphi_i \varphi_j | V^{(2)} | \varphi_i \varphi_j \rangle_a \\
 &\quad - \frac{1}{3} \sum_{i,j,k=1}^A a \langle \varphi_i \varphi_j \varphi_k | V^{(3)} | \varphi_i \varphi_j \varphi_k \rangle_a , \tag{A.33}
 \end{aligned}$$

which means that the ground-state energy is not equal to the sum of the A lowest single-particle energies.

Appendix A · Derivation of the Hartree-Fock Equations

Appendix B

Basic Concepts of Perturbation Theory

Perturbation theory provides a procedure to solve eigenvalue problems of the following form:

$$H|\Phi_i\rangle = (H_0 + W)|\Phi_i\rangle = E_i|\Phi_i\rangle . \quad (\text{B.1})$$

The Hamiltonian H can be divided into one part H_0 with known eigenvalues $E_i^{(0)}$ and eigenstates $|\Psi_i^{(0)}\rangle$: $H_0|\Psi_i^{(0)}\rangle = E_i^{(0)}|\Psi_i^{(0)}\rangle$, and the perturbation W which has to be small compared to H_0 with respect to its contributions to the full eigenvalues. In this case, it is possible to formulate an expansion that approximates the eigenvalues E_i and eigenstates $|\Phi_i\rangle$ of the full Hamiltonian step by step starting from $E_i^{(0)}$ and $|\Psi_i^{(0)}\rangle$, respectively.

For the formal expansion, the parameter λ is introduced [35]:

$$H = H_0 + \lambda W . \quad (\text{B.2})$$

Expressing the eigenenergies and eigenstates via power series yields

$$E_i = E_i^{(0)} + \lambda E_i^{(1)} + \lambda^2 E_i^{(2)} + \dots \quad (\text{B.3})$$

$$|\Phi_i\rangle = |\Psi_i^{(0)}\rangle + \lambda |\Psi_i^{(1)}\rangle + \lambda^2 |\Psi_i^{(2)}\rangle + \dots . \quad (\text{B.4})$$

The unperturbed states are assumed to be normalized: $\langle \Psi_i^{(0)} | \Psi_i^{(0)} \rangle = 1$. Furthermore, the following relation is obtained by inserting the power series (B.4) into the normalization condition $\langle \Psi_i^{(0)} | \Phi_i \rangle = 1$ under the requirement that the resulting equation is valid for arbitrary values of λ :

$$\langle \Psi_i^{(0)} | \Psi_i^{(n)} \rangle = 0 , \quad n \geq 1 . \quad (\text{B.5})$$

Inserting the power series (B.3) and (B.4) into the Schrödinger equation and sorting in powers of λ yields

$$\lambda^0 : \quad H_0|\Psi_i^{(0)}\rangle = E_i^{(0)}|\Psi_i^{(0)}\rangle \quad (\text{B.6})$$

$$\lambda^1 : \quad H_0|\Psi_i^{(1)}\rangle + W|\Psi_i^{(0)}\rangle = E_i^{(0)}|\Psi_i^{(1)}\rangle + E_i^{(1)}|\Psi_i^{(0)}\rangle \quad (\text{B.7})$$

$$\lambda^2 : \quad H_0|\Psi_i^{(2)}\rangle + W|\Psi_i^{(1)}\rangle = E_i^{(0)}|\Psi_i^{(2)}\rangle + E_i^{(1)}|\Psi_i^{(1)}\rangle + E_i^{(2)}|\Psi_i^{(0)}\rangle \quad (\text{B.8})$$

⋮

After multiplication with $\langle\Psi_i^{(0)}|$ and using Equation (B.5) we obtain the energies

$$\lambda^0 : \quad E_i^{(0)} = \langle\Psi_i^{(0)}|H_0|\Psi_i^{(0)}\rangle \quad (\text{B.9})$$

$$\lambda^1 : \quad E_i^{(1)} = \langle\Psi_i^{(0)}|W|\Psi_i^{(0)}\rangle \quad (\text{B.10})$$

$$\lambda^2 : \quad E_i^{(2)} = \langle\Psi_i^{(0)}|W|\Psi_i^{(1)}\rangle \quad (\text{B.11})$$

⋮

Hence, the first order energy correction is given by the expectation value of the perturbation W with the unperturbed states $|\Psi_i^{(0)}\rangle$. For the determination of the second order correction, the first order states $|\Psi_i^{(1)}\rangle$ have to be expressed via the unperturbed states. Therefore, Equation (B.7) is multiplied by $\langle\Psi_n^{(0)}|$ yielding

$$\langle\Psi_n^{(0)}|\Psi_i^{(1)}\rangle = \frac{\langle\Psi_n^{(0)}|W|\Psi_i^{(0)}\rangle}{E_i^{(0)} - E_n^{(0)}} , \quad (\text{B.12})$$

which is inserted in the expansion

$$|\Psi_i^{(1)}\rangle = \sum_n c_n^{(1)}|\Psi_n^{(0)}\rangle = \sum_{n \neq i} |\Psi_n^{(0)}\rangle \langle\Psi_n^{(0)}|\Psi_i^{(1)}\rangle . \quad (\text{B.13})$$

Together with Equation (B.11) the second order energy correction is obtained:

$$E_i^{(2)} = \sum_{\substack{n \\ n \neq i}} \frac{|\langle\Psi_i^{(0)}|W|\Psi_n^{(0)}\rangle|^2}{E_i^{(0)} - E_n^{(0)}} . \quad (\text{B.14})$$

The third and higher orders can be determined in an analogous manner. However, they are not needed throughout this thesis.

Appendix C

Basic Concepts of the Random Phase Approximation

Collective excitations can be investigated by applying the Random Phase Approximation (RPA) [47–49, 63] on the basis of a HF solution. For the derivation of the general RPA equations we start from the exact Schrödinger equation

$$H|\Psi_\nu\rangle = E_\nu|\Psi_\nu\rangle, \quad (\text{C.1})$$

and define the operators Q_ν^\dagger and Q_ν such that the excited state $|\Psi_\nu\rangle$ is created by the application of Q_ν^\dagger to the ground-state $|\Psi_0\rangle$:

$$|\Psi_\nu\rangle = Q_\nu^\dagger|\Psi_0\rangle \quad \text{and} \quad Q_\nu|\Psi_0\rangle = 0. \quad (\text{C.2})$$

Formally these operators can be written as

$$Q_\nu^\dagger = |\Psi_\nu\rangle\langle\Psi_0| \quad \text{and} \quad Q_\nu = |\Psi_0\rangle\langle\Psi_\nu|. \quad (\text{C.3})$$

Using these operators, the Schrödinger equation can be transformed into the equivalent equation of motion

$$[H, Q_\nu^\dagger]|\Psi_0\rangle = (E_\nu - E_0)Q_\nu^\dagger|\Psi_0\rangle. \quad (\text{C.4})$$

Multiplying this equation from the left with an arbitrary state $\langle\Psi_0|\delta Q$ and inserting terms of the form $\langle\Psi_0|Q_\nu^\dagger = \langle\Psi_0|HQ_\nu^\dagger = 0$ we arrive at

$$\langle\Psi_0|[\delta Q, [H, Q_\nu^\dagger]]|\Psi_0\rangle = (E_\nu - E_0)\langle\Psi_0|[\delta Q, Q_\nu^\dagger]|\Psi_0\rangle. \quad (\text{C.5})$$

This final form of the equation of motion is exact since the variation

$$\delta Q^\dagger |\Psi_0\rangle = \sum_{\nu \neq 0} \delta c_\nu Q^\dagger_\nu |\Psi_0\rangle = \sum_{\nu \neq 0} \delta c_\nu |\Psi_\nu\rangle \quad (\text{C.6})$$

exhausting the whole Hilbert space is arbitrary but orthogonal to the ground-state.

A crucial task is the choice of the specific form of the excitation operators Q^\dagger_ν . If the exact ground-state is approximated by the HF state and the operators Q^\dagger_ν describe 1p1h excitations of the HF state, the resultant equations build the Tamm-Dancoff method. However, in RPA an improved ansatz for the excitation operators is chosen:

$$Q^\dagger_\nu = \sum_{mi} X_{mi}^{(\nu)} a^\dagger_m a_i - \sum_{mi} Y_{mi}^{(\nu)} a^\dagger_i a_m . \quad (\text{C.7})$$

Here and in the following, the indices i, j refer to states below the Fermi energy, i.e. $\varepsilon_i, \varepsilon_j \leq \varepsilon_F$ with respect to the HF single-particle energies, and the indices m, n refer to states above the Fermi energy, i.e. $\varepsilon_m, \varepsilon_n \geq \varepsilon_F$. Hence, the operators $a^\dagger_m a_i$ and $a^\dagger_i a_m$ can be interpreted as ph-creation and ph-annihilation operators, respectively. The ground-state $|\Psi_0\rangle = |\text{RPA}\rangle$ is defined consistently via

$$Q_\nu |\text{RPA}\rangle = 0 , \quad (\text{C.8})$$

which can be understood as the HF ground-state containing additional ph-correlations.

The variation

$$\delta Q^\dagger |\text{RPA}\rangle = \sum_{mi} \delta X_{mi}^{(\nu)} a^\dagger_m a_i |\text{RPA}\rangle - \sum_{mi} \delta Y_{mi}^{(\nu)} a^\dagger_i a_m |\text{RPA}\rangle \quad (\text{C.9})$$

has to be performed independently for the two types of coefficients, $X_{mi}^{(\nu)}$ and $Y_{mi}^{(\nu)}$, yielding a set of two coupled equations

$$\begin{aligned} \langle \text{RPA} | [a^\dagger_i a_m, [H, Q^\dagger_\nu]] | \text{RPA} \rangle &= E_\nu^{\text{RPA}} \langle \text{RPA} | [a^\dagger_i a_m, Q^\dagger_\nu] | \text{RPA} \rangle \\ \langle \text{RPA} | [a^\dagger_m a_i, [H, Q^\dagger_\nu]] | \text{RPA} \rangle &= E_\nu^{\text{RPA}} \langle \text{RPA} | [a^\dagger_m a_i, Q^\dagger_\nu] | \text{RPA} \rangle \end{aligned} \quad (\text{C.10})$$

with the excitation energy $E_\nu^{\text{RPA}} = E_\nu - E_0$. These equations, that define the excitation operators Q^\dagger_ν via the coefficient matrices $X_{mi}^{(\nu)}$ and $Y_{mi}^{(\nu)}$, cannot be solved directly since the RPA ground-state is unknown. One can determine the RPA ground-state and the coefficient matrices simultaneously by applying an iterative scheme which is known as extended RPA. However, we will only use the standard RPA where an additional approximation is made in order to avoid the iteration procedure.

For the calculation of expectation values we assume that the RPA ground-state does not differ significantly from the HF state:

$$\begin{aligned}\langle \text{RPA} | [a_i^\dagger a_m, a_n^\dagger a_j] | \text{RPA} \rangle &= \delta_{ij} \delta_{mn} - \delta_{mn} \langle \text{RPA} | a_j a_i^\dagger | \text{RPA} \rangle - \delta_{ij} \langle \text{RPA} | a_n^\dagger a_m | \text{RPA} \rangle \\ &\approx \langle \text{HF} | [a_i^\dagger a_m, a_n^\dagger a_j] | \text{HF} \rangle = \delta_{ij} \delta_{mn} .\end{aligned}\quad (\text{C.11})$$

This is known as quasi-boson approximation as it would be exact if the ph-creation and -annihilation operators were bosonic operators. Within this approximation, the absolute squares of the amplitudes $X_{mi}^{(\nu)}$ and $Y_{mi}^{(\nu)}$ directly give the probability of finding the states $a_m^\dagger a_i | \text{RPA} \rangle$ and $a_i^\dagger a_m | \text{RPA} \rangle$, respectively, in the excited state $|\Psi_\nu\rangle$. Thus, the matrix elements of the one-body transition density $\varrho^{(1)}$ read

$$\begin{aligned}\varrho_{mi}^{(1)\nu} &= \langle \text{RPA} | a_i^\dagger a_m | \Psi_\nu \rangle = \langle \text{RPA} | [a_i^\dagger a_m, Q_\nu^\dagger] | \text{RPA} \rangle \\ &\approx \langle \text{HF} | [a_i^\dagger a_m, Q_\nu^\dagger] | \text{HF} \rangle = X_{mi}^{(\nu)} \\ \varrho_{im}^{(1)\nu} &= \langle \text{RPA} | a_m^\dagger a_i | \Psi_\nu \rangle = \langle \text{RPA} | [a_m^\dagger a_i, Q_\nu^\dagger] | \text{RPA} \rangle \\ &\approx \langle \text{HF} | [a_m^\dagger a_i, Q_\nu^\dagger] | \text{HF} \rangle = Y_{mi}^{(\nu)} .\end{aligned}\quad (\text{C.12})$$

The RPA is well-suited for the description of collective states which can be understood by looking closer at the quasi-boson approximation (C.11). This approximation is valid if many coefficients $X_{mi}^{(\nu)}$ are of the same order of magnitude, i.e. for excited states with collective character. Furthermore, the correlated ground-state $|\text{RPA}\rangle$ is approximated by the HF state which is only justified if the ground-state correlations are small, i.e. the amplitudes $Y_{mi}^{(\nu)}$ have to be small compared to $X_{mi}^{(\nu)}$.

The RPA equations can now be written in a compact matrix form

$$\begin{pmatrix} A & B \\ B^* & A^* \end{pmatrix} \begin{pmatrix} X^{(\nu)} \\ Y^{(\nu)} \end{pmatrix} = E_\nu^{\text{RPA}} \begin{pmatrix} 1 & 0 \\ 0 & -1 \end{pmatrix} \begin{pmatrix} X^{(\nu)} \\ Y^{(\nu)} \end{pmatrix}\quad (\text{C.13})$$

with the hermitian matrix A

$$A_{mi,nj} = \langle \text{HF} | [a_i^\dagger a_m, [H, a_n^\dagger a_j]] | \text{HF} \rangle = (\varepsilon_m - \varepsilon_i) \delta_{mn} \delta_{ij} + V_{mj,in}\quad (\text{C.14})$$

and the symmetric matrix B

$$B_{mi,nj} = -\langle \text{HF} | [a_i^\dagger a_m, [H, a_j^\dagger a_n]] | \text{HF} \rangle = V_{mn,ij} .\quad (\text{C.15})$$

In the RPA equations enter the matrix elements $V_{mj,in}$ between 1p1h-states of a general two-body interaction as well as matrix elements $V_{mn,ij}$ between 2p2h states.

Appendix C · Basic Concepts of the Random Phase Approximation

The energy eigenvalues E_ν^{RPA} are not necessarily real-valued since the non-hermitian eigenvalue problem (C.13) contains the metric tensor $\begin{pmatrix} 1 & 0 \\ 0 & -1 \end{pmatrix}$. The solutions of the RPA equations fulfill the orthogonality relation

$$\delta_{\mu\nu} = \sum_{mi} (X_{mi}^{(\mu)*} X_{mi}^{(\nu)} - Y_{mi}^{(\mu)*} Y_{mi}^{(\nu)}) \quad (\text{C.16})$$

as well as the closure relation

$$\delta_{mn}\delta_{ij} = \sum_{\nu} (X_{mi}^{(\nu)*} X_{nj}^{(\nu)} - Y_{mi}^{(\nu)*} Y_{nj}^{(\nu)}) . \quad (\text{C.17})$$

The energy expectation value of the RPA ground-state

$$\langle \text{RPA} | H | \text{RPA} \rangle = \langle \text{HF} | H | \text{HF} \rangle - \sum_{\nu} E_{\nu}^{\text{RPA}} \sum_{mi} |Y_{mi}^{(\nu)}|^2 \quad (\text{C.18})$$

is always lower than the HF energy as it takes into account higher correlations. However, the RPA-energy can even fall below the exact ground-state energy since it does not follow from a variational principle due to the approximations that were made during the derivation of the standard RPA equations.

The RPA ground-state defined by Equation (C.8) can be written as

$$|\text{RPA}\rangle = N_0 \exp \left\{ \frac{1}{2} \sum_{minj} Z_{mi,nj} a_m^\dagger a_i^\dagger a_n a_j \right\} |\text{HF}\rangle \quad (\text{C.19})$$

with the normalization constant N_0 and $\sum_{mi} X_{mi}^{(\nu)*} Z_{mi,nj} = Y_{nj}^{(\nu)*}$, i.e. the RPA ground-state is a coherent state of 2p2h-excitations of the HF ground-state.

Appendix D

Normal Ordering

For various applications including a three-body interaction is not feasible. Via the normal ordering one can derive an effective zero- plus one- plus two-body interaction with a residual three-body interaction, whose impact is expected to be negligible [65]. The normal ordering is defined with respect to a reference state, which is the Hartree-Fock ground-state in our case, as

$$\{a_\alpha a_\beta^\dagger\} = \begin{cases} -a_\beta^\dagger a_\alpha & \text{for } \varepsilon_\alpha > \varepsilon_F, \varepsilon_\beta > \varepsilon_F \\ a_\alpha a_\beta^\dagger = -a_\beta^\dagger a_\alpha & \text{for } \varepsilon_\alpha > \varepsilon_F, \varepsilon_\beta < \varepsilon_F \\ a_\alpha a_\beta^\dagger = -a_\beta^\dagger a_\alpha & \text{for } \varepsilon_\alpha < \varepsilon_F, \varepsilon_\beta > \varepsilon_F \\ a_\alpha a_\beta^\dagger & \text{for } \varepsilon_\alpha < \varepsilon_F, \varepsilon_\beta < \varepsilon_F \end{cases}, \quad (\text{D.1})$$

where a_β^\dagger and a_α create and annihilate a fermion with single-particle energy ε_β and ε_α , respectively, and ε_F indicates the Fermi-energy.

By rearranging the summands the normal ordered form of a general three-body interaction is obtained [65]:

$$\begin{aligned} & \frac{1}{36} \sum_{pqrstu} \langle pqr || stu \rangle a_p^\dagger a_q^\dagger a_r^\dagger a_u a_t a_s \\ &= \frac{1}{6} \sum_{ijk} \langle ijk || ijk \rangle + \frac{1}{2} \sum_{ijpq} \langle ijp || ijq \rangle \{a_p^\dagger a_q\} + \frac{1}{4} \sum_{ipqrs} \langle ipq || irs \rangle \{a_p^\dagger a_q^\dagger a_s a_r\} \\ &+ \frac{1}{36} \sum_{pqrstu} \langle pqr || stu \rangle \{a_p^\dagger a_q^\dagger a_r^\dagger a_u a_t a_s\}, \end{aligned} \quad (\text{D.2})$$

where $\langle pqr || stu \rangle$ denote the antisymmetrized three-body matrix elements. The indices i, j, k label occupied orbitals of the reference state while p, q, r, s, t, u refer to all

Appendix D · Normal Ordering

orbitals. The normal ordering of four and six creation and annihilation operators follows directly from the extension of definition (D.1).

In our existing programs for the various many-body methods enter the interactions not in the normal ordered but in the standard form. In principle, it is possible to change the program structure, however, it is more convenient to express the one- and two-body normal ordered interactions via the standard forms.

The normal ordered form of the one-body interaction reads

$$\sum_{ijpq} \langle ij|p||iq \rangle a_p^\dagger a_q = \sum_{ijk} \langle ij|k||ijk \rangle + \sum_{ijpq} \langle ij|p||iq \rangle \{a_p^\dagger a_q\} , \quad (D.3)$$

and for the two-body interaction we find

$$\begin{aligned} & \frac{1}{4} \sum_{ipqrs} \langle ipq||irs \rangle a_p^\dagger a_q^\dagger a_s a_r \\ &= \frac{1}{2} \sum_{ijk} \langle ij|k||ijk \rangle + \sum_{ijpq} \langle ij|p||iq \rangle \{a_p^\dagger a_q\} + \frac{1}{4} \sum_{ipqrs} \langle ipq||irs \rangle \{a_p^\dagger a_q^\dagger a_s a_r\} . \end{aligned} \quad (D.4)$$

Thus, the normal ordered three-body interaction can be rewritten:

$$\begin{aligned} & \frac{1}{36} \sum_{pqrst} \langle pqr||stu \rangle a_p^\dagger a_q^\dagger a_r^\dagger a_u a_t a_s \\ &= \frac{1}{6} \sum_{ijk} \langle ij|k||ijk \rangle - \frac{1}{18} \sum_{ijpq} \langle ij|p||iq \rangle a_p^\dagger a_q + \frac{1}{4} \sum_{ipqrs} \langle ipq||irs \rangle a_p^\dagger a_q^\dagger a_s a_r \\ &+ \frac{1}{36} \sum_{pqrst} \langle pqr||stu \rangle \{a_p^\dagger a_q^\dagger a_r^\dagger a_u a_t a_s\} . \end{aligned} \quad (D.5)$$

After discarding the residual three-body term $\frac{1}{36} \sum_{pqrst} \langle pqr||stu \rangle \{a_p^\dagger a_q^\dagger a_r^\dagger a_u a_t a_s\}$ the effective interaction can be easily included in all existing program codes for various many-body methods.

Appendix E

Figures

In this appendix are collected some figures that complete the discussions in Chapters 5 and 7, but reveal no further physical insight.

E.1 Hartree-Fock Results for the Contact Interaction

The following figures supplement the discussion in Section 5.2.

Appendix E · Figures

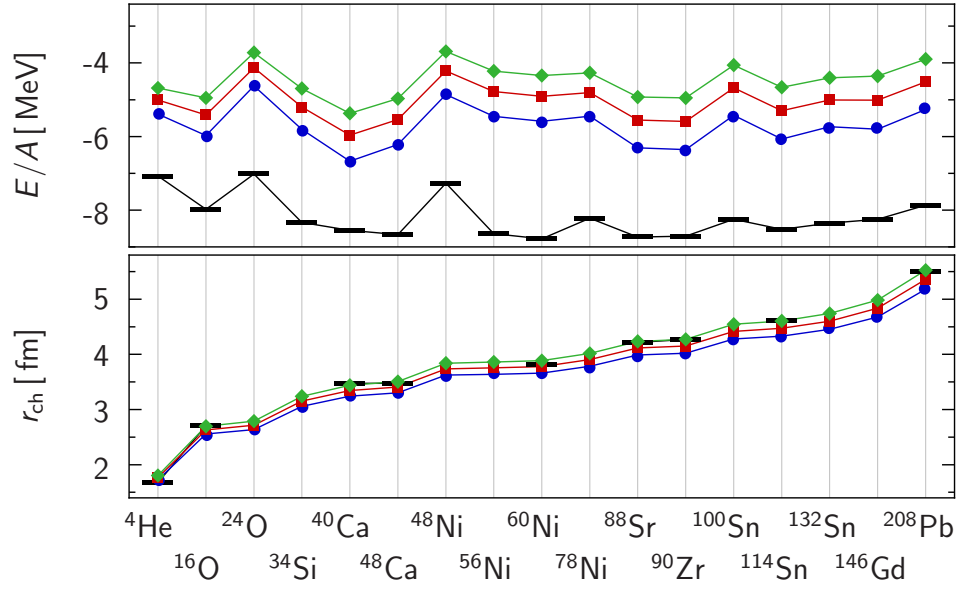


Figure E.1: Ground-state energies per nucleon and charge radii of selected closed-shell nuclei resulting from HF calculations for the UCOM(SRG) interaction with $\alpha = 0.16 \text{ fm}^4$, $e_{\text{max}} = 10$, $e_{3N} = 20$, and different three-body strengths: (●) $C_{3N} = 1.0 \text{ GeV fm}^6$, (■) $C_{3N} = 1.6 \text{ GeV fm}^6$, (◆) $C_{3N} = 2.2 \text{ GeV fm}^6$. The bars indicate the experimental values [30, 31].

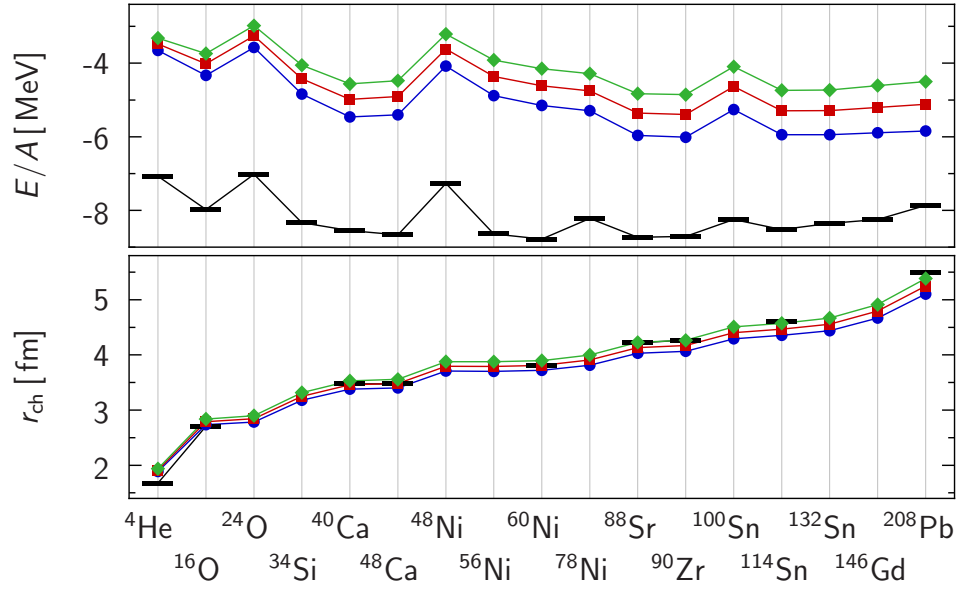


Figure E.2: Same as in Figure E.1 for the SRG interaction with $\alpha = 0.10 \text{ fm}^4$, $e_{\text{max}} = 10$, $e_{3N} = 20$, and (●) $C_{3N} = 3.8 \text{ GeV fm}^6$, (■) $C_{3N} = 4.3 \text{ GeV fm}^6$, (◆) $C_{3N} = 4.8 \text{ GeV fm}^6$.

E.1 · Hartree-Fock Results for the Contact Interaction

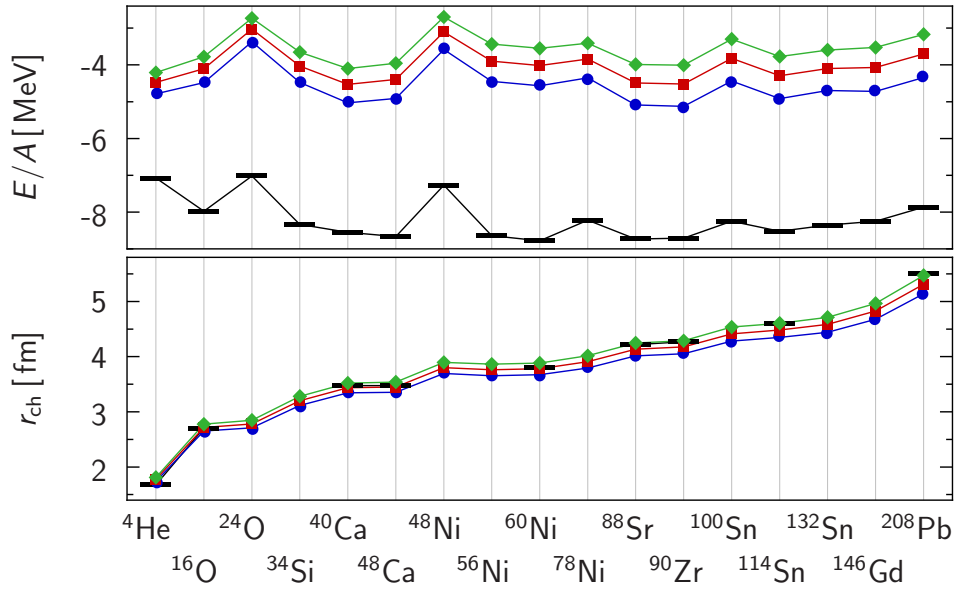


Figure E.3: Same as in Figure E.1 for the S-SRG interaction with $\alpha = 0.10 \text{ fm}^4$, $e_{\text{max}} = 10$, $e_{3N} = 20$, and (●) $C_{3N} = 1.5 \text{ GeV fm}^6$, (■) $C_{3N} = 2.0 \text{ GeV fm}^6$, (◆) $C_{3N} = 2.5 \text{ GeV fm}^6$.

E.2 Perturbative Energy Corrections for the Contact Interaction

The following figures supplement the discussion in Section 5.4.

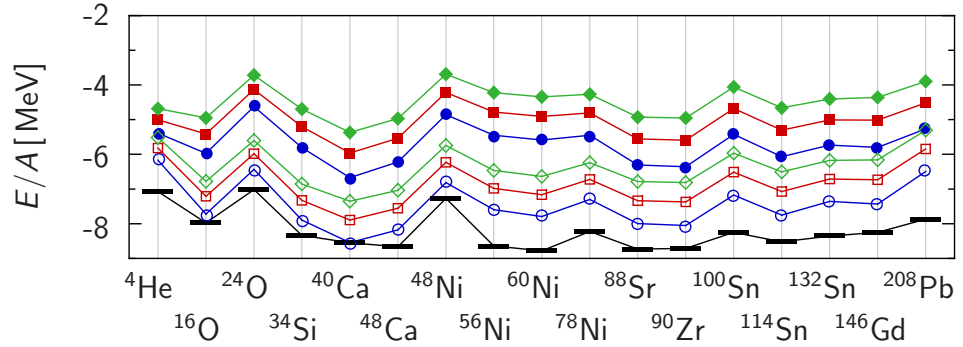


Figure E.4: Ground-state energies per nucleon based on the UCOM(SRG) interaction for $\alpha = 0.16 \text{ fm}^4$, $e_{\text{max}} = 10$, $e_{3N} = 20$, and different three-body strengths: (\bullet, \circ) $C_{3N} = 1.0 \text{ GeV fm}^6$, (\blacksquare, \square) $C_{3N} = 1.6 \text{ GeV fm}^6$, (\blacklozenge, \diamond) $C_{3N} = 2.2 \text{ GeV fm}^6$. Filled symbols indicate the HF energies, open symbols include the MBPT corrections. The bars indicate the experimental values [30].

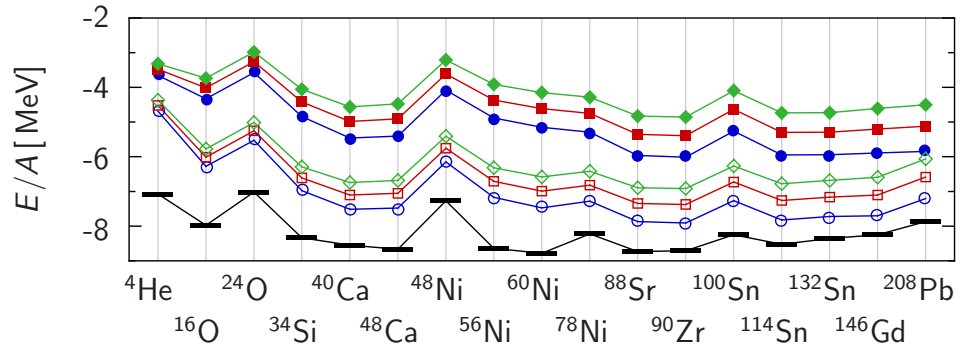


Figure E.5: Same as in Figure E.4 for the SRG interaction with $\alpha = 0.10 \text{ fm}^4$, $e_{\text{max}} = 10$, $e_{3N} = 20$, and (\bullet, \circ) $C_{3N} = 3.8 \text{ GeV fm}^6$, (\blacksquare, \square) $C_{3N} = 4.3 \text{ GeV fm}^6$, (\blacklozenge, \diamond) $C_{3N} = 4.8 \text{ GeV fm}^6$.

E.2 · Perturbative Energy Corrections for the Contact Interaction

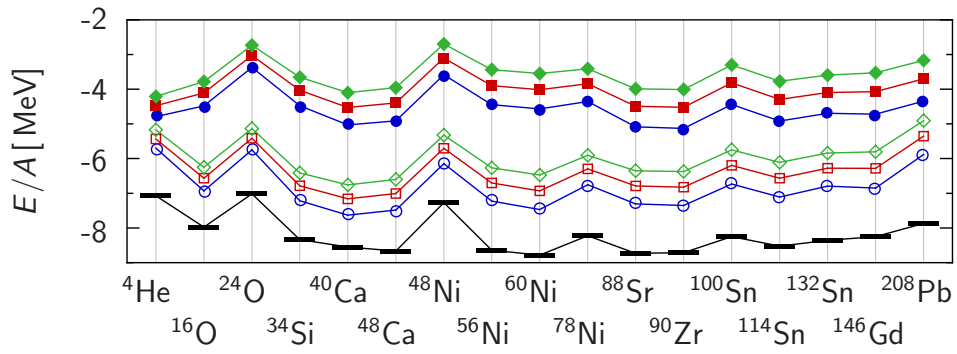


Figure E.6: Same as in Figure E.4 for the S-SRG interaction with $\alpha = 0.10 \text{ fm}^4$, $e_{\text{max}} = 10$, $e_{3N} = 20$, and (\bullet, \circ) $C_{3N} = 1.5 \text{ GeV fm}^6$, (\blacksquare, \square) $C_{3N} = 2.0 \text{ GeV fm}^6$, $(\blacklozenge, \diamond)$ $C_{3N} = 2.5 \text{ GeV fm}^6$.

E.3 Collective Excitations

The following figures supplement the discussion in Section 7.4.1.

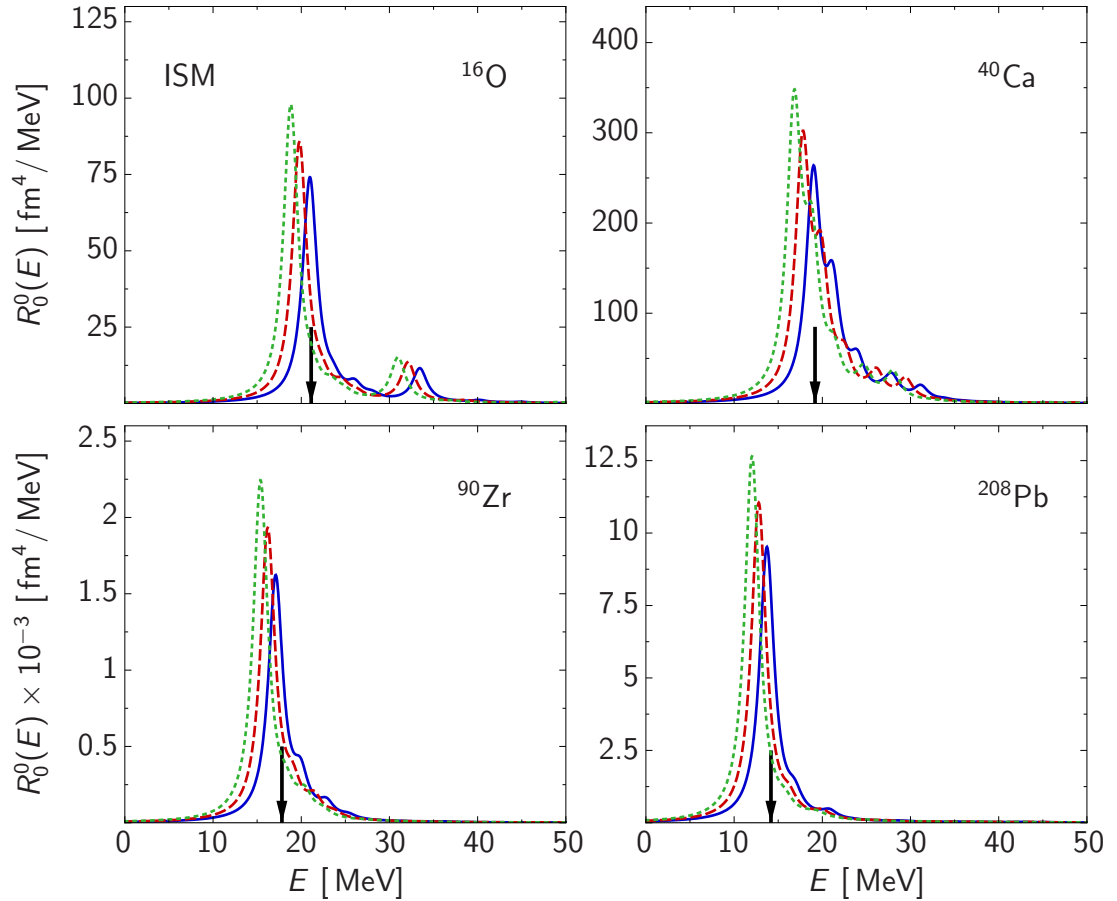


Figure E.7: Isoscalar monopole response based on the UCOM(SRG) interaction with $\alpha = 0.16 \text{ fm}^4$, $e_{\text{max}} = 10$ for different three-body strengths: (—) $C_{3N} = 1.0 \text{ GeV fm}^6$, (---) $C_{3N} = 1.6 \text{ GeV fm}^6$, (· · ·) $C_{3N} = 2.2 \text{ GeV fm}^6$. Centroid energies extracted from experiment [51–53] are indicated by arrows.

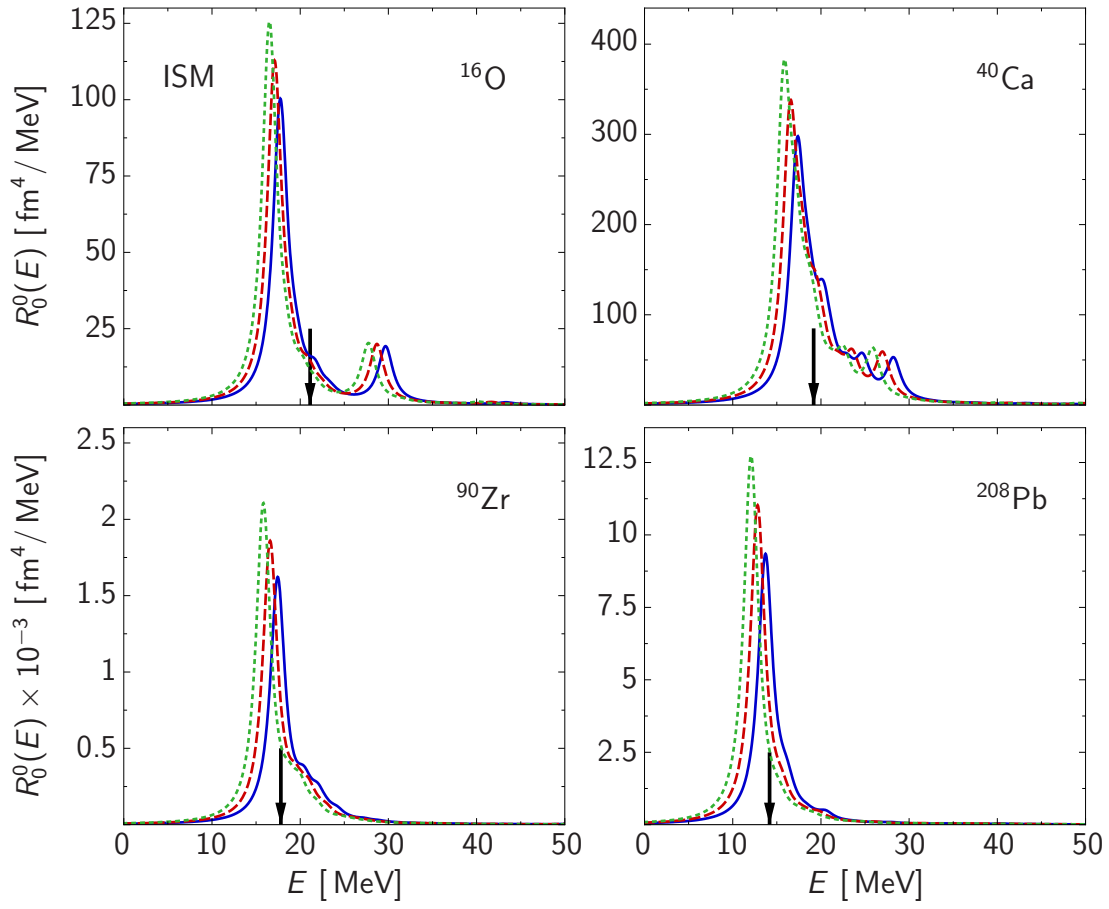


Figure E.8: Same as in Figure E.7 for the SRG interaction with $\alpha = 0.10 \text{ fm}^4$, $e_{\text{max}} = 10$, and (—) $C_{3N} = 3.8 \text{ GeV fm}^6$, (---) $C_{3N} = 4.3 \text{ GeV fm}^6$, (····) $C_{3N} = 4.8 \text{ GeV fm}^6$.

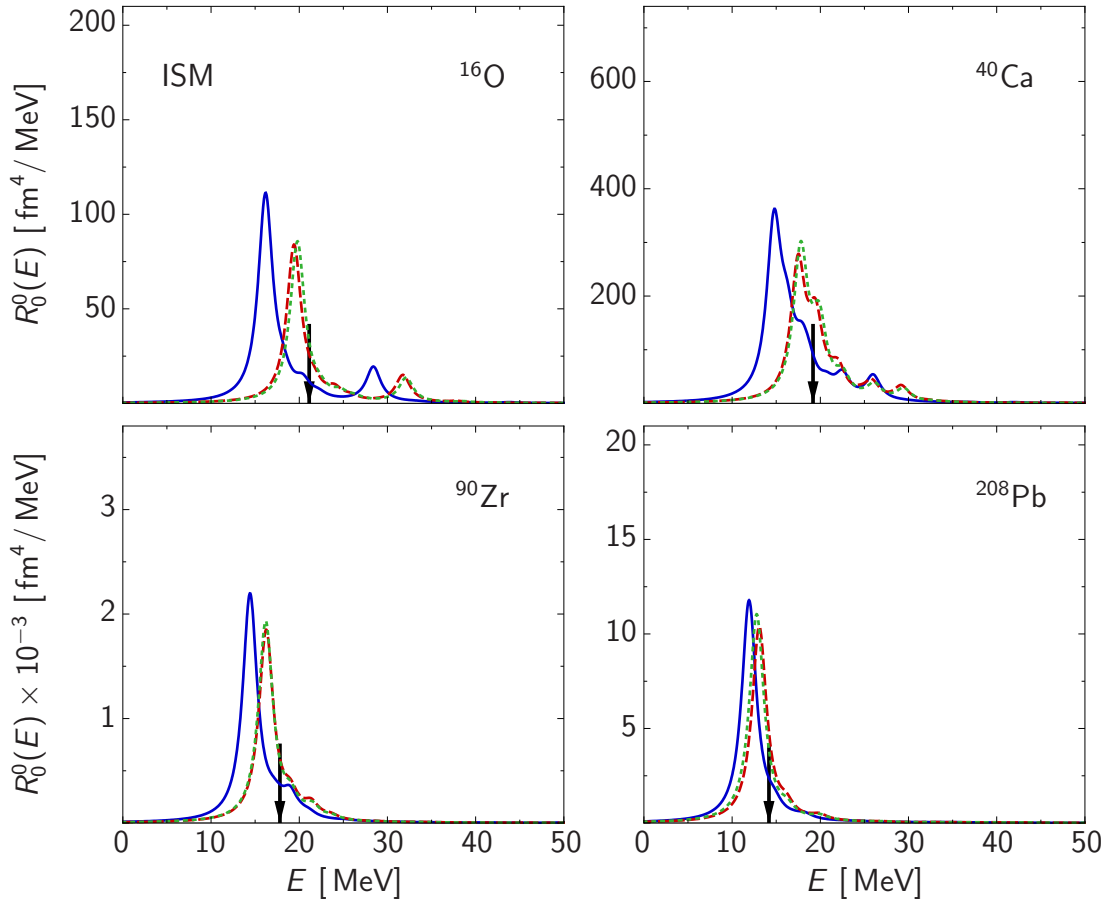


Figure E.9: Isoscalar monopole response based on the UCOM(SRG) interaction with $C_{3N} = 1.6 \text{ GeV fm}^6$, $e_{\text{max}} = 10$ for different flow parameters: (—) $\alpha = 0.04 \text{ fm}^4$, (---) $\alpha = 0.12 \text{ fm}^4$, (·····) $\alpha = 0.16 \text{ fm}^4$. Centroid energies extracted from experiment [51–53] are indicated by arrows.

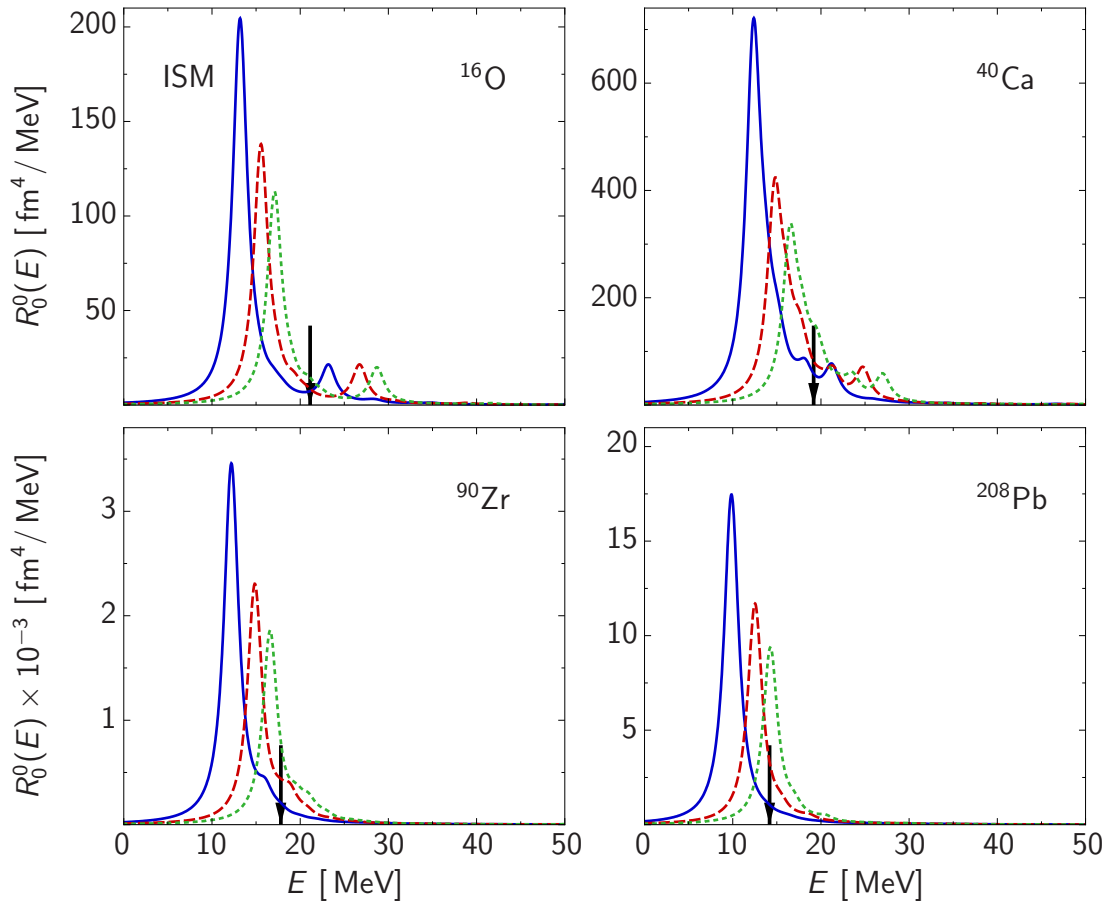


Figure E.10: Same as in Figure E.9 for the SRG interaction with $C_{3N} = 4.3 \text{ GeV fm}^6$, $e_{\text{max}} = 10$, and (—) $\alpha = 0.03 \text{ fm}^4$, (---) $\alpha = 0.06 \text{ fm}^4$, (····) $\alpha = 0.10 \text{ fm}^4$.

Appendix E · Figures

Appendix F

Notation

In the following, some frequently appearing symbols and acronyms are listed.

Quantum Numbers

e	major harmonic oscillator quantum number
n	principal harmonic oscillator quantum number
n_x	cartesian harmonic oscillator quantum number
l, m_l	single-particle orbital angular momentum
s, m_s	single-particle spin
j, m	single-particle total angular momentum
t, m_t	single-particle isospin
L, M_L	total orbital angular momentum
J, M	total angular momentum
T, M_T	total isospin

Symbols

N	neutron number
Z	proton number
A	mass number
ϵ_F	Fermi energy
m_N	nucleon mass
$c \left(\begin{matrix} j_1 & j_2 & J \\ m_1 & m_2 & M \end{matrix} \right)$	Clebsch-Gordan coefficient

Operators

H	Hamiltonian
T	kinetic energy
V_{NN}	two-body interaction
V_{3N}	three-body interaction
C, C_r, C_Ω	correlation operators: general, central, tensor
\tilde{O}	arbitrary correlated operator
\mathbf{x}	position operator
q_r	radial momentum operator
\mathbf{q}_Ω	orbital angular momentum operator
\mathbf{L}	orbital angular momentum
\mathbf{S}	spin
Π	projection operator

Acronyms

NN	nucleon-nucleon
3N	three-nucleon
AV18	Argonne V18
UCOM	Unitary Correlation Operator Method
SRG	Similarity Renormalization Group
HF	Hartree-Fock
MBPT	Many-Body Perturbation Theory
NCSM	No-Core Shell Model
RPA	Random Phase Approximation
ISM	Isoscalar Monopole
IVD	Isovector Dipole
ISQ	Isoscalar Quadrupole

Appendix F · Notation

Bibliography

- [1] Komitee für Hadronen- und Kernphysik. Hadronen- und Kernphysik – Status und Perspektiven, 2003.
- [2] Evgeny Epelbaum. Few-nucleon forces and systems in chiral effective field theory. *Prog. Part. Nucl. Phys.*, 57:654–741, 2006.
- [3] J. Langhammer. Consistent chiral three-nucleon interactions in nuclear structure. Master's thesis, TU Darmstadt, 2010.
- [4] A. Calci. Ab initio nuclear structure with SRG-transformed chiral NN plus NNN interactions. Master's thesis, TU Darmstadt, 2010.
- [5] R. B. Wiringa, V. G. J. Stoks, and R. Schiavilla. An accurate nucleon-nucleon potential with charge independence breaking. *Phys. Rev.*, C51:38–51, 1995.
- [6] R. Machleidt. The high-precision, charge-dependent bonn nucleon-nucleon potential (cd-bonn). *Phys. Rev.*, C63:024001, 2001.
- [7] V. G. J. Stoks, R. A. M. Klomp, C. P. F. Terheggen, and J. J. de Swart. Construction of high quality nn potential models. *Phys. Rev.*, C49:2950–2962, 1994.
- [8] H. Feldmeier, T. Neff, R. Roth, and J. Schnack. A unitary correlation operator method. *Nucl. Phys.*, A632:61–95, 1998.
- [9] Thomas Neff and Hans Feldmeier. Tensor correlations in the unitary correlation operator method. *Nucl. Phys.*, A713:311, 2003.
- [10] Robert Roth, Thomas Neff, and Hans Feldmeier. Nuclear Structure in the Framework of the Unitary Correlation Operator Method. *Prog. Part. Nucl. Phys.*, 65:50–93, 2010.
- [11] S. K. Bogner, R. J. Furnstahl, and R. J. Perry. Similarity Renormalization Group for Nucleon-Nucleon Interactions. *Phys. Rev.*, C75:061001, 2007.
- [12] P. Navratil, G. P. Kamuntavicius, and B. R. Barrett. Few-nucleon systems in translationally invariant harmonic oscillator basis. *Phys. Rev.*, C61:044001, 2000.

- [13] R. Roth, P. Papakonstantinou, N. Paar, H. Hergert, T. Neff, and H. Feldmeier. Hartree-fock and many-body perturbation theory with correlated realistic nn-interactions. *Phys. Rev.*, C73:044312, 2006.
- [14] N. Paar, P. Papakonstantinou, H. Hergert, and R. Roth. Collective multipole excitations based on correlated realistic nucleon-nucleon interactions. *Phys. Rev.*, C74:014318, 2006.
- [15] R. Roth, T. Neff, H. Hergert, and H. Feldmeier. Nuclear structure based on correlated realistic nucleon- nucleon potentials. *Nucl. Phys.*, A745:3, 2004.
- [16] R. Roth. *Effektive Wechselwirkungen für Quantenflüssigkeiten und Quantengase*. PhD thesis, TU Darmstadt, 2000.
- [17] T. Neff. *Short-Ranged Central and Tensor Correlations in Nuclear Many-Body Systems*. PhD thesis, TU Darmstadt, 2002.
- [18] R. Roth, H. Hergert, P. Papakonstantinou, T. Neff, and H. Feldmeier. Matrix elements and few-body calculations within the unitary correlation operator method. *Phys. Rev.*, C72:034002, 2005.
- [19] A. Günther, R. Roth, H. Hergert, and S. Reinhardt. Systematics of binding energies and radii based on realistic two-nucleon plus phenomenological three-nucleon interactions. *Phys. Rev.*, C82:024319, 2010.
- [20] Franz J. Wegner. Flow equations for hamiltonians. *Phys. Rep.*, 348:77–89, 2001.
- [21] Sergio Szpigel and Robert J. Perry. The similarity renormalization group. In A. N. Mitra, editor, *Quantum Field Theory. A 20th Century Profile*. Hindustan Publishing Co., New Delhi, 2000.
- [22] H. Hergert and R. Roth. The unitary correlation operator method from a similarity renormalization group perspective. *Phys. Rev.*, C75:051001, 2007.
- [23] R. Roth, S. Reinhardt, and H. Hergert. Unitary Correlation Operator Method and Similarity Renormalization Group: Connections and Differences. *Phys. Rev.*, C77:064003, 2008.
- [24] H. Hergert. *An Ab-Initio Approach to Pairing Phenomena Using Modern Effective Interactions*. PhD thesis, TU Darmstadt, 2008.
- [25] S. Reinhardt. Comparison and Connection of the Similarity Renormalization Group and the Unitary Correlation Operator Method. Diploma thesis, TU Darmstadt, 2008.

- [26] E. D. Jurgenson, P. Navratil, and R. J. Furnstahl. Evolution of Nuclear Many-Body Forces with the Similarity Renormalization Group. *Phys. Rev. Lett.*, 103:082501, 2009.
- [27] A. Zapp. Kernstruktur mit effektiven Dreiteilchenpotentialen. Diploma thesis, TU Darmstadt, 2006.
- [28] R. Roth. Die Methode der unitären Korrelatoren und ihre Anwendung auf kurzreichweitig abstoßende Nukleon-Nukleon-Wechselwirkungen. Diploma thesis, TU Darmstadt, 1997.
- [29] S. Eidelman et al. Review of particle physics. *Phys. Lett.*, B592:1, 2004.
- [30] G. Audi and A. H. Wapstra. The 1995 update to the atomic mass evaluation. *Nucl. Phys.*, A595:409–480, 1995.
- [31] H. De Vries, C. W. De Jager, and C. De Vries. Nuclear charge-density-distribution parameters from elastic electron scattering. *At. Data Nucl. Data Tables*, 36(3):495 – 536, 1987.
- [32] V. I. Isakov, K. I. Erokhina, H. Mach, M. Sanchez-Vega, and B. Fogelberg. On the difference between proton and neutron spin-orbit splittings in nuclei. *Eur. Phys. J.*, A14:29–36, 2002.
- [33] Y. Wang, C. C. Foster, R. D. Polak, J. Rapaport, and E. J. Stephenson. Proton- ^{90}Zr mean field between -60 and +185 MeV from a dispersive optical model analysis. *Phys. Rev.*, C47:2677–2689, 1993.
- [34] J. P. Delaroche, Y. Wang, and J. Rapaport. Neutron- ^{90}Zr mean field from a dispersive optical model analysis. *Phys. Rev.*, C39:391–404, 1989.
- [35] A. Szabo and N. S. Ostlund. *Modern Quantum Chemistry*. Dover Publications, Mineola, New York, 1st edition, 1996.
- [36] Robert Roth and Joachim Langhammer. Pade-resummed high-order perturbation theory for nuclear structure calculations. *Phys. Lett.*, B683:272–277, 2010.
- [37] I. Talmi. Nuclear spectroscopy with harmonic-oscillator wave functions. *Helv. Phys. Acta*, 25:185, 1952.
- [38] M. Moshinsky. Transformation brackets for harmonic oscillator functions. *Nucl. Phys.*, 13:104, 1959.
- [39] C. Cohen-Tannoudji, B. Diu, and F. Laloë. *Quantenmechanik*. Walter de Gruyter GmbH & Co. KG, Berlin, 2nd edition, 1999.

- [40] <http://www.wolfram.com/products/mathematica/index.html>.
- [41] L. Chaos-Cador and E. Ley-Koo. Common generating functions of complete harmonic oscillator wave functions and transformation brackets in D dimensions. *Int. J. Quant. Chem.*, 97:844–853, 2004.
- [42] D. A. Varshalovich, A. N. Moskalev, and V. K. Khersonskii. *Quantum Theory of Angular Momentum*. World Scientific, 1988.
- [43] P. Navratil, J. P. Vary, and B. R. Barrett. Large basis ab initio no-core shell model and its application to c-12. *Phys. Rev.*, C62:054311, 2000.
- [44] D. Vautherin and D. M. Brink. Hartree-Fock calculations with Skyrme's interaction. 1. Spherical nuclei. *Phys. Rev.*, C5:626–647, 1972.
- [45] M. Waroquier, K. Heyde, and H. Vincx. Antisymmetry in the three-nucleon interaction matrix elements. *Phys. Rev.*, C13:1664–1673, 1976.
- [46] O. Bohigas, A. M. Lane, and J. Martorell. Sum Rules for Nuclear Collective Excitations. *Phys. Rept.*, 51:267, 1979.
- [47] D. J. Rowe. *Nuclear Collective Motion*. Methuen and Co. Ltd., London, 1st edition, 1970.
- [48] J. Suhonen. *From Nucleons to Nucleus. Concepts of Microscopic Nuclear Theory*. Springer, Berlin, 1st edition, 2007.
- [49] P. Ring and P. Schuck. *The Nuclear Many-Body Problem*. Springer, 1st edition, 1980.
- [50] H. Hergert. personal communication.
- [51] Y. W. Lui, H. L. Clark, and D. H. Youngblood. Giant resonances in ^{16}O . *Phys. Rev.*, C64:064308, 2001.
- [52] D. H. Youngblood, Y. W. Lui, and H. L. Clark. Isoscalar E0, E1, and E2 strength in ^{40}Ca . *Phys. Rev.*, C63:067301, 2001.
- [53] D. H. Youngblood, H. L. Clark, and Y. W. Lui. Incompressibility of Nuclear Matter from the Giant Monopole Resonance. *Phys. Rev. Lett.*, 82:691–694, 1999.
- [54] S. F. LeBrun, A. M. Nathan, and S. D. Hoblit. Photon scattering in the giant dipole resonance region of ^{16}O . *Phys. Rev.*, C35:2005–2010, 1987.
- [55] A. Veyssi re, H. Beil, R. Berg re, P. Carlos, A. Lep tre, and A. De Miniac. A study of the photoneutron contribution to the giant dipole resonance of s-d shell nuclei. *Nucl. Phys. A*, 227(3):513 – 540, 1974.

- [56] B. L. Berman et al. Photoneutron Cross Sections for ^{90}Zr , ^{91}Zr , ^{92}Zr , ^{94}Zr , and ^{89}Y . *Phys. Rev.*, 162:1098–1111, 1967.
- [57] A. Veyssière, H. Beil, R. Bergère, P. Carlos, and A. Leprêtre. Photoneutron cross sections of ^{208}Pb and ^{197}Au . *Nucl. Phys. A*, 159(2):561 – 576, 1970.
- [58] F. E. Bertrand, G. R. Satchler, D. J. Horen, and A. van der Woude. Systematics of the isoscalar giant monopole resonance from 60 MeV inelastic proton scattering. *Phys. Lett. B*, 80(3):198 – 202, 1979.
- [59] S. Raman, C. W. G. Nestor, Jr, and P. Tikkanen. Transition probability from the ground to the first- excited $2+$ state of even-even nuclides. *Atom. Data Nucl. Data Tabl.*, 78:1–128, 2001.
- [60] J. Heisenberg, Jechiel Lichtenstadt, Costas N. Papanicolas, and J. S. McCarthy. Excitation of low lying natural parity levels in ^{208}Pb by inelastic electron scattering. *Phys. Rev.*, C25:2292–2308, 1982.
- [61] P. Papakonstantinou. personal communication.
- [62] Robert Roth. Importance Truncation for Large-Scale Configuration Interaction Approaches. *Phys. Rev.*, C79:064324, 2009.
- [63] K. L. G. Heyde. *The Nuclear Shell Model*. Springer, Berlin, Heidelberg, 2nd edition, 1994.
- [64] C. Stumpf. Entartete Vielteilchen-Störungstheorie und Padé-Resummation für Kernspektren. Bachelor thesis, TU Darmstadt, 2010.
- [65] G. Hagen, T. Papenbrock, D. J. Dean, A. Schwenk, A. Nogga, M. Włoch, and P. Piecuch. Coupled-cluster theory for three-body Hamiltonians. *Phys. Rev.*, C76:034302, 2007.
- [66] R. Roth. Theoretische Kernphysik, WS 2007/2008. Vorlesungsskript.

Danksagung

Im Laufe meiner Doktorarbeit haben mich viele Leute unterstützt.

An erster Stelle möchte ich mich bei Professor Robert Roth bedanken. Durch die Arbeit in seiner Gruppe habe ich viel gelernt. Er hat es auf vorbildliche Weise verstanden, den optimalen Mittelweg zu finden: Auf der einen Seite gewährte er ein selbst gewähltes Maß an Freiraum und auf der anderen Seite stand er stets als Ansprechpartner zur Verfügung.

Professor Jochen Wambach danke ich für die Übernahme des Zweitgutachtens.

Die TNP++ Gruppe hat während der vergangenen Jahre für eine anregende Arbeitsatmosphäre gesorgt. Dabei möchte ich besonders Joachim Langhammer, Angelo Calci und Panagiota Papakonstantinou hervorheben, die diese Arbeit Korrektur gelesen haben. Panagiota hat mir außerdem ihren RPA Code zur Verfügung gestellt. Obwohl Heiko Hergert inzwischen nicht mehr bei uns ist, hat er stets schnell und zuverlässig zur Beantwortung meiner Fragen beigetragen.

Bei der TU Darmstadt bedanke ich für die Gewährung eines Promotionsstipendiums.

Der Deutschen Forschungsgemeinschaft danke ich für die Unterstützung im Rahmen des Sonderforschungsbereiches 634.

Nicht zuletzt möchte ich an dieser Stelle meine Familie erwähnen, die mich alle nach Kräften und in unterschiedlicher Weise unterstützt haben.

Besonderer Dank geht an Marc und an Wienke für ihre ansteckende Lebensfreude.

Danke an alle!

Lebenslauf

Name: Anneke Ingeluse Günther, geb. Zapp
Geburtsdatum: 13. Mai 1983
Geburtsort: Eckernförde
Staatsangehörigkeit: deutsch
Familienstand: verheiratet, 1 Kind

Bildungsweg

8/1989 – 7/1990 Besuch der Grundschule Krempe, Schleswig-Holstein
8/1990 – 7/1992 Besuch der Deutschen Botschaftsschule Addis Abeba, Äthiopien
(Grundschule)
8/1992 – 7/1996 Besuch der Deutschen Botschaftsschule Addis Abeba, Äthiopien (Gym-
nasium)
8/1996 – 6/2001 Besuch des Nordsee-Gymnasium-Büsum, Schleswig-Holstein
6/2001 Abitur

9/2001 – 7/2003 Studium der Physik an der Christian-Albrechts-Universität Kiel
7/2003 Vordiplom Physik
10/2003 – 12/2006 Studium der Physik an der TU Darmstadt
12/2005 – 11/2006 Anfertigung der Diplomarbeit *"Kernstruktur mit effektiven Drei-
teilchenpotentialen"*
12/2006 Diplom

seit 1/2007 Promotionsstudium an der TU Darmstadt und Anfertigung der Disser-
tation
1/2007 – 4/2010 Stipendiatin eines Promotionsstipendiums der TU Darmstadt
seit 5/2010 Wissenschaftliche Mitarbeiterin am Institut für Kernphysik